Design Guideline of High-Packing-Density Composite Cathodes for All-Solid-State Lithium-Sulfur Batteries

Wenli Pan

Design Guideline of High-Packing-Density Composite Cathodes for All-Solid-State Lithium-Sulfur Batteries

Wenli Pan

Graduate School of Human and Environmental Studies

Kyoto University

Supervised by

Prof. Dr. Yoshiharu Uchimoto

Contents

Chapter 1 Introduction

1.1 Research background

With rapidly rising energy demands and increasing extreme weather, there is an urgent need to create a sustainable energy future and protect fragile ecology as well [1, 2]. However, these energy generations exhibit pronounced intermittency patterns, predominantly governed by meteorological and diurnal variations, which introduce considerable challenges pertaining to the consistent and reliable supply of renewable energy. To confront the intermittency challenge, smart grids have emerged to accommodate these renewable sources by optimizing energy flow and distribution[3, 4]. As the key technical of smart grids, secondary batteries have been paid more and more attention, affording the capability to store surplus energy during periods of heightened production while discharge during intervals of diminished generation. In addition, driven by the need to decrease carbon emissions from the transportation sector and improve energy utilization efficiency, electric vehicles (EVs) offer a clean and energy-efficient alternative, developing substantially in recent years[5]. Unlike the static grids, the rapidly increasing development of electric vehicles raises higher requirements for batteries with high energy density and good rate performance. As for both fields of smart grids and electric vehicles, rechargeable batteries play a crucial role because they represent an efficient means of storing and releasing energy electrochemically[6]. To meet these demands for sustainable and high-efficiency energy, an extensive worldwide search has been prompted for better secondary battery technologies for a few decades.

From the past few decades, the importance of portable energy storage devices has been raised. Many energy storage systems have been widely explored and used, such as fuel cells, supercapacitors, lead acid batteries and lithium-ion batteries[7, 8]. As the first commercially successful rechargeable batteries, lead acid batteries use Pb anode, PbO_2 cathode and concentrated H_2SO_4 aqueous solution as electrolyte [9]. The reversible electrochemistry reactions depend on the consumed and liberated sulfuric acid during discharge and charge, allowing the state of charge to be determined by measuring the specific gravity. Although lead-acid batteries still have an overwhelming share of the

secondary battery market due to their low-cost property, their further usability is limited by a low gravimetric energy density of about 40 Wh kg^{-1}. A supercapacitor, using an electric double layer with reversible redox reactions for electric charge storage, possesses fast storage capability and enhanced cyclic stability but a very low energy density[10]. Fuel cells are energy storage devices that convert chemical energy to electrical energy[11]. Fuels like hydrogen and oxygen pass through electrodes where they are converted to water. Although fuel cells have high energy conversion efficiency, high power density and low pollutant emission; the platinum metal catalyst and the limitation of operation conditions lead to high costs and undesirable outcomes from the industry side. Unlike those energy storage devices before, lithium-ion batteries (LIBs) possess high energy density, desirable cycling stability and affordable cost, having successfully revolutionized consumer electronics and electric-powered transportation over past 30 years[12, 13].

Throughout these years, though secondary batteries, especially LIBs have been successfully commercialized in people's daily lives, it will be a major challenge to developing LIBs to achieve simultaneous goals of high energy/power density, safety and lower cost when considering not only large-scale energy storage but also highly potential EVs market.

1.2 Lithium-ion batteries

1.2.1 The development of lithium-ion batteries

Lithium primary batteries were developed first before the lithium secondary batteries. Some of the earliest lithium batteries concepts came from Japan, where Panasonic assembled the $Li/(CN)_n$ battery for fishing floats[14]. The working principle is that lithium intercalates the carbon monofluoride lattice and forms lithium fluoride as a result of the following process: $Li+(CF)_n \rightarrow Li_x(CF)_n \rightarrow C + LiF$. And Sanyo developed one of the earliest lithium batteries with the Li/MnO_2 system[15]. The success of lithium primary batteries has sparked more and more research on lithium secondary batteries, which makes the reaction reversible.

The early work on lithium secondary batteries discovered that a range of electron-donating molecules and ions could intercalate into a layered structure material, in particular, TaS_2[16]. With the deep investigations of layered structure materials, titanium disulfide (TiS_2) has drawn much attention as an energy storage electrode. Lithium intercalation could form a single phase over the entire composition range of Li_xTiS_2 ($0 \leq x \leq 1$) [17]. The stable phase enables all the lithium to be extracted reversibly, without energy consumption for rearrangement of the host material. The Exxon company had put much effort into applying TiS_2 for lithium rechargeable batteries. A battery composed of TiS_2 as cathode and lithium metal as anode achieved almost 1000 cycles with deep charge and discharge, with low-capacity decay of less than 0.05% per cycle[18]. However, the uneven surface of lithium metal could cause different deposition rates and the formation of lithium dendrite on the anode, which hazards cycling stability and safety of the batteries. Although the researchers replaced lithium metal with Li-Al alloy to reduce the influence of lithium dendrite[19], Li-Al alloy as anode still suffers from high volume expansion, limited cycles and low diffusion rate of Li through the alloy[20]. Therefore, the lithium rechargeable batteries based on TiS_2 as cathode and Li-Al anode could only operate with shallow charge and discharge. Besides, many early works on lithium secondary batteries used sulfur S and lithium as the two electrodes and a salt as the electrolyte[21, 22]. This kind of battery operates at about 450 °C so that both electrodes and electrolytes are molten and can react. However, such batteries have issues such as self-discharge on standing, as well as the high resistance of the cathode.

In 1991, Sony made the first successfully commercialized LIBs, being composed of $LiCoO_2$ cathode with a carbon anode[23], which still dominate the lithium battery market now. The illustration of this battery is shown in Figure 1.1[24]. The charge-discharge reaction follows the equations below:

Cathode electrode：$Li_{1-x}CoO_2 + xLi^+ + xe^- \leftrightarrow LiCoO_2$

Anode electrode： $Li_xC_6 \leftrightarrow xLi^+ + xe^- + C_6$

Total reaction：$Li_{1-x}CoO_2 + Li_xC_6 \leftrightarrow LiCoO_2 + C_6$

Instead of Li metal or Li alloy that contain high-reactive Li, the carbon anode forms the compound LiC_6 during the lithiation process, thereby making batteries much safer. Though the use of graphitic carbon leads to the loss of 100-300 mV in cell potential, it is feasible to couple with the higher potential $LiCoO_2$ cathode. In the $LiCoO_2$ structure, lithium and cobalt ions are at octahedral 3a and 3b sites, respectively, and layers of cubic close-packed oxygen ions separate them. The unit cell of the layered form consists of three edge-shared CoO_6 octahedra separated by interstitial Li layers. The theoretical capacity of $LiCoO_2$ is 274 mAh $g^{-1,}$ while the maximum achievable is about 150 mAh g^{-1}, which is only half of the theoretical value[25]. Following the extraction of 50% of lithium from the parent structure, a transition from hexagonal to monoclinic phase occurs, impacting structural stability. This inherent instability diminishes the experimental electrochemical capacity and restricts lithium removal from the hexagonal lattice to 0.5. Furthermore, cobalt, a scarce metal comprising only approximately 0.0025% of the Earth's crust[26], is primarily sourced as a byproduct from copper or nickel mines. There is a growing concern that the extensive use of cobalt in EVs could deplete its reserves. Consequently, the limited specific capacity and anticipated rise in $LiCoO_2$ prices pose challenges to the rapid expansion of large-scale energy storage and EV markets.

The soaring expenses and restricted capacity associated with $LiCoO_2$ have prompted the development of new types of the materials by substituting cobalt with Mn and Ni to give $LiNi_{1-y-z}Mn_yCo_zO_2$ (NMC) [27]. In NMC, each transition metal serves a distinct purpose: Mn^{3+} tends to undergo oxidation during synthesis, transitioning to Mn^{4+} , which facilitates the reduction of Ni^{3+} to Ni^{2+} as the $Mn^{3+/4+}$ band lies above the $Ni^{2+/3+}$ band. Consequently, Mn^{4+} helps the incorporation of Ni as a stable Ni^{2+} into NMC and serves as a structural

stabilizer without participating in the charge–discharge process. Ni^{3+} can be charged to Ni^{4+} without loss of oxygen from the lattice, and Ni^{3+} also offers good structural stability. Hence, the trend to progressively increase the Ni content and decrease the Co content in NMC is due to the increased capacity and cost reduction.

1.2.2 The limits of lithium-ion batteries

Although LIBs still dominate the secondary battery market especially for portable devices such as cell phones and laptops, there are several drawbacks that limit LIBs application for smart grids and electric vehicles with higher requirements[28]. Nickel and manganese-substituted NMC possesses higher capacity with expected lower cost, a concern raised for poorer thermal stability with an increase in nickel content. Existing LIBs that use organic solvents as electrolytes are unsafe owing to their flammable property[29], which has hindered their application to state-of-the-art batteries and energy storage systems. Furthermore, demands for better performance are being predicted, such as for higher energy density suitable for electric vehicles capable of long-distance driving with short charging times and perfect safety compared to existing LIBs. However, performance enhancement is limited by safety concerns. First, fast charging is accompanied by lithium dendrite formation from a high current density, which is why lithium metal cannot be used as an anode material despite being the best anode material for LIB systems[30]. This also prevents the improvement of the energy density of LIBs. Therefore, next-generation batteries must be developed with safety, energy density, power density, and operation environment considered. Among the candidates for next-generation batteries, lithium-sulfur batteries (all-solid-state batteries), in which organic liquid electrolytes are replaced with solid electrolytes, have attracted attention and are expected to be promising. The following section discusses about the lithium-sulfur batteries.

1.3 Brief Introduction of Lithium-sulfur batteries

Lithium–sulfur batteries are promising lithium secondary batteries for next-generation energy storage devices. Unlike the traditional LIBs with transition metal oxides as cathodes and graphite as anode, lithium–sulfur batteries consist of elemental sulfur and lithium metal, as the cathode and anode, respectively. Due to the light weight of sulfur and lithium metal, they can deliver outstandingly high specific capacities, as 1675 mAh g^{-1} and 3860 mAh g^{-1}. Considering an average voltage of ~2.1 V, the energy density of lithium-sulfur batteries is theoretically anticipated to reach up to 2600 Wh kg^{-1}, which is five times as high as that of the current LIBs[31]. Moreover, elemental sulfur is abundant, inexpensive compared with metallic minerals, low-toxic, environmentally friendly, and degradable; it presents great potential for large-scale practical applications. Depending on the state of the electrolyte applied, lithium-sulfur batteries can be divided into liquid and all-solid-state systems.

Conventional lithium–sulfur batteries are mainly comprised of a cathode, an anode, and a liquid electrolyte with good ionic conductivity. The schematic illustration is shown in Figure 1.2[32]. As for cathodes for typical lithium–sulfur batteries, they are normally consist of sulfur as the active material, a conductive material such as the conductive carbon, a binder, and a current collector, which supports the electrode. It should be noted that some self-supporting cathodes with porous carbon materials do not require the use of binders and additional current collectors[33]. As for the anode side, metallic lithium foil is the most commonly used anode for lithium–sulfur batteries to realize highest energy density[34]. Organic ether electrolytes with dissolved lithium salts are commonly used for conventional liquid lithium-sulfur batteries. Between the cathode and anode, a polymer separator is used to separate the two electrodes. The final discharge product of lithium–sulfur batteries is Li_2S, and the corresponding electrochemical reaction is: $S_8 + 16Li^+ + 16e^- \rightarrow 8Li_2S$ (E = 2.15 V vs. Li^+/Li).

However, the practical application of lithium–sulfur batteries is still hindered by multiple fundamental problems and technical challenges, which include:

(1) The poor electronic and ionic conductivities of Li_2S and its corresponding oxidized product S[35]. Due to the electronic and ionic insulation nature, the active materials cannot be fully reversible, leading to the low utilization of active materials and far lower practical energy density than theoretical energy density. During the discharge process, the

precipitation of insulating Li_2S will lead to a passivation of the cathode, resulting in a sharp decline in the battery's performance.

(2) Polysulfide shuttle effect[36]. During the cycling process, the intermediate long-chain lithium polysulfides are easy to dissolve in the ether-based electrolyte, resulting in continuous loss of active materials, rapid fade of battery capacity, self-discharge and low coulombic efficiency.

(3) The huge volume expansion of sulfur during lithiation[37]. Due to the density difference between sulfur and lithium sulfide (S_8: 2.03 g cm^{-3}, Li_2S: 1.67 g cm^{-3}), the volume expansion rate of sulfur is as high as 80% when it is completely transformed into lithium sulfide, which may lead to the rupture and damage of the electrode.

(4) The unstable solid electrolyte interface (SEI) film[38]. Lithium metal reacts with the electrolyte and forms an unstable SEI film, reducing Li source and continuously consuming electrolyte.

Numerous strategies have been developed to tackle these challenges. One kind of strategy are aiming at development of the "host" materials to store active materials and inhibit the polysulfide dissolution[39, 40]. The "host" materials could have different architectures, such as the "interlayer" structures to sandwich active materials [41, 42], and the "core–shell" architectures to keep active materials inside [43, 44]. In addition to developing architectures for cathodes to suppress the dissolution of polysulfides, some strategies have been focused on electrolytes, such as developing concentrated electrolytes[45] and applying different electrolyte additives to alleviate polysulfide dissolution and to form more stable SEI [46]. Despite these efforts, these approaches have not fully resolved the challenges, particularly in the case of cathodes with high areal capacity loading (4–10 mAh cm^{-2}). To achieve the high areal capacity loading, the small fraction of electrochemical inactive materials (such as conductive additives and separator membranes) is required, while the most reported cathodes are commonly with excessive conductive additives (30~40 wt%). Meanwhile, the fabrication cost should be low and the corresponding batteries can exhibit higher energy densities[47]. Furthermore, significant safety concerns persist due to the instability of liquid electrolytes when in contact with lithium anode, resulting in issues like lithium metal corrosion, infinite volume expansion, dendrite growth, and, ultimately, thermal runaway [48].

One feasible method is replacing the flammable organic electrolyte with the solid electrolyte (SE) that has a nonflammable nature to construct solid-state lithium-sulfur batteries (SSLBs). Compared with the conventional lithium-sulfur batteries based on flammable liquid electrolytes, SSLBs could provide various advantages: (1) the cycling stability and coulombic efficiency could be improved because polysulfides can be blocked by SEs thus eliminating polysulfides shuttling effect[49]; (2) the stability of Li stripping/plating can be enhanced due to the higher mechanical strength[50]; (3) the safety of battery operation can be greatly improved since the SEs would not evaporate with thermal runaway and consequently do not cause undesirable fire hazards [51, 52]. Therefore, the trend of developing solid-state lithium-sulfur batteries, including quasi-solid-state and all-solid-state lithium-sulfur batteries (ASSLSBs), is increasing rapidly [53].

1.4 The all-solid-state lithium sulfur batteries

Given the concerns surrounding the shuttle effect and flammability inherent in organic liquid electrolytes, researchers have proposed solid-state lithium-sulfur batteries employing solid electrolytes (SEs) as potential solutions. It is believed that SEs can block the polysulfides dissolution and thus eliminate the shuttle effect. However, different electrochemical reactions may occur and new challenges have to be met after replacing liquid electrolyte with SE. Before discussing about the challenges and possible solutions, it is important to understand the working principle of solid-state lithium-sulfur batteries.

As shown in Figure 1.3, lithium-sulfur batteries with different kinds of solid-state electrolytes could demonstrate different charge-discharge curve behaviors [54]. The all-solid-state lithium-sulfur batteries (ASSLSBs) with poly(ethylene oxide) (PEO)-based SEs show a double plateau with one slope in the middle (Figure 3a), This behavior closely resembles that of lithium-sulfur batteries employing organic liquid electrolyte [55], which arises from some analogical structures between PEO-based electrolytes and ether-based electrolytes[56]. Therefore, the polysulfide shuttle effect could also be observed in PEO-based ASSLSBs, which is analogous to liquid lithium-sulfur batteries. The reactions during discharge include: the solid octa-atomic sulfur reacts with lithium-ions to form soluble long-chain polysulfides Li_2S_8 (the upper plateau of ~2.4 V); polysulfides Li_2S_8 forms soluble Li_2S_6 and Li_2S_4 through one phase transition (slope in the middle); soluble Li_2S_4 transforms to

solid Li_2S_2 and Li_2S (the long lower plateau of ~2.1 V); the final reaction is Li_2S_2 to Li_2S (< 1.9 V), which is a solid-solid transition with sluggish kinetics[57].

As for ASSLSBs based on inorganic SEs, such as sulfur-based and oxide-based electrolytes, there is only one slope with solid-solid reaction route, while the reaction mechanism is controversial [58]. Due to the single plateau behavior, some researchers believe the electrochemical reaction is based on the direct conversion reaction between S_8 and Li_2S without the formation of soluble polysulfides. However, some hold the view that intermediate polysulfides form in the solid state. In any case, the reaction kinetics is inherently sluggish in solid state[59], giving rise to new challenges of facilitating the reaction and guaranteeing high sulfur utilization based on both electronic and ionic insulating nature of S and Li_2S.

1.4.1 The cathodes for solid-state lithium-sulfur batteries

1.4.1.1 Composite cathodes with typical conductors

As the active material of cathodes for ASSLSBs, element sulfur S has extremely low electronic conductivity of ~ 5×10^{-30} S cm^{-1}, and its discharged product Li_2S has both low electronic conductivity (~10^{-9} S cm^{-1}) and ionic conductivity (~10^{-13} S cm^{-1}). Such an insulating nature becomes a common issue in both liquid lithium-sulfur batteries and ASSLSBs[35, 60]. The solution to these issues is relatively straightforward: to disperse electronic conductors like conductive carbons and ionic conductors such as SE well into active material to form a composite cathode with smooth electron transport pathway. The preparation process of composite cathodes for conventional lithium-sulfur involves admixing and dispersing the active materials, conductive additives and binder in a solvent to make slurry[61], which is subsequently coated on the aluminum foil as a current collector. Regarding the preparation of composite cathodes for ASSLSBs, the first step is mixing active materials and conductive additives as well-dispersed mixture. The powder mixture can be prepared as free-standing and solvent-free cathodes with a binder added, or it can be loaded onto the SE layer and pressed together into pellets.

To improve the electronic conductivities, the conductive carbon materials have received much attention because of several advantages: (1) their good electronic conductivities can meet the requirements for improving the electronic conductivity[61]; (2) their various morphologies can serve as different host materials for composite cathodes; (3) the carbon

materials with porous structure can not only relieve the volume change but also enhance charge transport and shorten distance of lithium-ion transport[39]. Graphite is also used for anode materials with outstanding electronic conductivity because its $sp^2 - sp^2$ hybrid bond and hexagonal structure allow electrons to be delocalized[62], which is commonly applied for improving the electronic conductivities of composite cathodes[63]. In addition to the graphite, various conductive carbon materials with high degree of graphitization[64] and different morphologies have been applied in the cathode materials of ASSLSBs, including acetylene black (AB) [65, 66], Super P [67, 68], Ketjen black (KB) [69], carbon fibers[70], carbon nanotubes[71], graphene nanosheets[72], reduced graphene oxide (rGO) [73], porous carbon materials[74], etc. Among them, the porous carbon materials can be synthesized with different templates. Accordingly, the porous carbon materials can be obtained with different sizes of pore, including microporous (D < 2 nm), mesoporous (2 nm < D < 50 nm) and microporous (D > 50 nm) carbon [37]. These carbon additives could shorten ionic and electronic transport pathways, thereby enhancing mixed conduction. Consequently, this porosity exerts a direct and substantial impact on the reaction kinetics of composite cathodes.

Besides carbon, conductive polymers also play an important role in lithium-sulfur batteries, such as polypyrrole, polyaniline, poly(3,4-(ethylenedioxy)thiophene) (PEDOT) [75-78]. Gracai et al. reported the sulfur-containing copolymer as active material for PEO-based ASSLSB to restrain the shuttle effect arising from polysulfides and thus to improve cycling stability of ASSLSB[79]. The sulfur-containing copolymer (p(S-DVB)) was synthesized from a mixture of sulfur and 3, 5-divinylbenzene. The composite cathode was then formed by mixing KB and PEO electrolyte. This p(S-DVB) composite cathode delivered a capacity of 650 mAh g^{-1} at 0.1 C under 70 °C after 50 cycles. Moreover, it was also claimed that the sulfur-containing polymer as an active material could mitigate the polysulfide shuttle effect.

Due to the poor Li-conduction of Li_2S which is a discharged product of sulfur, lithium transport pathway has to be established through the cathode composites. Similar to the conventional liquid electrolytes providing Li-conduction among active material particles, SEs, as the replacement with liquid electrolytes, are naturally regarded as lithium-ion conductors for ASSLSBs. As for the selection of proper SEs, sulfide-based SEs, such as $Li_{10}GeP_2S_{12}$ [80], Li_6PS_5Cl [81]and Li_7P_3S11 [82] possess high ionic conductivities of $10^{-3} \sim 10^{-2}$

S cm^{-1}, which are comparable to those of ether-based electrolytes. Meanwhile, sulfide-based SEs could keep relatively stable within the voltage range of ASSLSBs. Therefore, sulfide-based SEs have drawn much attention as lithium-ion conductors in cathodes for ASSLSBs. However, the major difference comes from the different physical states between liquid electrolytes and SEs. While the electrodes for conventional batteries can be easily wet by liquid electrolytes, in ASSLSBs, establishing lithium-ion conduction pathway presents challenges as the SEs cannot permeate the cathode matrix[83]. To realize a cathode composite with a well-dispersed mixture of the active material, conductive carbon and SE, proper methods for preparation need to be considered.

Prior to the preparation of composite cathodes for ASSLSBs, multiple parameters have to be evaluated, including a comprehensive assessment of methods such as dispersing, ball milling, heat treatment for vapor diffusion, or solvent-assist methods according to the different physical properties of materials. It is a common way to combine sulfur or Li_2S as active materials with carbon materials and SEs for composite cathodes. And a two-step combination is generally applied, including the combination of the active material with carbon materials first, then active material/carbon composite being mixed with SE[84]. Initially, the active material and carbon were simply mixed by grinding and the formed composite was subsequently mixed with SE. Nago et al. found that the composite cathodes prepared by ball-milling method demonstrated better electrochemical performance than those prepared by mortar mixing ones, indicating cathodes with smaller particle sizes are easier to realize the close contact among sulfur, carbon and SE[65]. However, the homogeneous mixture with a controlled particle size of sulfur is more desirable and it is difficult to realize such a fine control by ball-milling method.

Since the molten temperature of sulfur is 155 °C [85], other methods that take advantage of the molten sulfur were applied to impregnate sulfur into the porous carbon and to replace the step of admixing during cathode preparation. Following this method, Xu et al. reported a composite cathode construction by heating treatment at 155 °C for sulfur and rGO and then ball-milling with $Li_{9.54}Si_{1.74}P_{1.44}S_{11.7}Cl_{0.3}$ SE, and the schematic preparation is shown in Figure 1.4 [86]. Such a sulfur-based composite cathode displayed a discharge capacity of 969 mAh g^{-1} in the initial cycle at 0.05 C and maintained 827 mAh g^{-1} after 60 cycles. Hou et al. investigated the electronically interfacial contact between sulfur and carbon host

materials, reporting that the heat treatment enabled more intimate contact, thus possessing more effective electron transport than mechanical ball-milling method. The melt diffusion by heat treatment benefits the uniform distribution of sulfur and would not destroy the structure of carbon materials. Besides taking advantage of molten sulfur, sulfur deposition from the solution as a precipitate [87] was also applied to obtain a more homogeneous morphology and better electrochemical performance. Zhou et al. synthesized a composite cathode S@KB, where sulfur was obtained by the chemical reaction of sodium thiosulfate ($Na_2S_2O_3$) with hydrochloric acid (HCl, aq) and deposited on KB[88]. For comparison, sulfur was also mechanically mixed KB as S-KB, and S+KB was prepared by thoroughly mixing sulfur and KB at 155 °C. Their morphology is shown in Figure 1.5. While sulfur particles aggregate in both S-KB and S+KB composites, S@KB prepared by sulfur liquid deposition retains the morphology of well-distributed nanoparticles. With a composite polymer-ceramic electrolyte as the separator and ion conductor, the sulfur-based composite cathode delivered a specific capacity of 1108 mAh g^{-1} with an areal capacity of 1.77 mAh cm^{-2}, and cycled stably for 50 cycles.

As for preparing Li_2S-based cathode composites, different methods could be applied in addition to mortar grinding and ball-milling method by taking advantage of some properties of Li_2S. Since Li_3PS_4 glassy electrolyte can be formed during the ball milling method with starting materials of Li_2S and P_2S_5, and Li_2S itself works as an active material. Therefore, it is possible to prepare Li_2S-Li_3PS_4 composite with the in-situ formation of Li_3PS_4. For example, Peng at al. [89] involve ball-milling Li_2S with AB to form the electronic conductive network followed by in-situ formation of Li_3PS_4 SE on the Li_2S active material through the reaction of Li_2S and P_2S_5. The fabrication diagram is shown in Figure 1.6. With such a simple strategy, a triple-phase interface among Li_2S, carbon and SE can be constructed efficiently. The 85(92Li_2S-8P_2S_5)-15AB composite exhibits 1141.7 mAh $g_{(Li_2S)}^{-1}$ with 98% utilization of Li_2S and areal loading of 6 mg cm^{-2}.

1.4.1.2 Composite cathodes with nanoparticles

Although conductive additives such as carbon materials and SEs could enhance the electronic and ionic conductivity of cathode composites, unlike the liquid electrolytes that can have a good contact with electrodes, the solid-state electrolytes usually have inferior

solid-solid contact with electrodes[35, 90]. In addition, volume change of the active material may result in deteriorated surface contact. And the morphology of the cathode could change during the cycle with aggregated sulfur, which results in loss of contact with the electronic and ionic conductors and decreased capacity, as shown in Figure 1.7[91]. Since the electrochemical reaction can only occur where active materials are accessible to electrons and lithium ions, much effort has been made for structure engineering like nanosizing to increase the reaction interface.

The process of nanostructuring has been employed to enhance the surface area and decrease the lithium-ion diffusion distance in active materials, resulting in improved charge-transfer kinetics and a substantial reduction in oxidation overpotential. The widely adopted high-energy ball milling technique has been utilized for the large-scale production of sub-micrometer-sized particles. Cai et al. [92] reported a nanostructured Li_2S–carbon composite with particle sizes ranging from 200 to 500 nm by high-energy ball milling at 1060 rpm for 2 h. The electrode exhibited a moderate initial specific capacity of approximately 552 mAh g^{-1} at 0.2 C, based on the mass of Li_2S (1 C=1166 mA g^{-1}). Subsequently, Yan et al. [93] synthesized a Li_2S@C nanocomposite where Li_2S nanocrystals are uniformly dispersed in a conductive carbon matrix. Benefiting from this architecture, the Li_2S@C-$Li_7P_3S_{11}$ composite cathode exhibits excellent electrochemical performance, with high areal Li_2S loading (7 mg cm^{-2}) and high specific capacity of 1067 mAh g^{-1} based on Li_2S mass.

Besides the optimized ball-milling method, some other methods, such as microwave treatment, spark-plasma sintering (SPS) and liquid deposition, have been developed in order to obtain nanostructured Li_2S[94-96]. As reported by Hany et al., nanostructured Li_2S was successfully prepared using a microwave-assisted heat treatment at 200 °C[94]. The composite cathode consisted of nanostructured Li_2S, Li_3PS_4 SE and KB delivered a specific capacity of 840 mAh g^{-1} at 20 μA cm^{-2} in the initial discharge and kept 440 mAh g^{-1} at 100 μA cm^{-2} after 400 cycles. Spark plasma sintering (SPS), also known as pulsed electric current sintering (PECS), is a sintering technique that uses joule heating to enhance material transfer and produce dense materials in microstructure. And Takeuchi et al. applied SPS to prepare a composite of Li_2S and AB[96]. After mixing with sulfide SSE, the Li_2S-C-SSE composite cathode delivered the initial specific discharge capacity of 920 mAh g^{-1},

which realizes S utilization approaching to 80%. Jiang et al. deposited ultrasmall Li_2S (~15 nm) on carbon nanotube (CNT) via a liquid-phase method to improve electronic/ionic conductivities and relieve the volume change during cycling. The corresponding Li/75%Li_2S-24%P_2S_5-1%P_2O_5/$Li_{10}GeP_2S_{12}$/Li_2S-53%CNT ASSLSBs show a reversible capacity of 651.4 mAh g^{-1} under 1 C at 60 °C after 300 cycles. And with a higher cathode load of 5.08 mg cm^{-2}, a relatively high capacity of 556 mAh g^{-1} can still be achieved under 0.1 C after 20 cycles. These developed nanostructured materials could afford much flexibility for optimizing the composite cathodes with more necessary solid-solid contact, highly effective ion/electron transport and harmonious electrode-electrolyte interactions.

1.4.1.3 Composite cathodes with self-conductive active materials

Although conductive additives such as carbon and SEs possess high electronic and ionic conductivity, respectively, the insufficient electronic and ionic percolation through S or Li_2S as active materials leads to low utilization of active material and low practical energy density of ASSLSBs. To address this issue, improving the inherent low conductivities of active materials is a basic and fundamental strategy.

Li_2S is an antifluorite structure and crystalline in cubic crystal system (space group: $Fm\bar{3}m$). Li^+ is bonded to 4 equivalent S^{2-} and forms a mixture of corner- and edge-sharing LiS_4 tetrahedra, while S^{2-} is bonded to 8 equivalent Li^+. All Li-S bond lengths are 2.46 Å. The low intrinsic ionic conductivity of Li_2S originates from its extremely low concentration of lithium vacancies, which governs the charge carriers. To improve the ionic conductivity of Li_2S, heterovalence doping to substitute Li^+ or S^{2-} has been found to create lithium vacancies effectively due to the electrical neutrality. Lithium halides such as LiCl, LiBr and LiI were investigated for Li_2S doping[97, 98]. The heterovalence doping with halides partially replaces S^{2-}, leading to the formation of lithium vacancies accordingly. Among them, LiI doping could improve ionic conductivity to 10^{-6} S cm^{-1}. It was also found that doping metal into Li_2S structure could improve both electronic and ionic conductivities[98]. The early studies revealed that the incorporation of several kinds of transition metals, such as Fe, Co, Cu, etc., into the Li_2S lattice exhibited a lower activation potential[99]. Luo et al. [100] conducted a Density Functional Theory (DFT) calculation to model the impact of transition metal (Fe, Co, Ni, Cu, etc.) doping into Li_2S. They found Li_2S doped with iron (Fe) exhibited the lowest Li-vacancy formation energy during the delithiation phase. This

observation suggests that Fe doping exerts exceptional advantages during lithium ion extraction from Li_2S.

Transition metal sulfides, unlike the insulating nature of S and Li_2S, are known to have much higher electronic conductivity, which enhances electrochemical performance of ASSLBs. These transition metal sulfides, such as FeS_2[101], TiS_2[18], VS_4[102], etc., exhibit energy storage capability driven by conventional anionic redox. In addition, transition metal sulfide-based cathodes display the voltage plateau of ~ 2.0 V, which is analogous to sulfur and Li_2S for lithium-sulfur batteries[103]. Therefore, transition metal sulfides have the potential to be promising alternatives for sulfur cathodes in ASSLSBs. Due to their high electronic conductivities, transition metal sulfides are also electronic conductors for S-based or Li_2S-based cathode composites. CuS, a promising candidate as the active material for Li-S batteries due to its theoretical specific capacity of 560 mAh g^{-1} as well as high electronic conductivity of 10^3 S cm^{-1}, was initially severed as the active material for conventional lithium-sulfur batteries[104]. Later, the mixture of elemental sulfur, CuS and SEs such as Li_2S-SiS_2 and Li_2S-P_2S_5 was used as composite cathodes for ASSLSBs[105, 106]. The copper sulfide-sulfur cathode exhibited a reversible capacity of 850 mAh g^{-1} for over 800 cycles with the high areal capacity of 7 mAh cm^{-2} [107]. Additionally, FeS_2, as both active material and electronic conductor, was mixed with sulfur and $Li_{10}GeP_2S_{12}$ (LGPS) SE[108]. The mechanism and electrochemical performance of FeS_2-S-LGPS composite cathode is shown in Figure 1.8. The composite cathode delivered a capacity of 1121 mAh g^{-1} (based on the mass of FeS_2 and sulfur) at 30 mA g^{-1} with a single plateau behavior, suggesting that the lithiation-delithiation reactions occur. The applied transition metal sulfides with high electronic conductivities enable the replacement of electrochemically inactive carbon materials.

To optimize the electrochemical performance, composite cathodes must be designed to enhance both electronic and ionic conductivities, ensuring efficient transport of lithium ions and electrons accessible to the active materials. Moreover, the supply of ions and electrons would sacrifice attainable energy density due to the introduced inactive masses. Therefore, it is important to optimize the mixing ratio among components, which enables the achievement of high areal loading of sulfur and high active material content. What is

more, it is essential to maintain the framework of the electrode in order to eliminate the influence of volume change and loss of contact with conductors.

1.4.2 The solid-state electrolytes

As the key component of ASSLSBs, solid-state electrolytes (SEs) not only transport lithium-ion through the electrodes but also serve as the separator simultaneously between cathodes and anodes to prevent short circuits. Due to the bifunction in solid-state batteries, SEs should meet higher requirements, including (1) high ionic conductivity (~10^{-4} S cm^{-1}) and low electronic conductivity (10^{-8} S cm^{-1}) [109], (2) a high Li-ion transference number approaching unity, (3) a wide electrochemical window and pre-eminent chemical stability when interfacing with both cathode and anode materials, (4) intimate contact and good interfacial compatibility with both cathode and anode, (5) nontoxic and environmentally friendly and (6) feasible for assembling batteries[49], which are essential for the practical application of ASSLSBs. Plenty of SEs in pursuit of meeting most of these criteria have been synthesized and developed. Based on their different physical properties, they can be generally divided into three types: inorganic solid-state electrolytes, polymer solid-state electrolytes and composite solid-state electrolytes.

1.4.2.1 Classification of solid-state electrolytes: inorganic, polymer and composite solid-state electrolytes

(a) Inorganic solid-state electrolytes

Inorganic SEs represent a diverse and extensive class of materials, including various oxide and sulfide compounds, which are critical components in advanced energy storage systems. This family of materials includes noteworthy representatives of sulfide-based SEs such as thio-LISICON $Li_{10}GeP_2S_{12}$, Li_2S-P_2S_5 systems, argyrodites Li_6PS_5X (X=Cl, Br, I), etc., oxide-based SEs like sodium superionic conductors (NASICON), lithium superionic conductors (LISICON), garnet structures, perovskites, anti-perovskites, and so on. Although the ionic conductivities of inorganic SSEs vary significantly depending on their structures and composition, some sulfide electrolytes have high ionic conductivities that rival those of organic liquid electrolytes (~10^{-2} S cm^{-1}) [80, 110]. This feature is highly appealing for enhancing the performance of solid-state batteries and other electrochemical devices. Particularly for lithium-sulfur batteries, inorganic SSEs play a pivotal role in

mitigating the "shuttle effect" associated with the diffusion of polysulfide species. Thus, sulfide and oxide-based SSEs have been studied extensively in ASSLSBs.

The sulfide-based SEs can be divided into glassy, glassy-ceramic and crystalline SEs depending on their crystalline state. The Li_2S-P_2S_5[111] system was studied as glassy and glass-ceramic sulfide electrolytes, which are believed to have good interfacial compatibility with electrodes due to their lack of grain boundary and soft properties in favor of intimate contact with electrodes. The binary (100-x) Li_2S-xP_2S_5 (x is molar ratio) SEs show single phase with large x range between x=40 and x=80[112]. With lower Li_2S content ($x \leq 60$), the connection of P-S in Li_2S-P_2S_5 SEs shows more di-tetrahedral $P_2S_7^{4-}$ units, where two PS_4 tetrahedra connect with a shared S atom. The glassy Li_2S-P_2S_5 can be synthesized by the facile ball-milling method with starting materials of Li_2S and P_2S_5 and pressed into SE pellet using cold-pressing at room temperature, which is feasible for cell fabrication. The $75Li_2S$-$25P_2S_5$ (Li_3PS_4) glassy SE has all P-S connection as mono-tetrahedra PS_4^{3-} and shows highest ionic conductivity of 4×10^{-4} S cm^{-1} among the glassy Li_2S-P_2S_5 system. By heating the glassy powder of Li_2S-P_2S_5 just above the crystallization temperature, the glassy powder can crystalline into dense particles and form glassy-ceramic SE, which has fewer voids and higher ionic conductivity. For example, the $70Li_2S$-$30P_2S_5$ glass-ceramic SE was prepared by heat treatment for $70Li_2S$-$30P_2S_5$ glassy powder just above the crystallization temperature. By optimizing the heat treatment temperature, the ionic conductivity of the $70Li_2S$-$30P_2S_5$ glass-ceramic SE can be improved up to 1.7×10^{-2} S cm^{-1}, while the glassy $70Li_2S$-$30P_2S_5$ and crystalline $70Li_2S$-$30P_2S_5$ ($Li_7P_3S_{11}$) have ionic conductivities of 10^{-5} and 10^{-3} S cm^{-1}, respectively[113]. The superior ionic conductivity of glass-ceramic SE compared to glassy and crystalline ones is due to its unique microstructure. This microstructure combines crystalline particles with a highly ordered pathway for Li^+ transport and a glassy matrix with fewer voids. The illustration diagram is shown in Figure 1.9 [114].

In addition to glassy and glass-ceramic SEs, crystalline SEs have been developed and drawn substantial attention, such as thio-LISICON and argyrodite Li6PS5X (X=Cl, Br, I)) due to their outstanding ionic conductivities, ranging from 10^{-3} to 10^{-2} S cm^{-1} even at room temperature (RT). The thio-LISICON $Li_{3.25}Ge_{0.25}P_{0.75}S_4$ was first reported with high ionic conductivity of 2.2×10^{-3} S cm^{-1} [115]. The later studied $Li_{10}GeP_2S_{12}$ (LGPS) possesses an

extremely high ionic conductivity of 1.2×10^{-2} S cm^{-1} [80]. As Figure 1.10(a) shows, the three-dimensional framework of LGPS is composed of $(Ge_{0.5}P_{0.5})S_4$ tetrahedra, PS_4 tetrahedra, LiS_4 tetrahedra and LiS_6 octahedra. The $(Ge_{0.5}P_{0.5})S_4$ tetrahedra and LiS_6 octahedra connect with edge-sharing, forming a 1D chain along the *c* axis. These 1D chains are connected through PS_4 tetrahedra by corner-shared S atoms with LiS_6 octahedra. The 1D lithium conduction pathway along the *c* axis is formed by LiS_4 tetrahedra. Recently, $Li_{9.54}Si_{1.74}P_{1.44}S_{11.7}Cl_{0.3,}$ with highest ionic conductivity among all SEs of up to 2.5×10^{-2} S cm^{-1} has been proposed by Kanno's group. As Figure 1.10(b) shows, the extraordinary ionic conductivity of the latest reported SE originates from a three-dimensional lithium-ion pathway formed by the interplay of *c*-axis and the *ab*-plane.

Oxide electrolytes, like LISICON, NASICON, and garnet, have garnered significant interest due to their high ionic conductivity, wide electrochemical window, outstanding mechanical strength, and easy handling. Among these, garnet electrolytes, with the $A_3B_2C_3O_{12}$ chemical formula, have drawn much attention among oxide-based lithium-ion conductors because of the claimed high stability against reaction with lithium metal, moisture and typical electrodes. Notably, the initial studied $Li_5La_3M_2O_{12}$ (M = Nb, Ta) revealed an unsatisfied bulk conductivity of 10^{-6} S cm^{-1} at 25 °C[116]. Subsequently, $Li_7La_3Zr_2O_{12}$[117] (LLZO) was reported with a substantially enhanced total (considering both bulk and grain-boundary) ionic conductivity of 3×10^{-4} S cm^{-1} at room temperature (RT). The introduction of high-valence tantalum (Ta) dopants into the LLZO lattice, that is $Li_{6.4}La_3Zr_{1.4}Ta_{0.6}O_{12}$ (LLZTO), not only improves the ionic conductivity to 10^{-3} S cm^{-1}, but also enhances stability with lithium metal. In addition, NASICON-type SEs have also garnered significant attention as a promising class. In this context, $Li_{1+x}Al_yGe_{2-y}(PO_4)_3$[118], commonly referred to as LAGP, derived from the partial substitution of Al^{3+} in the lithium germanium phosphate $LiGe_2(PO_4)_3$ structure, represents a notable member within the NASICON-type SSE category due to its good chemical and electrochemical stability and high ionic conductivity of 10^{-4} S cm^{-1} at RT.

Although inorganic SEs have the high ionic conductivities of, their practical applications for ASSLSBs are still hindered by some issues, such as poor air stability, insufficient chemical stability or narrow electrochemical window. As for sulfide-based SEs, despite their remarkable ionic conductivity, they are not stable in the ambient environment, where

they will highly hydrate and generate toxic H_2S gas due to the weak P-S bond[119]. The degradation of sulfide SEs in ambient environment limits their synthesis process and cell fabrication in the glove box instead of the dry room commonly for large scale manufacture. Another major challenge is they are chemically unstable with lithium metal. While lithium alloys like Li-In (0.62 V versus Li) and Li-Al (0.37 V versus Li) are commonly employed in ASSLSBs with sulfide SEs to keep the sulfide surface from contact with lithium directly, the cell voltages will be sacrificed, leading to much lower practical energy density[66]. As for oxide SEs, despite their relatively high ionic conductivities and good air stability, their applications are mainly hindered by severe interfacial issues. Owing to different chemical potential between the SE and the cathode, redistribution of lithium ions will occur at the interface, where lithium ions are enriched on one side. In contrast, the other side is compensated with opposite carriers[120]. Consequently, a space-charge layer will form, which slows down the lithium-ion exchange between the SE and the cathode during battery operation. In addition, garnet electrolytes have large contact angle with lithium metal and it is lithiophobic, which results in large interfacial impedance.

(b) Polymer solid-state electrolytes

Different from inorganic SEs, polymer solid-state electrolytes (SPEs) are organic electrolytes as the composite consists of dissolved lithium salts and polar polymer hosts. SPEs possess advantages in developing high-energy-density all-solid-state batteries due to their superior flexibility, ease of preparation, and cost-effectiveness[121]. Among these SPEs, poly(ethylene oxide) (PEO)-based electrolytes are the most commonly employed in lithium-sulfur batteries. PEO is characterized by A repeating oxyethylene group structure denoted as $-CH_2-CH_2-O-$ as well as the polar groups: $-O-$, $-H-$, $-C-H-$ has the ability to dissolve salt, such as LiX (where X = I, Cl, Br, ClO_4, CF_3SO_3, AsF_6, BF_4, etc) [122]. The transport of lithium ions in SPEs depends on local relaxation and segmental motion of the polymer chains (Figure 1.11) [49]. The segmental mobility of PEO is largely influenced by temperature and it exhibits a considerably reduced rate at temperatures below the melting temperature of PEO, which is approximately 60 °C. Consequently, this diminished segmental motion leads to a comparatively low ionic conductivity at room temperature, which requires higher operating temperatures in lithium-sulfur batteries utilizing PEO-based electrolytes.

(c) Composite solid-state electrolytes

Composite solid-state electrolytes (CPEs) are combinations of inorganic particles as fillers and polymer SE as matrix, to complement their advantages. The fillers can be divided into inert and conductive types, depending on whether they possess structures with ionic transport pathways inside. As for the former, insulating materials such as SiO_2, TiO_2 and Al_2O_3, etc. are commonly chosen because they are low cost and highly stable[123]. Additionally, these passive fillers can stability the formation of SEI and alleviate shuttle effect. The lithium-conductor fillers like zeolites are capable of fast lithium transport thus, lithium ions cannot migrate only along polymer chains but also transport through the conductive fillers. However, the mechanism of improved ionic conductivity of CPEs by fillers still needs to be addressed.

In summary, lots of SEs, especially sulfides with high ionic conductivities comparable to liquid electrolyte, have been developed and employed to ASSLSBs. However, no perfect SE so far could meet all requirements for advanced ASSLSBs. The comparison of SEs is shown in Figure 1.12 [49]. Nevertheless, there are still many issues to be addressed, such as the poor air stability of sulfides, the insufficient interfacial contact with lithium metal of oxides, and deficient ionic conductivities of polymer and composite SSEs at room temperature.

1.4.2.2 Chemical stability and degradation of sulfide solid-state electrolytes

Sulfide SEs, with high ionic conductivities comparable to conventional liquid electrolytes, have attracted much attention. However, most sulfide SEs have to be handled under inert gas due to their instability with moisture. Sulfides undergo hydrolysis upon exposure to water, leading to the generation of H_2S gas, which results in structural changes, subsequently deteriorating the electrolyte's ionic conductivity. Notably, impurity peaks in the X-ray diffraction (XRD) pattern of Li_6PS_5Cl electrolyte were observed with exposure to ambient air only for 10 min[112]. The ionic conductivity declined from the initial value of 1.8×10^{-3} S cm^{-1} to 1.56, 1.43, and 0.87×10^{-3} S cm^{-1}, respectively, following exposure to air for 10 min, 1 h, and 24 h[124].

Tracking the H_2S generation can help probe the structure evolution of sulfide SEs with moisture. As a study conducted by Muramatsu et al. [119], the generation of H_2S was systematically monitored in Li_2S-P_2S_5 glasses with varying compositions of Li_2S (57%,

60%, 75%, and 80%) by using H_2S sensor and Raman spectroscopy. An immediate generation of H_2S upon exposure to air was observed and the quantity of H_2S generation correlated with the glass composition. The sulfide SE with the 75 mol% Li_2S exhibited the lowest H_2S production. Muramatsu et al. proposed that Li_2S-P_2S_5 electrolytes, which consist of PS_4^{3+} units, have higher air stability that Li_2S-P_2S_5 with $P_2S_7^{4+}$ units. Sahu et al. [125] tried to explain the chemical stability properties of sulfide SEs with the hard and soft acids and bases (HSAB) principle. Based on this principle, soft bases exhibit greater sensitivity to soft acids, while hard bases prefer reacting with hard acids. Given that O^{2-} functions as a stronger base than S^{2-}, it is more likely to react with the strong acid P^{5+}, which causes structural degradation and significant changes in the diffusion paths. Following this principle, some oxides P_2O_5, Sb_2O_5 and ZnO have been doped into sulfide SEs and found to improve air stability effectively[126, 127]. In addition to the replacement of soft bases S^{2-}, the replacement of acid P^{5+} is also a common way to improve air stability. For example, Sn is reported to substitute for P because Sn^{4+} is a softer acid than P^{5+} and the resultant Li_4SnS_4 exhibits excellent air stability[125].

Since the battery manufacture is commonly conducted in a dry room instead of the glove box, understanding the degradation behavior under conditions with a dew point of -50 to -20 °C is close to the practical production. Chen at al. exposed Li_6PS_5Cl in a dry room with a dew point of -45 °C [128]. They found that ionic conductivity decreased linearly with the first three hours of exposure and maintained most ionic conductivity as a value of 2.33×10^{-3} S cm^{-1} after 24 hours of exposure. The degraded SE showed partially recovered ionic conductivity of 2.77×10^{-3} S cm^{-1} after heat treatment at 550 °C for 8 hours. Then Morino at al. investigated the degradation mechanism of Li_6PS_5Cl in a dry room with a dew point of -20 °C after 1 hour of exposure and 24 hours of exposure by X-ray photoelectron spectroscopy (XPS), Raman spectroscopy, nuclear magnetic resonance (NMR) spectroscopy and diffuse reflectance infrared Fourier-transform spectroscopy (DRIFTS) [129]. It was found that the decomposition of SE originates from the elimination of S in PS_4^{3-} units by releasing H_2S and oxidized products such as phosphate, disulfide and carbonate. In addition, the decreased ionic conductivity of SE is partially due to the absorption of H_2O molecules on the surface and it is reversible after heat treatment for desorption of H_2O.

Although the degradation mechanism of SE simulated in a dry room has been reported, all of the measurements are ex-situ, different from the decomposed condition. In addition, the ionic conductivity decreases fast within 1 hour of exposure, while no research investigates the degradation within 1 hour of exposure with instant measurement. In-situ measurement may be needed for understanding the degradation behavior and mechanism simultaneously.

1.4.3 The anodes for solid-state lithium-sulfur batteries

Lithium metal, with high theoretical capacity of 3860 mAh g^{-1}, has lowest electrochemical potential (-3.04 V versus standard hydrogen electrode) and low density (0.534 g cm^{-3}) is considered an ideal anode material[27]. Unfortunately, the growth of dendrite on the surface of lithium metal, which results from inhomogeneous deposition and dissolution, and inevitable side reactions with electrolyte leads to dead lithium, infinite volume expansion and internal short circuit. Although SEs are expected to restrain the growth of lithium dendrite, the poor chemical stability of sulfide-based SEs and the undesirable interfacial contact of oxide-based SSEs are incompatible with lithium metal directly. And in the case of PEO-based SPEs, the soluble polysulfides would transport to anode side and react with lithium metal, forming insulating Li_2S_2 and Li_2S on the anode surface[38]. Therefore, it is necessary to modify lithium metal when coupling with present SEs for ASSLSBs. As one of the various modification approaches, artificial SEI is an effective way to protect lithium metal. For example, an ultrathin Al_2O_3 layer deposited on the PEO-based SPE at the anode side has inhibited shuttle effect and restricted the growth of lithium dendrite[130]. Upon contact with lithium metal, Al_2O_3 facilitated the formation of a highly ionic conducting Li-Al-O layer, which can protect the interface on the anode side from lithium corrosion. The corresponding ASSLSB exhibited a reversible capacity of 780 mAh g^{-1} after 100 cycles at a rate of 0.2 C and 60 °C.

Lithium alloys, such as Li-In, Li-Al, and Li-Si, are known to restrain the lithium dendrite growth and consequently exhibit good cyclability in ASSLBs[131]. Given the instability observed at the interface between lithium metal and the solid electrolyte, lithium alloys have been employed as alternatives to lithium metal to improve interface stability. Li-In alloys are particularly favored due to their consistent and stable lithium voltage (0.62 V vs. Li^+/Li) [132]. Nagata et al. demonstrated the success of Li-In alloy paired with sulfur as the

anode and cathode, respectively, achieving a high discharge capacity of 1550 mAh g^{-1} during the first discharge cycle, and stable cycling performance in subsequent cycles[133]. Utilizing lithium alloys as anodes in solid-state batteries is an effective strategy in preventing the formation of lithium dendrites and enhancing stability at the anode-electrolyte interface. However, compared with Li metal, lithium alloys have higher electrochemical potentials, leading to hundreds of millivoltage losses in cell voltage, which lowers the energy density of ASSLSBs.

1.5 Objective

As stated above, several issues should be addressed for the development and commercialization of ASSLSB. These issues are mainly related to the insufficient performance of cathodes, stemming from the electronic and ionic insulating nature of S and Li_2S as active materials, as well as the inferior stability of sulfide SEs. In this doctoral thesis, I aim at (1) improving the low intrinsic ionic conductivities of the core of cathodes—active materials; (2) establishing an electronic and ionic network through the whole composite cathodes, which enables electrons and lithium ions transport smoothly; (3) modifying the electron and ion paths to promote the rate capability of composite cathodes; (4) clarifying the degradation mechanism of sulfide SSEs for better fabrication of ASSLSBs. The performance of ASSLSBs is mainly limited by the sluggish kinetics of S and Li_2S, which arises from their low electronic and ionic conductivities. Therefore, it is critically important to enhance the intrinsic conductivities of S or Li_2S and improve the utilization of active materials. Furthermore, it is necessary to establish ion and electron transfer pathways within the composite cathode, and to optimize ion and electron transport for improved rate performance, ultimately to realize ASSLSBs energy storage systems with high energy density and power density.

For the thesis research, electrochemical performance was improved from the atomic scale in active materials to battery fabrications. Particularly, point defect in the structure of active material Li_2S was controlled by cationic/anionic doping. The structural evolution, particularly the relationship between the point defect and doping content, was revealed by synchrotron XRD and neutron diffraction (ND). The optimized Li_2S with sufficient point defect was capable of transporting lithium ions smoothly. On the cathode level, X-ray absorption spectroscopy (XAS) was the interface of active materials and conductors and related mechanisms during electrochemical reaction. Furthermore, X-ray Computed Tomography (CT) was utilized to demonstrate a conductive pathway through the composite cathode. Finally, XAS was used to clarify the degradation mechanism of sulfide SSEs, which provided structural understanding for battery fabrication.

1.6 Thesis outline

This doctoral thesis consists of six chapters, which target at developing high-performance ASSLSBs through structural, interfacial and morphological control in Li_2S active material and composite cathode.

Chapter 1 outlines the research background and fundamental principles of lithium-ion and lithium–sulfur batteries, particularly solid-state lithium-sulfur batteries. All-solid-state lithium sulfur batteries are introduced from the aspects of cathode materials, electrolytes, and anode materials. As the key point to improve the performance, cathode materials for solid-state lithium-sulfur batteries are discussed in detail.

Chapter 2 reports the point defect control in Li_2S structure by cation-anion-dual PI_3 doping to improve ionic transport in Li_2S cathode. In particular, the relationship between lithium vacancies and ionic conductivities are examined quantitatively by time-of-flight (TOF) neutron diffraction. By cation-anion-dual doping, ionic conductivities of Li_2S-PI_3 materials have been dramatically improved, which are capable for cathode without solid electrolytes added.

Chapter 3 reports a novel integrated cathode Li_2S-LiI-MoS_2 which has relatively high electronic and ionic conductivities (the order of 10^{-4} S cm^{-1}) without any carbon and solid electrolytes. Revealed by XAS, the charge compensation mechanism is involved in both Mo 4d and S 3p orbitals as cationic and anionic redox during the charging and discharging process. X-ray CT shows the ionic pathway provided by LiI-rich domain that forms during the first charge process.

Chapter 4 addresses the modification and optimization of electronic and ionic transport through the composite cathode and has developed Li_2S-LiI-MoS_2@Li_6PS_5Cl with high overall capacity and superb rate capability on the cathode level. X-ray CT is utilized to show morphology and conductive transport pathway through this composite cathode.

Chapter 5 clarifies the degradation mechanism of sulfide solid-state electrolytes using *in situ* soft XAS. It investigated the typical sulfide solid-state electrolyte $Li_{7-x}PS_{6-x}Cl_x$ under moisture with the dew point of -20 °C, which simulated the practical battery fabrication in dry room. With moisture exposure, the electronic structure around S and P continuously changed with exposure time and correlated with the decrease of the ionic conductivity. In

addition, the ionic conductivity of $Li_{7-x}PS_{6-x}Cl_x$ are partially recovered under vacuum heat treatment after exposure to the vapor atmosphere.

Chapter 6 draws the conclusion of the studies in this thesis and offers future prospects for lithium–sulfur batteries.

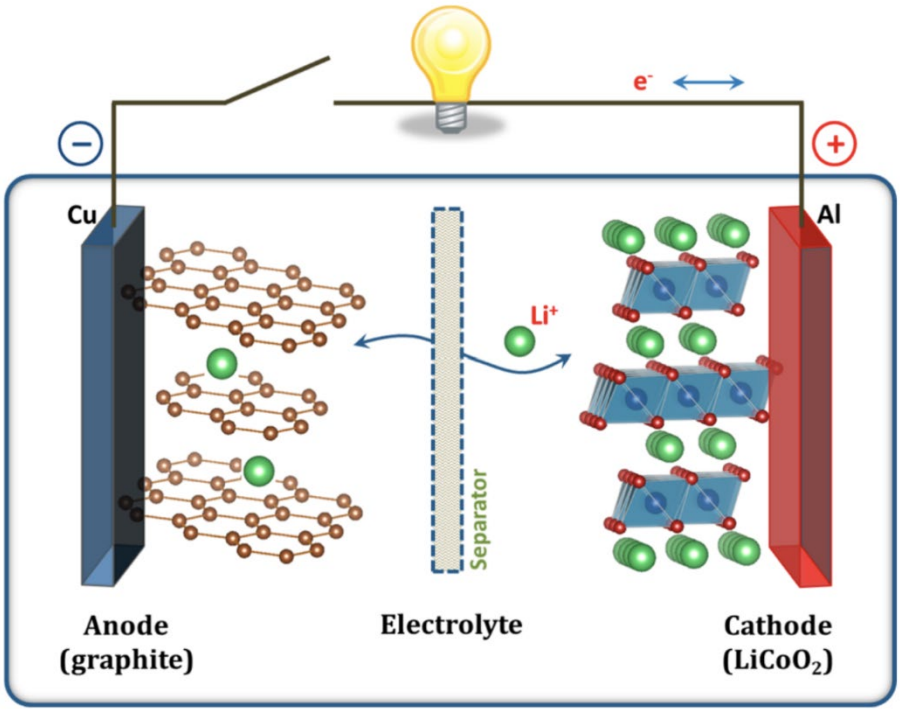

Figure 1.1 The schematic illustration of first commercialized lithium-ion batteries with $LiCoO_2$ as cathode and graphite as anode[24].

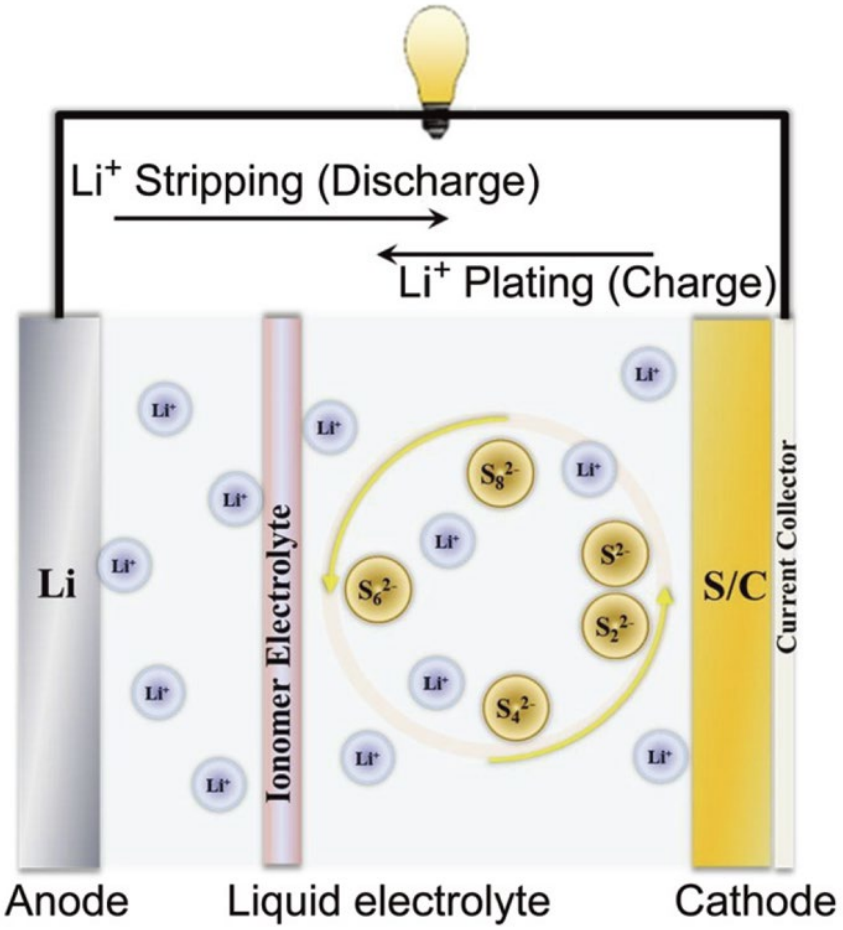

Figure 1.2 The schematic illustration of conventional lithium-sulfur batteries[32].

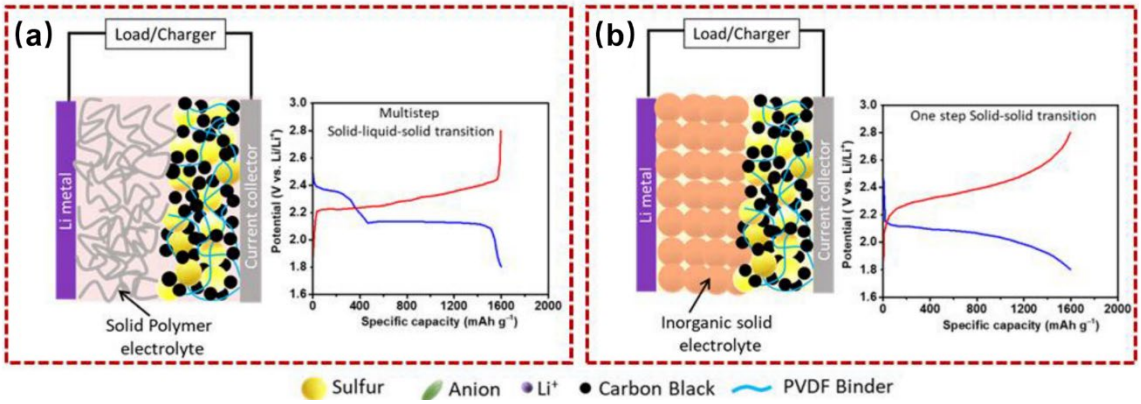

Figure 1.3 (a) The illustration of ASSLSB using solid polymer electrolyte and its corresponding charge-discharge behavior with two voltage plateau and one slope, which correspond to a multistep 'solid-liquid-solid' reaction due to the polysulfide dissolution in polymer matrix (b) the illustration of ASSLSB with inorganic solid-state electrolyte and its corresponding charge-discharge behavior with a one-step 'solid-solid' reaction, indicating no polysulfides dissolve into the solid-state electrolyte [54].

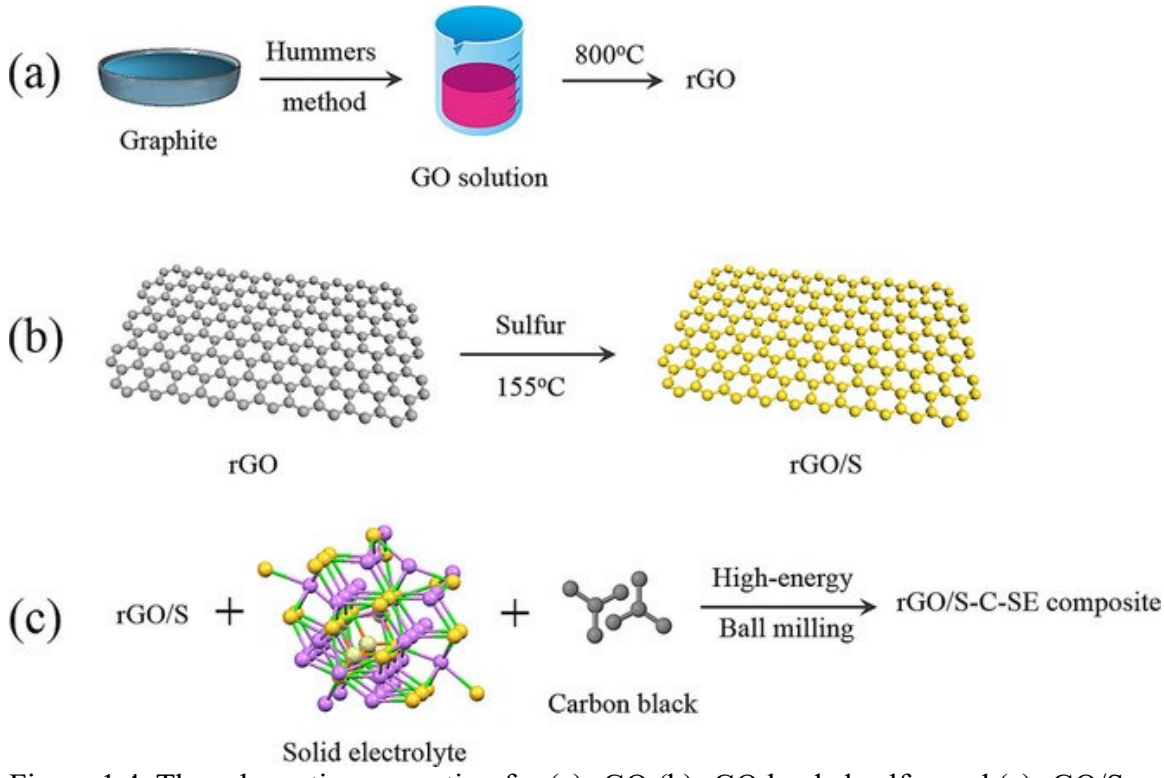

Figure 1.4. The schematic preparation for (a) rGO (b) rGO loaded sulfur and (c) rGO/S-C-SE composite[86].

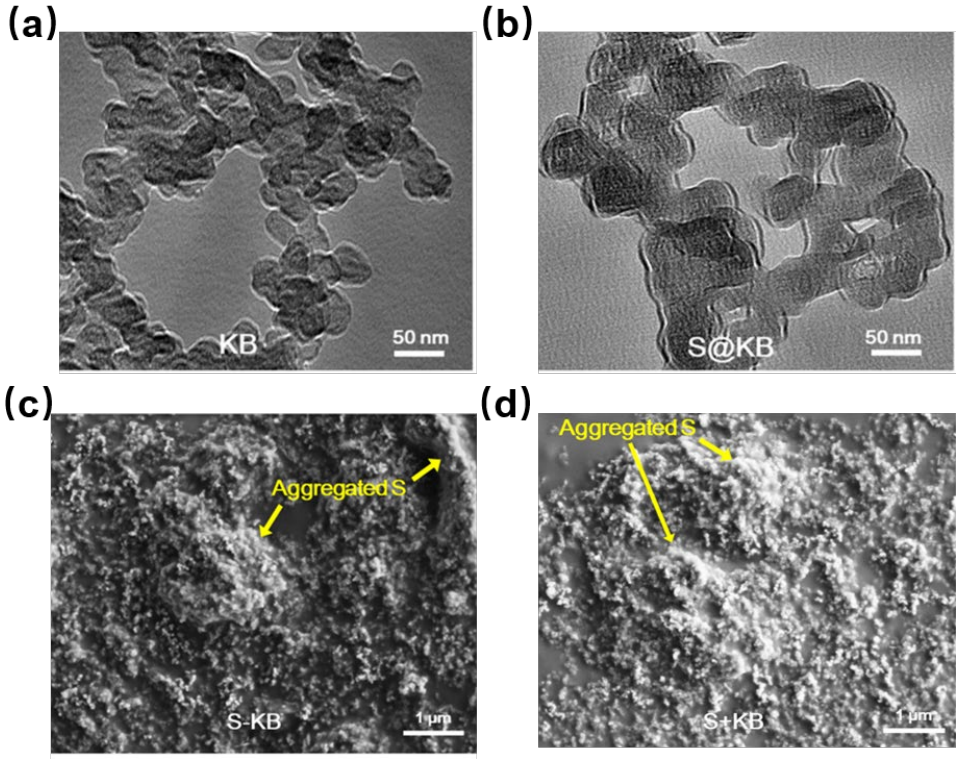

Figure 1.5 SEM images of (a) KB (b) S@KB (c) S-KB and (d) S+KB. Among them, S@KB is prepared by sulfur liquid deposition method[88].

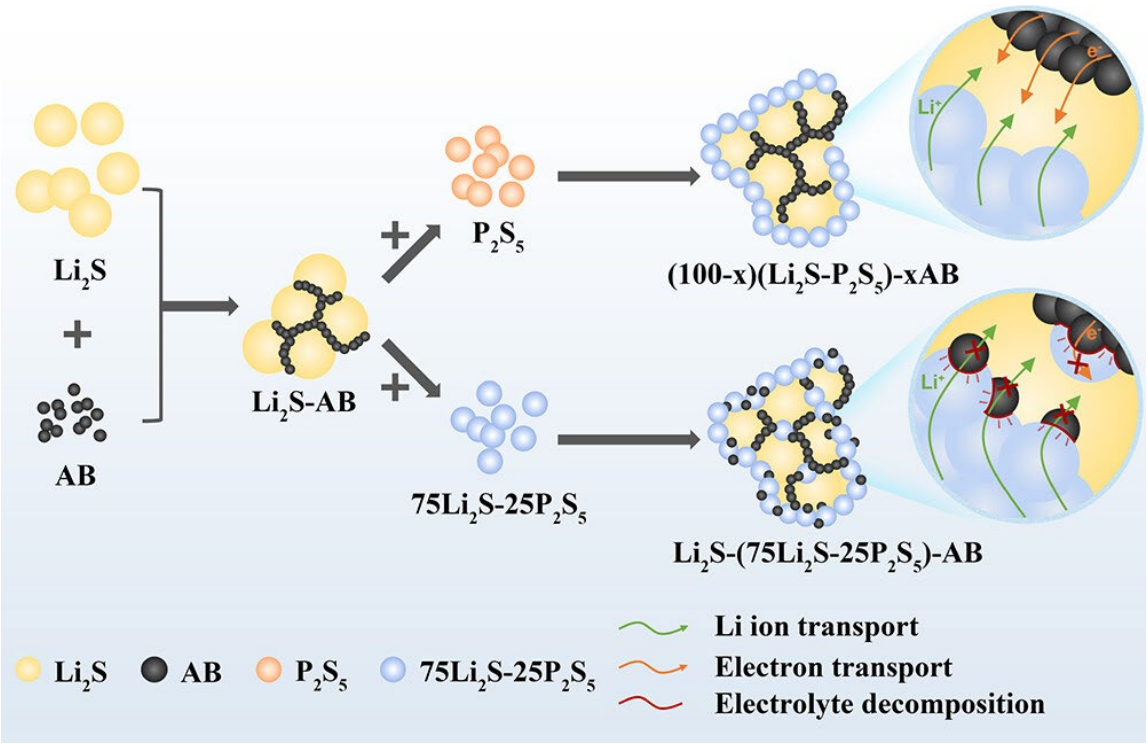

Figure 1.6. The preparation diagram of (100 – *x*)(aLi_2S-bP_2S_5)-*x*AB and Li_2S-(75Li_2S-25P_2S_5)-AB composites[89].

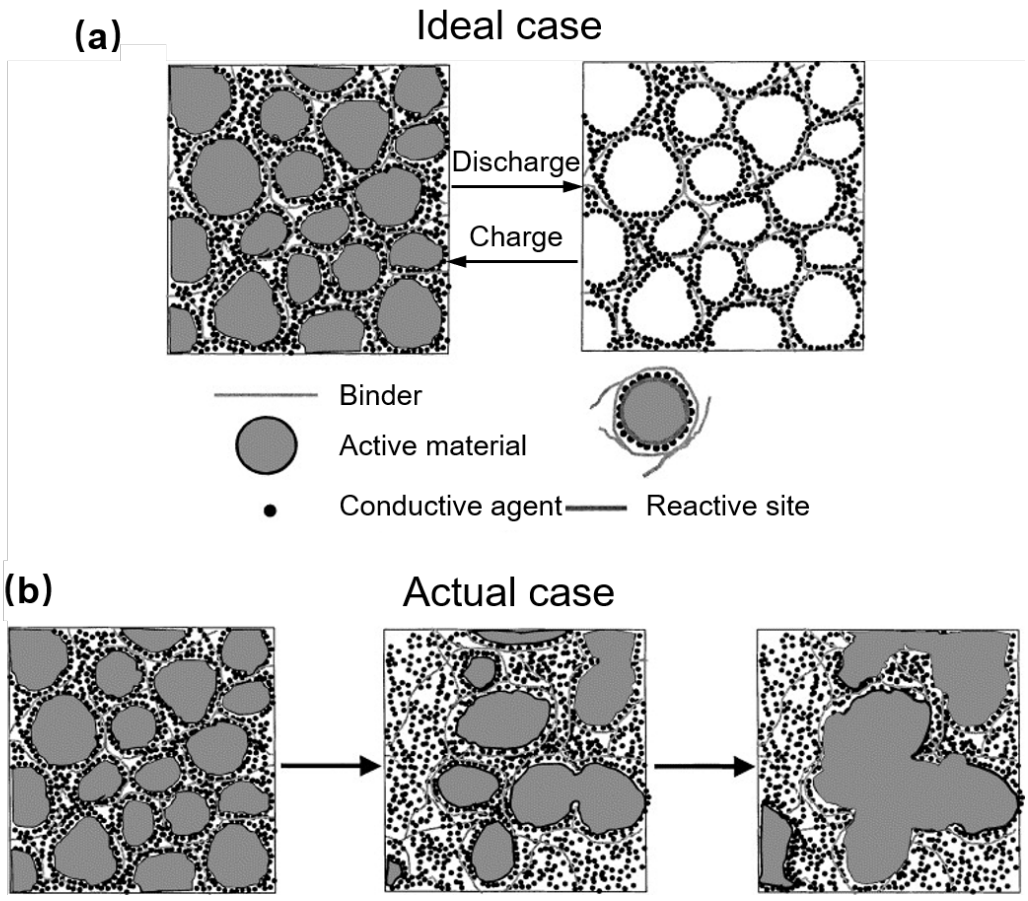

Figure 1.7 The morphology changes of composite cathode during charge-discharge in (a) an ideal case (top) with even distribution of active material surrounded by conductive agent and (b) practical case (bottom) where aggregates of sulfur particles together during cycling[91].

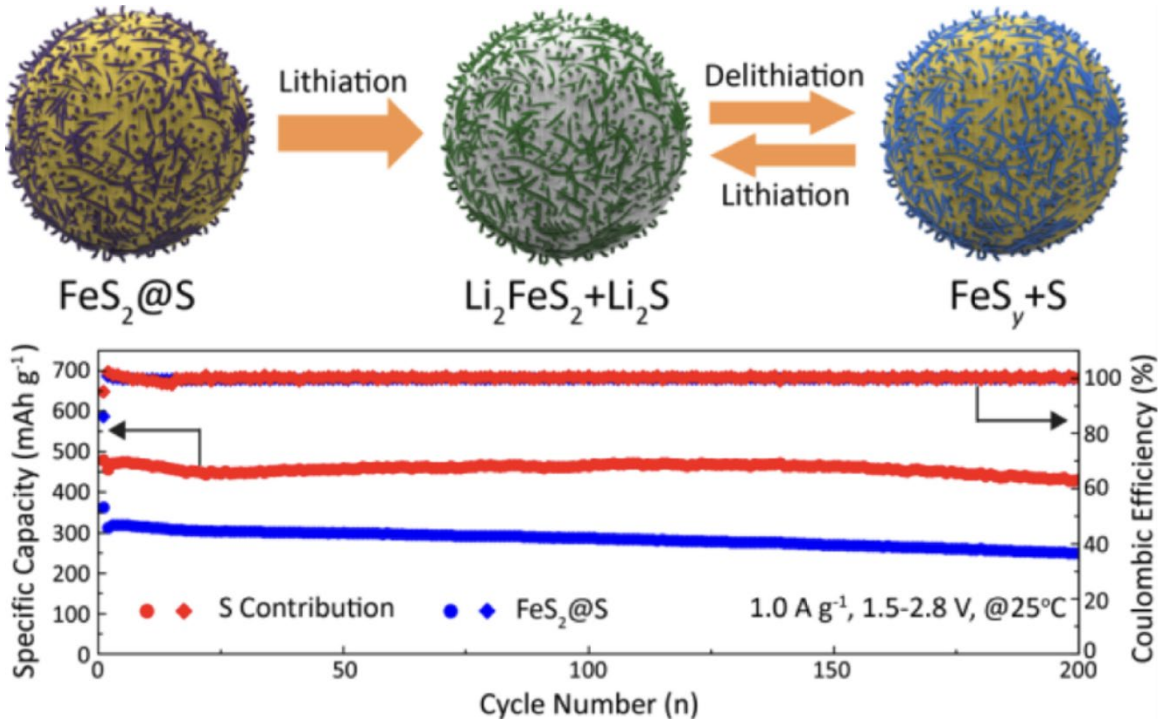

Figure 1.8 The illustration of reaction mechanism (top) and cyclic performances of the FeS_2@S-$Li_{10}GeP_2S_{12}$ composite (blue points, based on the total mass of FeS_2 and S) and the sulfur contribution (red points, based on sulfur mass) in all-solid-state lithium–sulfur batteries at 1000 mA g^{-1} for 200 cycles at room temperature[108].

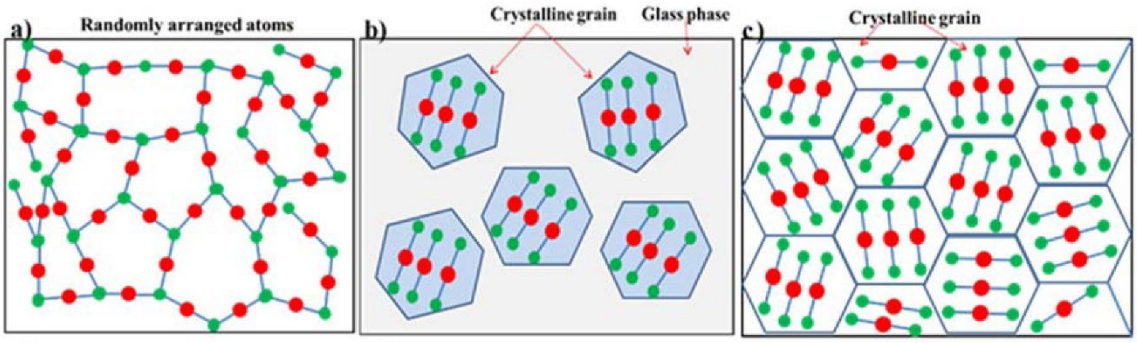

Figure 1.9. The microstructure differences among (a) glassy, (b) glass-ceramic and (c) crystalline solid electrolyte [114].

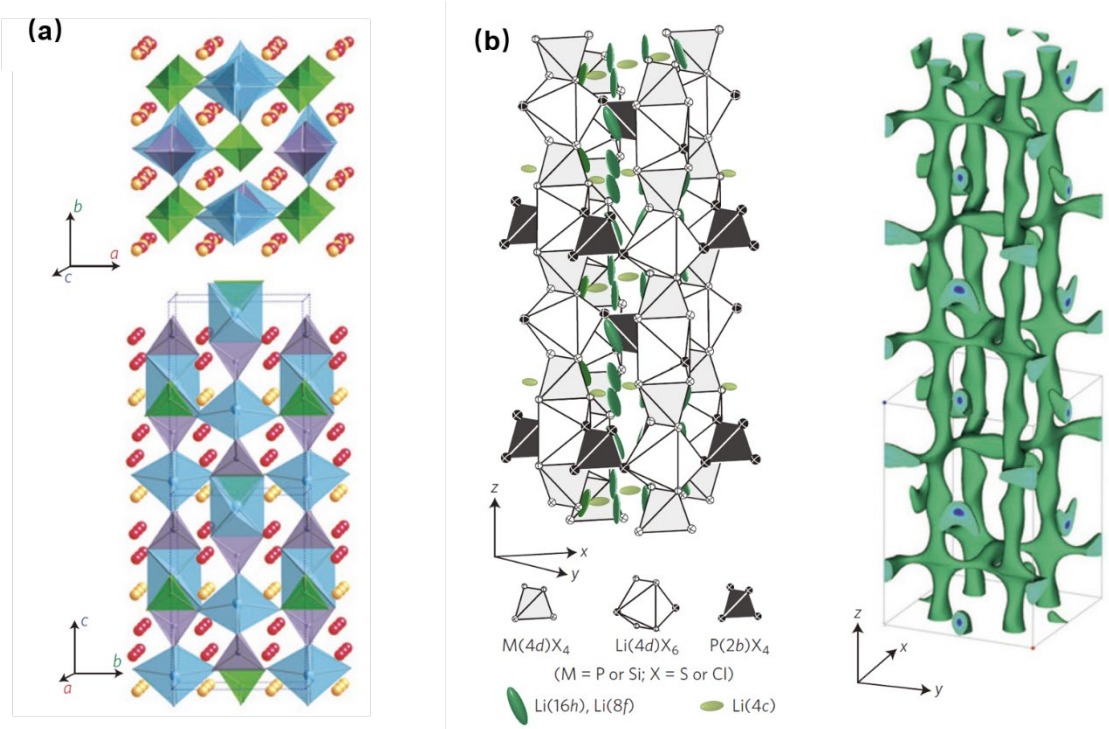

Figure 1.10 (a) The framework structure and lithium ions that participate in ionic conduction of $Li_{10}GeP_2S_{12}$[80]. (b) Crystal structure of $Li_{9.54}Si_{1.74}P_{1.44}S_{11.7}Cl_{0.3}$. The thermal ellipsoids are drawn with a 50% probability and corresponding nuclear distributions of Li atoms at 25 °C, calculated using the maximum entropy method at the iso-surface level of −0.06 fm $Å^{-3}$ [110].

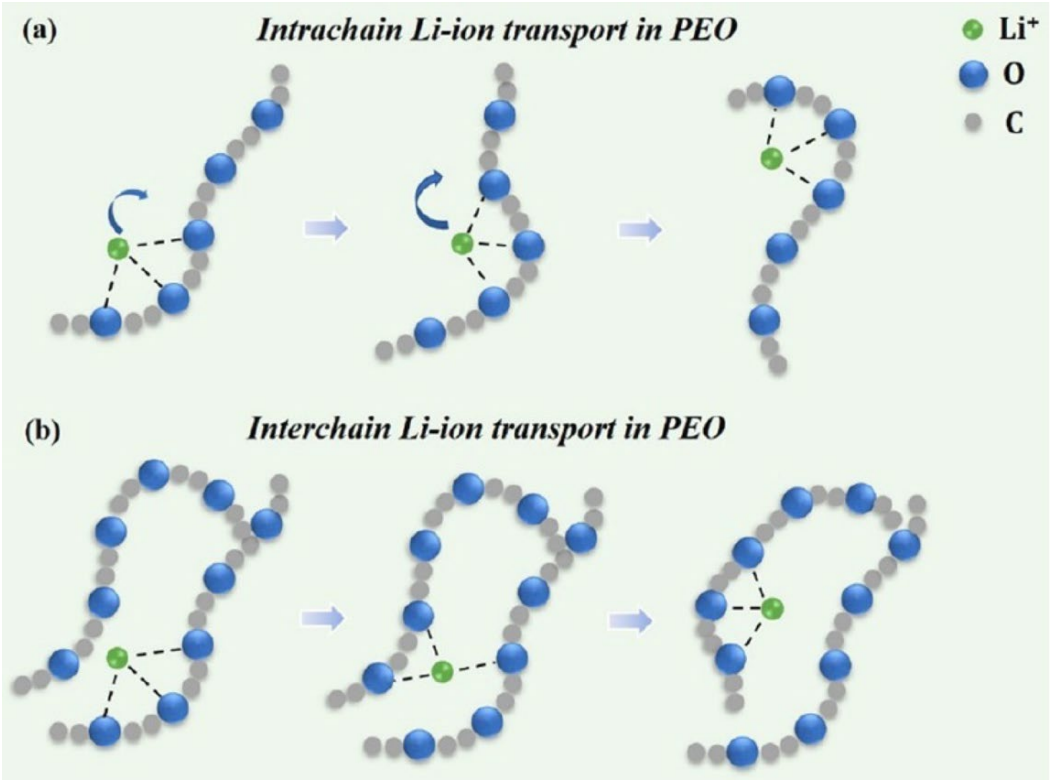

Figure 1.11 Schematic of (a) intrachain and (b) interchain Li-ion transport in PEO[49].

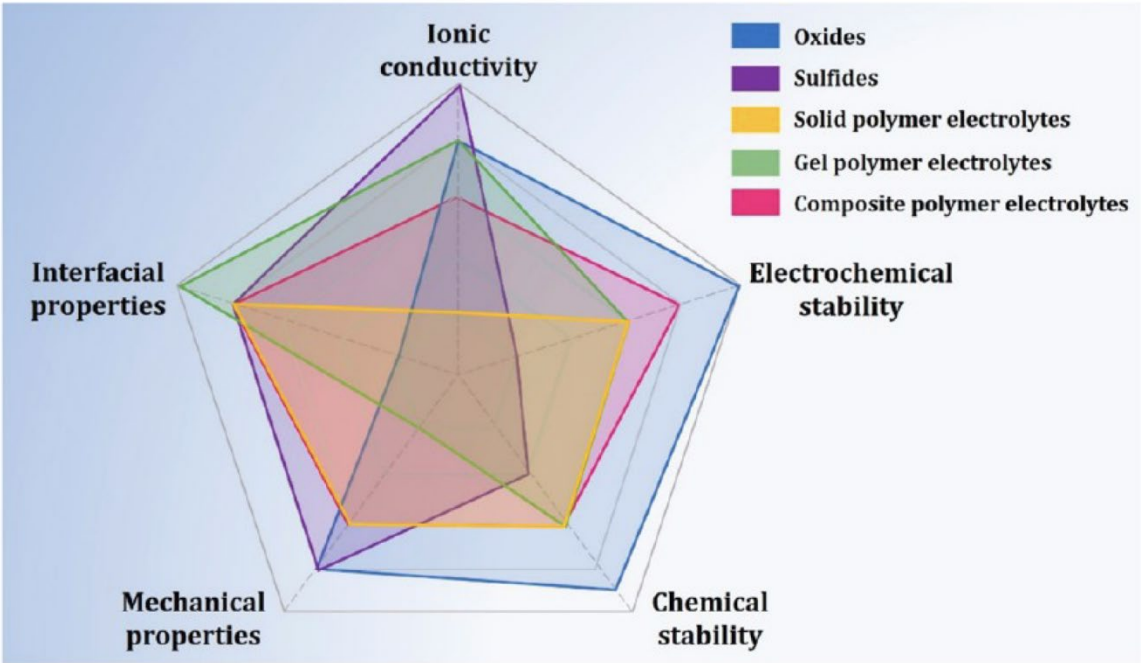

Figure 1.12 Comparison of different kinds of solid-state electrolytes. Radar charts of the performance of oxides, sulfides, solid polymers, gel polymers, and composite electrolytes[49].

References

(1) Armaroli, N.; Balzani, V. Towards an electricity-powered world. *Energy Environ. Sci.* **2011**, *4* (9), 3193-3222.

(2) Hayashi, A.; Hama, S.; Morimoto, H.; Tatsumisago, M.; Minami, T. Preparation of Li_2S–P_2S_5 amorphous solid electrolytes by mechanical milling. *J. Am. Chem. Soc.* **2001**, *84* (2), 477-479.

(3) Lee, K. T.; Jeong, S.; Cho, J. Roles of surface chemistry on safety and electrochemistry in lithium ion batteries. *Acc. Chem. Res.* **2013**, *46* (5), 1161-1170.

(4) Xu, J.; Cai, X.; Cai, S.; Shao, Y.; Hu, C.; Lu, S.; Ding, S. High-Energy Lithium-Ion Batteries: Recent Progress and a Promising Future in Applications. *Energy Environ. Mater.* **2023**, *6* (5), e12450.

(5) Armand, M.; Tarascon, J.-M. Building better batteries. *Nature* **2008**, *451* (7179), 652-657.

(6) Dunn, B.; Kamath, H.; Tarascon, J.-M. Electrical energy storage for the grid: a battery of choices. *Science* **2011**, *334* (6058), 928-935.

(7) Winter, M.; Brodd, R. J. What are batteries, fuel cells, and supercapacitors? *Chem. Rev.* **2004**, *104* (10), 4245-4270.

(8) Liang, Y.; Zhao, C. Z.; Yuan, H.; Chen, Y.; Zhang, W.; Huang, J. Q.; Yu, D.; Liu, Y.; Titirici, M. M.; Chueh, Y. L.; et al. A review of rechargeable batteries for portable electronic devices. *InfoMat* **2019**, *1* (1), 6-32. DOI: 10.1002/inf2.12000.

(9) Dell, R. Batteries: fifty years of materials development. *Solid State Ionics* **2000**, *134* (1-2), 139-158.

(10) Raza, W.; Ali, F.; Raza, N.; Luo, Y.; Kim, K.-H.; Yang, J.; Kumar, S.; Mehmood, A.; Kwon, E. E. Recent advancements in supercapacitor technology. *Nano Energy* **2018**, *52*, 441-473.

(11) Fujigaya, T.; Nakashima, N. Fuel cell electrocatalyst using polybenzimidazole-modified carbon nanotubes as support materials. *Adv. Mater.* **2013**, *25* (12), 1666-1681.

(12) Choi, J. W.; Aurbach, D. Promise and reality of post-lithium-ion batteries with high energy densities. *Nat. Rev. Mater.* **2016**, *1* (4), 1-16.

(13) Li, M.; Lu, J.; Chen, Z.; Amine, K. 30 Years of Lithium-Ion Batteries. *Adv. Mater.* **2018**, e1800561.

(14) Whittingham, M. S. Mechanism of reduction of the fluorographite cathode. *J. Electrochem. Soc.* **1975**, *122* (4), 526.

(15) Reddy, M. V.; Mauger, A.; Julien, C. M.; Paolella, A.; Zaghib, K. Brief history of early lithium-battery development. *Materials* **2020**, *13* (8), 1884.

(16) Gamble, F.; Osiecki, J. H.; Cais, M.; Pisharody, R.; DiSalvo, F.; Geballe, T. Intercalation complexes of Lewis bases and layered sulfides: a large class of new superconductors. *Science* **1971**, *174* (4008), 493-497.

(17) Whittingham, M. S. The role of ternary phases in cathode reactions. *J. Electrochem. Soc.* **1976**, *123* (3), 315.

(18) Whittingham, M. S. Lithium batteries and cathode materials. *Chem. Rev.* **2004**, *104* (10), 4271-4302.

(19) Rao, B.; Francis, R.; Christopher, H. Lithium-aluminum electrode. *J. Electrochem. Soc.* **1977**, *124* (10), 1490.

(20) Tarascon, J.-M.; Armand, M. Issues and challenges facing rechargeable lithium batteries. *Nature* **2001**, *414* (6861), 359-367.

(21) Vissers, D.; Tomczuk, Z.; Steunenberg, R. A preliminary investigation of high temperature lithium/iron sulfide secondary cells. *J. Electrochem. Soc.* **1974**, *121* (5), 665.

(22) Gay, E. C.; Vissers, D. R.; Martino, F. J.; Anderson, K. E. Performance Characteristics of Solid Lithium-Aluminum Alloy Electrodes. *J. Electrochem. Soc.* **1976**, *123* (11), 1591.

(23) Nagaura, T. Lithium ion rechargeable battery. *Prog. Batteries Sol. Cells* **1990**, *9*, 209.

(24) Goodenough, J. B.; Park, K.-S. The Li-ion rechargeable battery: a perspective. *J. Am. Chem. Soc.* **2013**, *135* (4), 1167-1176.

(25) Deng, D. Li-ion batteries: basics, progress, and challenges. *Energy Sci. Eng.* **2015**, *3* (5), 385-418.

(26) Torchio, R.; Marini, C.; Kvashnin, Y. O.; Kantor, I.; Mathon, O.; Garbarino, G.; Meneghini, C.; Anzellini, S.; Occelli, F.; Bruno, P. Structure and magnetism of cobalt at high pressure and low temperature. *Phys. Rev. B* **2016**, *94* (2), 024429.

(27) Liu, J.; Bao, Z.; Cui, Y.; Dufek, E. J.; Goodenough, J. B.; Khalifah, P.; Li, Q.; Liaw, B. Y.; Liu, P.; Manthiram, A. Pathways for practical high-energy long-cycling lithium metal batteries. *Nat. Energy* **2019**, *4* (3), 180-186.

(28) Thackeray, M. M.; Wolverton, C.; Isaacs, E. D. Electrical energy storage for transportation—approaching the limits of, and going beyond, lithium-ion batteries. *Energy Environ. Sci.* **2012**, *5* (7), 7854-7863.

(29) Guerfi, A.; Dontigny, M.; Charest, P.; Petitclerc, M.; Lagacé, M.; Vijh, A.; Zaghib, K. Improved electrolytes for Li-ion batteries: Mixtures of ionic liquid and organic electrolyte with enhanced safety and electrochemical performance. *J. Power Sources* **2010**, *195* (3), 845-852.

(30) Cao, D.; Sun, X.; Li, Q.; Natan, A.; Xiang, P.; Zhu, H. Lithium Dendrite in All-Solid-State Batteries: Growth Mechanisms, Suppression Strategies, and Characterizations. *Matter* **2020**, *3* (1), 57-94.

(31) Baek, M.; Shin, H.; Char, K.; Choi, J. W. New high donor electrolyte for lithium–sulfur batteries. *Adv. Mater.* **2020**, *32* (52), 2005022.

(32) Jin, Z.; Xie, K.; Hong, X. Review of electrolyte for lithium sulfur battery. *Acta Chim. Sinica* **2014**, *72* (1), 11.

(33) Pei, F.; Lin, L.; Ou, D.; Zheng, Z.; Mo, S.; Fang, X.; Zheng, N. Self-supporting sulfur cathodes enabled by two-dimensional carbon yolk-shell nanosheets for high-energy-density lithium-sulfur batteries. *Nat. Commun.* **2017**, *8* (1), 482.

(34) Seh, Z. W.; Sun, Y.; Zhang, Q.; Cui, Y. Designing high-energy lithium–sulfur batteries. *Chem. Soc. Rev.* **2016**, *45* (20), 5605-5634.

(35) Yuan, H.; Peng, H. J.; Huang, J. Q.; Zhang, Q. Sulfur redox reactions at working interfaces in lithium–sulfur batteries: a perspective. *Adv. Mater. Inter.* **2019**, *6* (4), 1802046.

(36) Mikhaylik, Y. V.; Akridge, J. R. Polysulfide shuttle study in the Li/S battery system. *J. Electrochem. Soc.* **2004**, *151* (11), A1969.

(37) Manthiram, A.; Fu, Y.; Chung, S. H.; Zu, C.; Su, Y. S. Rechargeable lithium-sulfur batteries. *Chem. Rev.* **2014**, *114* (23), 11751-11787.

(38) Lei, D.; Shi, K.; Ye, H.; Wan, Z.; Wang, Y.; Shen, L.; Li, B.; Yang, Q. H.; Kang, F.; He, Y. B. Progress and Perspective of Solid-State Lithium–Sulfur Batteries. *Adv. Funct. Mater.* **2018**, *28* (38).

(39) Liang, C.; Dudney, N. J.; Howe, J. Y. Hierarchically structured sulfur/carbon nanocomposite material for high-energy lithium battery. *Chem. Mater.* **2009**, *21* (19), 4724-4730.

(40) Chen, J.-j.; Zhang, Q.; Shi, Y.-n.; Qin, L.-l.; Cao, Y.; Zheng, M.-s.; Dong, Q.-f. A hierarchical architecture S/MWCNT nanomicrosphere with large pores for lithium sulfur batteries. *Phys. Chem. Chem. Phys.* **2012**, *14* (16), 5376-5382.

(41) Su, Y.-S.; Manthiram, A. A new approach to improve cycle performance of rechargeable lithium–sulfur batteries by inserting a free-standing MWCNT interlayer. *Chem. Commun.* **2012**, *48* (70), 8817-8819.

(42) Chen, L.; Yu, H.; Li, W.; Dirican, M.; Liu, Y.; Zhang, X. Interlayer design based on carbon materials for lithium–sulfur batteries: a review. *J. Mater. Chem. A* **2020**, *8* (21), 10709-10735.

(43) Yan, R.; Oschatz, M.; Wu, F. Towards stable lithium-sulfur battery cathodes by combining physical and chemical confinement of polysulfides in core-shell structured nitrogen-doped carbons. *Carbon* **2020**, *161*, 162-168.

(44) Gao, M.; Zhou, W.-Y.; Mo, Y.-X.; Sheng, T.; Deng, Y.; Chen, L.; Wang, K.; Tan, Y.; Zhou, H. Outstanding long-cycling lithium− sulfur batteries by core-shell structure of S@ Pt composite with ultrahigh sulfur content. *Adv. Powder Mater.* **2022**, *1* (1), 100006.

(45) Jiang, Z.; Zeng, Z.; Hu, W.; Han, Z.; Cheng, S.; Xie, J. Diluted high concentration electrolyte with dual effects for practical lithium-sulfur batteries. *Energy Storage Mater.* **2021**, *36*, 333-340.

(46) Luo, C.; Liang, X.; Sun, Y.; Lv, W.; Sun, Y.; Lu, Z.; Hua, W.; Yang, H.; Wang, R.; Yan, C.; et al. An organic nickel salt-based electrolyte additive boosts homogeneous catalysis for lithium-sulfur batteries. *Energy Storage Mater.* **2020**, *33*, 290-297.

(47) Ding, B.; Wang, J.; Fan, Z.; Chen, S.; Lin, Q.; Lu, X.; Dou, H.; Kumar Nanjundan, A.; Yushin, G.; Zhang, X.; et al. Solid-state lithium–sulfur batteries: Advances, challenges and perspectives. *Mater. Today* **2020**, *40*, 114-131.

(48) Cheng, X. B.; Zhang, R.; Zhao, C. Z.; Zhang, Q. Toward Safe Lithium Metal Anode in Rechargeable Batteries: A Review. *Chem. Rev.* **2017**, *117* (15), 10403-10473.

(49) Pan, H.; Cheng, Z.; He, P.; Zhou, H. A Review of Solid-State Lithium–Sulfur Battery: Ion Transport and Polysulfide Chemistry. *Energy Fuels* **2020**, *34* (10), 11942-11961.

(50) Cheng, X.-B.; Zhao, C.-Z.; Yao, Y.-X.; Liu, H.; Zhang, Q. Recent Advances in Energy Chemistry between Solid-State Electrolyte and Safe Lithium-Metal Anodes. *Chem* **2019**, *5* (1), 74-96.

(51) Ji, X.; Hou, S.; Wang, P.; He, X.; Piao, N.; Chen, J.; Fan, X.; Wang, C. Solid-State Electrolyte Design for Lithium Dendrite Suppression. *Adv. Mater.* **2020**, *32* (46), e2002741.

(52) Jiang, T.; He, P.; Wang, G.; Shen, Y.; Nan, C. W.; Fan, L. Z. Solvent-Free Synthesis of Thin, Flexible, Nonflammable Garnet-Based Composite Solid Electrolyte for All-Solid-State Lithium Batteries. *Adv. Energy Mater.* **2020**, *10* (12). DOI: 10.1002/aenm.201903376.

(53) Jaumaux, P.; Wu, J.; Shanmukaraj, D.; Wang, Y.; Zhou, D.; Sun, B.; Kang, F.; Li, B.; Armand, M.; Wang, G. Non-Flammable Liquid and Quasi-Solid Electrolytes toward Highly-Safe Alkali Metal-Based Batteries. *Adv. Funct. Mater.* **2020**, *31* (10). DOI: 10.1002/adfm.202008644.

(54) Bandyopadhyay, S.; Nandan, B. A review on design of cathode, anode and solid electrolyte for true all-solid-state lithium sulfur batteries. *Mater. Today Energy* **2023**, *31*.

(55) Hong, S.; Wang, Y.; Kim, N.; Lee, S. B. Polymer-based electrolytes for all-solid-state lithium–sulfur batteries: from fundamental research to performance improvement. *J. Mater. Sci.* **2021**, *56* (14), 8358-8382.

(56) Wild, M.; O'Neill, L.; Zhang, T.; Purkayastha, R.; Minton, G.; Marinescu, M.; Offer, G. J. Lithium sulfur batteries, a mechanistic review. *Energy Environ. Sci.* **2015**, *8* (12), 3477-3494.

(57) Zhou, L.; Danilov, D. L.; Eichel, R. A.; Notten, P. H. L. Host Materials Anchoring Polysulfides in Li–S Batteries Reviewed. *Adv. Energy Mater.* **2020**, *11* (15).

(58) Yamada, T.; Ito, S.; Omoda, R.; Watanabe, T.; Aihara, Y.; Agostini, M.; Ulissi, U.; Hassoun, J.; Scrosati, B. All Solid-State Lithium–Sulfur Battery Using a Glass-Type P_2S_5–Li_2S Electrolyte: Benefits on Anode Kinetics. *J. Electrochem. Soc.* **2015**, *162* (4), A646-A651.

(59) Fang, R.; Xu, H.; Xu, B.; Li, X.; Li, Y.; Goodenough, J. B. Reaction Mechanism Optimization of Solid-State Li–S Batteries with a PEO-Based Electrolyte. *Adv. Funct. Mater.* **2020**, *31* (2).

(60) Bruce, P. G.; Freunberger, S. A.; Hardwick, L. J.; Tarascon, J. M. Li-O_2 and Li-S batteries with high energy storage. *Nat. Mater.* **2011**, *11* (1), 19-29.

(61) Li, Z.; Huang, Y.; Yuan, L.; Hao, Z.; Huang, Y. Status and prospects in sulfur–carbon composites as cathode materials for rechargeable lithium–sulfur batteries. *Carbon* **2015**, *92*, 41-63.

(62) Kuc, A.; Seifert, G. Hexagon-preserving carbon foams: Properties of hypothetical carbon allotropes. *Phys. Rev. B* **2006**, *74* (21), 214104.

(63) Agostini, M.; Aihara, Y.; Yamada, T.; Scrosati, B.; Hassoun, J. A lithium–sulfur battery using a solid, glass-type P_2S_5–Li_2S electrolyte. *Solid State Ionics* **2013**, *244*, 48-51.

(64) Pichler, T.; Knupfer, M.; Golden, M.; Fink, J.; Rinzler, A.; Smalley, R. Localized and delocalized electronic states in single-wall carbon nanotubes. *Phys. Rev. Lett.* **1998**, *80* (21), 4729.

(65) Nagao, M.; Hayashi, A.; Tatsumisago, M. Sulfur–carbon composite electrode for all-solid-state Li/S battery with Li_2S–P_2S_5 solid electrolyte. *Electrochimica Acta* **2011**, *56* (17), 6055-6059.

(66) Kobayashi, T.; Imade, Y.; Shishihara, D.; Homma, K.; Nagao, M.; Watanabe, R.; Yokoi, T.; Yamada, A.; Kanno, R.; Tatsumi, T. All solid-state battery with sulfur electrode and thio-LISICON electrolyte. *J. Power Sources* **2008**, *182* (2), 621-625.

(67) Zhai, P.; Peng, N.; Sun, Z.; Wu, W.; Kou, W.; Cui, G.; Zhao, K.; Wang, J. Thin laminar composite solid electrolyte with high ionic conductivity and mechanical strength towards advanced all-solid-state lithium–sulfur battery. *J. Mater. Chem. A* **2020**, *8* (44), 23344-23353.

(68) Chen, M.; Adams, S. High performance all-solid-state lithium/sulfur batteries using lithium argyrodite electrolyte. *J. Solid State Electrochem.* **2014**, *19* (3), 697-702.

(69) Santiago, A.; Castillo, J.; Garbayo, I.; Saenz de Buruaga, A.; Coca Clemente, J. A.; Qiao, L.; Cid Barreno, R.; Martinez-Ibañez, M.; Armand, M.; Zhang, H.; et al. Salt Additives for Improving Cyclability of Polymer-Based All-Solid-State Lithium–Sulfur Batteries. *ACS Appl. Energy Mater.* **2021**, *4* (5), 4459-4464.

(70) Phuc, N. H. H.; Takaki, M.; Muto, H.; Reiko, M.; Kazuhiro, H.; Matsuda, A. Sulfur–Carbon Nano Fiber Composite Solid Electrolyte for All-Solid-State Li–S Batteries. *ACS Appl. Energy Mater.* **2020**, *3* (2), 1569-1573.

(71) Zhang, Q.; Huang, N.; Huang, Z.; Cai, L.; Wu, J.; Yao, X. CNTs@S composite as cathode for all-solid-state lithium-sulfur batteries with ultralong cycle life. *J. Energy Chem.* **2020**, *40*, 151-155.

(72) Zhang, Y.; Zhao, Y.; Bakenov, Z. A novel lithium/sulfur battery based on sulfur/graphene nanosheet composite cathode and gel polymer electrolyte. *Nanoscale Res. Lett.* **2014**, *9*, 1-7.

(73) Yao, X.; Huang, N.; Han, F.; Zhang, Q.; Wan, H.; Mwizerwa, J. P.; Wang, C.; Xu, X. High-performance all-solid-state lithium–sulfur batteries enabled by amorphous sulfur-coated reduced graphene oxide cathodes. *Adv. Energy Mater.* **2017**, *7* (17), 1602923.

(74) Lee, J.; Kim, J.; Hyeon, T. Recent progress in the synthesis of porous carbon materials. *Adv. Mater.* **2006**, *18* (16), 2073-2094.

(75) Xiao, L.; Cao, Y.; Xiao, J.; Schwenzer, B.; Engelhard, M. H.; Saraf, L. V.; Nie, Z.; Exarhos, G. J.; Liu, J. A soft approach to encapsulate sulfur: polyaniline nanotubes for lithium-sulfur batteries with long cycle life. *Adv. Mater.* **2012**, *24* (9), 1176-1181.

(76) Fu, Y.; Manthiram, A. Core-shell structured sulfur-polypyrrole composite cathodes for lithium-sulfur batteries. *Rsc Adv.* **2012**, *2* (14), 5927-5929.

(77) Ma, G.; Wen, Z.; Jin, J.; Lu, Y.; Wu, X.; Wu, M.; Chen, C. Hollow polyaniline sphere@sulfur composites for prolonged cycling stability of lithium–sulfur batteries. *J. Mater. Chem. A* **2014**, *2* (27), 10350-10354.

(78) Nagata, H.; Chikusa, Y. All-solid-state lithium–sulfur batteries using a conductive composite containing activated carbon and electroconductive polymers. *Chem. Lett.* **2014**, *43* (8), 1335-1336.

(79) Gracia, I.; Youcef, H. B.; Judez, X.; Oteo, U.; Zhang, H.; Li, C.; Rodriguez-Martinez, L. M.; Armand, M. S-containing copolymer as cathode material in poly (ethylene oxide)-based all-solid-state Li-S batteries. *J. Power Sources* **2018**, *390*, 148-152.

(80) Kamaya, N.; Homma, K.; Yamakawa, Y.; Hirayama, M.; Kanno, R.; Yonemura, M.; Kamiyama, T.; Kato, Y.; Hama, S.; Kawamoto, K. A lithium superionic conductor. *Nat. Mater.* **2011**, *10* (9), 682-686.

(81) Indrawan, R. F.; Gamo, H.; Nagai, A.; Matsuda, A. Chemically Understanding the Liquid-Phase Synthesis of Argyrodite Solid Electrolyte Li_6PS_5Cl with the Highest Ionic Conductivity for All-Solid-State Batteries. *Chem. Mater.* **2023**, *35* (6), 2549-2558.

(82) Chang, D.; Oh, K.; Kim, S. J.; Kang, K. Super-Ionic Conduction in Solid-State $Li_7P_3S_{11}$-Type Sulfide Electrolytes. *Chem. Mater.* **2018**, *30* (24), 8764-8770.

(83) Umeshbabu, E.; Zheng, B.; Yang, Y. Recent Progress in All-Solid-State Lithium−Sulfur Batteries Using High Li-Ion Conductive Solid Electrolytes. *Electrochem. Energy Rev.* **2019**, *2* (2), 199-230.

(84) Choi, H. U.; Jin, J. S.; Park, J.-Y.; Lim, H.-T. Performance improvement of all-solid-state Li-S batteries with optimizing morphology and structure of sulfur composite electrode. *J. Alloys Compd.* **2017**, *723*, 787-794.

(85) Nagao, M.; Hayashi, A.; Tatsumisago, M. Electrochemical performance of all-solid-state Li/S batteries with sulfur-based composite electrodes prepared by mechanical milling at high temperature. *Energy Technology* **2013**, *1* (2-3), 186-192.

(86) Xu, R.; Wu, Z.; Zhang, S.; Wang, X.; Xia, Y.; Xia, X.; Huang, X.; Tu, J. Construction of all-solid-state batteries based on a sulfur-graphene composite and $Li_{9.54}Si_{1.74}P_{1.44}S_{11.7}Cl_{0.3}$ solid electrolyte. *Chem. Eur. J.* **2017**, *23* (56), 13950-13956.

(87) Zhang, Y.; Liu, T.; Zhang, Q.; Zhang, X.; Wang, S.; Wang, X.; Li, L.; Fan, L.-Z.; Nan, C.-W.; Shen, Y. High-performance all-solid-state lithium–sulfur batteries with sulfur/carbon nano-hybrids in a composite cathode. *J. Mater. Chem. A* **2018**, *6* (46), 23345-23356.

(88) Zhou, C.; Bag, S.; He, T.; Lv, B.; Thangadurai, V. A 20 °C operating high capacity solid-state Li-S battery with an engineered carbon support cathode structure. *Applied Materials Today* **2020**, *19*, 100585.

(89) Peng, J.; Zheng, X.; Wu, Y.; Li, C.; Lv, Z.; Zheng, C.; Liu, J.; Zhong, H.; Gong, Z.; Yang, Y. Li_2S-Based Composite Cathode with in Situ-Generated Li_3PS_4 Electrolyte on Li2S for Advanced All-Solid-State Lithium–Sulfur Batteries. *ACS Appl. Mater. Interfaces* **2023**, *15* (16), 20191-20199.

(90) Banerjee, A.; Wang, X.; Fang, C.; Wu, E. A.; Meng, Y. S. Interfaces and interphases in all-solid-state batteries with inorganic solid electrolytes. *Chem. Rev.* **2020**, *120* (14), 6878-6933.

(91) Jeon, B. H.; Yeon, J. H.; Kim, K. M.; Chung, I. J. Preparation and electrochemical properties of lithium–sulfur polymer batteries. *J. Power Sources* **2002**, *109* (1), 89-97.

(92) Cai, K.; Song, M.-K.; Cairns, E. J.; Zhang, Y. Nanostructured Li_2S–C composites as cathode material for high-energy lithium/sulfur batteries. *Nano Lett.* **2012**, *12* (12), 6474-6479.

(93) Yan, H.; Wang, H.; Wang, D.; Li, X.; Gong, Z.; Yang, Y. In situ generated Li_2S–C nanocomposite for high-capacity and long-life all-solid-state lithium sulfur batteries with ultrahigh areal mass loading. *Nano Lett.* **2019**, *19* (5), 3280-3287.

(94) El-Shinawi, H.; Cussen, E. J.; Corr, S. A. A facile synthetic approach to nanostructured Li_2S cathodes for rechargeable solid-state Li–S batteries. *Nanoscale* **2019**, *11* (41), 19297-19300.

(95) Lodovico, L.; Milad Hosseini, S.; Varzi, A.; Passerini, S. Amorphous Lithium Sulfide as Lithium-Sulfur Battery Cathode with Low Activation Barrier. *Energy Technology* **2019**, *7* (12), 1801013.

(96) Takeuchi, T.; Kageyama, H.; Nakanishi, K.; Tabuchi, M.; Sakaebe, H.; Ohta, T.; Senoh, H.; Sakai, T.; Tatsumi, K. All-solid-state lithium secondary battery with Li_2S–C composite positive electrode prepared by spark-plasma-sintering process. *J. Electrochem. Soc.* **2010**, *157* (11), A1196.

(97) Arnold, W.; Buchberger, D. A.; Li, Y.; Sunkara, M.; Druffel, T.; Wang, H. Halide doping effect on solvent-synthesized lithium argyrodites Li_6PS_5X (X= Cl, Br, I) superionic conductors. *J. Power Sources* **2020**, *464*, 228158.

(98) Lorger, S.; Usiskin, R. E.; Maier, J. Transport and charge carrier chemistry in lithium sulfide. *Adv. Funct. Mater.* **2019**, *29* (6), 1807688.

(99) Obrovac, M.; Dahn, J. Electrochemically active lithia/metal and lithium sulfide/metal composites. *Electrochem. Solid State Lett.* **2002**, *5* (4), A70.

(100) Luo, G.; Zhao, J.; Wang, B. First-principles study of transition metal doped Li_2S as cathode materials in lithium batteries. *J. Renew. Sustain. Energy* **2012**, *4* (6).

(101) Ulissi, U.; Ito, S.; Hosseini, S. M.; Varzi, A.; Aihara, Y.; Passerini, S. High Capacity All-Solid-State Lithium Batteries Enabled by Pyrite-Sulfur Composites. *Adv. Energy Mater.* **2018**, *8* (26), 1801462.

(102) Zhang, Q.; Wan, H.; Liu, G.; Ding, Z.; Mwizerwa, J. P.; Yao, X. Rational design of multi-channel continuous electronic/ionic conductive networks for room temperature vanadium tetrasulfide-based all-solid-state lithium-sulfur batteries. *Nano Energy* **2019**, *57*, 771-782.

(103) Grayfer, E. D.; Pazhetnov, E. M.; Kozlova, M. N.; Artemkina, S. B.; Fedorov, V. E. Anionic redox chemistry in polysulfide electrode materials for rechargeable batteries. *ChemSusChem* **2017**, *10* (24), 4805-4811.

(104) Chung, J.-S.; Sohn, H.-J. Electrochemical behaviors of CuS as a cathode material for lithium secondary batteries. *J. Power Sources* **2002**, *108* (1-2), 226-231.

(105) Hayashi, A.; Ohtomo, T.; Mizuno, F.; Tadanaga, K.; Tatsumisago, M. Rechargeable lithium batteries, using sulfur-based cathode materials and Li_2S–P_2S_5 glass-ceramic electrolytes. *Electrochim. Acta* **2004**, *50* (2-3), 893-897.

(106) Machida, N.; Shigematsu, T. An all-solid-state lithium battery with sulfur as positive electrode materials. *Chem. Lett.* **2004**, *33* (4), 376-377.

(107) Hosseini, S. M.; Varzi, A.; Ito, S.; Aihara, Y.; Passerini, S. High loading CuS-based cathodes for all-solid-state lithium sulfur batteries with enhanced volumetric capacity. *Energy Storage Mater.* **2020**, *27*, 61-68.

(108) Mwizerwa, J. P.; Zhang, Q.; Han, F.; Wan, H.; Cai, L.; Wang, C.; Yao, X. Sulfur-embedded FeS_2 as a high-performance cathode for room temperature all-solid-state lithium–sulfur batteries. *ACS Appl. Mater. Interfaces* **2020**, *12* (16), 18519-18525.

(109) Zheng, F.; Kotobuki, M.; Song, S.; Lai, M. O.; Lu, L. Review on solid electrolytes for all-solid-state lithium-ion batteries. *J. Power Sources* **2018**, *389*, 198-213.

(110) Kato, Y.; Hori, S.; Saito, T.; Suzuki, K.; Hirayama, M.; Mitsui, A.; Yonemura, M.; Iba, H.; Kanno, R. High-power all-solid-state batteries using sulfide superionic conductors. *Nat. Energy* **2016**, *1* (4), 1-7.

(111) Mercier, R.; Malugani, J.-P.; Fahys, B.; Robert, G. Superionic conduction in Li_2S-P_2S_5-LiI-glasses. *Solid State Ion.* **1981**, *5*, 663-666.

(112) Zhang, Q.; Cao, D.; Ma, Y.; Natan, A.; Aurora, P.; Zhu, H. Sulfide-Based Solid-State Electrolytes: Synthesis, Stability, and Potential for All-Solid-State Batteries. *Adv. Mater.* **2019**, *31* (44), e1901131.

(113) Seino, Y.; Ota, T.; Takada, K.; Hayashi, A.; Tatsumisago, M. A sulphide lithium super ion conductor is superior to liquid ion conductors for use in rechargeable batteries. *Energy Environ. Sci.* **2014**, *7* (2), 627-631.

(114) Fu, L.; Engqvist, H.; Xia, W. Glass-Ceramics in Dentistry: A Review. *Materials* **2020**, *13* (5).

(115) Kanno, R.; Murayama, M. Lithium ionic conductor thio-LISICON: the Li_2S-GeS_2-P_2S_5 system. *J. Electrochem. Soc.* **2001**, *148* (7), A742.

(116) Thangadurai, V.; Kaack, H.; Weppner, W. J. Novel fast lithium ion conduction in garnet-type $Li_5La_3M_2O_{12}$ (M= Nb, Ta). *J. Am. Chem. Soc.* **2003**, *86* (3), 437-440.

(117) Murugan, R.; Thangadurai, V.; Weppner, W. Fast lithium ion conduction in garnet-type $Li_7La_3Zr_2O_{12}$. *Angew. Chem. Int. Ed.* **2007**, *46* (41), 7778-7781.

(118) Aono, H.; Sugimoto, E.; Sadaoka, Y.; Imanaka, N.; Adachi, G.-y. Electrical Properties and Sinterability for Lithium Germanium Phosphate $Li_{1+x}M_xGe_{2-x}(PO_4)_3$, M= Al, Cr, Ga, Fe, Sc, and In Systems. *Bull. Chem. Soc. Jpn.* **1992**, *65* (8), 2200-2204.

(119) Muramatsu, H.; Hayashi, A.; Ohtomo, T.; Hama, S.; Tatsumisago, M. Structural change of Li_2S–P_2S_5 sulfide solid electrolytes in the atmosphere. *Solid State Ion.* **2011**, *182* (1), 116-119.

(120) Zhang, Q.; Kong, Y.; Gao, K.; Wen, Y.; Zhang, Q.; Fang, H.; Ma, C.; Du, Y. Research progress on space charge layer effect in lithium-ion solid-state battery. *Sci. China Technol. Sci.* **2022**, *65* (10), 2246-2258.

(121) Xue, Z.; He, D.; Xie, X. Poly (ethylene oxide)-based electrolytes for lithium-ion batteries. *J. Mater. Chem. A* **2015**, *3* (38), 19218-19253.

(122) Agrawal, R.; Pandey, G. Solid polymer electrolytes: materials designing and all-solid-state battery applications: an overview. *J. Phys. D: Appl. Phys.* **2008**, *41* (22), 223001.

(123) Judez, X.; Piszcz, M.; Coya, E.; Li, C.; Aldalur, I.; Oteo, U.; Zhang, Y.; Zhang, W.; Rodriguez-Martinez, L. M.; Zhang, H. Stable cycling of lithium metal electrode in nanocomposite solid polymer electrolytes with lithium bis (fluorosulfonyl) imide. *Solid State Ion.* **2018**, *318*, 95-101.

(124) Zhang, Z.; Zhang, L.; Liu, Y.; Yu, C.; Yan, X.; Xu, B.; Wang, L.-m. Synthesis and characterization of argyrodite solid electrolytes for all-solid-state Li-ion batteries. *J. Alloys Compd.* **2018**, *747*, 227-235.

(125) Sahu, G.; Lin, Z.; Li, J.; Liu, Z.; Dudney, N.; Liang, C. Air-stable, high-conduction solid electrolytes of arsenic-substituted Li_4SnS_4. *Energy Environ. Sci.* **2014**, *7* (3), 1053-1058.

(126) Liu, G.; Xie, D.; Wang, X.; Yao, X.; Chen, S.; Xiao, R.; Li, H.; Xu, X. High air-stability and superior lithium ion conduction of $Li_{3+3x}P_{1-x}Zn_xS_{4-x}O_x$ by aliovalent substitution of ZnO for all-solid-state lithium batteries. *Energy Storage Mater.* **2019**, *17*, 266-274.

(127) Xu, X.; Wen, Z.; Yang, X.; Zhang, J.; Gu, Z. High lithium ion conductivity glass-ceramics in $Li_2O–Al_2O_3–TiO_2–P_2O_5$ from nanoscaled glassy powders by mechanical milling. *Solid State Ion.* **2006**, *177* (26-32), 2611-2615.

(128) Chen, Y.-T.; Marple, M. A. T.; Tan, D. H. S.; Ham, S.-Y.; Sayahpour, B.; Li, W.-K.; Yang, H.; Lee, J. B.; Hah, H. J.; Wu, E. A.; et al. Investigating dry room compatibility of sulfide solid-state electrolytes for scalable manufacturing. *J. Mater. Chem. A* **2022**, *10* (13), 7155-7164.

(129) Morino, Y.; Sano, H.; Kawamoto, K.; Fukui, K.-i.; Takeuchi, M.; Sakuda, A.; Hayashi, A. Degradation of an argyrodite-type sulfide solid electrolyte by a trace of water: A spectroscopic analysis. *Solid State Ion.* **2023**, *392*.

(130) Shi, Y.; Fan, Z.; Ding, B.; Li, Z.; Lin, Q.; Chen, S.; Dou, H.; Zhang, X. Atomic-scale Al_2O_3 modified PEO-based composite polymer electrolyte for durable solid-state Li–S batteries. *J. Electroanal. Chem.* **2021**, *881*, 114916.

(131) Park, C.-M.; Kim, J.-H.; Kim, H.; Sohn, H.-J. Li-alloy based anode materials for Li secondary batteries. *Chem. Soc. Rev.* **2010**, *39* (8), 3115-3141.

(132) Pan, H.; Zhang, M.; Cheng, Z.; Jiang, H.; Yang, J.; Wang, P.; He, P.; Zhou, H. Carbon-free and binder-free Li-Al alloy anode enabling an all-solid-state Li-S battery with high energy and stability. *Sci. Adv.* **2022**, *8* (15), eabn4372.

(133) Nagata, H.; Chikusa, Y. All-Solid-State Lithium–Sulfur Battery with High Energy and Power Densities at the Cell Level. *Energy Technol.* **2016**, *4* (4), 484-489.

Chapter 2 Improving Electrochemical Performance of Li_2S Cathode Based on Point Defect Control with Cation/Anion Dual Doping

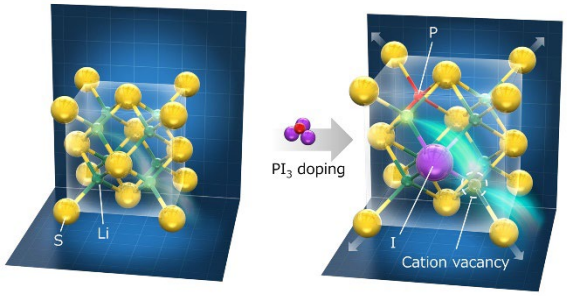

Li_2S is a promising cathode candidate for all-solid-state batteries (ASSBs) because of its high theoretical capacity and availability of coupling with Li-free anode or anode less electrode. However, ionically insulating Li_2S leads to excess conductive additives, low sulfur utilization and sluggish kinetics, which hinders for ASSBs to implement the high energy density potential. Improving the intrinsic conductivity of Li_2S is the key to solve this issue. In this study, PI_3-doped Li_2S cathodes were synthesized and the relationship between lithium vacancies and ionic conductivities was examined quantitatively by time-of-flight (TOF) neutron diffraction. By cation-anion-dual doping, ionic conductivities of Li_2S-PI_3 materials were improved to 10^{-4} S cm^{-1}, which is capable for cathode without solid electrolytes added. Simply mixed with carbon, the Li_2S-PI_3-C cathode shows a high overall cathode capacity of 541 mAh g^{-1} with high S utilization of 82% at 0.05 C and capacity of 207 mAh g^{-1} at 1 C at room temperature, realizing high energy density with good rate performance.

2.1 Introduction

All-solid-state batteries (ASSBs) with sulfide-based solid electrolytes (SEs) are expected to be the next generation of storage batteries, because they possess potential with high energy density due to the bipolar structure, good power density due to the highly ion-conductive SE, and reliable safety due to the absence of organic solvents[1-3]. Among the cathode materials for ASSBs with sulfide electrolytes, Li_2S is a promising candidate due to its high theoretical capacity of 1167 mAh g^{-1} and the availability of Li-free anode such as Si and anode-less electrodes[4, 5]. However, because of extremely low ionic conductivity (10^{-9} S cm^{-1})[6, 7] and much insulation during charging with S_8 formation, it is necessary to mix Li_2S with a large amount of sulfide SEs as composite cathodes[8, 9]. These excessive SEs in the cathodes without contributing to capacity reduce the energy density of the whole cathode composites, which impedes the practical application of Li_2S-based cathodes for ASSBs with sulfide electrolytes.

In order to solve the issue, two types of methods have been widely studied: (1) to develop sulfide SEs with high ionic conductivity[10, 11], and (2) to improve the apparent ionic conductivity of the cathode composites by increasing dispersion of sulfide SEs in cathode composites[1, 12]. As for the former one, several SE with high ionic conductivity have been developed, such as Li_6PS_5Cl[13], $Li_7P_3S_{11}$[14], $Li_{10}GeP_2S_{12}$[15], $Li_{9.54}Si_{1.74}P_{1.44}S_{11.7}Cl_{0.3}$[16] and $Li_{9.54}[Si_{0.6}Ge_{0.4}]_{1.74}P_{1.44}S_{11.1}Br_{0.3}O_{0.6}$[17]. As for the later, different techniques have been used to fabricate composite electrodes with a liquid phase to control the dispersion state of the sulfide solid electrolytes in the cathode composites[18-25]. Although these approaches are effective in reducing the amount of sulfide SEs in cathode composites, the decomposition of SEs and the degradation at the cathode/SEs interface within the composite cathode during charging and discharging results in a continuous increase of impedance and poor cycling stability[26, 27].

As a different approach from the methods mentioned above, several studies have been devoted to improve the ionic conductivity of Li_2S itself by controlling point defects in the structure[28-31]. It has been reported the insulting nature of Li_2S has associated with its stable antifluorite structure, which is consists of strong bond energy[31]. Therefore, point defect controlling by doping is probably capable of improving the ionic conductivity of Li_2S. Among different possible doping materials, lithium halide is proven to be effective in

improving the ionic conductivity because of the introduction of lithium vacancies in Li_2S structure due to electrical neutrality[28-31]. In lithium halide doped Li_2S, it has been reported that LiI doped Li_2S ($80Li_2S$-20LiI) showed the ionic conductivity of 2×10^{-6} S cm^{-1} at 25 °C[32-34]. Recently, it has been reported that AlI_3 doped Li_2S ($95Li_2S$-5 AlI_3) showed a relatively higher ionic conductivity of 4.5×10^{-6} S cm^{-1} at room temperature because both Al^{3+} and I^- are dissolved into the Li_2S structure[35]. These results indicate that introducing lithium vacancies in the Li_2S structure by dual doping cation as well as anion with metal iodide is useful to improve the ionic conductivity of Li_2S. However, the relationship between the amount of the cation vacancy and ionic conductivity in metal-iodide-doped Li_2S has not been clearly understood because quantitative evaluation of cation vacancies has not been performed. Considering that S^{2-} is a soft Lewis base, it would be preferable to use a cation that is a soft Lewis acid to increase the amount of solid solution for the doped metal cation.

In this study, to address the above-mentioned issues, we prepared PI_3-doped Li_2S cathode materials and examined the relationship between the amount of the cation vacancy and ionic conductivity by using time-of-flight (TOF) neutron diffraction, which is sensitive to detect light element. It is found that the optimized Li_2S-PI_3 ($93.5Li_2S$-$6.25PI_3$) shows high ionic conductivity of 10^{-4} S cm^{-1}. Simply mixed with carbon, its composite shows a high overall cathode capacity of 541 mAh g^{-1} at 0.05 C and 207 mAh g^{-1} at 1 C under 25°C.

2.2 Experimental Section

2.2.1 Material Synthesis

The (100-x)Li_2S-$x$$PI_3$ samples (x=0, 2.5, 3, 4, 5, 6.25 and 7.5) in this study were prepared using ball milling. Stoichiometric amounts of Li_2S (99% purity, Aldrich) and PI_3 (99% purity, Aldrich) were hand-ground in a mortar for 0.5 h, followed by mechanical mixing with ZrO_2 balls at 530 rpm for 40 h. The Li_2S-PI_3-C cathode composites were prepared Li_2S-PI_3 samples and Cnovel MJ(4)030 (Toyo Tanso) with a 90:10 weight ratio by ball milling at 500 rpm for 10 h. The Li_3PS_4 glass powder used to fabricate the solid electrolyte layer with the ionic conductivity of 5×10^{-4} S cm^{-1} was prepared via ball milling using a

previously reported procedure[36]. Li_2S (99% purity, Aldrich) and P_2S_5 (99% purity, Aldrich) powders with a 3:1 molar ratio were mechanically mixed using ZrO_2 balls at 600 rpm for 16 h. All experiments were performed in a dry Ar-filled glovebox.

2.2.2 Characterization

The synchrotron X-ray diffraction (XRD) for the as-prepared (100-*x*)Li_2S-*x*PI_3 samples (*x* = 0, 2.5, 5, 6.25 and 7.5) was measured at the BL02B2 beamline at SPring-8, Japan. Time-of-flight (TOF) neutron diffraction was conducted on (100-*x*)Li_2S-*x*PI_3 samples (*x*=0, 2.5, 5, 6.25, 7.5) at BL20 (iMATERIA) beamline in J-PARK, Japan. The Rietveld refinement was performed with Jana[37]. And these Li_2S-PI_3 samples were also measured by photoelectron spectroscope (XPS, VersaProbe III). Scanning electron microscope (SEM, Hitachi SU-8220) and energy dispersive X-ray spectroscopy (EDS, Horiba X-max^N) mapping were used for (100-*x*)Li_2S-*x*PI_3 samples (*x* = 0, 2.5, 5, 6.25, 7.5) and the cross section of the 93.75Li_2S-6.25PI_3-C/Li_3PS_4 pellet. The X-ray absorption spectroscopy (XAS) of S *K*-edge for the cathode materials after galvanostatic measurements was measured without air exposure at the BL6N1 beamline of the Aichi Synchrotron Radiation Center, Japan.

2.2.3 Electrochemical Measurements

The electrochemical performance of the Li_2S-PI_3-C cathode materials was analyzed using a two-electrode cell. The Li_2S-PI_3-C composites were used as cathode materials without adding solid electrolyte to them, and the prepared Li_3PS_4 was used as the solid electrolyte layer of the cell. The Li_2S-PI_3-C cathode materials (4 mg) and the Li_3PS_4 (80 mg) for solid electrolyte layer were placed in a polycarbonate tube with a diameter of 10 mm and were pressed under a pressure of 360 MPa. The cross-section SEM and EDS mapping for Li_2S-PI_3-C/Li_3PS_4 pellet shown in Figure 2.1, that the Li_3PS_4 layer, with a thickness of about 550 μm, is uniformly covered by Li_2S-PI_3-C, which has the thickness of 28 μm" and "All the calculations for specific capacities are based on the mass of cathode composites. 1 C is the weight proportion of Li_2S in Li_2S-PI_3-C cathode times theoretical capacity of Li_2S (1167 mAh g^{-1}). A Li−In alloy layer was placed on the solid electrolyte at the opposite side to the cathode layer and served as the anode[38]. Two stainless-steel rods, which were added to the cathode and anode sides by applying a pressure of 120 MPa, were used as current collectors. The cell assembly was performed

in a dry Ar-filled glovebox. Electrochemical tests for the cells were performed with discharge and charge cutoff voltages of 0 (0.62 V vs. Li) and 3.0 V (3.62 V vs. Li), respectively, at 25 °C. All the calculations for specific capacities are based on the mass of cathode composites. 1 C is the weight proportion of Li_2S in Li_2S-PI_3-C cathode times theoretical capacity of Li_2S (1167 mAh g^{-1}). Alternating current (AC) impedance was conducted to measure the ionic conductivities of the (100-*x*)Li_2S-*x*PI_3 by using Modulab XM ECS (Solartron Analytical)[38]. The materials were loaded into a polycarbonate tube with a diameter of 10 mm and pressed into pellets under a pressure of 360 MPa and set between two stainless-steel current collector plates. The AC amplitude was 10 mV, and the applied frequency ranged between 1 MHz and 0.1 Hz.

2.3 Results and Discussion

2.3.1 Phase and Structure

The crystal structures of (100-*x*)Li_2S-*x*PI_3 (*x* = 0, 2.5, 5, 6.25, and 7.5) were examined by synchrotron XRD and TOF neutron diffraction. In the synchrotron XRD (Figure 2.2), all sharp peaks of (100-*x*)Li_2S-*x*PI_3 (*x* = 0, 2.5, 5, 6.25) were assigned to Li_2S (space group: $Fm\bar{3}m$) while a broad peak appeared around 7.1° in addition to the sharp peaks might attributed to PI_3 or LiI in the 92.5Li_2S-7.5PI_3 (*x* = 7.5). The lattice constants and site occupancy of each element in the (100-*x*)Li_2S-*x*PI_3 (*x* = 0, 2.5, 5, 6.25 and 7.5) were calculated by Rietveld analysis for the neutron diffraction patterns because the neutron beam is more sensitive to light element such as lithium than X-ray (Figure 2.2(b)-(c), Figure 2.3, Table 2.1). In order to obtain more accurate results, refinement conducted on the series of Li_2S-PI_3 samples was based on all of QA, BS and LA bank data. As shown in Figure 2.2(b) and 2.2(c), both lattice constant and lithium site vacancy of (100-*x*)Li_2S-*x*PI_3 increased linearly with the increment of PI_3 content up to *x* = 6.25, and increased slightly from *x* = 6.25 to *x* = 7.5. The linear lattice expansion with PI_3 content is because PI_3 was doped into the Li_2S structure with the substitution of larger I^- (ionic radii: 2.2 Å) than S^{2-} (ionic radii: 1.84 Å)[39]. The P^{3+} and I^- occupied the lithium site and sulfur site in the Li_2S structure, respectively, leading to the linearly increased lithium site vacancy for compensation to keep the electrical neutrality (Figure 2.2(c) and Table 2.1). The minor change of lattice constant and lithium site vacancy from *x* = 6.25 to *x* = 7.5 indicates that a solid solution limit exists between *x* = 6.25 and *x* = 7.5, which is in agreement with the

observation of the broad peak in the sample with x = 7.5 in XRD. Besides, XPS S 2p, P 2p and I 3d measurements have been conducted for (100-x)Li_2S-$x$$PI_3$ (x = 0, 2.5, 5, 6.25 and 7.5) samples to confirm the formation of solid solution further, which shown in Figure 2.4. In the P 2p and I 3d regions, no peak was observed in the sample with x = 0 but a peak was observed at 132.4 eV and 619.1 eV, respectively, with addition of PI_3 (x =2.5, 5, 6.25 and 7.5). The peak intensity in the P 2p and I 3d regions increased from x = 4 to x = 6.25 and slightly increase from x = 6.25 to x = 7.5. In the S 2p region, two peaks attributed to $S2p_{1/2}$ and $S2p_{3/2}$ were observed around 160.0 eV and 161.2 eV[40, 41] in the sample with x = 0. The binding energy of the two peaks shifted to higher energy with increase of x value. These results indicate the change of electronic structure of S in Li_2S with doping[35], which supports the formation of solid solution further.

2.3.2 Electrochemical Performance

To examine the effect of the crystal structure of (100-x)Li_2S-$x$$PI_3$ on its ionic conductivity, AC impedance spectroscopy at 25°C was performed for (100-x)Li_2S-$x$$PI_3$ (x = 2.5, 3, 4, 5, 6.25 and 7) (Figure 2.6). Fig. 1d shows a plot between the ionic conductivities and lithium site vacancy of the (100-x)Li_2S-$x$$PI_3$ (x = 0, 2.5, 5, 6.25 and 7.5). The ionic conductivity of (100-x)Li_2S-$x$$PI_3$ was largely increased from 10^{-9} S cm^{-1} with increase of lithium site vacancy to 6.8×10^{-5} S cm^{-1} (x = 6.25) and increased slightly to 8.5×10^{-5} S cm^{-1} (x = 7.5) (Figure 2.2(d)). The particle sizes shown in Figure 2.5 of (100-x)Li_2S-$x$$PI_3$ (x = 2.5, 5, 6.25 and 7.5) were similar with a few micrometers, indicating that they did not influence the ionic conductivity. The ionic conductivity of ~10^{-4} S cm^{-1} has the same order of magnitude as that of Li_3PS_4, which is a typical solid electrolyte for all-solid-state batteries[42, 43]. Therefore, it is possible to take advantage of high-conductivity Li_2S-PI_3 for cathode materials without SE.

To evaluate the electrochemical performance, the (100-x)Li_2S-$x$$PI_3$ (x = 2.5, 3, 4, 5, 6.25 and 7.5) samples were mixed with CNovel as electron additive to prepare cathode composites, in which the ratio of (100-x)Li_2S-$x$$PI_3$: CNovel = 9:1 wt%. The galvanostatic charge-discharge curves at 0.05 C under 25°C are shown in Figure 2.7(a). The (100-x)Li_2S-$x$$PI_3$-C cathode x=2.5 did not deliver any capacity probably because of the insufficient ionic conductivity shown in Fig. 1d. The (100-x)Li_2S-$x$$PI_3$-C cathode with higher PI_3 content than x = 2.5 exhibited reversible charge/discharge curves with a single plateau for each

process. The dQ/dV plot obtained from Figure 2.7(a) (Figure 2.8) shows one peak during the charge process around 2.6 V in each sample. The voltage corresponds to the typical transformation of Li_2S to S_8 via polysulfides[44], meaning that the PI_3 doping does not provide an additional reaction in the cathode composites. The discharge capacities for cathodes with x = 3, 4, 5, 6.25 and 7.5 were 30, 319, 560, 541 and 459 mAh g^{-1}. The rate capability of the (100-x)Li_2S-$x$$PI_3$-C cathodes was measured at 0.05, 0.1, 0.2, 0.5 and 1 C (Figure 2.7(b)). Although the (100-x)Li_2S-$x$$PI_3$-C cathode with x = 5 showed the highest capacity at the low rate of 0.05 C, the capacity retention at higher rates increased with the amount of PI_3 contents. It is because the Li_2S content in the electrode decreases with increasing PI_3 content despite the improved ionic conductivity (Figure 2.2(d)). Among them, the (100-x)Li_2S-xPI_3-C cathode with x = 6.25 achieved both high capacity and good rate performance.

The charge-discharge capacity remains stable at various current densities. The (100-x)Li_2S-xPI_3-C with x = 6.25 provided a discharge capacity of 541 mAh g^{-1} at 0.05 C and 207 mAh g^{-1} 1 C (1 C = 657 mAh g^{-1}), respectively. As evident from Figure 2.7(b), the capacity values are significantly higher than those of other cathode materials. After the C-rate is dropped back to 0.05 C, the capacity increased to 528 mAh g^{-1}, showing good reversibility after charge-discharge process at high C-rates. Meanwhile, the (100-x)Li_2S-$x$$PI_3$-C with x = 6.25 maintained satisfied cycling stability of 95% after 50 cycles, with an average Columbic efficiency of 99.8% from 31st cycle to 50th cycle, while 96Li_2S-4PI_3-C maintained only 39 % of its initial capacity after 50 cycles, which supports the improved performance with PI_3 doping and the effectiveness of creating point defect in Li_2S. To better understand the improved rate performance on the battery level, the EIS measurements were conducted for those batteries with (100-x)Li_2S-$x$$PI_3$-C cathode ($x$ = 4, 5, 6.25 and 7.5) at pristine state. The proper equivalent circuit model has been fitted for EIS data (shown in Figure 2.9, Figure 2.10 and Table 2.2). A semicircle was observed in each battery and the resistance of semicircle is attributed to charge transfer resistance (R_{ct}) It is because capacitances of those samples were 10^{-6} to 10^{-5} F [45, 46], which were assigned to be interface between the Li_2S-PI_3-C cathodes and Li_3PS_4 SE layer. The values of R_{ct} decreased with PI_3 content, demonstrating faster ion transport through the interface, which benefits rate performance. Moreover, the apparent ionic conductivities for (100-x)Li_2S-$x$$PI_3$ (x = 2.5, 3,

4, 5, 6.25 and 7.5) at first full-charge state were measured based on Cottrell and Nernst−Einstein equations (Figure 2.7(d), Figure 2.11). The apparent ionic conductivity was significantly increased with increase of PI_3 content up to $x = 6.25$ and increased slightly from $x = 6.25$ to $x = 7.5$. The apparent ionic conductivities of $(100\text{-}x)Li_2S\text{-}xPI_3$ ($x = 6.25$ and 7.5) were relatively high (4.1×10^{-5} S cm^{-1} for the cathode with $x = 6.25$). This means that these cathodes kept high effective ionic conductivity at charging state, leading to the good rate performance. Based on the discussion above, the capacities on the cathode level, rate performance, cycling stability, and effective ionic conductivities at full-charge state are all improved with introducing point defects in Li_2S structure, which proves our strategy is feasible.

2.3.2 Reaction Mechanism

To examine charge compensation mechanism of the $(100\text{-}x)Li_2S\text{-}xPI_3$ with $x = 6.25$, which is optimized sample, XAS for S *K*-edge was performed (Figure 2.12). Before charge process, two characteristic peaks attributed to Li_2S[47] were observed at 2472.6 and 2475.3 eV. When charging to 150 mAh g^{-1}, the intensity of the peaks assigned to Li_2S at 2472.6 and 2475.3 eV was decreased while two peaks appeared at 2470.2 and 2471.8 eV. These two peaks at 2470.2 and 2471.8 eV were assigned to the S 1s to π^* state transition associated with polysulfides[48] and the S 1s to S-S π^* state transition of element sulfur[49], respectively. For the further charge, the peaks assigned to Li_2S and polysulfides showed decrease in intensity while the intensity of the peak assigned to S_8 at 2471.8 eV was increased. These results indicate the charge compensation during charging results from the transformation from Li_2S to S_8 via polysulfide in the cathode. For the discharge process to 300 mAh g^{-1}, the intensity of the peak assigned to S_8 at 2471.8 eV was decreased while those of the peaks assigned to polysulfides and Li_2S were increased, indicating S_8 is under the lithiation process. For the further discharge, the intensity of the peaks assigned to polysulfides and S_8 was decreased and the peaks assigned to Li_2S remained increased. The spectrum of the cathode at the full charge state was in good agreement with that of the cathode at the before charge state. These results show that the transformation between Li_2S and S_8 with polysulfide occurred reversibly, corresponding to the good reversibility in the charge/discharge cycling.

Finally, the energy density and power density of the 93.75Li_2S-6.25PI_3-C cathode based on overall cathode weight were compared with other conventional cathodes for all-solid-state Li-S batteries (Figure 2.13).[28, 35, 49-54] Among them, the 93.75Li_2S-6.25PI_3-C cathode shows highest energy density and power density. These results are due to the fact that controlling defects in Li_2S through cation/anion dual doping dramatically increased the ionic conductivity of Li_2S itself, and thereby reduced the amount of sulfide solid electrolyte in the cathode composite.

Conclusion

In this study, (100-*x*)Li_2S-*x*PI_3 cathodes were synthesized by ball-milling method. TOF neutron diffraction and ionic conductivity measurement proves the ionic conductivity of the (100-*x*)Li_2S-*x*PI_3 is improved by formation of lithium vacancies with the increase of PI_3 content. The PI_3 content-optimized 93.75Li_2S-6.25PI_3 shows good ionic conductivity around 10^{-4} S cm^{-1}, which is capable for cathode without SEs. Under 25 ℃, the the 93.75Li_2S-6.25PI_3-C cathode composite shows a high overall cathode capacity of 541 mAh g^{-1} with high S utilization of 82% at 0.05 C. It delivers 207 mAh g^{-1} at 1 C and shows high reversibility after high current density. The XAS for S K-edge confirms that the charge compensation of the cathode is performed by the transformation between Li_2S and S_8 with polysulfide and the transformation is reversible. The lithium site vacancy in Li_2S structure can be controlled precisely by PI_3 doping, improving the ionic conductivity drastically enough to use the Li_2S-PI_3 as cathode without SE. The developed high-performance Li_2S-PI_3-C cathode shows the successful strategy of cation-anion dual doping, which paves the way for practical application of ASSBs at room temperature.

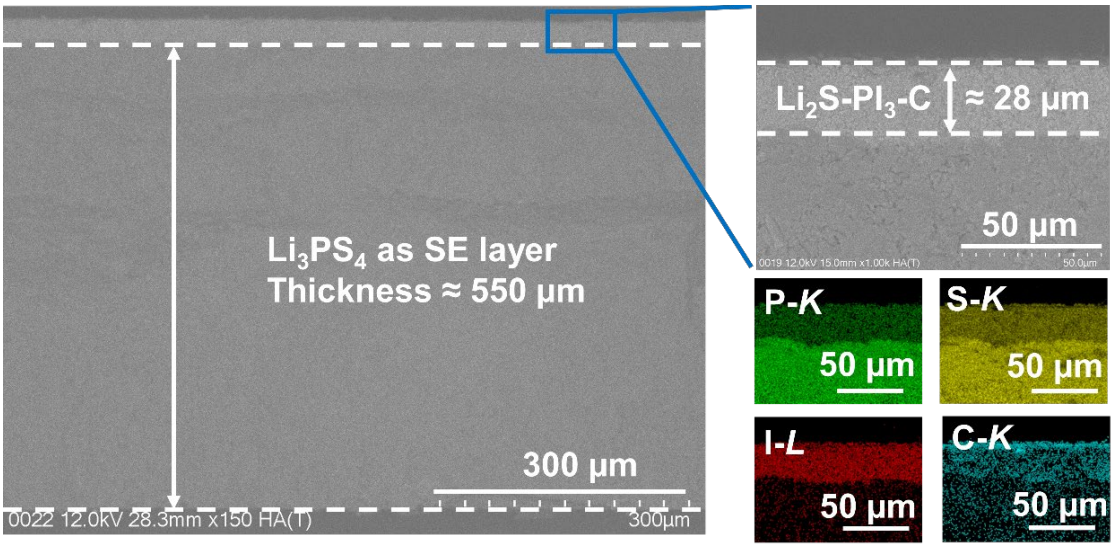

Figure 2.1 The cross-section SEM with EDS mapping of Li_2S-PI_3-C/Li_3PS_4 pellet.

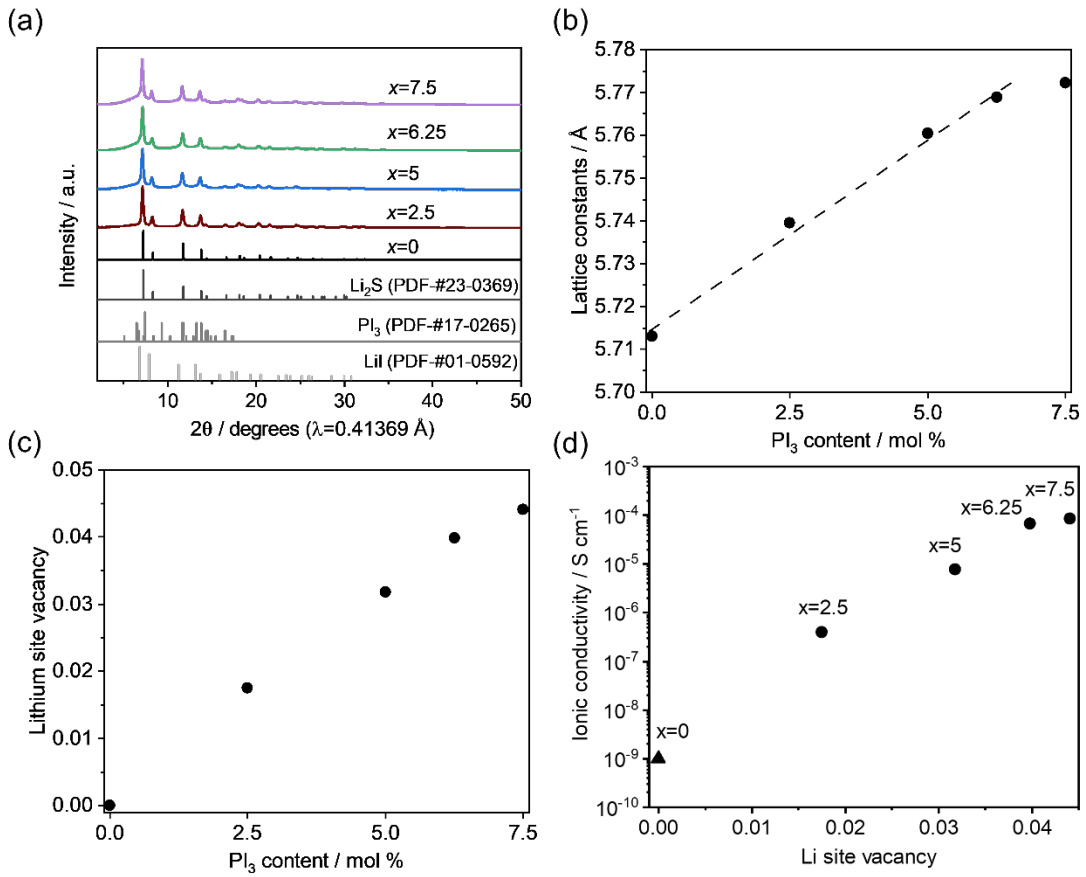

Figure 2.2 Phase characterization of Li_2S-PI_3. (a) Synchrotron XRD patterns of (100-x) Li_2S-$x$$PI_3$ (x = 0, 2.5, 5, 6.25 and 7.5), with PI_3 and LiI for comparison. (b) The lattice constants of (100-x) Li_2S-$x$$PI_3$ (x = 0, 2.5, 5, 6.25 and 7.5) by Rietveld refinement of TOF neutron diffraction. (c) The relationship between PI_3 content of (100-x) Li_2S-$x$$PI_3$ (x = 0, 2.5, 5, 6.25 and 7.5) and Li vacancy. (d) The relationship between Li vacancy and ionic conductivities of (100-x) Li_2S-$x$$PI_3$ (x= 0, 2.5, 5, 6.25, 7.5). The ionic conductivity of Li_2S marked as triangle is cited as reported previously.[38]

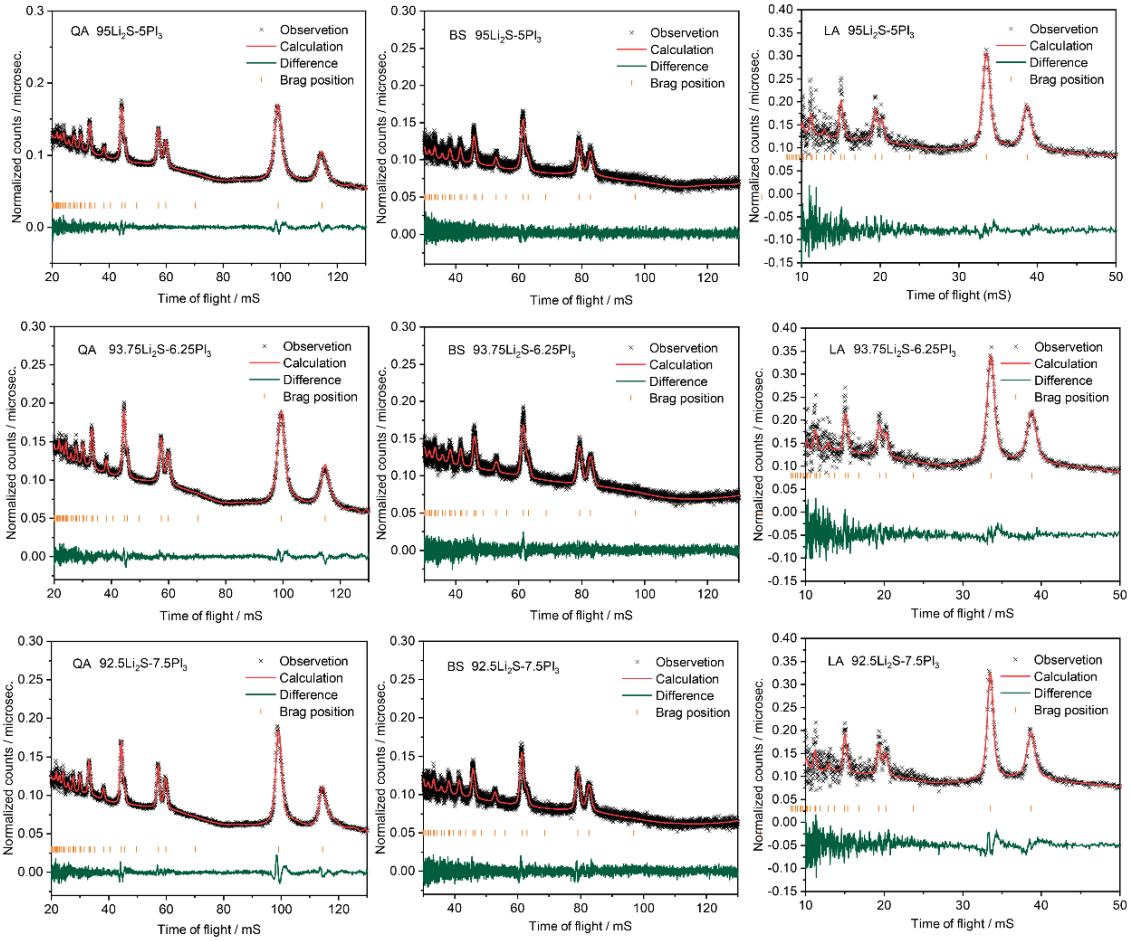

Figure 2.3 Rietveld refinement results performed with TOF neutron diffraction data using all of QA, BS and LA detectors to determine the structural parameters more precisely for Li_2S, $97.5Li_2S$-$2.5PI_3$, $95Li_2S$-$5PI_3$, $93.75Li_2S$-$6.25PI_3$, $92.5Li_2S$-$7.5PI_3$.

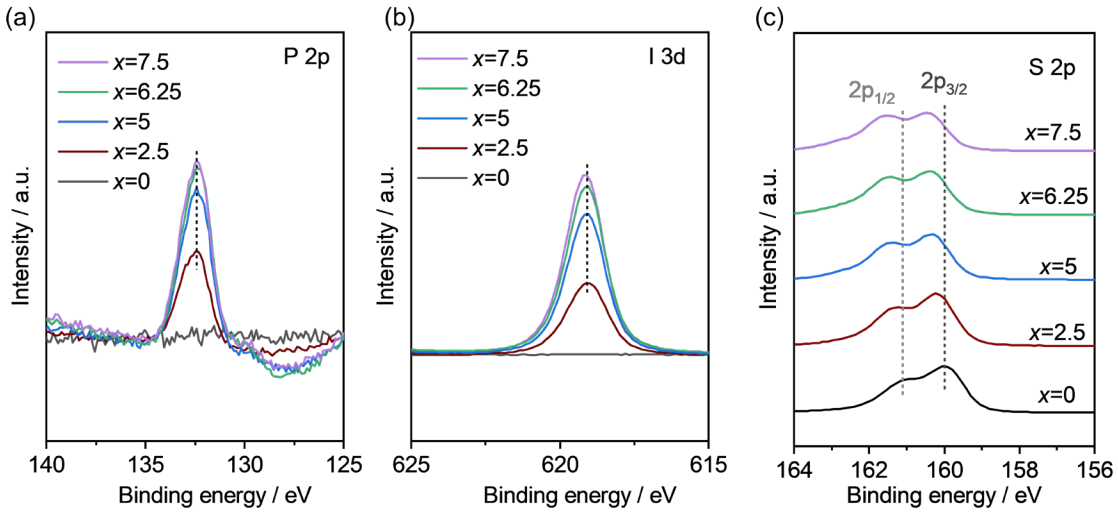

Figure 2.4 XPS P 2p, I 3d and S 2p for (100-*x*) Li_2S-*x* PI_3 (x=0, 2.5, 5, 6.25, 7.5).

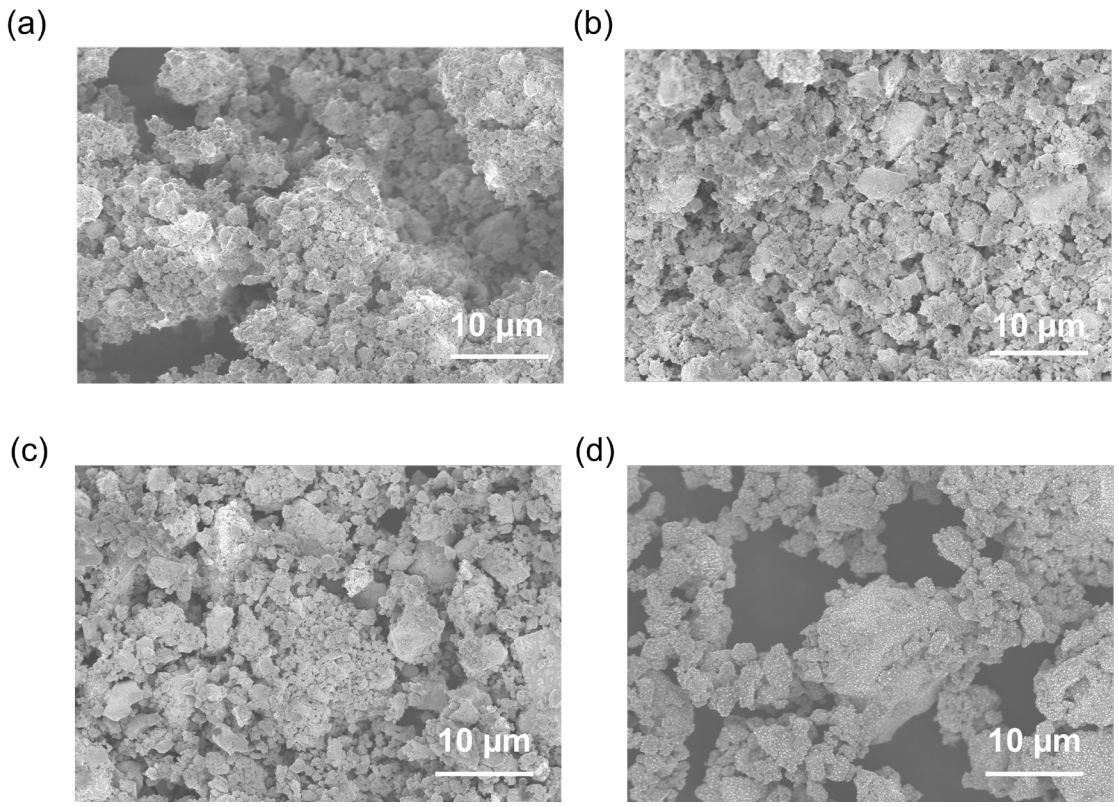

Figure 2.5 XPS P 2p, I 3d and S 2p for (100-*x*) Li_2S-*x* PI_3 (x=0, 2.5, 5, 6.25, 7.5).

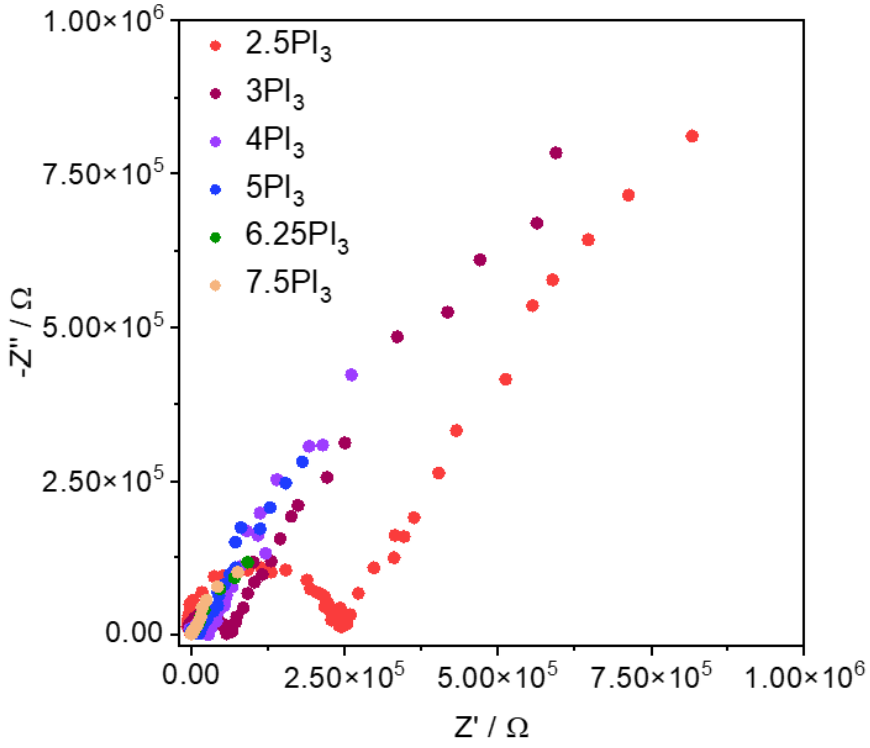

Figure 2.6 The Nyquist plots of (100-*x*)Li_2S-*x*PI_3 (x=2.5, 3, 4, 5, 6.25, 7.5).

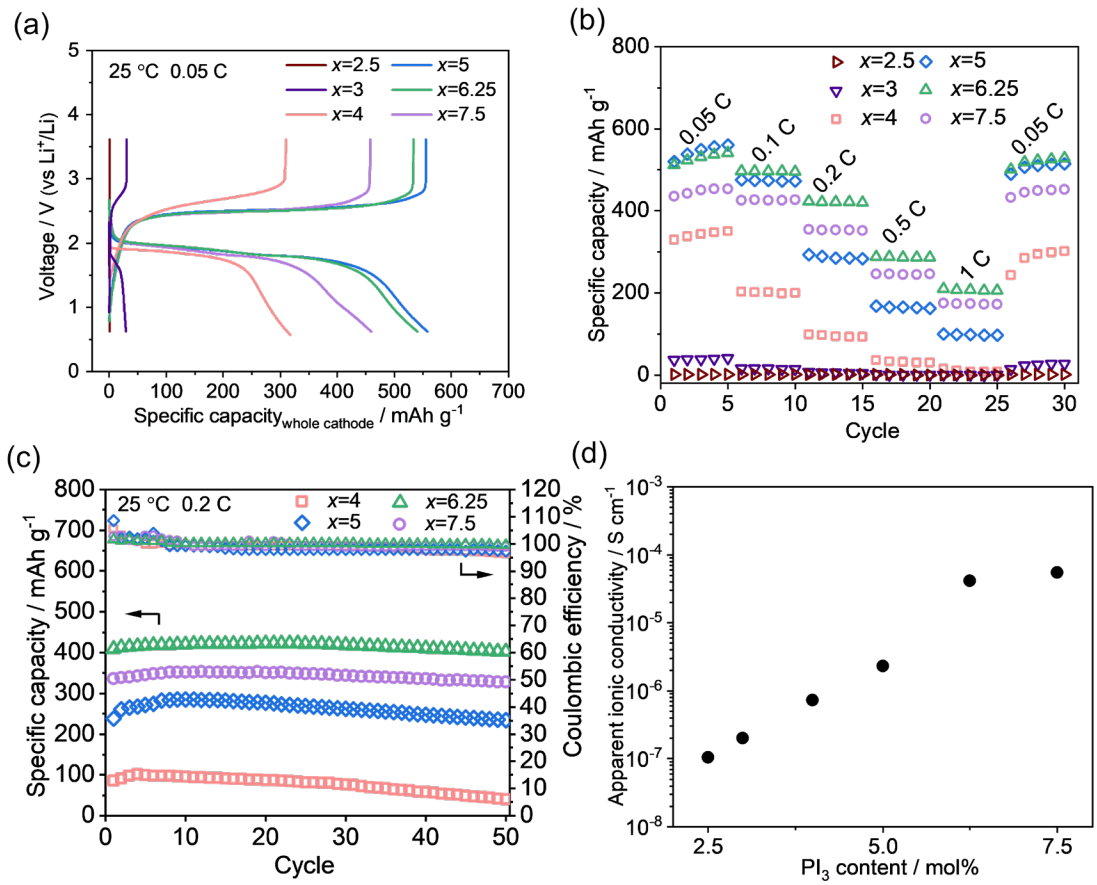

Figure 2.7 The electrochemical performance of (100-*x*)Li_2S-*x*PI_3-C (*x* = 2.5, 3, 4, 5, 6.25, 7.5) cathode composites. Specific capacities were calculated based on the overall mass of cathode. (a) Galvanostatic charge-discharge curves at 0.05 C. (b) The specific capacities at different C-rates. (c) Cycling stability at 0.2 C. (d) The apparent ionic conductivity for first full charge. All the calculations for specific capacities are based on the mass of cathode composites. 1 C is the weight proportion of Li_2S in Li_2S-PI_3-C cathode times theoretical capacity of Li_2S (1167 mAh g^{-1}).

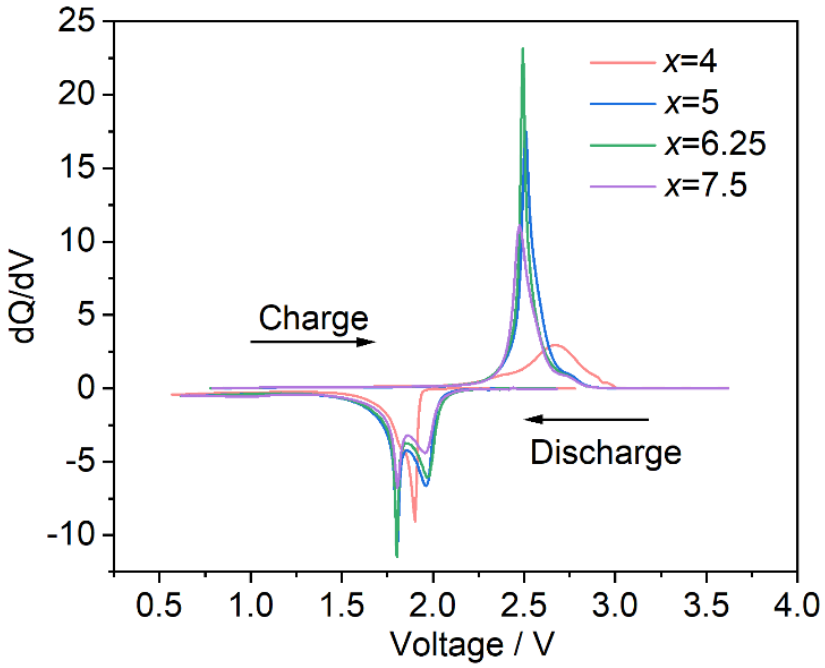

Figure 2.8 The differential capacity (dQ/dV) plot of (1-*x*) Li_2S-*x*PI_3 (*x*=4-7.5).

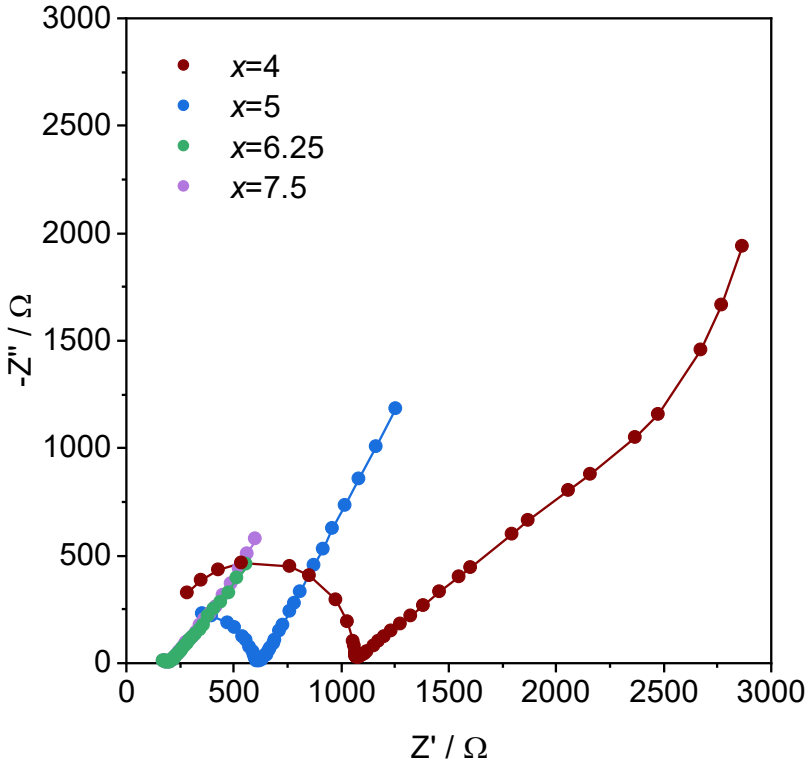

Figure 2.9 The EIS and the fitting results by equivalent circuit model for the batteries with (100-*x*)Li_2S-*x*PI_3-C (x=4, 5, 6.25 and 7.5) as cathode at pristine state.

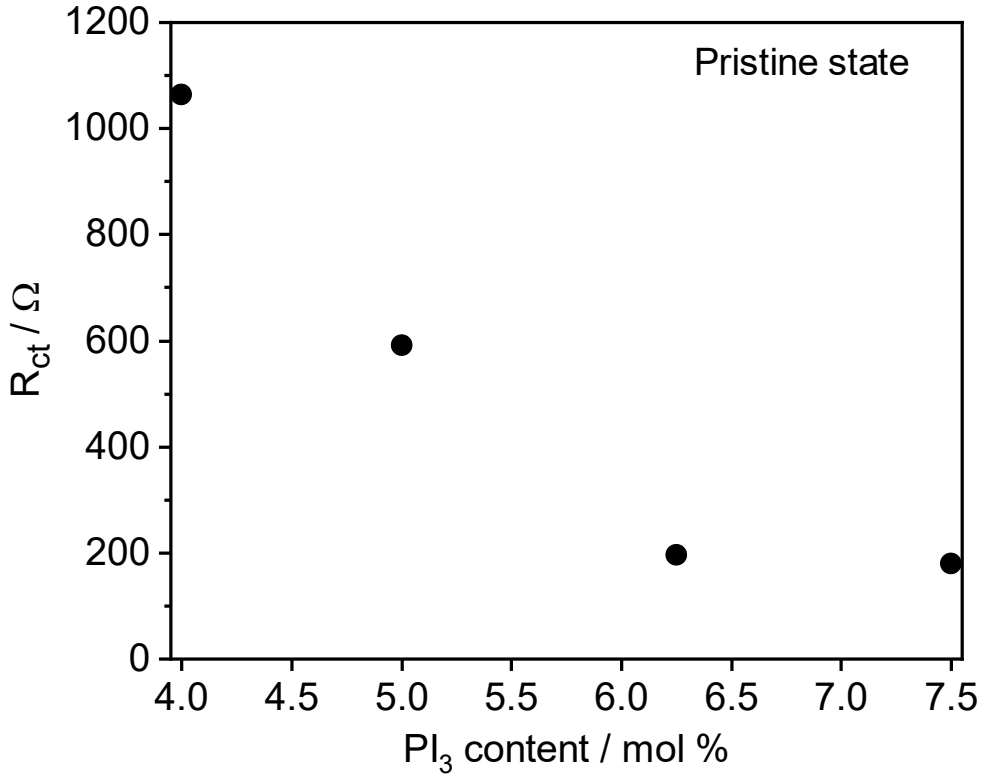

Figure 2.10 The Rct obtained by equivalent circuit model for the batteries with (100-*x*)Li_2S-*x*PI_3-C (x=4, 5, 6.25 and 7.5) as cathode at pristine state.

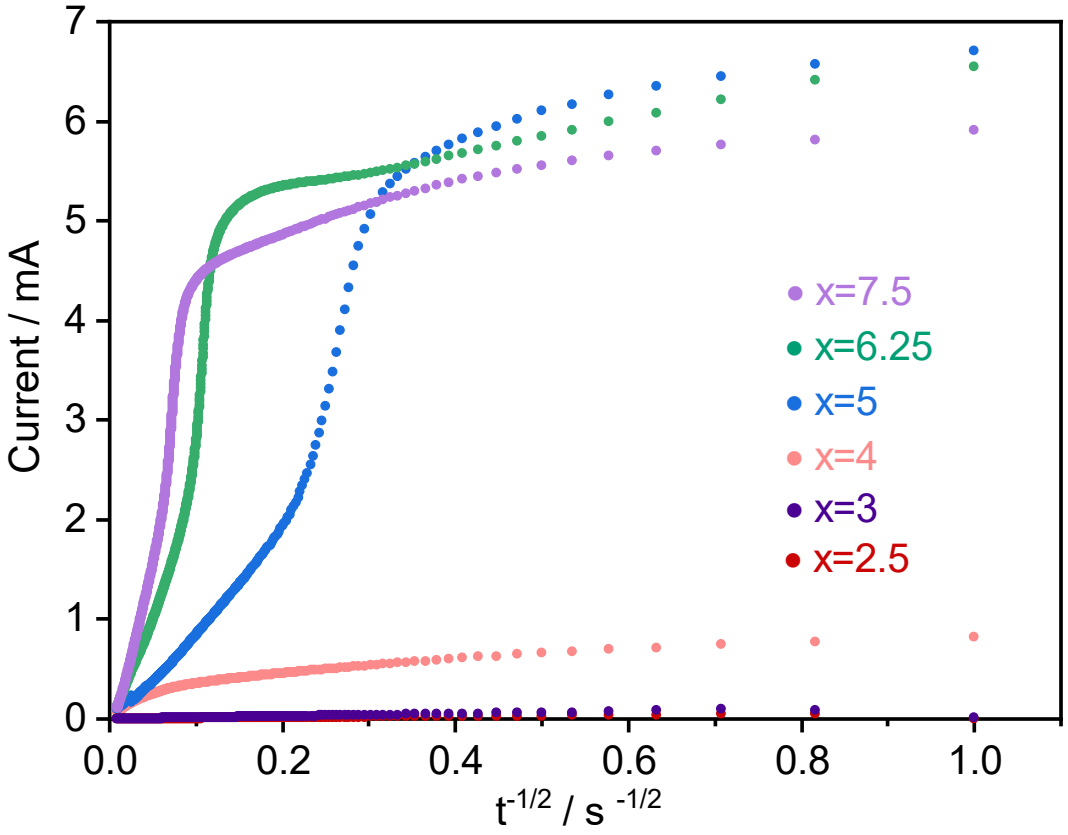

Figure 2.11 The Cottrell plots of (100-x)Li_2S-xPI_3-C (x=2.5, 3, 4, 5, 6.25, 7.5).

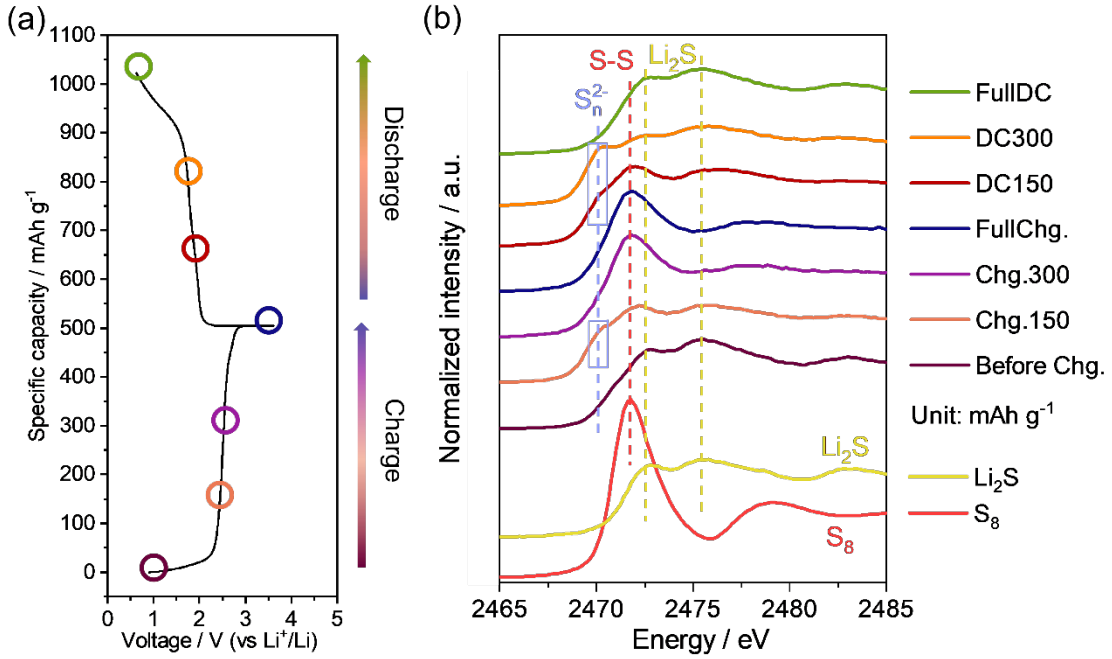

Figure 2.12 Reaction mechanism of $93.75Li_2S$-$6.25PI_3$-C. (a) Charge-discharge curves at different state during second cycle (b) Corresponding S K-edge XANES spectra during second cycle, with Li_2S and S_8 as standard materials.

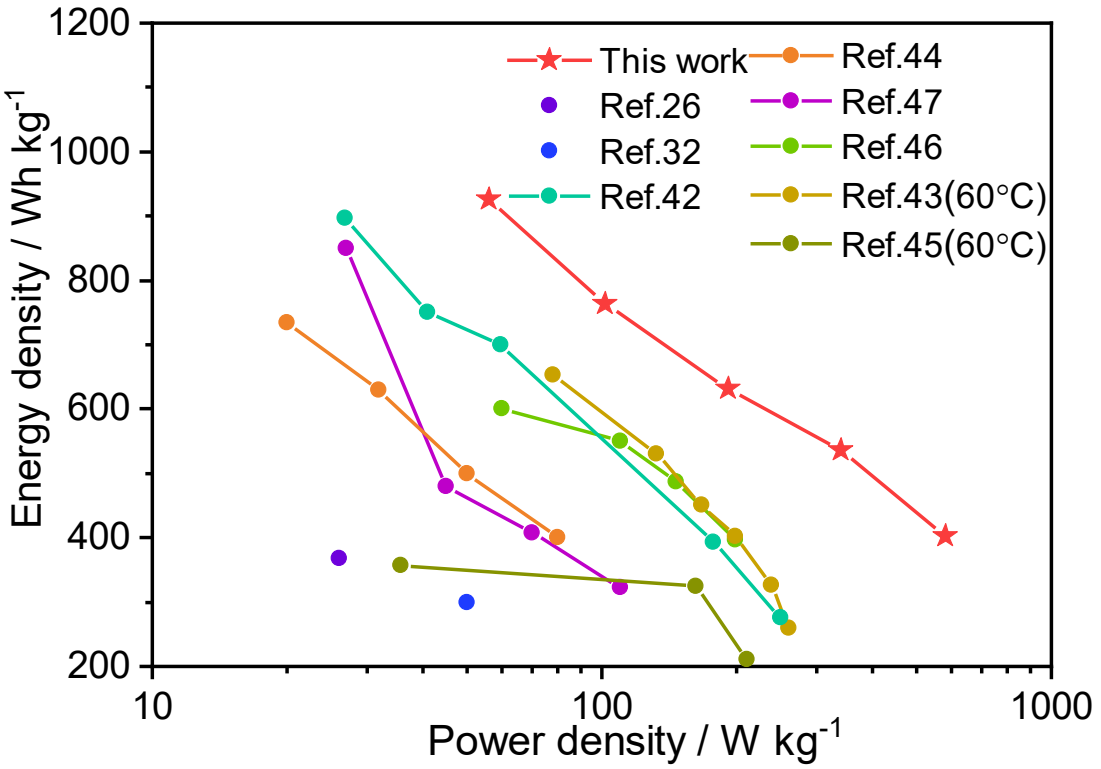

Figure 2.13 Comparison among different cathode composites for all-solid-state Li-S batteries for their energy densities and power densities of different cathode composites at cathode level.

Table 2.1 The structure information obtained by Rietveld refinement of TOF neutron diffraction.

(a) The space group of Li_2S is $Fm\bar{3}m$. Standard deviations are shown in parentheses. The final R factors and lattice parameters are R_p=5.20% $_wR_p$=4.83%, RF_{obs}=8.96% and RF_{wobs}=5.98%. a=b=c=5.7130(3) Å.

Atom	Site	g	x	y	z	B (Å^2)
Li/P	8c	0.998/0	1/4	1/4	1/4	1.50(10)
S/I	4a	0.998/0.002(1)	0	0	0	1.26(8)

(b) The space group of $97.5Li_2S$-$2.5PI_3$ is $Fm\bar{3}m$. Standard deviations are shown in parentheses. The final R factors and lattice parameters are R_p=5.19% $_wR_p$=4.56%, RF_{obs}=7.81% and RF_{wobs}=5.62%. a=b=c=5.7395(2) Å.

Atom	Site	g	x	y	z	B (Å^2)
Li/P	8c	0.979/0.004	1/4	1/4	1/4	1.59(5)
S/I	4a	0.979/0.021(1)	0	0	0	1.17(4)

(c) The space group of $95Li_2S$-$5PI_3$ is $Fm\bar{3}m$. Standard deviations are shown in parentheses. The final R factors and lattice parameters are R_p=2.67% $_wR_p$=2.64%, RF_{obs}=4.06% and RF_{wobs}=2.84%. a=b=c=5.7605(7) Å.

Atom	Site	g	x	y	z	B (Å^2)
Li/P	8c	0.962/0.006	1/4	1/4	1/4	1.58(2)
S/I	4a	0.962/0.038(1)	0	0	0	0.98(5)

(d) The space group of $93.75Li_2S$-$6.25PI_3$ is $Fm\bar{3}m$. Standard deviations are shown in parentheses. The final R factors and lattice parameters are R_p=2.60% $_wR_p$=2.60%, RF_{obs}=3.85% and RF_{wobs}=2.99%. a=b=c=5.7689(2) Å.

Atom	Site	g	x	y	z	B (Å^2)
Li/P	8c	0.952/0.008	1/4	1/4	1/4	1.28(6)
S/I	4a	0.952/0.048(1)	0	0	0	0.68(3)

(e) The space group of $92.5Li_2S$-$7.5PI_3$ is $Fm\bar{3}m$. Standard deviations are shown in parentheses. The final R factors and lattice parameters are R_p=4.26% $_wR_p$=5.16%, RF_{obs}=5.46% and RF_{wobs}=4.45%. a=b=c=5.7723(2) Å.

Atom	Site	g	x	y	z	B (Å^2)
Li/P	8c	0.947/0.009	1/4	1/4	1/4	1.21(6)
S/I	4a	0.947/0.053(1)	0	0	0	1.12(7)

Table 2.2 The parameters of EIS fitting by equivalent circuit model for the batteries with (100-*x*)Li_2S-*x*PI_3-C (x=4, 5, 6.25 and 7.5) as cathode at pristine state.

PI_3 content	4	5	6.25	7.5
R_1 (Ω)	9.89	10.02	9.93	10.04
CPE-T	1.53×10^{-9}	2.52×10^{-9}	5.78×10^{-9}	6.18×10^{-9}
CPE-P	0.785	0.857	0.862	0.804
Rct (Ω)	1063.3	590.2	195.4	`180.1
W-R	143.4	120.5	113.4	111.5
W-T	0.008	0.016	0.018	0.019
W-P	0.309	0.288	0.342	0.345
C (μF)	1.05	14.36	40.34	42.52

References

(1) Wu, J.; Liu, S.; Han, F.; Yao, X.; Wang, C. Lithium/sulfide all-solid-state batteries using sulfide electrolytes. *Adv. Mater.* **2021**, *33* (6), 2000751.

(2) Wang, C.; Liang, J.; Zhao, Y.; Zheng, M.; Li, X.; Sun, X. All-solid-state lithium batteries enabled by sulfide electrolytes: from fundamental research to practical engineering design. *Energy Environ. Sci.* **2021**, *14* (5), 2577-2619.

(3) Wang, C.; Kim, J. T.; Wang, C.; Sun, X. Progress and Prospects of Inorganic Solid-State Electrolyte-Based All-Solid-State Pouch Cells. *Adv. Mater.* **2023**, *35* (19), 2209074.

(4) Wang, L.; Wang, Y.; Xia, Y. A high performance lithium-ion sulfur battery based on a Li_2S cathode using a dual-phase electrolyte. *Energy Environ. Sci.* **2015**, *8* (5), 1551-1558.

(5) Xiang, J.; Zhao, Y.; Wang, L.; Zha, C. The presolvation strategy of Li_2S cathodes for lithium–sulfur batteries: a review. *J. Mater. Chem. A* **2022**, *10* (19), 10326-10341.

(6) Yang, Y.; Zheng, G.; Cui, Y. Nanostructured sulfur cathodes. *Chem. Soc. Rev.* **2013**, *42* (7), 3018-3032.

(7) Altorfer, F.; Bührer, W.; Anderson, I.; Schärpf, O.; Bill, H.; Carron, P.; Smith, H. Lithium diffusion in the superionic conductor Li_2S. *Phys. B: Condens* **1992**, *180*, 795-797.

(8) Chung, S. H.; Chang, C. H.; Manthiram, A. Progress on the critical parameters for lithium–sulfur batteries to be practically viable. *Adv. Funct. Mater.* **2018**, *28* (28), 1801188.

(9) Fang, R.; Zhao, S.; Sun, Z.; Wang, D. W.; Cheng, H. M.; Li, F. More reliable lithium-sulfur batteries: status, solutions and prospects. *Adv. Mater.* **2017**, *29* (48), 1606823.

(10) Yang, H.; Wu, N. Ionic conductivity and ion transport mechanisms of solid-state lithium-ion battery electrolytes: A review. *Energy Sci. Eng.* **2022**, *10* (5), 1643-1671.

(11) Wang, Y.; Wu, Y.; Wang, Z.; Chen, L.; Li, H.; Wu, F. Doping strategy and mechanism for oxide and sulfide solid electrolytes with high ionic conductivity. *J. Mater. Chem. A* **2022**, *10* (9), 4517-4532.

(12) Ali, M.; Doh, C.-H.; Lee, Y.-J.; Kim, B.-G.; Park, J.-W.; Park, J.; Park, G.; Lee, W.-J.; Lee, S.-M.; Ha, Y.-C. Current Trends in Nanoscale Interfacial Electrode Engineering for Sulfide-Based All-Solid-State Li-Ion Batteries. *Energy Technol.* **2021**, *9* (5), 2001096.

(13) Hänsel, C.; Kundu, D. The stack pressure dilemma in sulfide electrolyte based Li metal solid-state batteries: a case study with Li_6PS_5Cl solid electrolyte. *Adv. Mater. Interfaces* **2021**, *8* (10), 2100206.

(14) Chang, D.; Oh, K.; Kim, S. J.; Kang, K. Super-ionic conduction in solid-state $Li_7P_3S_{11}$-type sulfide electrolytes. *Chem. Mater.* **2018**, *30* (24), 8764-8770.

(15) Kamaya, N.; Homma, K.; Yamakawa, Y.; Hirayama, M.; Kanno, R.; Yonemura, M.; Kamiyama, T.; Kato, Y.; Hama, S.; Kawamoto, K. A lithium superionic conductor. *Nat. Mater.* **2011**, *10* (9), 682-686.

(16) Kato, Y.; Hori, S.; Saito, T.; Suzuki, K.; Hirayama, M.; Mitsui, A.; Yonemura, M.; Iba, H.; Kanno, R. High-power all-solid-state batteries using sulfide superionic conductors. *Nat. Energy* **2016**, *1* (4), 1-7.

(17) Li, Y.; Song, S.; Kim, H.; Nomoto, K.; Kim, H.; Sun, X.; Hori, S.; Suzuki, K.; Matsui, N.; Hirayama, M. A lithium superionic conductor for millimeter-thick battery electrode. *Science* **2023**, *381* (6653), 50-53.

(18) Teragawa, S.; Aso, K.; Tadanaga, K.; Hayashi, A.; Tatsumisago, M. Liquid-phase synthesis of a Li_3PS_4 solid electrolyte using N-methylformamide for all-solid-state lithium batteries. *J. Mater. Chem. A* **2014**, *2* (14), 5095-5099.

(19) Yubuchi, S.; Teragawa, S.; Aso, K.; Tadanaga, K.; Hayashi, A.; Tatsumisago, M. Preparation of high lithium-ion conducting Li_6PS_5Cl solid electrolyte from ethanol solution for all-solid-state lithium batteries. *J. Power Sources* **2015**, *293*, 941-945.

(20) Phuc, N. H. H.; Morikawa, K.; Mitsuhiro, T.; Muto, H.; Matsuda, A. Synthesis of plate-like Li_3PS_4 solid electrolyte via liquid-phase shaking for all-solid-state lithium batteries. *Ionics* **2017**, *23*, 2061-2067.

(21) Rosero-Navarro, N. C.; Kinoshita, T.; Miura, A.; Higuchi, M.; Tadanaga, K. Effect of the binder content on the electrochemical performance of composite cathode using Li_6PS_5Cl precursor solution in an all-solid-state lithium battery. *Ionics* **2017**, *23*, 1619-1624.

(22) Rosero-Navarro, N. C.; Miura, A.; Tadanaga, K. Composite cathode prepared by argyrodite precursor solution assisted by dispersant agents for bulk-type all-solid-state batteries. *J. Power Sources* **2018**, *396*, 33-40.

(23) Yen, Y.-J.; Chung, S.-H. Lithium–sulfur cells with a sulfide solid electrolyte/polysulfide cathode interface. *J. Mater. Chem. A* **2023**, *11* (9), 4519-4526.

(24) Le Mong, A.; Kim, D. Self-healable, super Li-ion conductive, and flexible quasi-solid electrolyte for long-term safe lithium sulfur batteries. *J. Mater. Chem. A* **2023**, *11* (12), 6503-6521.

(25) Zhao, R.; Yang, J.; Han, X.; Wang, Y.; Ni, Q.; Hu, Z.; Wu, C.; Bai, Y. Stabilizing Zn Metal Anodes via Cation/Anion Regulation toward High Energy Density Zn-Ion Batteries. *Adv. Energy Mater.* **2023**, *13* (8), 2203542.

(26) Brahmbhatt, T.; Yang, G.; Self, E. C.; Nanda, J. Cathode–sulfide solid electrolyte interfacial instability: challenges and solutions. *Front. Energy Res.* **2020**, *8*, 570754.

(27) Morino, Y.; Tsukasaki, H.; Mori, S. Microscopic Degradation Mechanism of Argyrodite-Type Sulfide at the Solid Electrolyte–Cathode Interface. *ACS Appl. Mater. Interfaces* **2023**, *15* (19), 23051-23057.

(28) Qu, W.; Lu, Z.; Geng, C.; Wang, L.; Guo, Y.; Zhang, Y.; Wang, W.; Lv, W.; Yang, Q. H. Targeted Catalysis of the Sulfur Evolution Reaction for High-Performance Lithium-Sulfur Batteries. *Adv. Energy Mater.* **2022**, *12* (38), 2202232.

(29) Hakari, T.; Hayashi, A.; Tatsumisago, M. Li_2S-Based Solid Solutions as Positive Electrodes with Full Utilization and Superlong Cycle Life in All-Solid-State Li/S Batteries. *Adv. Sustain. Syst.* **2017**, *1* (6), 1700017.

(30) Hakari, T.; Hayashi, A.; Tatsumisago, M. Highly utilized lithium sulfide active material by enhancing conductivity in all-solid-state batteries. *Chem. Lett.* **2015**, *44* (12), 1664-1666.

(31) Zha, C.; Wang, S.; Liu, C.; Zhao, Y.; He, B.; Lyu, C.; Li, J.; Ji, S.; Chen, S.; San Hui, K. Single-atom tailoring of Li_2S to Form Li_2S_2 for building better lithium-sulfur batteries. *Energy Storage Mater.* **2022**, *47*, 79-86.

(32) Fujita, Y.; Hakari, T.; Sakuda, A.; Deguchi, M.; Kawasaki, Y.; Tsukasaki, H.; Mori, S.; Tatsumisago, M.; Hayashi, A. Li_2S–LiI Solid Solutions with Ionic Conductive Domains for Enhanced All-Solid-State Li/S Batteries. *ACS Appl. Energy Mater.* **2022**, *5* (8), 9429-9436.

(33) Kim, J. T.; Hao, X.; Wang, C.; Sun, X. Cathode materials for single-phase solid-solid conversion Li-S batteries. *Matter* **2023**.

(34) Wu, F.; Lee, J. T.; Nitta, N.; Kim, H.; Borodin, O.; Yushin, G. Lithium iodide as a promising electrolyte additive for lithium–sulfur batteries: mechanisms of performance enhancement. *Adv. Mater.* **2015**, *27* (1), 101-108.

(35) Gamo, H.; Maeda, T.; Hikima, K.; Deguchi, M.; Fujita, Y.; Kawasaki, Y.; Sakuda, A.; Muto, H.; Phuc, N. H. H.; Hayashi, A. Synthesis of an AlI_3-doped Li_2S positive electrode with superior performance in all-solid-state batteries. *Mater. Adv.* **2022**, *3* (5), 2488-2494.

(36) Yamamoto, K.; Yang, S.; Takahashi, M.; Ohara, K.; Uchiyama, T.; Watanabe, T.; Sakuda, A.; Hayashi, A.; Tatsumisago, M.; Muto, H. High ionic conductivity of liquid-phase-synthesized Li_3PS_4 solid electrolyte, comparable to that obtained via ball milling. *ACS Appl. Energy Mater.* **2021**, *4* (3), 2275-2281.

(37) Petříček, V.; Dušek, M.; Palatinus, L. Crystallographic computing system JANA2006: general features. *Z. Kristallogr. Cryst. Mater.* **2014**, *229* (5), 345-352.

(38) Santhosha, A.; Medenbach, L.; Buchheim, J. R.; Adelhelm, P. The indium− lithium electrode in solid-state lithium-ion batteries: phase formation, redox potentials, and interface stability. *Batter. Supercaps* **2019**, *2* (6), 524-529.

(39) Shannon, R. Acta Crystallogr., Sect. A: Cryst. Phys., Diffr., Theor. Gen. Crystallogr. *Acta Crystallogr. Sect. A: Cryst. Phys., Diffr., Theor. Gen. Crystallogr* **1976**, *32*, 751.

(40) Meng, X.; Comstock, D. J.; Fister, T. T.; Elam, J. W. Vapor-phase atomic-controllable growth of amorphous Li2S for high-performance lithium–sulfur batteries. *Acs Nano* **2014**, *8* (10), 10963-10972.

(41) Fan, Q.; Jiang, J.; Zhang, S.; Zhou, T.; Pang, W. K.; Gu, Q.; Liu, H.; Guo, Z.; Wang, J. Accelerated Polysulfide Redox in Binder-Free Li2S Cathodes Promises High-Energy-Density Lithium–Sulfur Batteries. *Adv. Energy Mater.* **2021**, *11* (32), 2100957.

(42) Liu, Z.; Fu, W.; Payzant, E. A.; Yu, X.; Wu, Z.; Dudney, N. J.; Kiggans, J.; Hong, K.; Rondinone, A. J.; Liang, C. Anomalous high ionic conductivity of nanoporous β-Li_3PS_4. *J. Am. Chem. Soc.* **2013**, *135* (3), 975-978.

(43) Stöffler, H.; Zinkevich, T.; Yavuz, M.; Hansen, A.-L.; Knapp, M.; Bednarcik, J.; Randau, S.; Richter, F. H.; Janek, J. r.; Ehrenberg, H. Amorphous versus crystalline Li_3PS_4: local structural changes during synthesis and Li ion mobility. *J. Phys. Chem. C* **2019**, *123* (16), 10280-10290.

(44) Zhang, L.; Sun, D.; Feng, J.; Cairns, E. J.; Guo, J. Revealing the electrochemical charging mechanism of nanosized Li2S by in situ and operando X-ray absorption spectroscopy. *Nano Lett.* **2017**, *17* (8), 5084-5091.

(45) Irvine, J. T.; Sinclair, D. C.; West, A. R. Electroceramics: characterization by impedance spectroscopy. *Adv. Mater.* **1990**, *2* (3), 132-138.

(46) Zhang, W.; Weber, D. A.; Weigand, H.; Arlt, T.; Manke, I.; Schröder, D.; Koerver, R.; Leichtweiss, T.; Hartmann, P.; Zeier, W. G. Interfacial processes and influence of composite cathode microstructure controlling the performance of all-solid-state lithium batteries. *ACS Appl. Mater. Interfaces* **2017**, *9* (21), 17835-17845.

(47) Zhao, E.; Wang, J.; Li, F.; Jiang, Z.; Yang, X.-Q.; Wang, F.; Li, H.; Yu, X. Exploring reaction dynamics in lithium–sulfur batteries by time-resolved operando sulfur K-edge X-ray absorption spectroscopy. *Chem. Commun.* **2019**, *55* (34), 4993-4996.

(48) Cuisinier, M.; Cabelguen, P.-E.; Evers, S.; He, G.; Kolbeck, M.; Garsuch, A.; Bolin, T.; Balasubramanian, M.; Nazar, L. F. Sulfur speciation in Li–S batteries determined by operando X-ray absorption spectroscopy. *J. Phys. Chem. Lett.* **2013**, *4* (19), 3227-3232.

(49) Mwizerwa, J. P.; Zhang, Q.; Han, F.; Wan, H.; Cai, L.; Wang, C.; Yao, X. Sulfur-embedded FeS_2 as a high-performance cathode for room temperature all-solid-state lithium–sulfur batteries. *ACS Appl. Mater. Interfaces* **2020**, *12* (16), 18519-18525.

(50) Yan, H.; Wang, H.; Wang, D.; Li, X.; Gong, Z.; Yang, Y. In situ generated Li2S–C nanocomposite for high-capacity and long-life all-solid-state lithium sulfur batteries with ultrahigh areal mass loading. *Nano Lett.* **2019**, *19* (5), 3280-3287.

(51) Zhang, Y.; Liu, T.; Zhang, Q.; Zhang, X.; Wang, S.; Wang, X.; Li, L.; Fan, L.-Z.; Nan, C.-W.; Shen, Y. High-performance all-solid-state lithium–sulfur batteries with sulfur/carbon nano-hybrids in a composite cathode. *J. Mater. Chem. A* **2018**, *6* (46), 23345-23356.

(52) Yao, X.; Huang, N.; Han, F.; Zhang, Q.; Wan, H.; Mwizerwa, J. P.; Wang, C.; Xu, X. High-performance all-solid-state lithium–sulfur batteries enabled by amorphous sulfur-coated reduced graphene oxide cathodes. *Adv. Energy Mater.* **2017**, *7* (17), 1602923.

(53) Zhang, Q.; Huang, N.; Huang, Z.; Cai, L.; Wu, J.; Yao, X. CNTs@ S composite as cathode for all-solid-state lithium-sulfur batteries with ultralong cycle life. *J. Energy Chem.* **2020**, *40*, 151-155.

(54) Hou, L.-P.; Yuan, H.; Zhao, C.-Z.; Xu, L.; Zhu, G.-L.; Nan, H.-X.; Cheng, X.-B.; Liu, Q.-B.; He, C.-X.; Huang, J.-Q. Improved interfacial electronic contacts powering high sulfur utilization in all-solid-state lithium–sulfur batteries. *Energy Storage Mater.* **2020**, *25*, 436-442.

Chapter 3 Developing Electron/Ion Dual Conductive Integrated Cathode Using Cationic/Anionic Redox for High-Energy-Density All-Solid-State Lithium-Sulfur Batteries

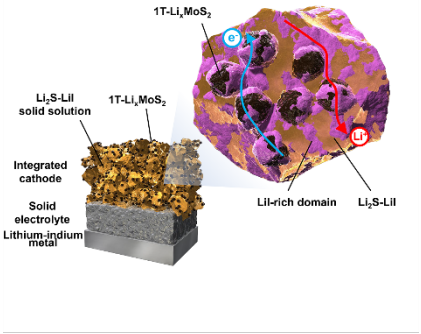

All-solid-state lithium-sulfur batteries (ASSLSB), composed of sulfur cathode and lithium metal anode with high theoretical capacity, have a potentially higher energy density by weight than a typical lithium-ion battery (LIB). However, due to insulating sulfur, a relatively large proportion of electronic (carbon) and ionic (solid electrolyte) conductors are mixed for cathode fabrication, leading to inferior practical capacity. Herein, we report a novel integrated cathode Li_2S-LiI-MoS_2 which has relatively high electronic and ionic conductivities (the order of 10^{-4} S cm^{-1}) without any carbon and solid electrolyte. The ASSLSB with integrated Li_2S-LiI-MoS_2 cathode delivers a remarkably high energy density of 1020 Wh kg^{-1} at the cathode level at room temperature. By applying precise X-ray diffraction, pair distribution function analysis and X-ray computed tomography, it is found that the formation of an ionic conducting phase composed mainly of LiI during discharge is responsible for the high-rate capability. Furthermore, X-ray absorption fine structure (XAFS) has also revealed the charge compensation mechanism and ascertained the involvement of both Mo 4d and S 3p orbitals during the charging and discharging process. It is believed the strategy will pave the way for developing high practical energy density at room temperature for all-solid-state batteries.

3.1 Introduction

Power sources with high gravimetric energy density are critical elements in cutting-edge technologies for aircraft and drone applications. Among the numerous energy storage systems, all-solid-state lithium-sulfur batteries (ASSLSBs) have drawn much attention due to the remarkably high theoretical energy density (>2000 Wh kg^{-1}), which is generated by both high theoretical capacity of S (1675 mAh g^{-1}) or Li_2S (1167 mAh g^{-1}) as cathode and lithium metal (3860 mAh g^{-1}) as anode[1, 2]. This battery also has the advantage of being inexpensive because it uses sulfur, which is an abundant resource, as its cathode, and is expected to be expanded into applications such as stationary storage batteries. Besides, compared to liquid system, solid electrolytes could block the shuttle effect and provide higher safety[3-5].

Although ASSLSBs promise to exceed the theoretical energy density of typical LIBs, the practical performance is far from satisfied, most notably in energy density. Sulfur and the discharge product Li_2S have low ionic and electronic conductivity and must be mixed with solid electrolyte and carbon materials when forming a composite electrode. To realize lithium-ion and/or electron transport, a significant fraction of non-active solid electrolytes and carbon need to be added into the cathode composite, which dilutes the energy density largely[6, 7]. Specifically, it is common to use sulfide-based solid electrolytes (SSE) with high ionic conductivity, such as Li_3PS_4, $Li_{10}GeP_2S_{12}$ and lithium argyrodite Li_6PS_5X (X= Cl, Br) and high electronic conductivity carbon materials, such as acetylene black (AB), Ketjenblack (KB) and vapor grown carbon fiber (VGCF) as conductive additives[8]. And these non-active conductive additives usually account for 50% to 75% of the cathode mass and lead to low active material content[9, 10].

To fill the gap between the theoretical and practical energy density of ASSLSBs, much effort has been put into constructing ionic and electronic pathways in the cathode composite more effectively. As doping with lithium halides LiX (X=Cl, Br, I) in sulfide active material is an effective way to improve ionic conductivity and electrochemical stability[11]. With LiI doping, the ionic conductivity of Li_2S-LiI is improved to 10^{-6} S cm^{-1}, which is two orders of magnitude higher than that of Li_2S[12]. The content of Li_2S in the cathode composite could be promoted, which results from the reduced Li^+/S^{2-} interaction and enhanced rate capability[13, 14]. However, lithium halides are non-electroactive species

and the rate capability is improved at the expense of specific capacity. To reduce non-active conductors further, the ideal alternatives should have not only good electronic conductivity, but also rich Li^+ storage sites and good Li^+ diffusion property[15-18]. In that context, transition metal sulfides have been reported to substitute carbon partially or totally, such as FeS_2 and VS_2, leading to a capacity between 350 to 400 mAh g^{-1} based on whole cathode mass[19, 20]. S-Mo_6S_8 cathode is reported to remove all non-active additives in cathode composite, achieving an overall cathode capacity of 483 mAh g^{-1} at 70 °C, with the energy densities of 777 Wh kg^{-1} correspondingly[21]. While the active material content is improved, the fully conductor-substituted cathode materials still show limited performance, especially at room temperature. Therefore, it is challenging and significant to realize the cathode without carbon and SSE at room temperature, and the specific capacity as well as energy density at the cathode level remains to be improved further.

Herein, to address the abovementioned issues, we developed an integrated cathode Li_2S-LiI-MoS_2 without any carbon and SSE in composite, where Li_2S-LiI solid solution and metallic (1T) Li*x*MoS_2 provide good electron/ion dual conductivity. Benefiting from its entire electronic/ionic network, the Li_2S-LiI-MoS_2 cathode plays dual-function roles of both delivering capacity and conducting electron/ion by itself. Comprehensive and advanced analytical techniques, especially synchrotron X-ray absorption spectroscopy (XAS), high-energy X-ray diffraction and pair distribution function analysis, and X-ray computed tomography, have revealed the origin of the excellent electrode properties of the developed materials.

3.2 Experimental Section

3.2.1 Material synthesis

The (1-*x*)Li_2S-*x*LiI (*x*= 0.05, 0.1, 0.15, 0.2, 0.25) and (1-*y*)(0.8Li_2S-0.2LiI)-*y*MoS_2 (*x*=0, 0.05, 0.1, 0.15, 0.2) samples in this study were prepared using ball milling. Stoichiometric amounts of Li_2S (99% purity, Mitsuwa), MoS_2 (99% purity, Kojundo), and LiI (99% purity, Aldrich) were hand-mixed in a mortar for 0.5 h, followed by mechanical mixing with ZrO_2 balls at 530 rpm for 80 h. The Li_3PS_4 glass powder used to fabricate the SE was prepared via ball milling using a previously reported procedure, as follows[22]. Li_2S (99% purity, Aldrich) and P_2S_5 (99% purity, Aldrich) powders with a 3:1 molar ratio were mechanically

mixed using ZrO_2 balls at 600 rpm for 16 h. All experiments were performed in a dry Ar-filled glovebox.

3.2.2 Characterization

The synchrotron X-ray diffraction (XRD) profiles of the as-prepared The (1-*x*)Li_2S-*x*LiI (*x*= 0.05, 0.1, 0.15, 0.2, 0.25) and (1-*y*)(0.8Li_2S-0.2LiI)-*y*MoS_2 (*x*=0, 0.05, 0.1, 0.15, 0.2) cathode materials and Pair Distribution Function (PDF) were obtained at the BL02B2 beamline of SPring-8, Japan. Rietveld structure refinements using GSAS program and PDF analysis using PDF gui were carried out[23].

Raman measurements in the 100-500 cm^{-1} range were performed using a DXR3 Smart Raman spectrometer (Thermo Fisher Scientific) with a 532 nm diode-pumped solid-state laser at room temperature. The scanning electron microscopy (SEM) images and energy dispersive X-ray spectroscopy (EDX) profiles of the as-prepared 0.85(0.8Li_2S-0.2LiI)-0.15MoS_2 were recorded using Hitachi's SU-8200 series cold field emission scanning electron microscopy device.

The X-ray absorption spectroscopy (XAS) of Mo *K*-edge for the cathode materials were recorded at BL14B2 beamline of the SPring-8, Japan. The S *K*-edge XAS of the cathode materials were recorded at the BL6N1 beamline of the Aichi Synchrotron Radiation Center, Japan. X-ray CT analysis of the cathode materials was performed using a phase-contrast method at the BL20XU beamline of the SPring-8, Japan[24]. The voxel size of the reconstructed images was 62.4 nm. XAS and CT analyses were performed for the cathodes after the cells were tested galvanostatic measurements, disassembled and collected the cathodes in a dry Ar-filled glovebox without exposing the cathode materials to air.

3.2.3 Electrochemical Measurements

The electrochemical performance of the 0.85[(1-*x*)Li_2S-*x*LiI]-0.15MoS_2 and (1-*y*)(0.8Li_2S-0.2LiI)-*y*MoS_2 cathode materials was analyzed using a two-electrode cell. The (1-*x*)(0.8Li_2S-0.2LiI)-*x*MoS_2 and 0.85[(1-*y*)Li_2S-*y*LiI]-0.15MoS_2 composites were used as cathode materials without adding conductive materials and SE to them, and the prepared Li_3PS_4 was used as the solid-state electrolyte (SE) of the cell. The 0.85[(1-*x*)Li_2S-*x*LiI]-0.15MoS_2 and (1-*y*)(0.8Li_2S-0.2LiI)-*y*MoS_2 cathode materials with 4 mg mass loading (corresponding to ~30 μm of thickness) and the SE layer with 80 mg were placed in a

polycarbonate tube with a diameter of 10 mm and were pressed together under a pressure of 360 MPa. A Li−In alloy layer was placed on the SE layer at the opposite side to the cathode layer and served as the anode[25, 26]. Two stainless-steel rods, which were added to the cathode and anode sides by applying a pressure of 120 MPa, were used as current collectors. Cell assembly was performed in a dry Ar-filled glovebox. Electrochemical tests were performed at a current density of 25 mA g^{-1} with discharge and charge cutoff voltages of 0 (0.62 V vs. Li^+/Li) and 3.0 V (3.62 V)[27], respectively, at 25 °C.

To measure the electronic and ionic conductivities of the 0.85[(1-*x*)Li_2S-*x*LiI]-0.15MoS_2 and (1-*y*)(0.8Li_2S-0.2LiI)-*y*MoS_2 composites, direct current (DC) polarization and alternating current (AC) impedance were measured, respectively. The cathode materials were pressed into pellets under a pressure of 360 MPa and set between two stainless-steel current collectors. The applied voltage for DC polarization using HZ-7000 (Hokuto Denko) is 1 V and maintained 0.5 h to obtain the stable current. During the test, the mold was under 120 MPa pressure for the good contact between the pellet sample and current collectors. The electronic conductivity is calculated following $\sigma = \frac{L}{RS} = \frac{LI}{SV}$, where *R* is the resistance of Li_2S-LiI-MoS_2, which can be calculated by corresponding current and applied voltage, *I* is the stable current, *L* is the thickness of Li_2S-LiI-MoS_2 pellet, *V* is the applied voltage and *S* is the cross-sectional area of the pellet. As for the measurement of ionic conductivities, Li_2S-LiI-MoS_2 was first pressed into a pellet in a mold, the same as the electronic conductivity measurement procedure. Then Li_3PS_4, a common solid-state electrolyte with good ionic conductivity (10^{-4} S cm^{-1}) and negligible electronic conductivity (10^{-8} S cm^{-1})[28], was used as the electron blocking layer on both sides of Li_2S-LiI-MoS_2 pellet. The total impedance of Li_3PS4 | Li_2S-LiI-MoS_2 | Li_3PS_4 was measured by Modulab XM ECS using alternating current (AC) impedance technique. The AC amplitude was 10 mV, and the applied frequency ranged between 1 MHz and 0.1 Hz. By subtracting the impedance of Li_3PS_4 from the total impedance, the impedance of Li_2S-LiI-MoS_2 can be obtained and used to calculate the corresponding ionic conductivity.

A potential step method was used to measure the lithium ion diffusion coefficient of the 0.85[(1-*x*)Li_2S-*x*LiI]-0.15MoS_2 and (1-*y*)(0.8Li_2S-0.2LiI)-*y*MoS_2 cathode materials. The constant potential of 3.0 V was applied to the cells, which was the same as the upper cut-off voltage of charge process. The time dependence of the current was monitored using

the Modulab XM ECS (Solartron Analytical). The apparent diffusion coefficients of the composite cathode materials were calculated using the Cottrell equation:

$$i = \frac{nFAD^{1/2}C}{\sqrt{\pi t}},$$

where i is the current, n is the maximum number of electrons that can participate into the reaction per formula unit, F is the Faraday constant, A is the geometric area, D is the diffusion coefficient, C is the lithium ion concentration, and t is the time. The apparent ionic conductivity of the cathode composites during the potential step was estimated using the Nernst−Einstein equation:

$$\sigma = \frac{CZ^2F^2D}{RT},$$

where σ is the ionic conductivity, Z is the charge valence, R is the gas constant, and T is the absolute temperature.

3.3 Result and Discussion

3.3.1 Optimization and Phase Characterization

A series of Li_2S-LiI-MoS_2 samples using Li_2S, LiI and MoS_2 as raw materials were synthesized by a one-step ball-milling method. As the performance of the cathode in all-solid-state batteries is usually limited by ion transport[29, 30], the proportion of LiI was firstly optimized to improve ionic conductivity, as (1-*x*)Li_2S-*x*LiI (*x*=0.05, 0.1, 0.15, 0.2. 0.25). The synchrotron XRD patterns, corresponding lattice constants and iodine occupancy in Li_2S structure obtained from Rietveld refinement are shown in Figure 3.1 (a)-(c) and Figure 3.2. As depicted in Figure 3.1 (a), the hump at a low angle of about 6.8 ° is probably due to the halo signal from the glassy capillaries, which are holders of samples for Synchrotron XRD. With a low LiI content of 5 mol%, the lattice constant is 5.744 Å, larger than pure Li_2S (5.718 Å), which is because larger iodine ions partially occupy the site of sulfur ions. As for the sample with $x \leq 0.2$, all peaks were assigned to Li_2S (space group: $Fm\bar{3}m$) while peaks attributed to LiI appeared in the sample with x = 0.25. Both the lattice constants based on the Li_2S phase and iodine occupancy in Li_2S structure increased linearly with LiI content until x = 0.2 and did not change over x = 0.25. These results suggest Li_2S-LiI solid solution phase is obtained by ball milling method and the limit of solid solubility is x = 0.2. At the composition of x = 0.2, the sample showed highest ionic conductivity of 1.5×10^{-6} S cm^{-1} at 25°C (Figure 3.1 (c)), which was in good agreement with previous report[12].

With optimal composition of LiI (x = 0.2), the proportion of MoS_2, (1-y)(0.8Li_2S-0.2LiI)-$y$$MoS_2$ (y = 0, 0.05, 0.1, 0.15, 0.2) was optimized further. Synchrotron XRD and Rietveld refinement were performed for samples to identify phases of the samples and to calculate the corresponding lattice constants (Figure 3.3 (a)-(b), Figure 3.4). In the as-prepared cathodes of (1-y)(0.8Li_2S-0.2LiI)-$y$$MoS_2$ (y=0, 0.05, 0.1), all peaks were assigned to Li_2S (space group: $Fm\bar{3}m$). In contrast to these samples, broad peaks appeared around 3.7, 8.9, and 15.1 ° in addition to the peaks attributed to Li_2S in the as- prepared cathodes of (1-y)(0.8Li_2S-0.2LiI)-$y$$MoS_2$ (y= 0.15, 0.2). The peak positions were close to the starting material 2H-MoS_2 ($P6_3/mmc$) and 1T-MoS_2 ($P\bar{3}m1$). Due to the weak and broad reflection, it is impractical to identify the origin of the peaks only with the XRD patterns. Therefore, we used further analytical techniques to examine it as discussed later. The lattice constant of Li_2S phase in the (1-y)(0.8Li_2S-0.2LiI)-$y$$MoS_2$ was larger than Li_2S because LiI was doped in Li_2S structure (Figure 3.1 (a)-(b)) and remained unchanged with increasing MoS_2 contents (Figure 3.3 (b)). These results indicate that the Mo cation was not doped in the Li_2S structure. The electronic and ionic conductivities were significantly improved with increase of MoS_2 contents (Figure 3.3 (c)-(d)). Especially when y = 0.1, 0.15 and 0.2, electronic and ionic conductivities were higher than 1×10^{-4} S cm^{-1}, which are possibly capable of being cathode materials without other conductive additives. To confirm that, charge / discharge measurements of the (1-y)(0.8Li_2S-0.2LiI)-$y$$MoS_2$ were performed as shown in Figure S6. When x = 0.2 of LiI and y=0.15 of MoS_2, the cathode delivered highest discharge capacity over 500 mAh g^{-1} with the current density of 25 mA g^{-1} at 25°C. Consequently, further experiments were performed for the 0.85(0.8Li_2S-0.2LiI)-0.15MoS_2 as the optimized one. To examine the structure of the 0.85(0.8Li_2S-0.2LiI)-0.15MoS_2, Raman spectroscopy, Pair distribution function (PDF) analysis and S K-edge XANES measurement with linear combination fitting were conducted for it.

As shown in Raman spectra (Figure 3.5), the 0.85(0.8Li_2S-0.2LiI)-0.15MoS_2 did not exhibit peaks at 378 cm^{-1} and 404 cm^{-1}, which are attributed to $E^1{}_{2\,g}$ and A_{1g} modes in the starting material MoS_2 (2H-phase), but exhibited two peaks at ~150 cm^{-1} and 220 cm^{-1}, marked as J_1 and J_2 respectively. The peak positions were in good agreement with those of MoS_2 with 1T-phase[31-33], indicating that 1T-phase MoS_2 was formed in the 0.85(0.8Li_2S-0.2LiI)-0.15MoS_2. To confirm the existence of 1T-phase MoS_2 in the bulk of 0.85(0.8Li_2S-

0.2LiI)-0.15MoS_2, the PDF analysis was performed (Figure 3.3(e) and Figure 3.6). The refinement of PDF for 0.85(0.8Li_2S-0.2LiI)-0.15MoS_2 fitting with 1T-phase MoS_2 showed better result (Rw:18.7%) than fitting with 2H-MoS_2 (Rw:23.5%)[33], indicating that 1T-phase MoS_2 exists in the bulk of 0.85(0.8Li_2S-0.2LiI)-0.15MoS_2. The electronic structure of S in the 0.85(0.8Li_2S-0.2LiI)-0.15MoS_2 was examined by S *K*-edge XANES measurement with linear combination fitting (Figure 3.7). The fitting result with polysulfide was better than that without polysulfide, indicating that phase transition from Li_2S to polysulfide with delithiation occurred in the 0.85(0.8Li_2S-0.2LiI)-0.15MoS_2. This result was in agreement with the no change of lattice constant of Li_2S with increase of MoS_2 content (Figure 3.3(b)). Since it has been 2H-phase MoS_2 undergoes a phase transition to 1T-phase MoS_2 when Li^+ is inserted[34], the 1T-phase MoS_2 and polysulfide formation observed in the 0.85(0.8Li_2S-0.2LiI)-0.15MoS_2 suggest that Li^+ in Li_2S was inserted into 2H-phase MoS_2 by ball milling, forming 1T-phase Li_xMoS_2. It has been reported that 1T-phase MoS_2 has high electronic conductivity and that 1T-phase Li_xMoS_2 is capable of Li^+ insertion and extraction[34, 35]. Therefore, in the (1-y)(0.8Li2S-0.2LiI)-yMoS_2, the increasing amount of 1T-phase Li_xMoS_2 with increasing the MoS_2 content improved the electronic and ionic conductivities (Figure 3.3(c)-(d)).

3.3.2 Electrochemical Performance

Electrochemical performances of the optimized Li_2S-LiI-MoS_2 (0.85(0.8Li_2S-0.2LiI)-0.15MoS_2) as the integrated cathode without any carbon or SSE was further examined. As for galvanostatic charge-discharge at 25 °C in Figure 3.9, the 0.85(0.8Li_2S-0.2LiI)-0.15MoS_2 showed a capacity of 349 mAh g^{-1} at 25 mA g^{-1}, with a voltage plateau of 2.6 V in the first charge. In the first discharge, 0.85(0.8Li_2S-0.2LiI)-0.15MoS_2 cathode showed a capacity of 491 mAh g^{-1}. Among subsequent a few cycles, the polarization of 0.85(0.8Li_2S-0.2LiI)-0.15MoS_2 cathode was alleviated and capacity was increased (Figure 3.10), resulting in a remarkable discharge capacity of 530 mAh g^{-1} in the 10th cycle.

To evaluate the rate capabilities, integrated cathode 0.85(0.8Li_2S-0.2LiI)-0.15MoS_2 was tested under different current densities of 25, 50, 100, 200 mA g^{-1}, shown in Figure 3.9 (b). The integrated Li_2S-LiI-MoS_2 cathode delivered discharge capacities of 530, 517, 473, 371 mAh $g^{-1,}$ correspondingly with almost 100 % of coulombic efficiency. The capacity retention was about 70% at 200 mA g^{-1} compared to the specific capacity at 25 mA g^{-1}. The

long-term stability of 0.85(0.80Li_2S-0.20LiI)-0.15MoS_2 was also measured. As Figure 3.11 shows, there was no capacity decay after 500 cycles at 100 mA g^{-1} at 25 °C, demonstrating superior long-term stability than reported surfur-based cathodes that contain carbon and SE. The long-term stability of typical cathodes for all-solid-state Li-S batteries usually suffers from loss of contact between conductors and active materials due to volume change during the transformation between Li_2S and S_8 [36]. Moreover, the conductive carbon causes degradation of SE in composite cathodes[37], which is evitable in our integrated Li_2S-LiI-MoS_2 cathode.

The Li_2S-LiI-MoS_2 cathode showed high capacity and low overpotential without solid electrolytes and carbon as additives into the composite, which is advantage for overall energy density. Figure 3.9 © shows, in the case of Li metal is anode, the comparison of power densities and energy densities based on the whole cathode of 0.85(0.8Li_2S-0.2LiI)-0.15MoS_2 with previous cathode composites in ASSLSBs.[12, 21, 38-45] The integrated S-MoS_2 cathode reported previously shows relatively high energy density because of the absence of non-active conductors, under the condition of 70°C and significantly low power density. Compared to these cathodes in ASSBs, 0.85(0.8Li_2S-0.2LiI)-0.15MoS_2 cathode in this work, shows a remarkably high energy density of 1020 Wh kg^{-1} at 46 W kg^{-1} under 25 °C, which delivers highest energy density among those of the cathodes for ASSLSBs with the same power density. Moreover, it shows 384 Wh kg^{-1} with high power density of ~600 W kg^{-1} at 25 °C, which is even better than the reported cathode based on sulfur with lithium lanthanum titanium oxide/carbon (LLTO/C) nanofibers at 55 °C. The superior energy density output under high power density of the Li_2S-LiI-MoS_2 cathode at room temperature demonstrates sufficient electron/ion supply in the all-solid-state composite electrode.

3.3.3 Understanding of the Mechanism of Electrochemical Reaction

As mentioned above, the 0.85(0.8Li_2S-0.2LiI)-0.15MoS_2 cathode after several cycles shows high energy density, compared to previous cathode materials. To elucidate the charge compensation mechanism of the 0.85(0.8Li_2S-0.2LiI)-0.15MoS_2, Mo *K*-edge and S *K*-edge X-ray absorption spectroscopy (XAS) were conducted at different state of charge during 1st cycle and 5th cycle (Figure 3.12 and Figure 3.13). In Mo *K*-edge XAS of the 1st cycle, the absorption edge of the pristine sample slightly shifted to the lower energy compared to the starting material MoS_2 (2H-phase) (Figure 13(b)-(c)), which shows that the pristine

sample was reduced lightly compared to the starting material MoS_2. This is probably due to the insertion of Li^+ into MoS_2 and the formation of Li_xMoS_2 during ball milling process, which was proved by Raman and PDF analysis. The absorption edge shifted to the higher energy for charging to 100 mAh g^{-1}, and did not shift further with subsequent charge. This indicates that the Mo was oxidized due to the extraction of Li^+ from Li_xMoS_2 until the charge of 100 mAh g^{-1}. After full discharge, the absorption edge shifted to the lower energy than that of the initial state, which shows a transition to a more reduced state. In the S *K*-edge XAS, the peak intensities at 2472.7 and 2475.4 eV attributed to Li_2S decreased, while the peak intensity at 2471.7 eV attributed to S_8 increased with charge process. This shows that a conversion reaction from Li_2S to S_8 occurred during charge process[46, 47]. After full discharge, the peak intensity at 2470.6 eV attributed to MoS_2 decreased and the peak intensities at 2472.7 and 2475.4 eV attributed to Li_2S increased. Compared to the initial state, the large reduction of Mo and the significant change in the electronic structure of S attributed to MoS_2 after discharge indicate insertion of Li^+ into the 1T-Li_xMoS_2 in the $0.85(0.8Li_2S\text{-}0.2LiI)\text{-}0.15MoS_2$. This reaction results in the higher initial discharge capacity than the charge capacity.

In Mo *K*-edge XAS of the 5th cycle (Figure 4b and c), the absorption edge of the sample before charge substantially shifted to the higher energy for charging to 100 mAh g^{-1}, and gradually shifted further for subsequent charging. This indicates that the Mo largely contributed to the charge compensation with the charge of 100 mAh g^{-1} and the contribution became relatively small after the charge state of 100 mAh g^{-1}. As for the full discharge, the absorption edge returned to the same energy as the pristine sample, which shows the Mo redox occurred reversibly. In the S *K*-edge XAS of the 5th cycle (Figure 12(d)), one peak attributed to MoS_2 was observed at 2470.6 eV, and two peaks attributed to Li_2S were observed at 2472.7 and 2475.4 eV in the sample before charging. The intensity of peak at 2470.6 eV decreased for charging to 100 mAh g^{-1}, which may be caused by largely oxidation of Mo (Figure 12(b)-(c)). During the subsequent charge process, the peak intensities at 2472.7 and 2475.4 eV attributed to Li_2S decreased while the peak intensity at 2471.7 eV attributed to S_8 increased. This shows a conversion reaction from Li_2S to S_8 during charging. After discharge, the XANES shape was similar to that of the pristine sample, which shows the S redox occurred reversibly. The capacity contribution of 1T-

MoS_2 is calculated by combining the theoretical capacity of MoS_2 and assuming the real reacted electron number of MoS_2 based on Mo K-edge XANES. The theoretical capacity of MoS_2 with a 4-electron transfer reaction is 670 mAh g^{-1}, based on the reaction $MoS_2 + 4Li^+ + 4e^- \rightarrow Mo + Li_2S$. Considering the MoS_2 content in $85(80Li_2S\text{-}20LiI)\text{-}15MoS_2$, the capacity contribution of 1T-MoS_2 is no more than 206 mAh g^{-1}. The actual reacted electron can be inferred by assuming a linear relationship between the oxidation number of Mo and the energy of Mo K-edge XANES. As Figure 3.14 shows, about 2.4 electrons participate in the reaction, corresponding to the capacity of 125 mAh g^{-1}, which is also in good agreement with the capacity related to the second voltage plateau starting at about 1.1 V vs. Li^+/Li in the discharge curve (Figure 3.12(a)). Both Mo *K*-edge and S *K*-edge XAS spectra prove the reversible cationic redox of Mo and anionic redox of S, which leads to the high energy density and reversibility of the $0.85(0.8Li_2S\text{-}0.2LiI)\text{-}0.15MoS_2$ cathode.

3.3.4 Understanding of the Good Power Density

The $0.85(0.8Li_2S\text{-}0.2LiI)\text{-}0.15MoS_2$ cathode shows high power density as well as high energy density, compared to previous cathode materials. To clarify the reason for the high power density, apparent ionic conductivity, crystal structure and morphology of the $0.85(0.8Li_2S\text{-}0.2LiI)\text{-}0.15MoS_2$ during charge/discharge processes were examined. The apparent ionic conductivity of the $0.85[(1\text{-}x)Li_2S\text{-}xLiI]\text{-}0.15MoS_2$ (x = 0.05, 0.10, 0.15, 0.20, 0.25) cathodes was measured using a potential step method combined with the Cottrell and Nernst−Einstein equations (Figure 3.15(a) and Figure 3.16). The apparent ionic conductivity increased with the LiI content until x = 0.20, and the value at x = 20 ($0.85(0.8Li_2S\text{-}0.2LiI)\text{-}0.15MoS_2$) was 6.6×10^{-5} S cm^{-1}. This result shows that the $0.85(0.8Li_2S\text{-}0.2LiI)\text{-}0.15MoS_2$ cathode has relatively high ionic conductivity even after first charge process, which leads to the high power density of the cathode. Structural change for $0.85(0.8Li_2S\text{-}0.2LiI)\text{-}0.15MoS_2$ upon the first cycle was examined by synchrotron XRD (Figure 5b). Before charging, all Bragg peaks were assigned to Li_2S (space group: $Fm\bar{3}m$) and In (space group: *I4/mmm*), which was impurity from the anode in the XRD sample preparation procedure. During charging, the intensity of the peaks attributed to the Li_2S structure decreased while new peaks attributed to LiI (space group: $Fm\bar{3}m$) appeared with stronger intensity as the charging proceeded. In the subsequent discharge, the intensity of the peaks attributed to the Li_2S structure increased while the LiI peaks remained with

decreased intensity. These results show LiI phase formed from the Li_2S-LiI solid solution in the $0.85(0.8Li_2S\text{-}0.2LiI)\text{-}0.15MoS_2$ during the first charge and could keep in the cathode after first cycle. In addition, the peaks of LiI remain visible after the second and fifth cycles, indicating the good stability of LiI phase in $0.85(0.8Li_2S\text{-}0.2LiI)\text{-}0.15MoS_2$ cathode after the second and fifth cycle (shown in Figure 3.17).

The formed LiI phase and its morphology were further confirmed by Computed Tomography (CT) (Figure 5c-f). Tthese CT images approximately represent the density distribution of the object. Before charging, as all elements were uniformly distributed in the $0.85(0.8Li_2S\text{-}0.2LiI)\text{-}0.15MoS_2$ (Figure 3.18), no contrast was observed in the CT image except in the void areas (Figure 3.15(c)), which were regions of low density (blank). During charge process, region with high density (blue color) appeared and increased uniformly with charging. In the subsequent discharge, the region with high density remained although the region was decreased. Considering the XRD results (Figure 3.15(b)), the region with high density is attributed to the formation of LiI from Li_2S-LiI solid solution.

It has been reported that the formed LiI domain can work as an ionic conduction path in other LiI doped cathodes to suppress decreasing the ionic conductivity of cathodes during charging[48]. Meanwhile, as for the aspect of electronic conductivity, the $0.85(0.8Li_2S\text{-}0.2LiI)\text{-}0.15MoS_2$ cathode possesses good electronic transportability at pristine state, which is due to the good electronic conductivity of 1T-MoS_2 (10-100 S cm^{-1})[49]. It is reported that the high electronic conductivity is because the electronic states of 1T-MoS_2 around Fermi level are composed of partially filled Mo 4d and S 3p states, which is based on the results of the density of states (DOS)[50]. Moreover, with the different electric charge of Mo in 1T MoS_2, the shape of DOS patterns remains nearly unchanged[51], which indicates the lithiated Li*x*MoS_2 could keep electronic conductivities as high as 1T-MoS_2 during charge and discharge. Resulting from high electronic and ionic conductivities at pristine state, stably high electronic conductivity of Li*x*MoS_2 and the high apparent ionic conductivity originated from the formed LiI domain during charging, the integrated $0.85(0.8Li_2S\text{-}0.2LiI)\text{-}0.15MoS_2$ cathode realize remarkable energy density and high power density without carbon and SE in the cathode composite.

Conclusion

In summary, we have successfully synthesized Li_2S-LiI-MoS_2 integrated cathode with high electronic and ionic conductivities over 10^{-4} S cm^{-1} by one-step ball-milling method. Without any carbon and solid electrolytes additives in cathode composite, the optimized Li_2S-LiI-MoS_2 integrated cathode ($0.85(0.8Li_2S$-$0.2LiI)$-$0.15MoS_2$) delivers the highest energy density of 1020 Wh kg^{-1} at the cathode level and superior power density to other cathodes for ASSLSB. The utilization of the reversible cationic redox of Mo and anionic redox of S in the $0.85(0.8Li_2S$-$0.2LiI)$-$0.15MoS_2$ cathode leads to the high energy density. The high electronic and ionic conductivities at pristine state and the formed LiI domain during charging lead to the high power density. The design strategy used in the Li_2S-LiI-MoS_2 is useful to realize ASSBs with high energy and power densities.

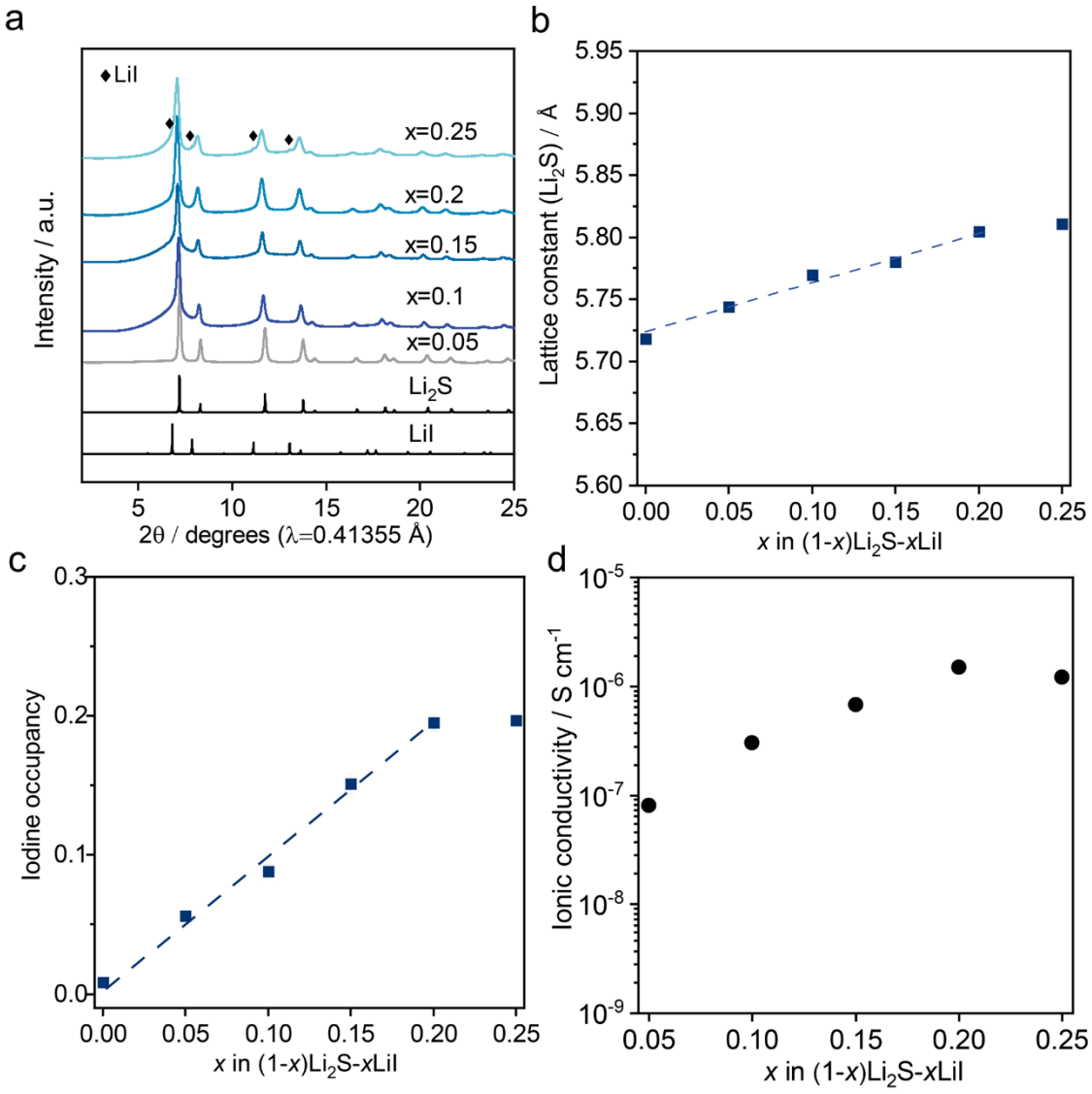

Figure 3.1 (a) The synchrotron XRD patterns for (1-*x*)Li_2S-*x*LiI (*x*=0.05, 0.1, 0.15, 0.2, 0.25) with comparison of Li_2S and LiI as raw materials. The clubs correspond to LiI. (b) The lattice constant (a=b=c) of the main phase in (1-*x*)Li_2S-*x*LiI. (c) The iodine occupancy in Li_2S structure of (1-*x*)Li_2S-*x*LiI . (d) The ionic conductivities of (1-*x*)Li_2S-*x*LiI at 25 °C.

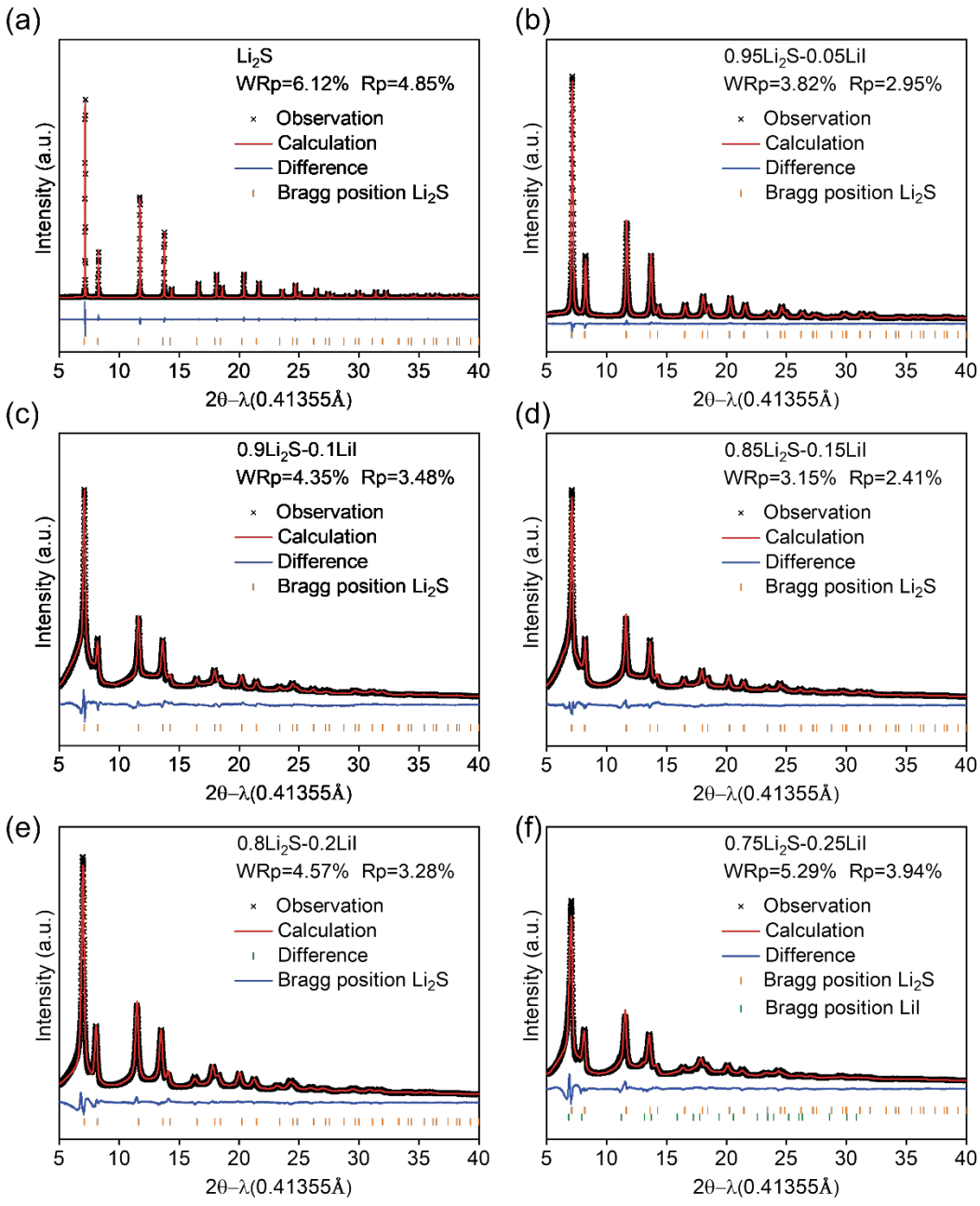

Figure 3.2 Rietveld refinement patterns of the synchrotron XRD data for (1-*x*)Li_2S-*x*LiI) (*x*=0, 0.05, 0.1, 0.15, 0.2, 0.25). The experimental data (black crosses), calculated results (red lines) and their difference (blue lines) are shown. Vertical lines indicate the Bragg position of Li_2S (upper row, orange) and LiI (lower row, green).

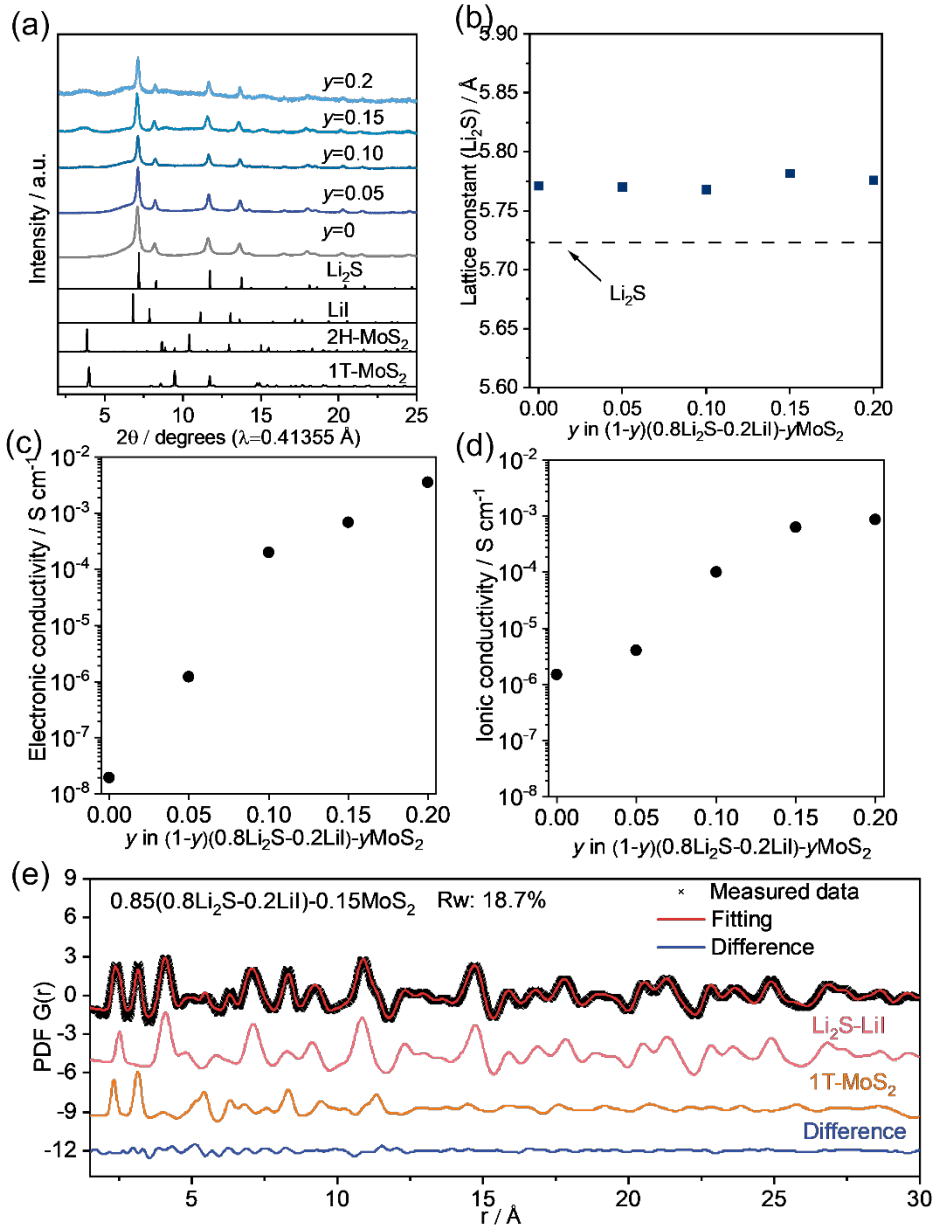

Figure 3.3 The phase characterization of Li_2S-LiI-MoS_2. (a) Synchrotron XRD patterns of ball-milling products (1-*y*)(0.8Li_2S-0.2LiI)-*y*MoS_2 (*y*=0, 0.05, 0.1, 0.15, 0.2) with comparison of Li_2S, LiI and 2H-MoS_2 (*P6₃/mmc*) as raw materials. The XRD pattern of 1T-MoS_2 (*P*$\bar{3}$*m1*) is simulated from cif file of 1T-MoS_2 by Fullprof. (b) Lattice constants of Li_2S phase in (1-*y*)(0.8Li_2S-0.2LiI)-*y*MoS_2, (c) Electronic and (d) Ionic conductivities of (1-*y*)(0.8Li_2S-0.2LiI)-*y*MoS_2. (e) PDF result of 0.85(0.8Li_2S-0.2LiI)-0.15MoS_2.

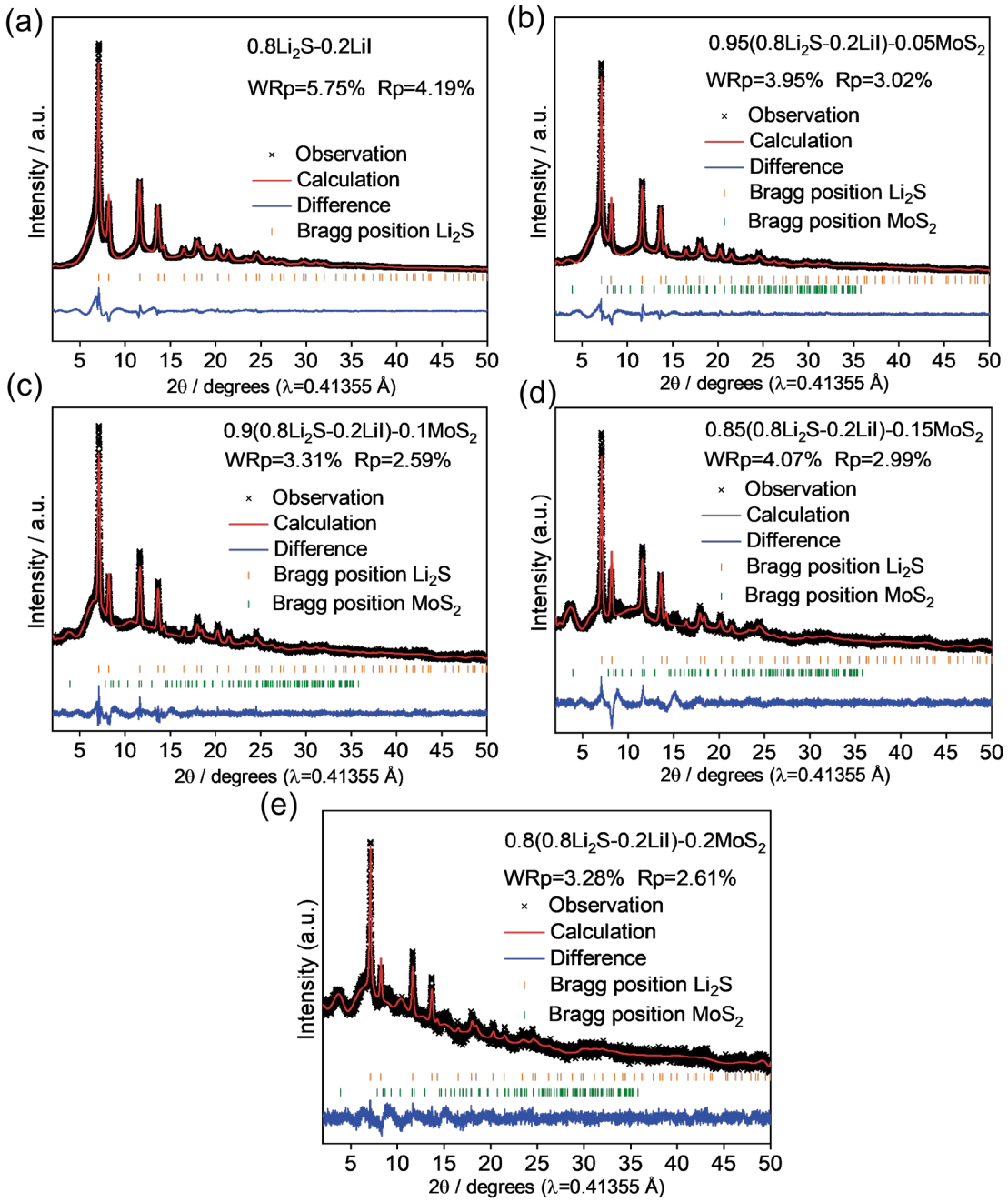

Figure 3.4 Rietveld refinement patterns of the synchrotron XRD data for (1-*y*)(0.8Li_2S-0.2LiI)-*y*MoS_2 (*y*=0, 0.05, 0.1, 0.15, 0.2). The experimental data (black crosses), calculated results (red lines) and their difference (blue lines) are shown. Vertical lines indicate the Bragg position of Li_2S (upper row, orange) and MoS_2 (lower row, green).

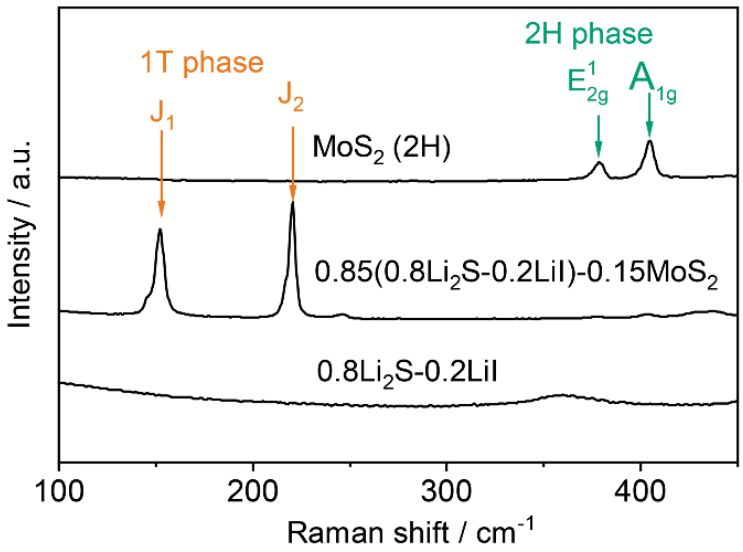

Figure 3.5 Raman spectra of MoS_2 (2H phase), 0.85(0.8Li_2S-0.2LiI)-0.15MoS_2 and 0.8Li_2S-0.2LiI.

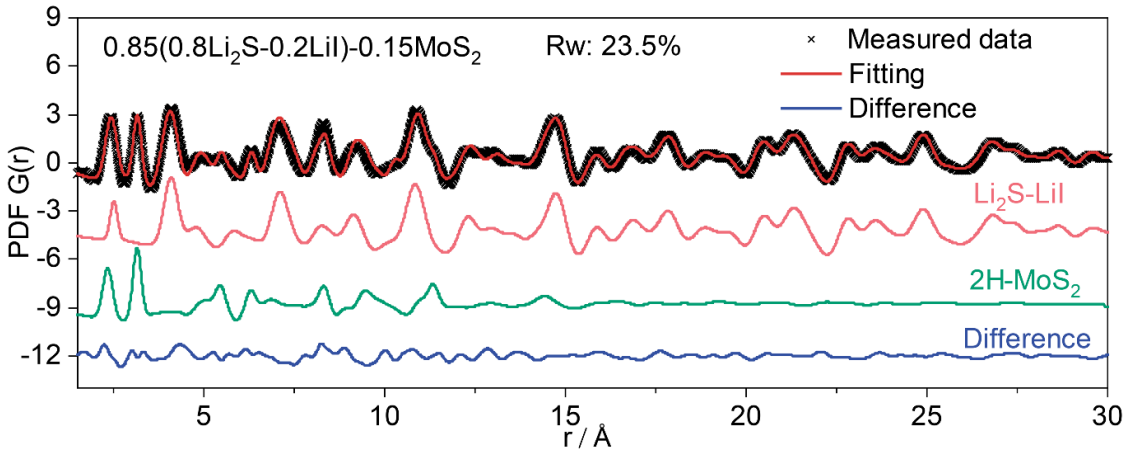

Figure 3.6 Pair Distribution Function analysis of (a) $0.85(0.8Li_2S\text{-}0.2LiI)\text{-}0.15MoS_2$ by fitting with Li_2S-LiI and 2H-MoS_2. The experimental data (black crosses), calculated results (red lines) and their difference (blue lines) are shown.

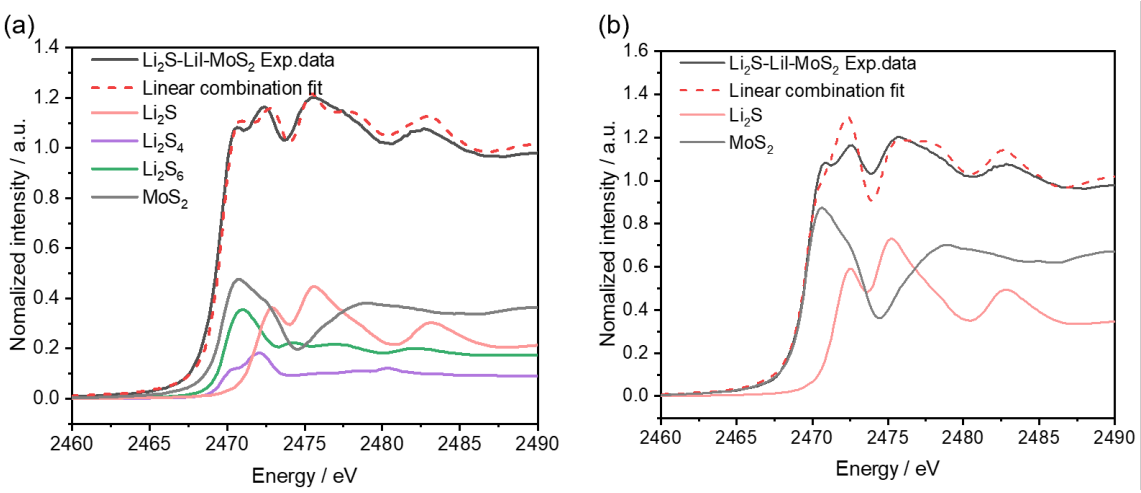

Figure 3.7 Linear combination fitting of pristine $0.85(0.8Li_2S\text{-}0.2LiI)\text{-}0.15MoS_2$ by assuming (a) with polysulfides (b) without polysulfides.

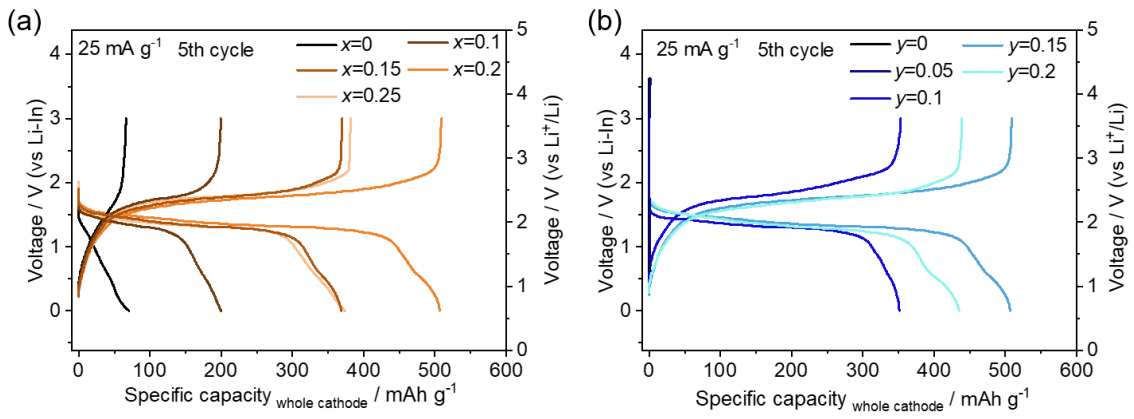

Figure 3.8 The galvanostatic charge/discharge of (a) 0.85[(1-*x*)Li_2S-*x*LiI]-0.15MoS_2 (*x*=0, 0.1, 0.15, 0.2, 0.25) and (b) (1-y)(0.8Li_2S-0.2LiI)-*y*MoS_2 (*y*=0.05, 0.1, 0.15, 0.2) at 25 mA g^{-1}.

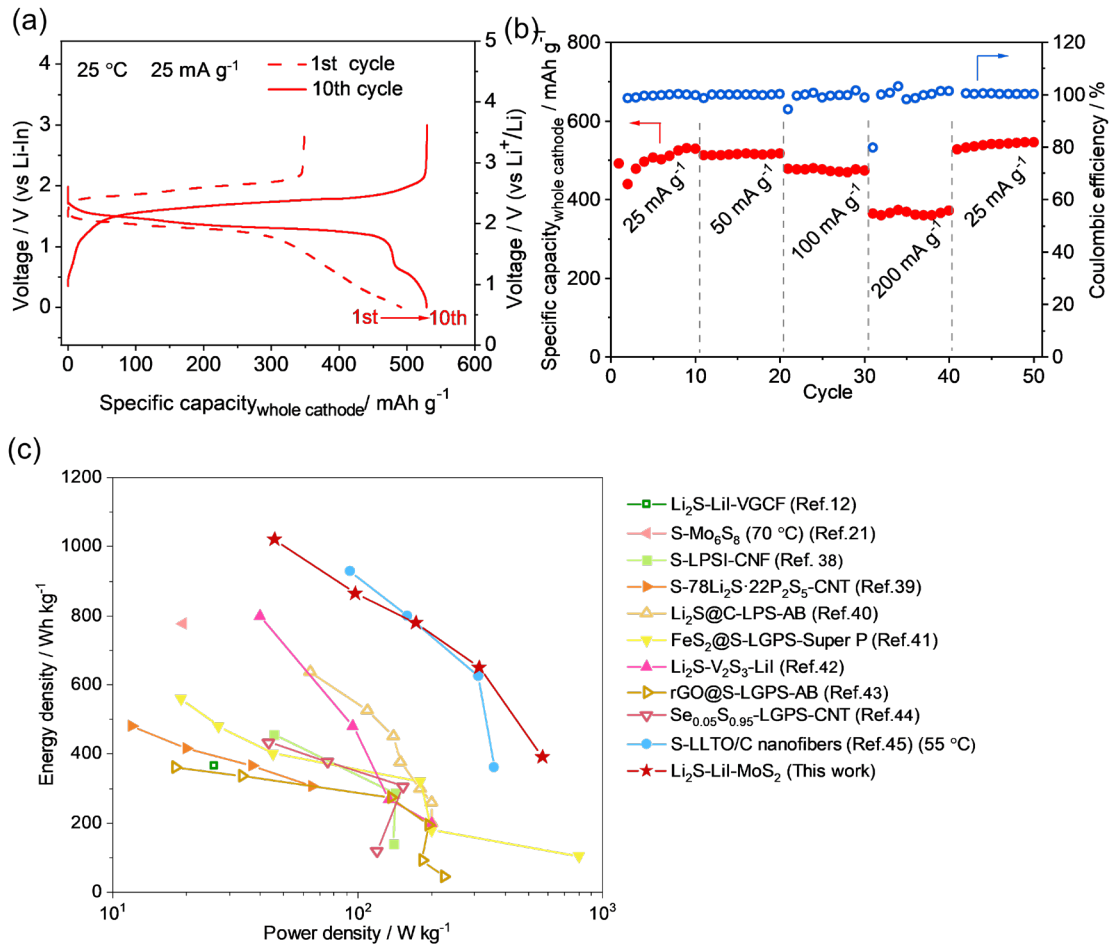

Figure 3.9 The electrochemical performance of $0.85(0.8Li_2S\text{-}0.2LiI)\text{-}0.15MoS_2$. (a) The charge-discharge curves of $0.85(0.8Li_2S\text{-}0.2LiI)\text{-}0.15MoS_2$ as cathode composite at 25°C at the current density of 25 mA g^{-1}. (b) The rate performance and corresponding Coulombic efficiency. (c) Comparison of energy density and power density among different cathode composites for all-solid-state lithium-sulfur batteries and lithium metal as anode. The composite cathodes reported previously include Li_2S-LiI-vapor grown carbon fiber[12], S-Mo_6S_8 [21], S-$0.67Li_3PS_4$•0.33LiI-carbon nano fiber[38], S-$78Li_2S\cdot 22P_2S_5$-carbon nanotubes[39], Li_2S@C-$Li_7P_3S_{11}$-acetylene black[40], FeS_2@S-$Li_{10}GeP_2S_{12}$-Super P[41], Li_2S-V_2S_3-LiI[42], reduced graphene oxide@S-$Li_{10}GeP_2S_{12}$-acetylene black[43], $Se_{0.05}S_{0.95}$-$Li_{10}GeP_2S_{12}$-carbon nanotubes[44], and S-lithium lanthanum oxide/caron nanofibers[45].

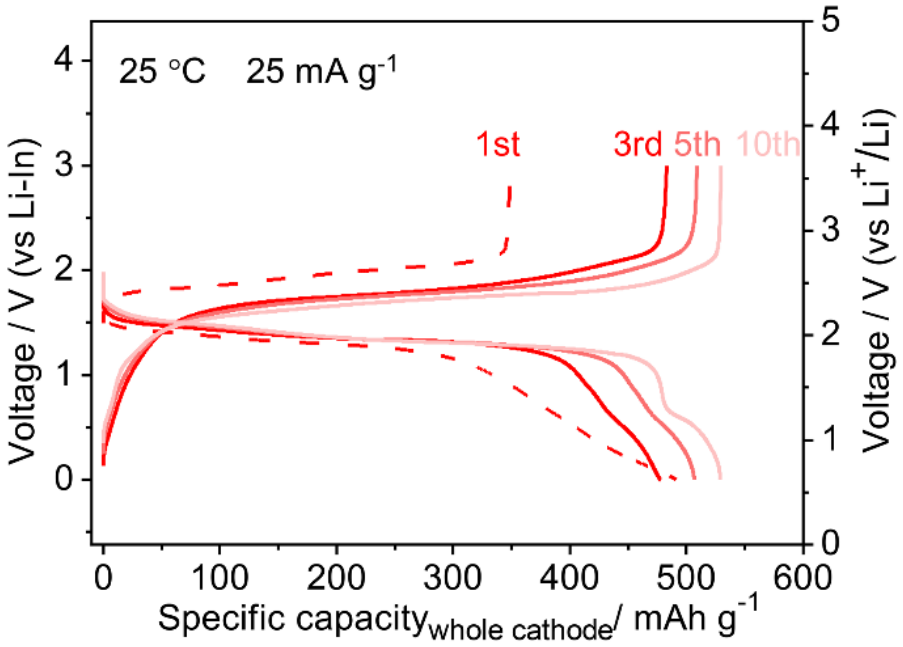

Figure 3.10 The galvanostatic charge/discharge curves of $0.85(0.8Li_2S\text{-}0.2LiI)\text{-}0.15MoS_2$ during 1st, 3rd, 5th and 10th cycle at 25 mA g^{-1}.

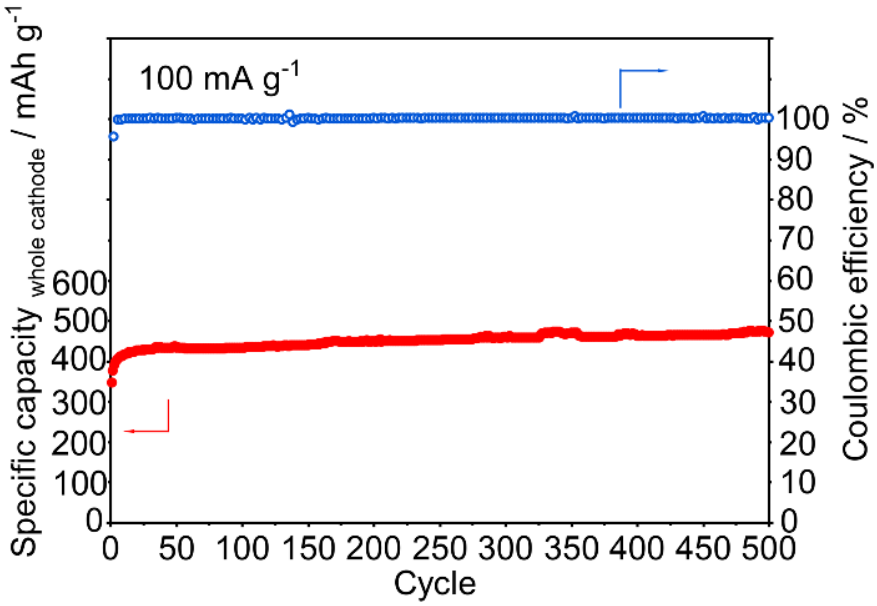

Figure 3.11 Cycling stability of $85(80Li_2S\text{-}20LiI)\text{-}15MoS_2$ at 100 mA g^{-1} at 25 °C.

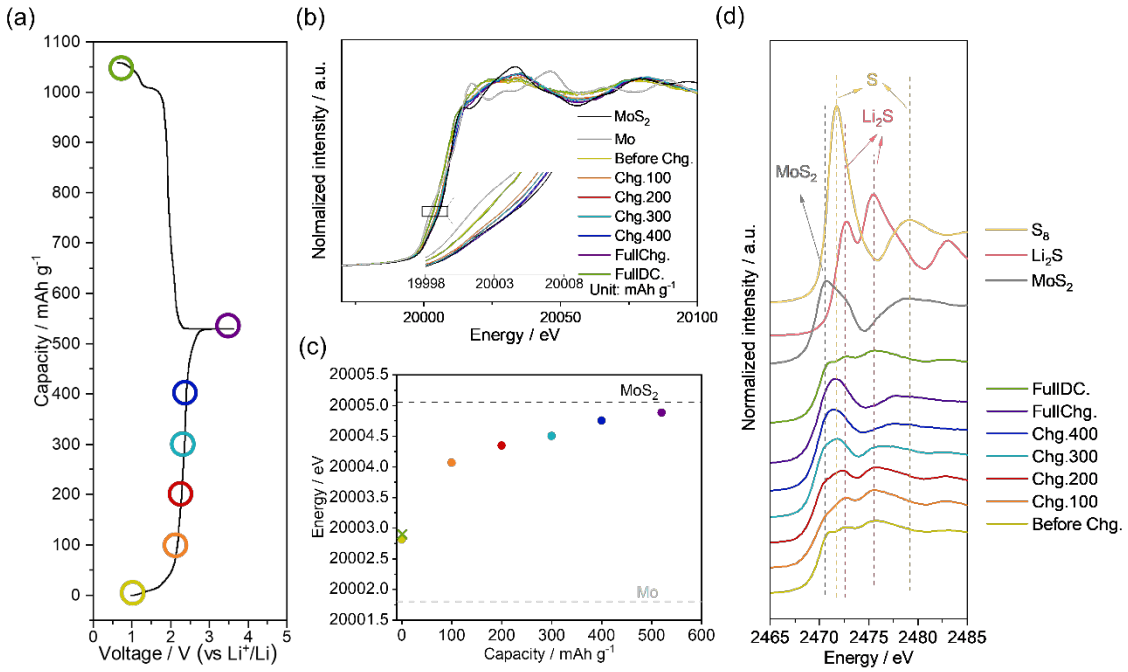

Figure 3.12 Mechanism of electrochemical reaction of $0.85(0.8Li_2S\text{-}0.2LiI)\text{-}0.15MoS_2$ cathode during the fifth cycle. (a) The 5th charge-discharge curves of $0.85(0.8Li_2S\text{-}0.2LiI)\text{-}0.15MoS_2$ cathode. (b) Mo *K*-edge XANES of $0.85(0.8Li_2S\text{-}0.2LiI)\text{-}0.15MoS_2$ cathode at different state of charge. (c) Enlarged part of Figure 4b about absorption energies for $Li_2S\text{-}LiI\text{-}MoS_2$ cathode, which delivers different capacities. Circle marks correspond to before charge and charge state, and the cross mark corresponds to the difference between fifth charge capacity and discharge capacity. (d) S *K*-edge XANES of $0.85(0.8Li_2S\text{-}0.2LiI)\text{-}0.15MoS_2$ cathode at different state of charge.

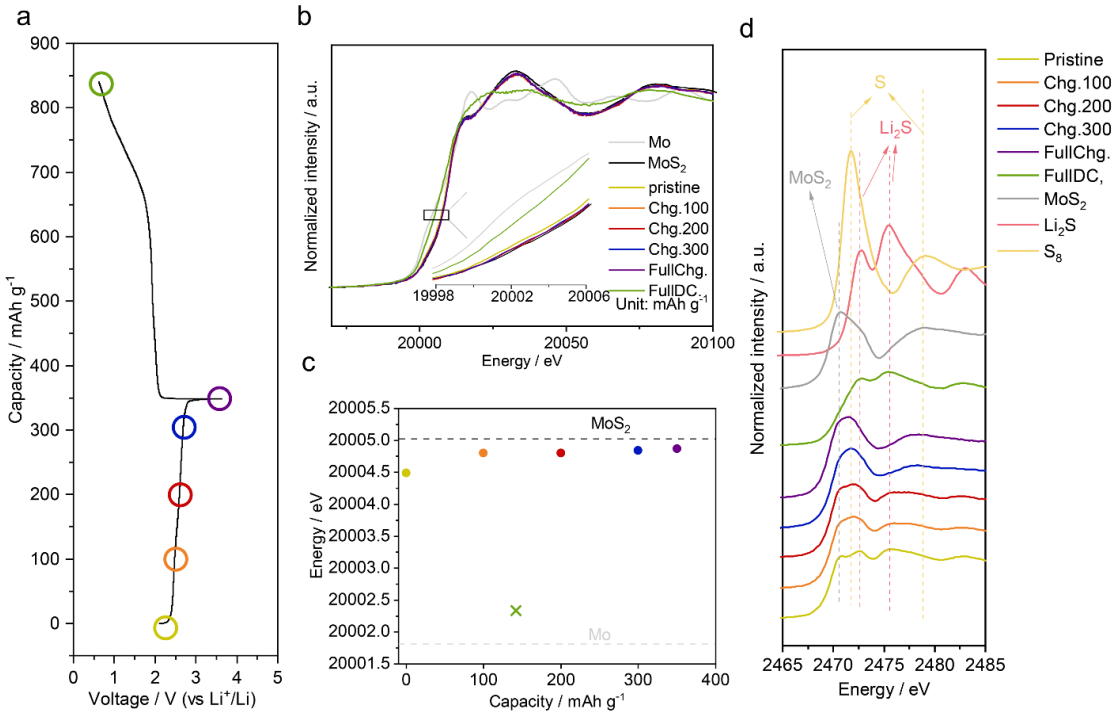

Figure 3.13 Mechanism of electrochemical reaction of $0.85(0.8Li_2S\text{-}0.2LiI)\text{-}0.15MoS_2$ cathode during first cycle. (a) The first charge-discharge curves of $0.85(0.8Li_2S\text{-}0.2LiI)\text{-}0.15MoS_2$ cathode. (b) Mo *K*-edge XANES of $0.85(0.8Li_2S\text{-}0.2LiI)\text{-}0.15MoS_2$ cathode at different state of charge. (c) Enlarged part of figure S7b about absorption energies for $Li_2S\text{-}LiI\text{-}MoS_2$ cathode which delivers different capacities. Circle marks correspond to pristine and charge state, and the cross mark corresponds to the difference between first charge capacity and discharge capacity. (d) S *K*-edge XANES of $0.85(0.8Li_2S\text{-}0.2LiI)\text{-}0.15MoS_2$ cathode at different state of charge.

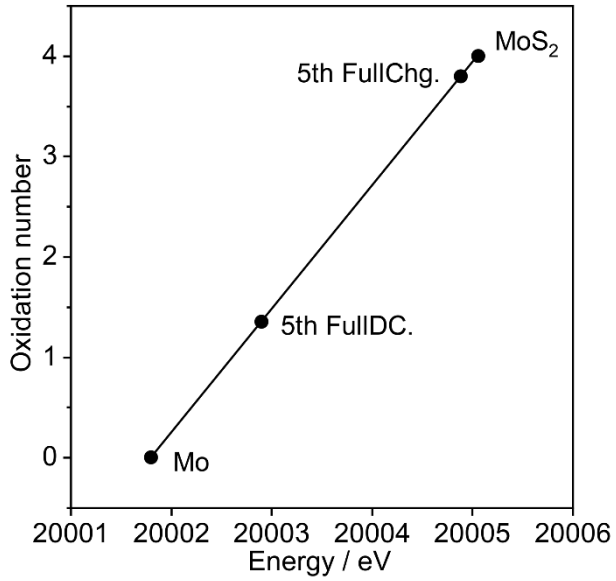

Figure 3.14 The relationship between oxidation number of Mo and the energy of Mo *K*-edge XANES.

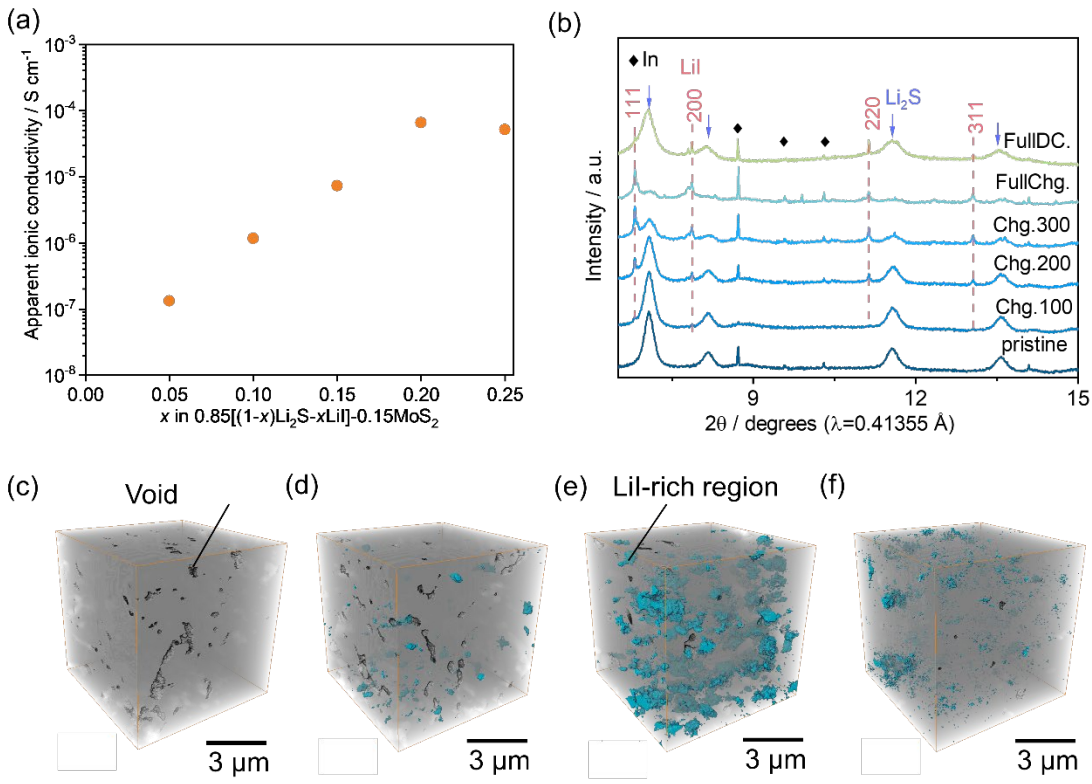

Figure 3.15 The function of LiI in Li_2S-LiI-MoS_2. (a) The apparent ionic conductivities at full charge state of 0.85[(1-*x*)Li_2S-*x*LiI]-0.15MoS_2 at 25 °C. (b) Synchrotron XRD patterns of 0.85(0.8Li_2S-0.2LiI)-0.15MoS_2 at pristine state, charge state with cut-off capacity of 100, 200 and 300 mAh g^{-1}, full-charge state and full-discharge state at the 1st cycle. The pink dash lines point to the position of LiI. The peaks of Indium are marked as diamonds. The blue arrows correspond to Li_2S-type phase. Computed Tomography (CT) of 0.85(0.8Li_2S-0.2LiI)-0.15MoS_2 cathode at (c) pristine (d) cut-off at 175 mAh g^{-1} (equal to half of first full charge capacity) (e) full-charge (f) full-discharge state. Blank parts and blue regions indicated correspond to the voids and LiI-rich domains in 0.85(0.8Li_2S-0.2LiI)-0.15MoS_2 cathode, respectively.

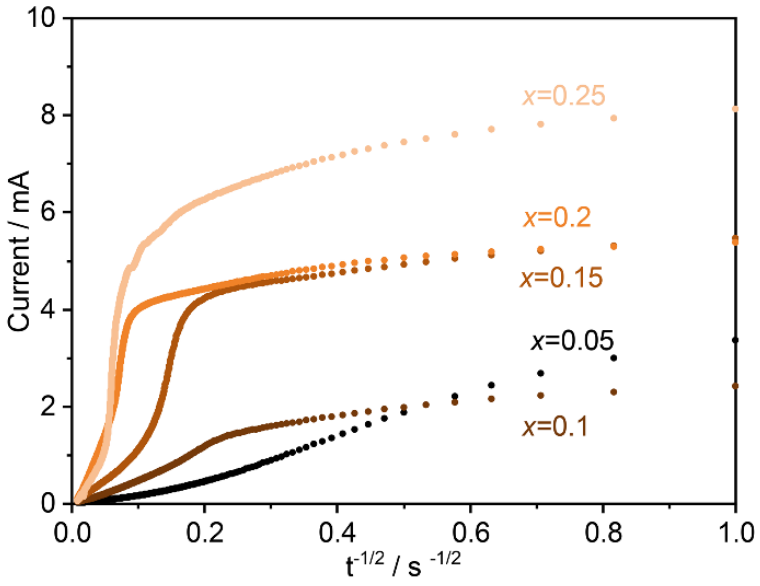

Figure 3.16 Cottrell plots of $0.85[(1-x)Li_2S$-$xLiI]$-$0.15MoS_2$ (x=0.05, 0.1, 0.15, 0.2, 0.25).

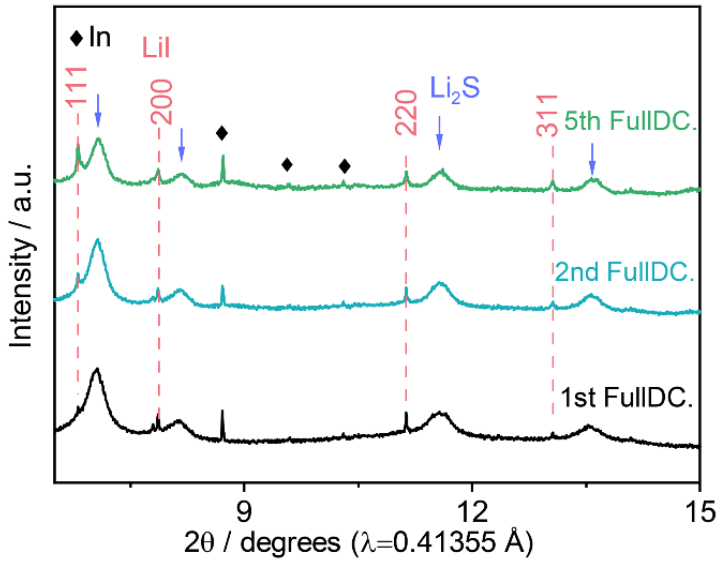

Figure 3.17 Synchrotron XRD patterns of 85(80Li_2S-20LiI)-15MoS_2 after 1st, 2nd and 5th cycle.

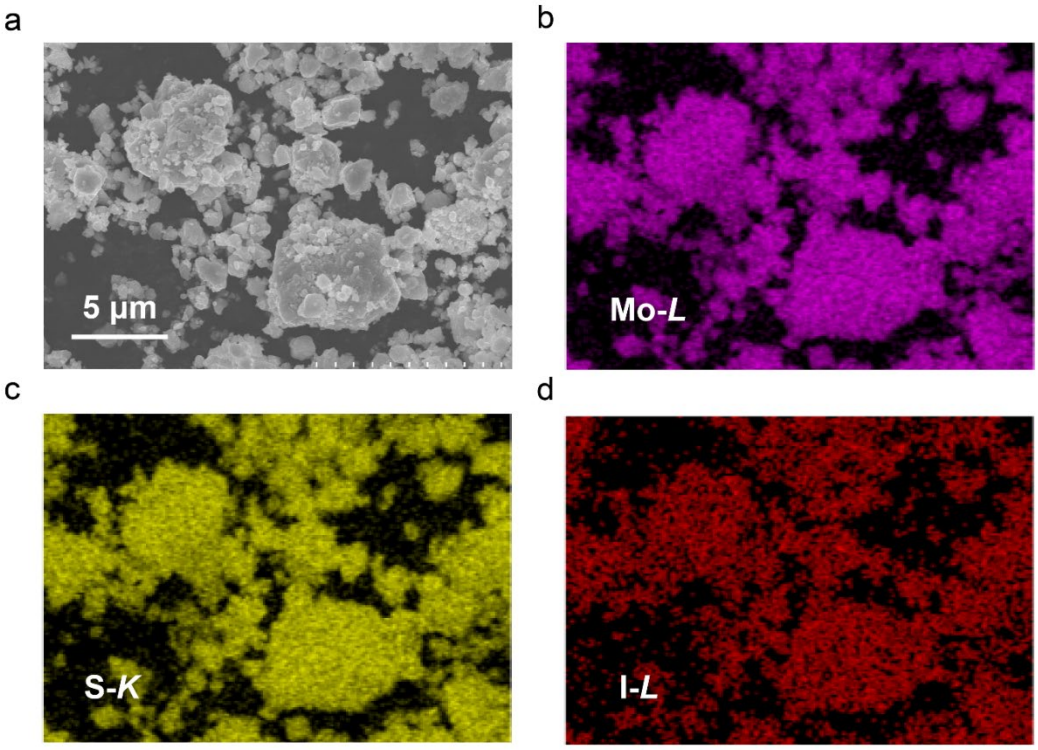

Figure 3.18 SEM image and mapping for as-prepared $0.85(0.8Li_2S\text{-}0.2LiI)\text{-}0.15MoS_2$ powder.

References

(1) Huang, Y.; Lin, L.; Zhang, C.; Liu, L.; Li, Y.; Qiao, Z.; Lin, J.; Wei, Q.; Wang, L.; Xie, Q. Recent advances and strategies toward polysulfides shuttle inhibition for high-performance Li–S batteries. *Adv. Sci.* **2022**, *9* (12), 2106004.

(2) Jiang, J.; Fan, Q.; Chou, S.; Guo, Z.; Konstantinov, K.; Liu, H.; Wang, J. Li_2S-Based Li-Ion Sulfur Batteries: Progress and Prospects. *Small* **2021**, *17* (9), 1903934.

(3) Yang, X.; Luo, J.; Sun, X. Towards high-performance solid-state Li–S batteries: from fundamental understanding to engineering design. *Chem. Soc. Rev.* **2020**, *49* (7), 2140-2195.

(4) Hou, L.-P.; Zhang, X.-Q.; Li, B.-Q.; Zhang, Q. Challenges and promises of lithium metal anode by soluble polysulfides in practical lithium–sulfur batteries. *Mater. Today* **2021**, *45*, 62-76.

(5) Liu, B.; Zhang, J.-G.; Xu, W. Advancing lithium metal batteries. *Joule* **2018**, *2* (5), 833-845.

(6) Lee, H.; Oh, P.; Kim, J.; Cha, H.; Chae, S.; Lee, S.; Cho, J. Advances and prospects of sulfide all-solid-state lithium batteries via one-to-one comparison with conventional liquid lithium ion batteries. *Adv. Mater.* **2019**, *31* (29), 1900376.

(7) Song, Y.-X.; Shi, Y.; Wan, J.; Lang, S.-Y.; Hu, X.-C.; Yan, H.-J.; Liu, B.; Guo, Y.-G.; Wen, R.; Wan, L.-J. Direct tracking of the polysulfide shuttling and interfacial evolution in all-solid-state lithium–sulfur batteries: a degradation mechanism study. *Energy Environ. Sci.* **2019**, *12* (8), 2496-2506.

(8) Ding, B.; Wang, J.; Fan, Z.; Chen, S.; Lin, Q.; Lu, X.; Dou, H.; Kumar Nanjundan, A.; Yushin, G.; Zhang, X.; et al. Solid-state lithium–sulfur batteries: Advances, challenges and perspectives. *Mater. Today* **2020**, *40*, 114-131.

(9) Nagata, H.; Chikusa, Y. A lithium sulfur battery with high power density. *J. Power Sources* **2014**, *264*, 206-210.

(10) Suzuki, K.; Kato, D.; Hara, K.; Yano, T.-a.; Hirayama, M.; Hara, M.; Kanno, R. Composite Sulfur Electrode Prepared by High-Temperature Mechanical Milling for use in an All-Solid-State Lithium–Sulfur Battery with a $Li_{3.25}Ge_{0.25}P_{0.75}S_4$ Electrolyte. *Electrochim. Acta* **2017**, *258*, 110-115.

(11) Wu, F.; Lee, J. T.; Nitta, N.; Kim, H.; Borodin, O.; Yushin, G. Lithium iodide as a promising electrolyte additive for lithium-sulfur batteries: mechanisms of performance enhancement. *Adv. Mater.* **2015**, *27* (1), 101-108.

(12) Hakari, T.; Hayashi, A.; Tatsumisago, M. Li_2S-Based Solid Solutions as Positive Electrodes with Full Utilization and Superlong Cycle Life in All-Solid-State Li/S Batteries. *Adv. Sustain. Syst.* **2017**, *1* (6).

(13) Wan, H.; Zhang, B.; Liu, S.; Zhang, J.; Yao, X.; Wang, C. Understanding LiI-LiBr Catalyst Activity for Solid State Li_2S/S Reactions in an All-Solid-State Lithium Battery. *Nano Lett.* **2021**, *21* (19), 8488-8494.

(14) Xu, R.; Yue, J.; Liu, S.; Tu, J.; Han, F.; Liu, P.; Wang, C. Cathode-Supported All-Solid-State Lithium–Sulfur Batteries with High Cell-Level Energy Density. *ACS Energy Lett.* **2019**, *4* (5), 1073-1079.

(15) Liu, X.; Huang, J. Q.; Zhang, Q.; Mai, L. Nanostructured Metal Oxides and Sulfides for Lithium-Sulfur Batteries. *Adv. Mater.* **2017**, *29* (20).

(16) Liang, K.; Marcus, K.; Zhang, S.; Zhou, L.; Li, Y.; De Oliveira, S. T.; Orlovskaya, N.; Sohn, Y. H.; Yang, Y. NiS_2/FeS Holey Film as Freestanding Electrode for High-Performance Lithium Battery. *Adv. Energy Mater.* **2017**, *7* (22).

(17) Luo, Q.; Tian, R.; Wu, A.; Dong, X.; Jin, X.; Zhou, S.; Huang, H. In-built durable Li–S counterparts from Li–TiS_2 batteries. *Mater. Today Energy* **2020**, *17*.

(18) Xu, H.; Manthiram, A. Hollow cobalt sulfide polyhedra-enabled long-life, high areal-capacity lithium-sulfur batteries. *Nano Energy* **2017**, *33*, 124-129.

(19) Ulissi, U.; Ito, S.; Hosseini, S. M.; Varzi, A.; Aihara, Y.; Passerini, S. High Capacity All-Solid-State Lithium Batteries Enabled by Pyrite-Sulfur Composites. *Adv. Energy Mater.* **2018**, *8* (26).

(20) Xu, S.; Kwok, C. Y.; Zhou, L.; Zhang, Z.; Kochetkov, I.; Nazar, L. F. A High Capacity All Solid-State Li-Sulfur Battery Enabled by Conversion-Intercalation Hybrid Cathode Architecture. *Adv. Funct. Mater.* **2020**, *31* (2).

(21) Li, M.; Liu, T.; Shi, Z.; Xue, W.; Hu, Y. S.; Li, H.; Huang, X.; Li, J.; Suo, L.; Chen, L. Dense All-Electrochem-Active Electrodes for All-Solid-State Lithium Batteries. *Adv. Mater.* **2021**, *33* (26), e2008723.

(22) Yamamoto, K.; Yang, S.; Takahashi, M.; Ohara, K.; Uchiyama, T.; Watanabe, T.; Sakuda, A.; Hayashi, A.; Tatsumisago, M.; Muto, H.; et al. High Ionic Conductivity of Liquid-Phase-Synthesized Li_3PS_4 Solid Electrolyte, Comparable to That Obtained via Ball Milling. *ACS Appl. Energy Mater.* **2021**, *4* (3), 2275-2281.

(23) Farrow, C. L.; Juhas, P.; Liu, J. W.; Bryndin, D.; Bozin, E. S.; Bloch, J.; Proffen, T.; Billinge, S. J. PDFfit2 and PDFgui: computer programs for studying nanostructure in crystals. *J. Phys. Condens. Matter* **2007**, *19* (33), 335219.

(24) Takeuchi, A.; Uesugi, K.; Uesugi, M.; Toda, H.; Hirayama, K.; Shimizu, K.; Matsuo, K.; Nakamura, T. High-energy x-ray nanotomography introducing an apodization Fresnel zone plate objective lens. *Rev. Sci. Instrum.* **2021**, *92* (2), 023701.

(25) Nagao, M.; Hayashi, A.; Tatsumisago, M. Sulfur–carbon composite electrode for all-solid-state Li/S battery with Li_2S–P_2S_5 solid electrolyte. *Electrochim. Acta* **2011**, *56* (17), 6055-6059.

(26) Santhosha, A. L.; Medenbach, L.; Buchheim, J. R.; Adelhelm, P. The Indium−Lithium Electrode in Solid-State Lithium-Ion Batteries: Phase Formation, Redox Potentials, and Interface Stability. *Batter. Supercaps* **2019**, *2* (6), 524-529.

(27) Takada, K.; Aotani, N.; Iwamoto, K.; Kondo, S. Solid state lithium battery with oxysulfide glass. *Solid State Ionics* **1996**, *86*, 877-882.

(28) Kudu, Ö. U.; Famprikis, T.; Cretu, S.; Porcheron, B.; Salager, E.; Demortiere, A.; Courty, M.; Viallet, V.; Mercier, T. L.; Fleutot, B.; et al. Structural details in Li_3PS_4: Variety in thiophosphate building blocks and correlation to ion transport. *Energy Storage Mater.* **2022**, *44*, 168-179.

(29) Wang, T.; Zhu, J.; Wei, Z.; Yang, H.; Ma, Z.; Ma, R.; Zhou, J.; Yang, Y.; Peng, L.; Fei, H.; et al. Bacteria-Derived Biological Carbon Building Robust Li-S Batteries. *Nano Lett.* **2019**, *19* (7), 4384-4390.

(30) Lu, Y.; Huang, X.; Song, Z.; Rui, K.; Wang, Q.; Gu, S.; Yang, J.; Xiu, T.; Badding, M. E.; Wen, Z. Highly stable garnet solid electrolyte based Li-S battery with modified anodic and cathodic interfaces. *Energy Storage Mater.* **2018**, *15*, 282-290.

(31) Jiao, Y.; Hafez, A. M.; Cao, D.; Mukhopadhyay, A.; Ma, Y.; Zhu, H. Metallic MoS_2 for High Performance Energy Storage and Energy Conversion. *Small* **2018**, *14* (36), e1800640.

(32) Geng, X.; Sun, W.; Wu, W.; Chen, B.; Al-Hilo, A.; Benamara, M.; Zhu, H.; Watanabe, F.; Cui, J.; Chen, T. P. Pure and stable metallic phase molybdenum disulfide nanosheets for hydrogen evolution reaction. *Nat. Commun.* **2016**, *7*, 10672.

(33) Er, E.; Hou, H.-L.; Criado, A.; Langer, J.; Möller, M.; Erk, N.; Liz-Marzán, L. M.; Prato, M. High-Yield Preparation of Exfoliated 1T-MoS_2 with SERS Activity. *Chem. Mater.* **2019**, *31* (15), 5725-5734.

(34) Lei, Z.; Zhan, J.; Tang, L.; Zhang, Y.; Wang, Y. Recent Development of Metallic (1T) Phase of Molybdenum Disulfide for Energy Conversion and Storage. *Adv. Energy Mater.* **2018**, *8* (19).

(35) Bai, J.; Zhao, B.; Zhou, J.; Si, J.; Fang, Z.; Li, K.; Ma, H.; Dai, J.; Zhu, X.; Sun, Y. Glucose-Induced Synthesis of 1T-MoS_2 /C Hybrid for High-Rate Lithium-Ion Batteries. *Small* **2019**, *15* (14), e1805420.

(36) Ohno, S.; Koerver, R.; Dewald, G.; Rosenbach, C.; Titscher, P.; Steckermeier, D.; Kwade, A.; Janek, J.; Zeier, W. G. Observation of Chemomechanical Failure and the Influence of Cutoff Potentials in All-Solid-State Li–S Batteries. *Chem. Mater.* **2019**, *31* (8), 2930-2940.

(37) Ohno, S.; Rosenbach, C.; Dewald, G. F.; Janek, J.; Zeier, W. G. Linking Solid Electrolyte Degradation to Charge Carrier Transport in the Thiophosphate-Based Composite Cathode toward Solid-State Lithium-Sulfur Batteries. *Adv. Funct. Mater.* **2021**, *31* (18).

(38) Phuc, N. H. H.; Takaki, M.; Muto, H.; Reiko, M.; Kazuhiro, H.; Matsuda, A. Sulfur–Carbon Nano Fiber Composite Solid Electrolyte for All-Solid-State Li–S Batteries. *ACS Appl. Energy Mater.* **2020**, *3* (2), 1569-1573.

(39) Zhang, Y.; Liu, T.; Zhang, Q.; Zhang, X.; Wang, S.; Wang, X.; Li, L.; Fan, L.-Z.; Nan, C.-W.; Shen, Y. High-performance all-solid-state lithium–sulfur batteries with sulfur/carbon nano-hybrids in a composite cathode. *J. Mater. Chem. A* **2018**, *6* (46), 23345-23356.

(40) Yan, H.; Wang, H.; Wang, D.; Li, X.; Gong, Z.; Yang, Y. In Situ Generated Li(2)S-C Nanocomposite for High-Capacity and Long-Life All-Solid-State Lithium Sulfur Batteries with Ultrahigh Areal Mass Loading. *Nano Lett.* **2019**, *19* (5), 3280-3287.

(41) Mwizerwa, J. P.; Zhang, Q.; Han, F.; Wan, H.; Cai, L.; Wang, C.; Yao, X. Sulfur-Embedded FeS_2 as a High-Performance Cathode for Room Temperature All-Solid-State Lithium-Sulfur Batteries. *ACS Appl. Mater. Interfaces* **2020**, *12* (16), 18519-18525.

(42) Shigedomi, T.; Fujita, Y.; Kishi, T.; Motohashi, K.; Tsukasaki, H.; Nakajima, H.; Mori, S.; Tatsumisago, M.; Sakuda, A.; Hayashi, A. Li_2S–V_2S_3–LiI Bifunctional Material as the Positive Electrode in the All-Solid-State Li/S Battery. *Chem. Mater.* **2022**, *34* (21), 9745-9752.

(43) Yao, X.; Huang, N.; Han, F.; Zhang, Q.; Wan, H.; Mwizerwa, J. P.; Wang, C.; Xu, X. High-Performance All-Solid-State Lithium–Sulfur Batteries Enabled by Amorphous Sulfur-Coated Reduced Graphene Oxide Cathodes. *Adv. Energy Mater.* **2017**, *7* (17).

(44) Zhang, Y.; Sun, Y.; Peng, L.; Yang, J.; Jia, H.; Zhang, Z.; Shan, B.; Xie, J. Se as eutectic accelerator in sulfurized polyacrylonitrile for high performance all-solid-state lithium-sulfur battery. *Energy Storage Mater.* **2019**, *21*, 287-296.

(45) Wang, L.; Yin, X.; Li, B.; Zheng, G. W. Mixed Ionically/Electronically Conductive Double-Phase Interface Enhanced Solid-State Charge Transfer for a High-Performance All-Solid-State Li-S Battery. *Nano Lett.* **2022**, *22* (1), 433-440.

(46) Zhang, L.; Sun, D.; Feng, J.; Cairns, E. J.; Guo, J. Revealing the Electrochemical Charging Mechanism of Nanosized Li_2S by in Situ and Operando X-ray Absorption Spectroscopy. *Nano Lett.* **2017**, *17* (8), 5084-5091.

(47) Ng, S. F.; Lau, M. Y. L.; Ong, W. J. Lithium-Sulfur Battery Cathode Design: Tailoring Metal-Based Nanostructures for Robust Polysulfide Adsorption and Catalytic Conversion. *Adv. Mater.* **2021**, *33* (50), e2008654.

(48) Yamamoto, K.; Xiao, Y.; Watanabe, T.; Sakuda, A.; Takahashi, M.; Pan, W.; Nakanishi, K.; Matsunaga, T.; Uesugi, M.; Takeuchi, A.; et al. High-Packing-Density Electrodes by Self-forming Ion Conduction Pathway During Charge Process for All-Solid-State Lithium Ion Batteries. *J. Phys. Chem. C* **2023**, *127* (30), 14656-14665.

(49) Acerce, M.; Voiry, D.; Chhowalla, M. Metallic 1T phase MoS2 nanosheets as supercapacitor electrode materials. *Nat. Nanotechnol.* **2015**, *10* (4), 313-318.

(50) Tang, Q.; Jiang, D.-e. Stabilization and Band-Gap Tuning of the 1T-MoS_2 Monolayer by Covalent Functionalization. *Chem. Mater.* **2015**, *27* (10), 3743-3748.

(51) Huang, Q.; Shen, J.; Lu, Y.; Ye, R.; Gong, S. Insights into the Structural Evolution of MoS_2 from the Semiconductive 2H to Metallic 1T Phase. *J. Phys. Chem. C* **2023**, *127* (35), 17406-17414.

Chapter 4 Tuning the ionic and electronic paths in Li_2S-based cathode for high-rate performance all-solid-state lithium-sulfur batteries

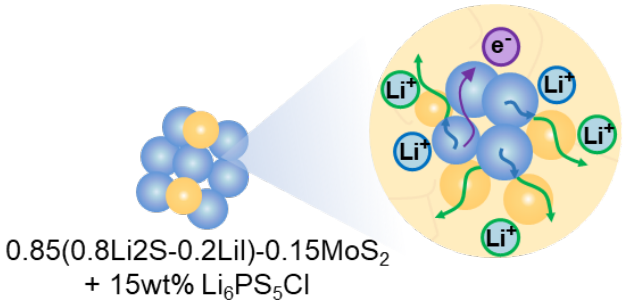

All-solid-state lithium-sulfur batteries (ASSLSBs) based on sulfur or lithium sulfide (Li_2S) as cathodes are one of the most promising candidates for next-generation energy storage devices due to their high theoretical energy density and good safety features. However, despite the promising outlook, the practical application of ASSLSBs is impeded due to the electronically and ionically insulating nature of S and Li_2S. Consequently, even with carbon and solid-state electrolytes (SSEs) addition, the electron and lithium-ion cannot transport smoothly through the cathode. Therefore, it is imperative to establish and tune effective electron/ion transport paths in the composite cathode to achieve high performance. In the present study, electronically/ionically dual conductive active material Li_2S-LiI-MoS_2 and high ionically conductive Li_6PS_5Cl SSE were coupled and modified to control ionic and electronic paths in Li_2S-based cathode composite. The optimized composite cathode possessed an overall gravimetric capacity of 423 mAh g^{-1} at 0.5 C and 308 mAh g^{-1} at 2 C with respect to the total mass of the cathode. The corresponding ASSLSBs achieved distinctively high energy with acceptable power density. The in-depth analysis by X-ray computed tomography revealed the three-dimensional conductive pathway in the composite cathode.

4.1 Introduction

Nowadays, there has been a growing interest in smart grids and the electric vehicles market due to their high efficiency and reduced fossil fuel consumption[1, 2]. High-performance rechargeable batteries are considered a key component to fulfill the dream of large-scale implementation of these advanced technologies. Among various alternatives, lithium-sulfur batteries are regarded as one of the most promising candidates for their potentially superior energy density (~2600 Wh kg^{-1}) and low cost compared with conventional lithium-ion batteries[3, 4]. Despite the high energy density, the severe safety concerns allied with the use of flammable organic electrolytes and rapid polysulfide dissolution remain major issues that hinder their practical application[5]. In that context, switching from conventional organic electrolytes to all solid-state electrolytes (SSEs) could address safety concerns and shuttle effects, which are the major roadblocks for conventional lithium-sulfur batteries[6]. Despite the different electrolytes, the core electrodes of conventional lithium-sulfur batteries and ASSLSBs are the same. Sulfur and its full-lithiated product Li_2S are commonly used as active materials for cathodes[7]. Especially, Li_2S-based active materials offer advantages: (1) Li_2S can be easily coupled with lithium-free anode such as Si, Sn, P, etc., thus negating the need for lithium metal as anode and providing higher safety[8]; (2) Due to the light relative molecular mass, Li_2S could offer high theoretical capacity of 1167 mAh g^{-1}[9]; (3) the high melting point (938 °C) makes it possible for operation at higher temperature. However, due to the electronically and ionically insulating nature, it is necessary to create electron and lithium-ion pathways through the Li_2S-based materials for cathodes.

Many efforts have been devoted to developing electron-ion conductive Li_2S-based cathodes. As for the electronic aspect, conductive carbonaceous materials are commonly used to improve the electronic conductivity of Li_2S-based cathodes, such as acetylene black[10, 11], graphene[12, 13], carbon nanotubes[14, 15] and nanofibers[16-18]. Although electronic conductivities have been effectively improved, there is a limited improvement in enhancing sulfur utilization and rate performance of these ASSLSBs due to the limited ionic conductivities of cathodes. To construct an ionic pathway, there are two typical methods: (1) to mix Li_2S active material with highly conductive SSEs to facilitate the lithium ions transport through SSEs particles[19, 20] and (2) to promote the ionic pathway associated with

Li_2S itself, by conducting structural engineering of Li_2S, such as nano-structuring and doping[21, 22]. In the first approach, numerous sulfide solid-state electrolytes with high ionic conductivities have been developed, such as Li_6PS_5Cl[23], $Li_7P_3S_{11}$[24], $Li_{10}GeP_2S_{12}$[25], $Li_{9.54}Si_{1.74}P_{1.44}S_{11.7}Cl_{0.3}$[26] and $Li_{9.54}[Si_{0.6}Ge_{0.4}]_{1.74}P_{1.44}S_{11.1}Br_{0.3}O_{0.6}$[27], which show remarkable ionic conductivities of 10^{-3}~10^{-2} S cm^{-1}. However, due to the insulating nature of Li_2S[28, 29], the electrochemical reaction can only occur where the lithium ions and electrons contact the Li_2S active material, that is, the interface between Li_2S particles and conductors[8].

Structural engineering of Li_2S was conducted to increase the active region to shorten the lithium-ion diffusion length and to construct the lithium-ion pathway associated with Li_2S itself[30, 31]. For example, Han et al. reported a nanocomposite consisting of a homogeneous distribution of nanosized Li_2S, Li_6PS_5Cl and carbon[32]. Although the contacting interface and overall conductivities of the composite cathode were significantly increased, the specific capacity only delivered 830 mAh g^{-1} at 50 mA g^{-1} based on Li_2S mass with a sulfur utilization of 71 %, which demonstrates the performance is still hindered by the low conductivity of Li_2S itself. Further research shows that the ionic and electronic transport properties can be improved by doping[33, 34]. Luo et al. conducted DFT calculations and found among different transition metals (Fe, Co, Ni, Cu, etc.) as dopants, Fe-doped Li_2S showed the lowest formation energy of lithium vacancy, suggesting Fe doping was most desirable[35]. Subsequently, Takeuchi et al. prepared Fe-substituted Li_2S by ball milling, and the cathode delivered a discharge capacity of 760 mAh g^{-1} at 0.04 C[36]. In addition to transition metal doping, halogen doping was also studied[37, 38]. Fujita et al. revealed that lithium iodide (LiI) and Li_2S could form a solid solution with higher ionic conductivity (10^{-6} S cm^{-1}) and LiI-rich domains created during charge with an ionic conductive structure, providing an ionic pathway through the composite cathode[37]. However, without SSEs, the Li_2S-LiI-C cathode could only deliver capacity with intermittent charge and discharge, indicating the insufficient ionic conductivity of doped Li_2S.

Among many such attempts, our group recently reported two Li_2S-based composite cathodes, Li_2S-PI_3-C and Li_2S-LiI-MoS_2, with significantly improved electronic and ionic conductivity[39, 40]. These materials can function as composite electrodes at low rates without adding a solid electrolyte, and delivered high specific capacity based on the total cathode

mass with sulfur utilization of ~80 %. However, rate performance at high current densities is still unsatisfactory and due to insufficient ionic conduction, the energy density is reduced when high power densities are pursued. Hence, there is still plenty of room for improving the performance of Li_2S-based cathode by either adding SSEs and carbon as conductors or conducting structural engineering for Li_2S itself. At this point, the improvement of ionic conductivity by substituting other elements for Li_2S has been optimized, and it is necessary to design a composite electrode with as small a quantity of the solid electrolyte phase uniformly dispersed as possible to improve rate capability further.

In this study, we have coupled highly electronic and ionic conductive $0.85(0.8Li_2S$-$0.2LiI)$-$0.15MoS_2$ (the numbers in the composition are in molar ratios) with Li_6PS_5Cl as SSE, possessing high ionic conductivity as composite cathodes for ASSLSBs. Herein, the ionic and electronic pathways is tuned by varying the ratio of $0.85(0.8Li_2S$-$0.2LiI)$-$0.15MoS_2$ to Li_6PS_5Cl. With an optimized ratio (mass ratio of Li_6PS_5Cl=15 wt%), the composite cathode delivered a high overall cathode capacity of 423 mAh g^{-1} at 0.5 C, equivalent to the sulfur utilization of 74%. The corresponding ASSLSBs possessed high energy density with power density. The morphology of the composite cathodes and conductive pathway were understood by X-ray computed tomography (CT), which could guide for optimizing microstructure and electrochemical performance of composite cathodes.

4.2 Experimental Section

4.2.1 Material synthesis

Firstly, the $0.85(0.8Li_2S$-$0.2LiI)$-$0.15MoS_2$ sample (the numbers in the composition are in molar ratios) was prepared using the ball milling method. Stoichiometric amounts of Li_2S (99% purity, Mitsuwa), MoS_2 (99% purity, Kojundo), and LiI (99% purity, Aldrich) were hand-mixed in a mortar for 0.5 h, followed by mechanical mixing with ZrO_2 balls at 530 rpm for 80 h. Then the prepared $0.85(0.8Li_2S$-$0.2LiI)$-$0.15MoS_2$ (simplified as Li_2S-LiI-MoS_2) was mixed by hand in a mortar for 30 minutes with the different mass ratio of Li_6PS_5Cl provided by LIBTEC with an argyrodite structure to form the composite cathodes $(100$-$x)Li_2S$-LiI-MoS_2-xLi_6PS_5Cl (x=0, 5, 10, 15, 20, 30, 40, 50, 100 (wt%)). The Li_3PS_4 glass powder was prepared via ball milling method to fabricate the solid-state electrolyte layer. It was prepared by adding a 3:1 mixture of Li_2S and P_2S_5 to a ZrO_2 pot (45 mL) with

ZrO_2 balls mechanically milled for 16 h at 600 rpm. All the preparation and sample collection were done under an Ar atmosphere.

4.2.2 Characterization

The synchrotron X-ray diffraction (XRD) for the as-prepared (100-*x*)Li_2S-LiI-MoS_2-*x*LPSCl (*x*=0, 5, 10, 15, 20, 30, 40, 50, 100 (wt%)) was measured at the BL02B2 beamline at SPring-8, Japan. Scanning electron microscope (SEM, Hitachi SU-8220) and energy dispersive X-ray spectroscopy (EDS, Horiba X-max^N) mapping were used for (100-*x*)Li_2S-LiI-MoS_2-*x*Li_6PS_5Cl (*x*=0, 5, 10, 15, 20, 30, 40, 50, 100 (wt%)) powder. X-ray computed tomography (CT) was utilized to investigate the morphology of the (100-*x*)Li_2S-LiI-MoS_2-*x*Li_6PS_5Cl (*x*=0, 5, 10, 15, 20, 30, 40, 50, 100) pellets and conducted at BL20XU in the SPring-8, Japan[41]. All of these characterizations for materials were measured without air exposure.

4.2.3 Electrochemical Measurements

To measure the electronic and ionic conductivities of the (100-*x*)Li_2S-LiI-MoS_2-*x*LPSCl (*x*=0, 5, 10, 15, 20, 30, 40, 50, 100 (wt%)) composites, direct current (DC) polarization and alternating current (AC) impedance were measured, respectively. The cathode materials were pressed into pellets under a pressure of 360 MPa and set between two stainless-steel current collectors. The applied voltage for DC polarization using HZ-7000 (Hokuto Denko) is 1 V and maintained for 0.5 h to obtain the stable current. The mold was under 120 MPa pressure during the test for good contact between the pellet sample and current collectors. The electronic conductivity is calculated by using the following equation $\sigma = \frac{L}{RS} = \frac{LI}{SV}$, where *R* is the resistance of (100-*x*)Li_2S-LiI-MoS_2-*x*Li_6PS_5Cl, which can be calculated by corresponding current and applied voltage, *I* is the stable current, *L* is the thickness of (100-*x*)Li_2S-LiI-MoS_2-*x*LPSCl pellet, *V* is the applied voltage, and *S* is the cross-sectional area of the pellet. For ionic conductivities measurements, (100-*x*)Li_2S-LiI-MoS_2-*x*LPSCl with a mass of 80 mg was first pressed into a pellet in a mold, similiar to the electronic conductivity measurement procedure mentioned above. Then Li_3PS_4, a common solid-state electrolyte with high ionic conductivity (10^{-4} S cm^{-1}) and negligible electronic conductivity (10^{-8} S cm^{-1}) [42], was used as the electron blocking layer on both sides of (100-*x*)Li_2S-LiI-MoS_2-*x*Li_6PS_5Cl pellet. The total impedance of Li_3PS4 | (100-*x*)Li_2S-LiI-MoS_2-*x*Li_6PS_5Cl

| Li_3PS_4 was measured by Modulab XM ECS using alternating current (AC) impedance technique. The AC amplitude was 10 mV, and the applied frequency ranged between 1 MHz and 0.1 Hz. By subtracting the impedance of Li_3PS_4 from the total impedance, the impedance of (100-*x*)Li_2S-LiI-MoS_2-*x*Li_6PS_5Cl can be obtained and used to calculate the corresponding ionic conductivity.

The electrochemical performance of the (100-*x*)Li_2S-LiI-MoS_2-*x*Li_6PS_5Cl (*x*=0, 5, 10, 15, 20, 30, 40, 50, 100 (wt%)) cathode materials was analyzed using a two-electrode cell. The (100-*x*)Li_2S-LiI-MoS_2-*x*Li_6PS_5Cl (*x*=0, 5, 10, 15, 20, 30, 40, 50 (wt%)) samples were used as composite cathodes, and the prepared Li_3PS_4 was used as the solid-state electrolyte (SE) of the cell. The (100-*x*)Li_2S-LiI-MoS_2-*x*Li_6PS_5Cl (*x*=0, 5, 10, 15, 20, 30, 40, 50 (wt%)) cathode materials with 4 mg mass loading (corresponding to the thickness of ~30 μm), and 80 mg SE layer were placed in a polycarbonate tube with a diameter of 10 mm and were pressed together under a pressure of 360 MPa. A Li−In alloy layer was placed on the SE layer on the opposite side of the cathode layer and served as the anode. Two stainless-steel rods, added to the cathode and anode sides by applying a pressure of 120 MPa, serve as current collectors. Cell assembly was performed in a dry Ar-filled glovebox. Electrochemical tests were performed at different C-rates with discharge and charge cutoff voltages of 0 (0.62 V vs. Li^+/Li) and 3.0 V (3.62 V) [43], respectively, at 25 °C. The calculation of C-rate is based on the theoretical capacity of Li_2S (1167 mAh g^{-1}) and MoS_2 (670 mAh g^{-1}) multiplied by their mass fraction in the cathode composite. As for the optimized cathode (100-*x*)Li_2S-LiI-MoS_2-*x*Li_6PS_5Cl (*x* =15 wt%), 1 C=570 mA g^{-1}.

4.2.4 CT analysis

The X-ray CT images of (100-*x*)Li_2S-LiI-MoS_2-*x*Li_6PS_5Cl (*x*=0, 5, 10, 15, 20, 30, 40, 50, 100 (wt%)) pellets measured at BL20XU in the SPring-8 were reconstructed by convolution backprojection method. Segmentation of the voids, Li_2S-LiI-MoS_2, and Li_6PS_5Cl electrolyte phase was analyzed using a grayscale threshold based on the contrast of the density distribution in the CT images. The volume fraction of each phase was calculated based on the segmented data. Volume rendering for 3D display was performed using the commercially available Avizo software. The tortuosity factor of Li_2S-LiI-MoS_2 and Li_6PS_5Cl was calculated from each segmented data using Matlab app (TauFactor) [44]. The calculation was based on the equation $D^{eff} = D\frac{\varepsilon}{\tau}$, where ε is the volume fraction of

the conductive phase, D is the intrinsic diffusivity of the conductive phase, D^{eff} is the effective diffusivity and τ is the tortuosity factor.

4.3 Results and Discussion

The 0.85(0.8Li_2S-0.2LiI)-0.15MoS_2 (the numbers in the composition are in molar ratios) sample was selected as the active material in this work since it possesses high ionic conductivity and electronic conductivity as reported in our previous work[40]. LiI could form solid solution with Li_2S and the solid solubility is 20 mol%, creating lithium vacancies and improving ionic conductivity. Various fraction of MoS_2 was optimized with 0.8Li_2S-0.2LiI (in molar ratio) [37]. Due to Li^+ from Li_2S insertion into MoS_2 during ball milling process, metallic 1T-Li_xMoS_2 formed and provided not only high electronic but also capability of Li^+ insertion and extraction [45]. With 15 mol% of MoS_2, the 0.85(0.8Li2S-0.2LiI)-0.15MoS_2 cathode exhibited optimized overall cathode capacity of 530 mAh g^{-1}at about 0.04 C. In this work, the active material Li_2S-LiI-MoS_2 was mixed with varying mass fractions of Li_6PS_5Cl to prepare composite cathodes. The phase of as-prepared (100-x)Li_2S-LiI-MoS_2-$x$$Li_6PS_5Cl$ (x=0, 5, 10, 15, 20, 30, 40, 50, 100 (wt%)) was characterized by synchrotron XRD and their XRD patterns and corresponding lattice constants are shown in Figure 4.1. As evident from Figure 1a, when x=0, all sharp peaks could be assigned to the structure analogous to Li_2S ($Fm\bar{3}m$), which is due to the formation of Li_2S-LiI solid solution and iodine incorporated into the structure of Li_2S. The humps at about 3.6°, 8.9° and 15.1° were assigned to the 1T-phase of MoS_2 with Li^+ inserted as Li_yMoS_2.As evident from Figure 1, with the addition of Li_6PS_5Cl, other sharp peaks assigned to argyrodite Li_6PS_5Cl appear. The intensity of these peaks attributed to Li_6PS_5Cl becomes stronger and more robust with an increase in Li_6PS_5Cl amount. On the other hand, the peaks of Li_2S-LiI-MoS_2 become weaker, which is in agreement with the change in their mass ratio. The lattice constants of Li_2S phase and Li_6PS_5Cl phase in Figure 4.1b and 4.1c obtained by Le Bail refinement in Figure 4.2 remain stable with different Li_6PS_5Cl content, indicating no interaction between Li_2S-LiI-MoS_2 and Li_6PS_5Cl during mixing. In addition, the crystallite size D_c of Li_6PS_5Cl particles in (100-x)Li_2S-LiI-MoS_2-$x$$Li_6PS_5Cl$ samples were calculated based on the Scherrer equation:

$$D_c = K\lambda/\beta cos\theta,$$

where K is a dimensionless shape factor and equals to 0.9 here, λ is the wavelength of beamline, β is the actual measurement of the peak full width at half maximum intensity (FWHM), θ is the Bragg position. As shown in Figure 4.1d, the average crystallite sizes of Li_6PS_5Cl in samples with different Li_6PS_5Cl content were similar, which means the mixing process does not change the morphology of Li_6PS_5Cl SSE particles. Figure 4.3 (a)-(i) show SEM with backscattered-electron images of the (100-x)Li_2S-LiI-MoS_2-$x$$Li_6PS_5Cl$ (x=0, 5, 10, 15, 20, 30, 40, 50, 100 (wt%)) powder and their corresponding EDS mapping for sulfur (yellow), molybdenum (lime green), iodine (red), chlorine (purple) and phosphorous (green). Because the yield of backscattered electrons is associated with atomic number, the Li_2S-LiI-MoS_2 particles and Li_6PS_5Cl particles can be distinguished by the different brightness in SEM images as Li_2S-LiI-MoS_2 contains heavier elements such as iodine and molybdenum but Li_6PS_5Cl only contains lighter elements. With x increasing, the proportion of darker regions corresponding to Li_6PS_5Cl particles increases, and the brighter areas corresponding to Li_2S-LiI-MoS_2 decrease, which agrees with their mass ratio, XRD results, and EDS mapping. The particles of Li_2S-LiI-MoS_2 and Li_6PS_5Cl show similar sizes below 10 μm. With $x \leq 15$, Li_6PS_5Cl particles disperse in the composite materials, while agglomeration appears and becomes severe when the mass ratio of Li_6PS_5Cl is larger than 20% as shown in Figure 4.3 (e)-(i). The aggregation of the solid electrolyte particles is undesirable since it cannot provide effective contact with active material for lithium transport but increases the inactive mass.

Before assembling batteries with composite cathodes, the electronic and ionic conductivities of (100-x)Li_2S-LiI-MoS_2-$x$$Li_6PS_5Cl$ (x=0, 5, 10, 15, 20, 30, 40, 50, 100 (wt%)) were measured by DC polarization and AC impedance, respectively. The Li_6PS_5Cl used in this study has a good ionic conductivity of 2.3×10^{-3} S cm^{-1} (Figure 4.4). Due to the high ionic conductivity of Li_6PS_5Cl, the ionic conductivities of (100-x)Li_2S-LiI-MoS_2-x Li_6PS_5Cl shown in Figure 4.5 increase gradually from 6.4×10^{-4} to 2.3×10^{-3} S cm^{-1} when x is increased from 0 to 100 wt%, which benefits smooth lithium ion transport. As Figure 2b shows, with $x \leq 15$ wt%, the electronic conductivities decrease slightly with more Li_6PS_5Cl content and still show a relatively high value of 10^{-4} S cm^{-1}, which is probably because the well-dispersed Li_6PS_5Cl particles barely influence the electronic pathway in composite cathodes. However, the electronic conductivities of (100-x)Li_2S-LiI-MoS_2-x

Li_6PS_5Cl decline rapidly with more Li_6PS_5Cl ($x \geq 20$ wt%), because the agglomerated Li_6PS_5Cl particles with extremely low electronic conductivity (10^{-8} S cm^{-1}) block the electron transport through composite cathodes.

Further, to demonstrate the practical applicability of the composite as a cathode, a battery was assembled and subjected to the galvanostatic charge-discharge measurement. Figure 4.6 shows charge–discharge curves of the (100-*x*)Li_2S-LiI-MoS_2-*x*Li_6PS_5Cl (*x*=0, 5, 10, 15, 20, 30, 40, 50 (wt%)) composite cathodes at 0.5 C at 25 °C. The (100-*x*)Li_2S-LiI-MoS_2-*x*Li_6PS_5Cl composite cathodes deliver specific capacities of 250, 280, 392, 423, 399, 302, 256, and 203 mAh g^{-1}, respectively. It is noteworthy that the capacities are calculated based on the total mass of composite cathodes. The capacities increase with Li_6PS_5Cl content initially with Li_6PS_5Cl mass ratio up to 15 wt% and decrease with higher *x* values. The highest specific capacity is achieved with x = 15 at 0.5 C, as 423 mAh g^{-1} with sulfur utilization over 70%, while Li_2S-LiI-MoS_2 without Li_6PS_5Cl only delivers 250 mAh g^{-1} (sulfur utilization ≈ 37%). It is because the electrochemical reaction is limited by ionic transport when $x \leq 15$, and the Li_6PS_5Cl addition probably increases the ionically conductive pathway and facilitates lithium-ion transport. On the other hand, although the excessive Li_6PS_5Cl added as an ionic conductor could improve the ionic conductivities of overall composite cathodes to some degree, the electronic pathway is possibly blocked by Li_6PS_5Cl particles, leading to impeded electron transport and inferior electrochemical performance. Meanwhile, the massive introduction of ionic conductors would result in low active material content and sacrifice the overall energy density.

To evaluate the influence of electronic/ionic pathway on the electrochemical reaction, rate capabilities of (100-*x*)Li_2S-LiI-MoS_2-*x*Li_6PS_5Cl (*x*=0, 5, 10, 15, 20, 30, 40, 50 (wt%)) composite cathodes were investigated at various C rates and shown in Figure 4.6b. Although the cathode Li_2S-LiI-MoS_2 without Li_6PS_5Cl shows higher capacity at a low C-rate (0.1 C, 0.2 C), the capacity decreases rapidly with increasing C-rate from 0.5 C to 2 C, demonstrating insufficient rate capability. By contrast, the composite cathodes display better rate performance when $15 \leq x \leq 40$, benefiting from the improved lithium-ion transport. Mainly, 85Li_2S-LiI-MoS_2-15Li_6PS_5Cl (wt%) shows good overall cathode capacity of 356 and 308 mAh g^{-1} at 1C and 2C, respectively. However, it should be noted that, with *x*= 50, the composite cathode shows inferior rate performance though its ionic

conductivity is higher than those of other composite cathodes with less Li_6PS_5Cl content, probably resulting from obstructed electron transport, which indicates the importance of electronic pathway construction in composite cathodes. As shown in Figure 4.6c, when x = 15, the composite cathode shows high capacity retention of over 96% at 1 C after 50 cycles, while the cathode Li_2S-LiI-MoS_2 without Li_6PS_5Cl only has the capacity retention of 70% at 1 C after 50 cycles, which suggests that the fewer active materials participate into the electrochemical reaction due to insufficient ionic transport pathway.

To better understand the conductive pathway through composite cathodes, X-ray CT images were conducted and analyzed for the morphology of (100-*x*)Li_2S-LiI-MoS_2-*x*LPSCl (*x*=0, 5, 10, 15, 20, 30, 40, 50, 100 (wt%)) cathodes pellets. The distribution of Li_2S-LiI-MoS_2 and Li_6PS_5Cl can be distinguished as the former contains some heavy elements such as I and Mo, which results in the brighter image of CT, and Li_6PS_5Cl consists of light elements that lead to the dim image. These CT images approximately represent the density distribution of the object. As shown in Figure 4.7, the blue region corresponding to Li_2S-LiI-MoS_2 and the grey region corresponding to Li_6PS_5Cl solid-state electrolyte are surrounded by each other. With a higher proportion of Li_6PS_5Cl, the grey region increases with fewer blue regions, which is in good agreement with the SEM images. The volume fraction of Li_2S-LiI-MoS_2, Li_6PS_5Cl and void obtained from CT analysis (Figure 4b and Table S2) is similar to the results calculated by mass ratio and densities in Table S1, demonstrating the accuracy of CT analysis. All (100-*x*)Li_2S-LiI-MoS_2-*x* Li_6PS_5Cl (*x*=0, 5, 10, 15, 20, 30, 40, 50, 100 (wt%)) cathodes display as dense pellets with low void fraction than 7 vol%.

The tortuosity factors of Li_2S-LiI-MoS_2 active material and Li_6PS_5Cl SSE were shown in Figure 4.7c as a blue line and grey line, respectively. Among them, the tortuosity factor of Li_2S-LiI-MoS_2 is inversely related with both electrons and lithium ions transportability along the particles of active material. The tortuosity factor of Li_6PS_5Cl is associated with the lithium-ion conduction along SSE between active material particles. With x = 5 and 10, the tortuosity factor of Li_6PS_5Cl is 92.39 and 20.36, respectively, indicating insufficient lithium conduction along SSE particles. The tortuosity factor slumps to 5.40 with x = 15 and shows a steady decrease with more Li_6PS_5Cl content, indicating the effective lithium-ion pathway among active material particles. On the other hand, the tortuosity factor of

Li_2S-LiI-MoS_2 increases steadily with Li_6PS_5Cl content, reflecting reduced ion- and electron-conduction along the active material. A small volume fraction of ion- or electron-conduction media is detrimental to electrochemical performance[45]. The cathode with 15 wt% Li_6PS_5Cl possesses low tortuosity factor of both active material and SSE, indicating facile electron and lithium ion transport through the cathode. The relationship between the contact area and the Li_6PS_5Cl mass ratio is shown in Figure 4.7d. With *x* from 0 to 15, the contact area increases substantially, indicating more reactive interfaces are created effectively with Li_6PS_5Cl. And when *x* increased from 15 to 30, changes in the increased trend of the contact area is reduced. Moreover, with $x > 30$, the contact area between Li_2S-LiI-MoS_2 and Li_6PS_5Cl decreases. This is because the proportion of Li_2S-LiI-MoS_2 is low, and the newly introduced Li_6PS_5Cl contact with itself instead provides effective contact with Li_2S-LiI-MoS_2, which is undesirable since it cannot increase the interface for reaction and lithium transport but increases the inactive mass.

By modifying and optimizing the electronic/ionic pathway in composite cathodes, the 85Li_2S-LiI-MoS_2-15Li_6PS_5Cl (wt%) cathode achieves a high specific capacity with optical rate capability. To prove the effectiveness of our our strategy, a comparison of both energy densities and power densities was conducted among different composite cathodes for ASSLSBs[13, 16, 38, 46-52]. As shown in Figure 4.8, in the case of Li metal as anode, the comparison of power densities and energy densities was based on the whole composite cathodes with previous cathode composites in ASSLSBs. The previously reported lithium lanthanum titanium oxide/carbon (LLTO/C) nanofibers possess relatively high energy density and medium power density. But, the operating temperature is 55 °C, which limits its practical application. The integrated S-Mo_6S_8 cathode[46] reported previously shows relatively high energy density because of the absence of non-active conductors under the condition of 70 °C, and significantly low power density demonstrating the severe condition for electron/ion path through the S-Mo_6S_8 cathode. As for our previous work[39, 40], Li_2S-PI_3-C and Li_2S-LiI-MoS_2, eliminating solid electrolyte and all common electronic/ionic conductors, respectively, possess high energy densities with medium power densities at room temperature, but there is still some room for improvement. In this work, by modifying both the electronic and ionic paths in the cathode, the 85Li_2S-LiI-MoS_2-15Li_6PS_5Cl (wt%) composite cathode possesses high energy density and superior power density. These results

are achieved with the cathode mass loading of 5.10 mg cm^{-2} and the areal capacity of 2.15 mAh cm^{-2} (based on overall cathode capacity of 423 mAh g^{-1} at 0.5 C). The results demonstrate the importance of ionic and electronic paths to the electrochemical performance of the overall composite cathode. By controlling the ionic and electronic paths, the composite cathode can be developed practically for ASSLSBs with high energy density and good power density.

Conclusion

The electron and ion transport pathway could be tuned by combining and modifying the electronic/ionic conductive material Li_2S-LiI-MoS_2 with high ionic conductive Li_6PS_5Cl. With an optimized ratio (mass ratio of Li_6PS_5Cl=15 wt%), the composite cathode delivered a high overall cathode capacity of 423 mAh g^{-1} at 0.5 C, equal to the sulfur utilization of 74 %. And it exhibits good rate performance with a capacity of 308 mAh g^{-1} at 2 C. The corresponding ASSLBs achieved both high energy density and power density. The three-dimensional morphology and conductive pathway were understood by X-ray CT images.

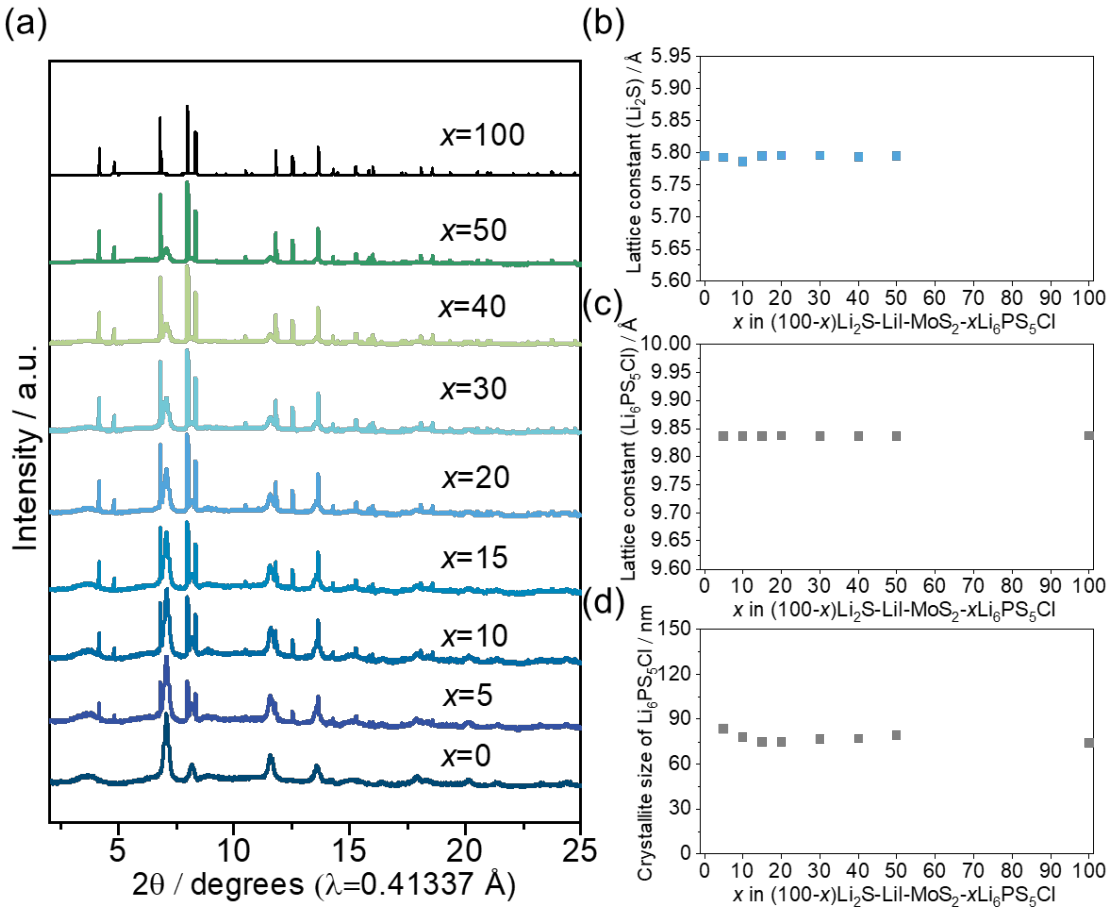

Figure 4.1 The structure of (100-*x*)Li_2S-LiI-MoS_2-*x*Li_6PS_5Cl (*x*=0, 5, 10, 15, 20, 30, 40, 50, 100 (wt%)). (a) XRD patterns of (100-*x*)Li_2S-LiI-MoS_2-*x*Li_6PS_5Cl. Corresponding lattice constant of (b) Li_2S phase and (c) Li_6PS_5Cl phase. (d) Crystallite size of Li_6PS_5Cl in (100-*x*)Li_2S-LiI-MoS_2-*x*Li_6PS_5Cl.

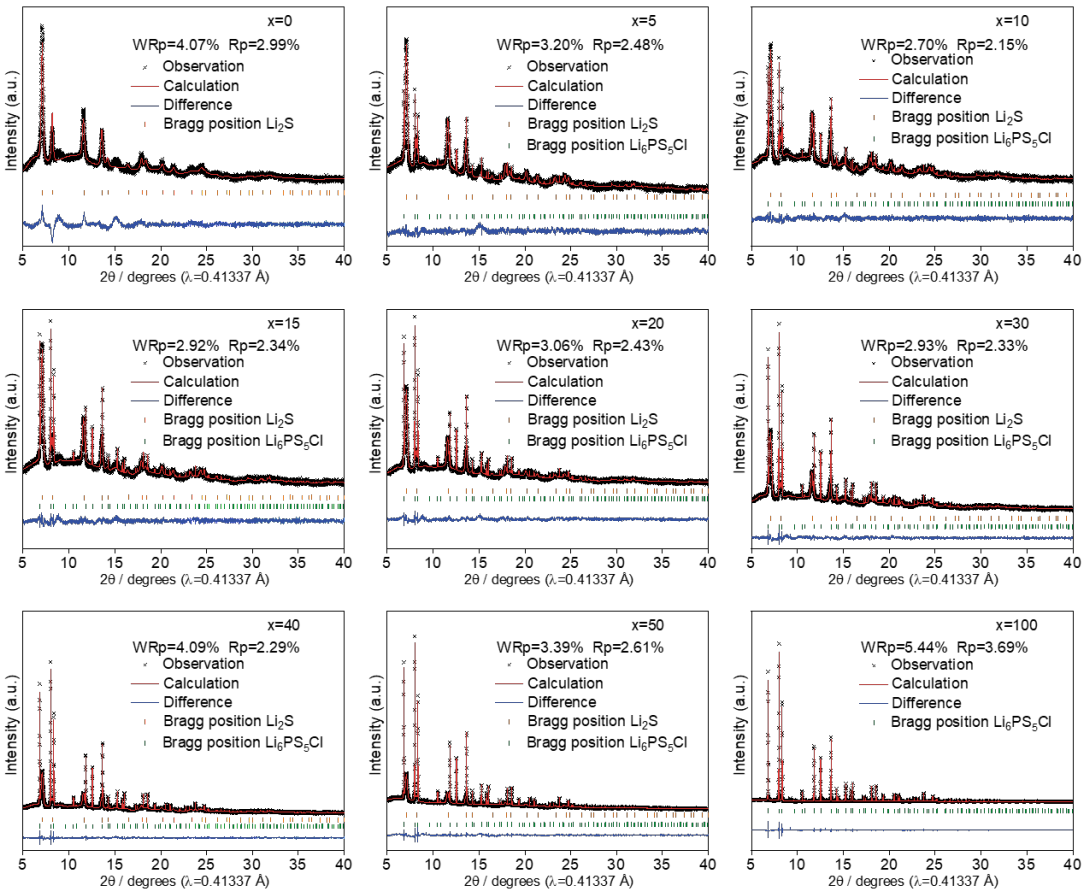

Figure 4.2 Le Bail refinement for (100-*x*)Li_2S-LiI-MoS_2-*x*Li_6PS_5Cl (*x*=0, 5, 10, 15, 20, 30, 40, 50, 100 (wt%)).

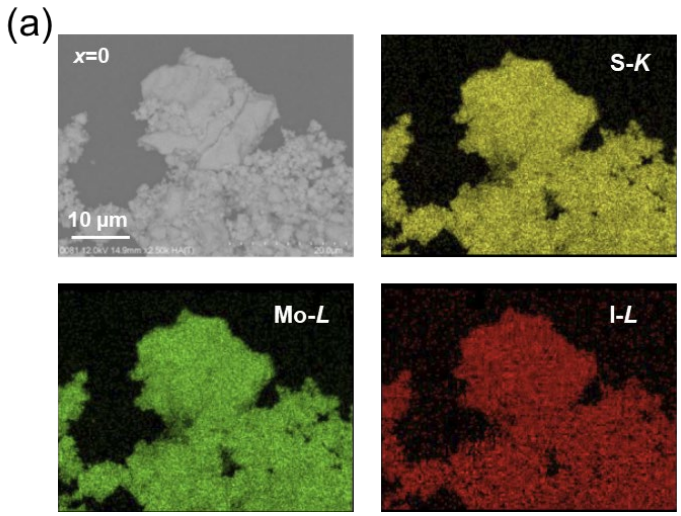

Figure 4.3 (a) SEM and EDS mapping of (100-x)Li_2S-LiI-MoS_2-xLi_6PS_5Cl (x=0, 5, 10, 15, 20, 30, 40, 50, 100 (wt%)). (a) x=0.

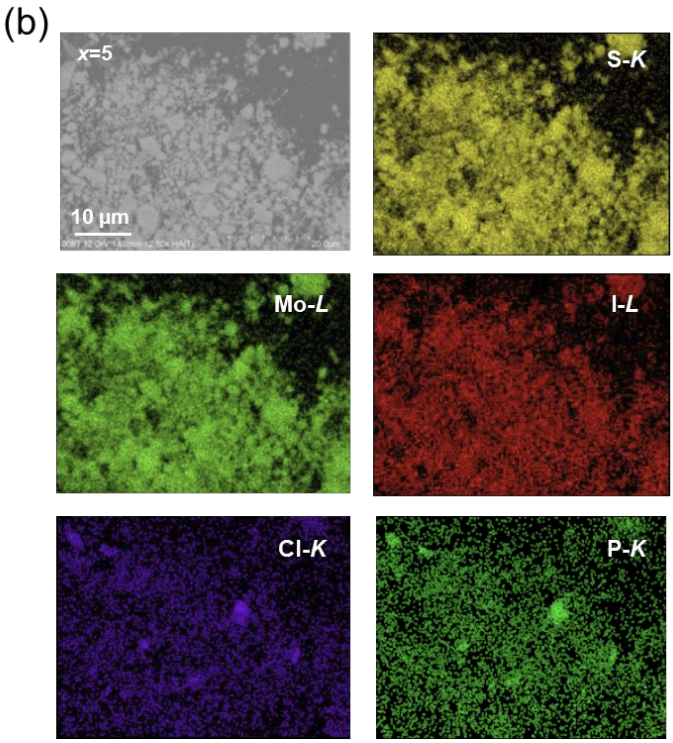

Figure 4.3 (b) SEM and EDS mapping of (100-x)Li_2S-LiI-MoS_2-xLi_6PS_5Cl (x=0, 5, 10, 15, 20, 30, 40, 50, 100 (wt%)). (b) x=5.

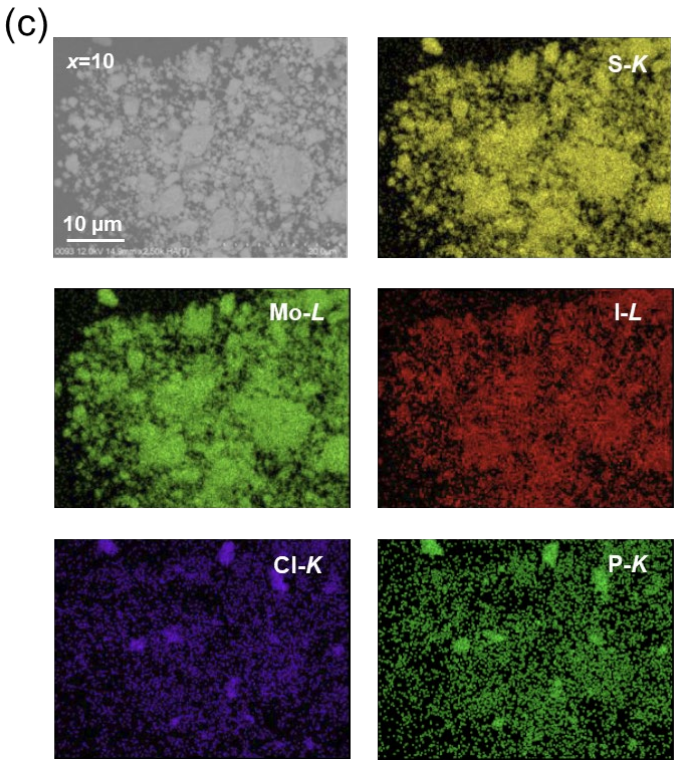

Figure 4.3 (c) SEM and EDS mapping of (100-*x*)Li_2S-LiI-MoS_2-*x*Li_6PS_5Cl (*x*=0, 5, 10, 15, 20, 30, 40, 50, 100 (wt%)). (c) *x*=10.

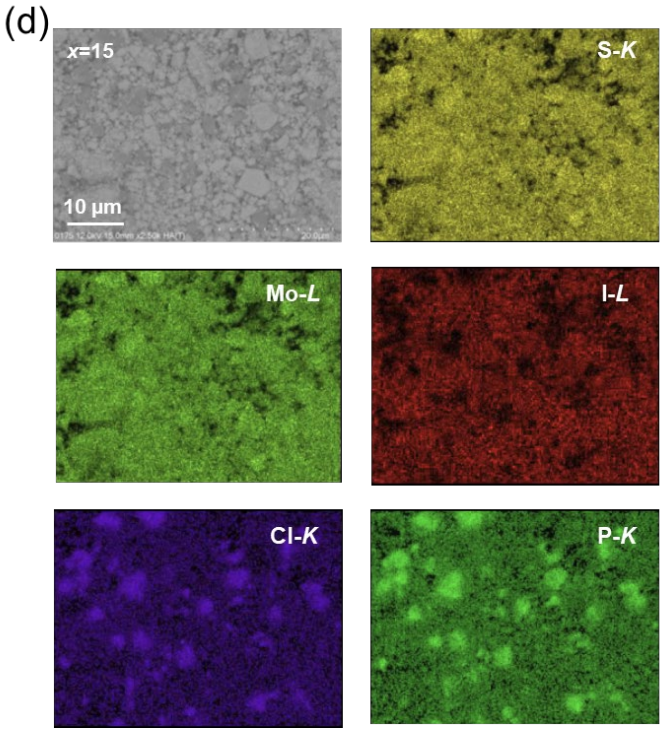

Figure 4.3 (d) SEM and EDS mapping of (100-*x*)Li_2S-LiI-MoS_2-*x*Li_6PS_5Cl (*x*=0, 5, 10, 15, 20, 30, 40, 50, 100 (wt%)). (d) *x*=15.

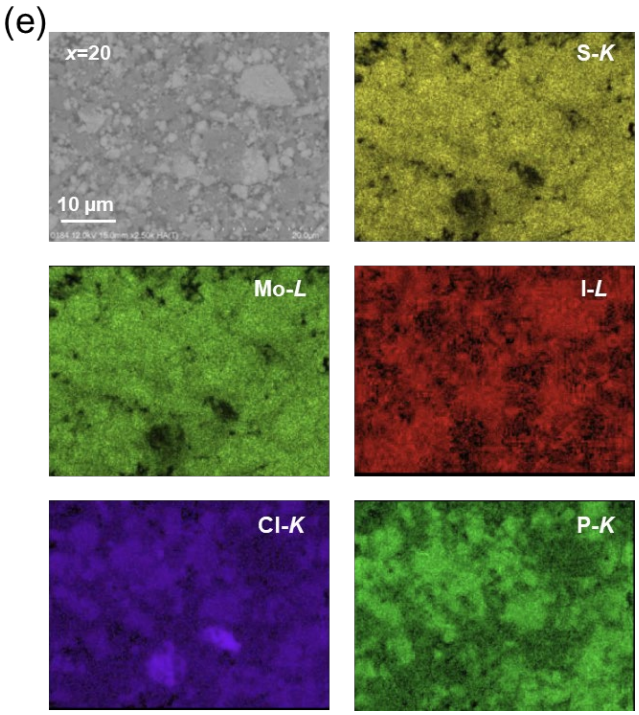

Figure 4.3 (e) SEM and EDS mapping of (100-x)Li_2S-LiI-MoS_2-$x$$Li_6PS_5Cl$ (x=0, 5, 10, 15, 20, 30, 40, 50, 100 (wt%)). (e) x=20.

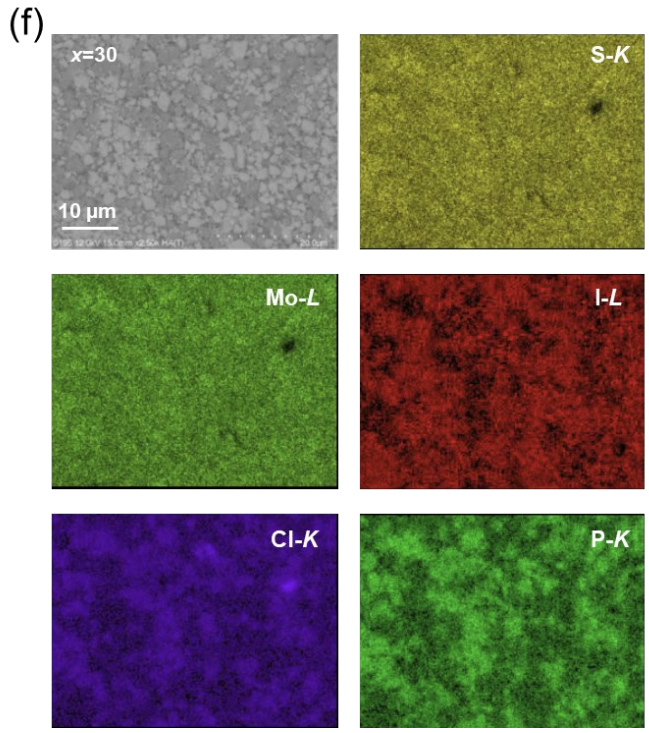

Figure 4.3 SEM and EDS mapping of (100-x)Li_2S-LiI-MoS_2-$x$$Li_6PS_5Cl$ (x=0, 5, 10, 15, 20, 30, 40, 50, 100 (wt%)). (f) x=30.

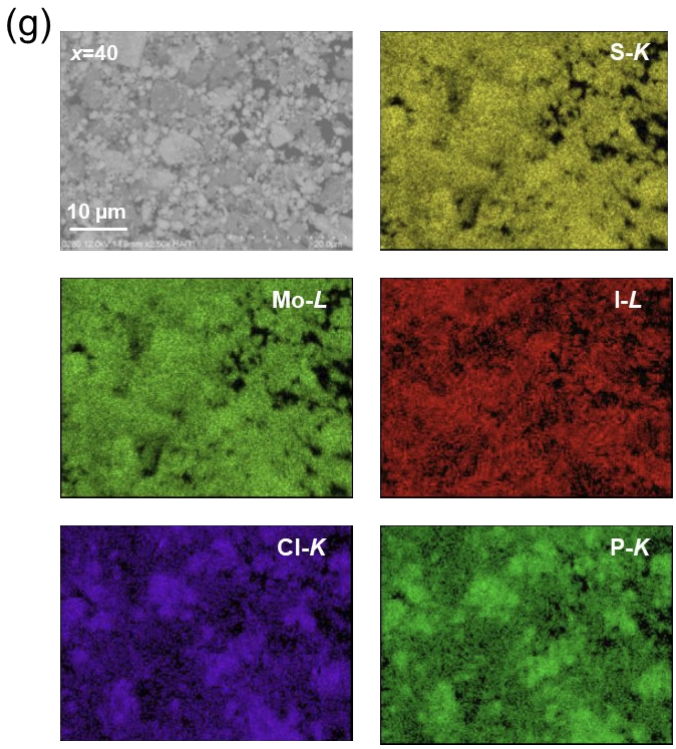

Figure 4.3 SEM and EDS mapping of (100-*x*)Li_2S-LiI-MoS_2-*x*Li_6PS_5Cl (*x*=0, 5, 10, 15, 20, 30, 40, 50, 100 (wt%)). (g) *x*=40.

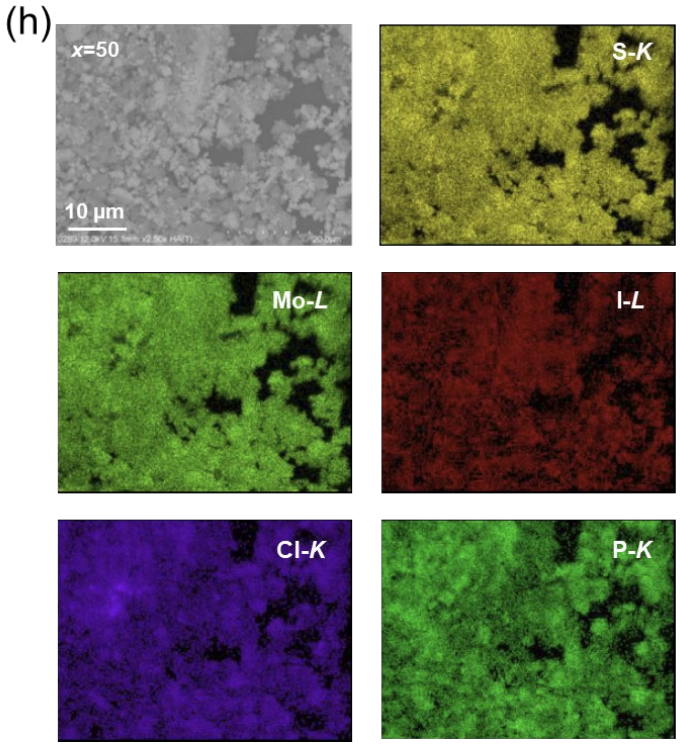

Figure 4.3 SEM and EDS mapping of (100-*x*)Li_2S-LiI-MoS_2-*x*Li_6PS_5Cl (*x*=0, 5, 10, 15, 20, 30, 40, 50, 100 (wt%)). (h) *x*=50.

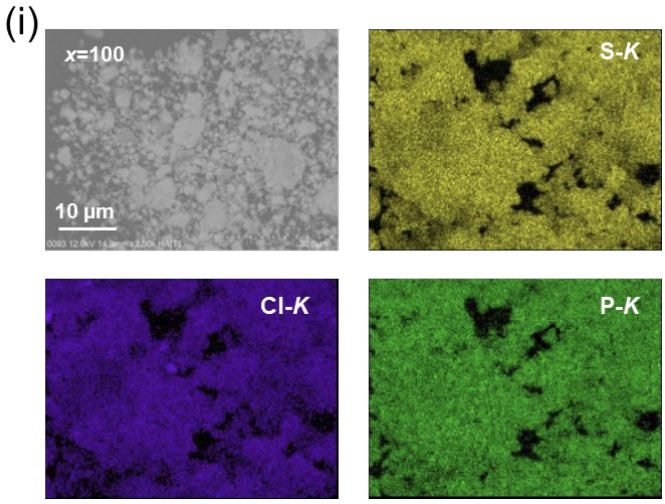

Figure 4.3 SEM and EDS mapping of (100-x)Li_2S-LiI-MoS_2-xLi_6PS_5Cl (x=0, 5, 10, 15, 20, 30, 40, 50, 100 (wt%)). (i) x=100.

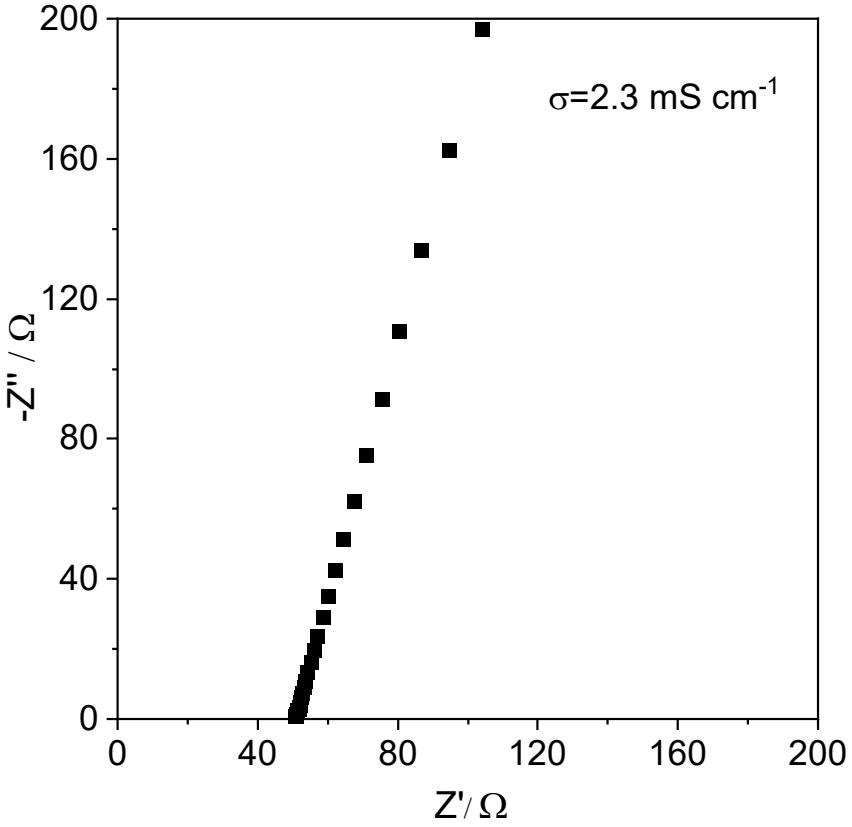

Figure 4.4 AC impedance measurement for Li_6PS_5Cl. The corresponding ionic conductivity is 2.3×10^{-3} S cm^{-1}.

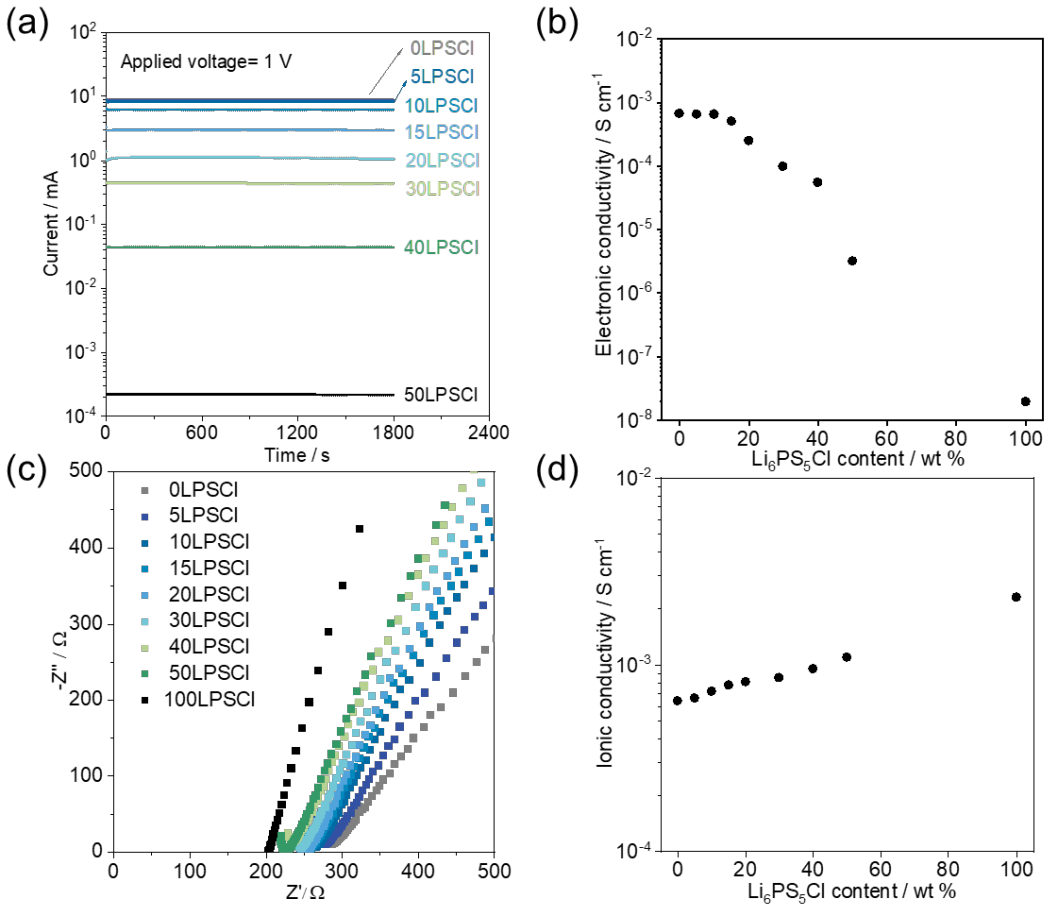

Figure 4.5 The measurements and values of electronic and ionic conductivities of (100-*x*)Li_2S-LiI-MoS_2-*x*LPSCl (*x*=0, 5, 10, 15, 20, 30, 40, 50, 100). (a) DC polarization for (100-*x*)Li_2S-LiI-MoS_2-*x*LPSCl (*x*=0, 5, 10, 15, 20, 30, 40, 50, 100) and (b) corresponding electronic conductivities. (c) AC impedance measurement for Li_3PS4 | (100-*x*)Li_2S-LiI-MoS_2-*x*LPSCl | Li_3PS_4 and (d) corresponding ionic conductivities of (100-*x*)Li_2S-LiI-MoS_2-*x*LPSCl (*x*=0, 5, 10, 15, 20, 30, 40, 50, 100).

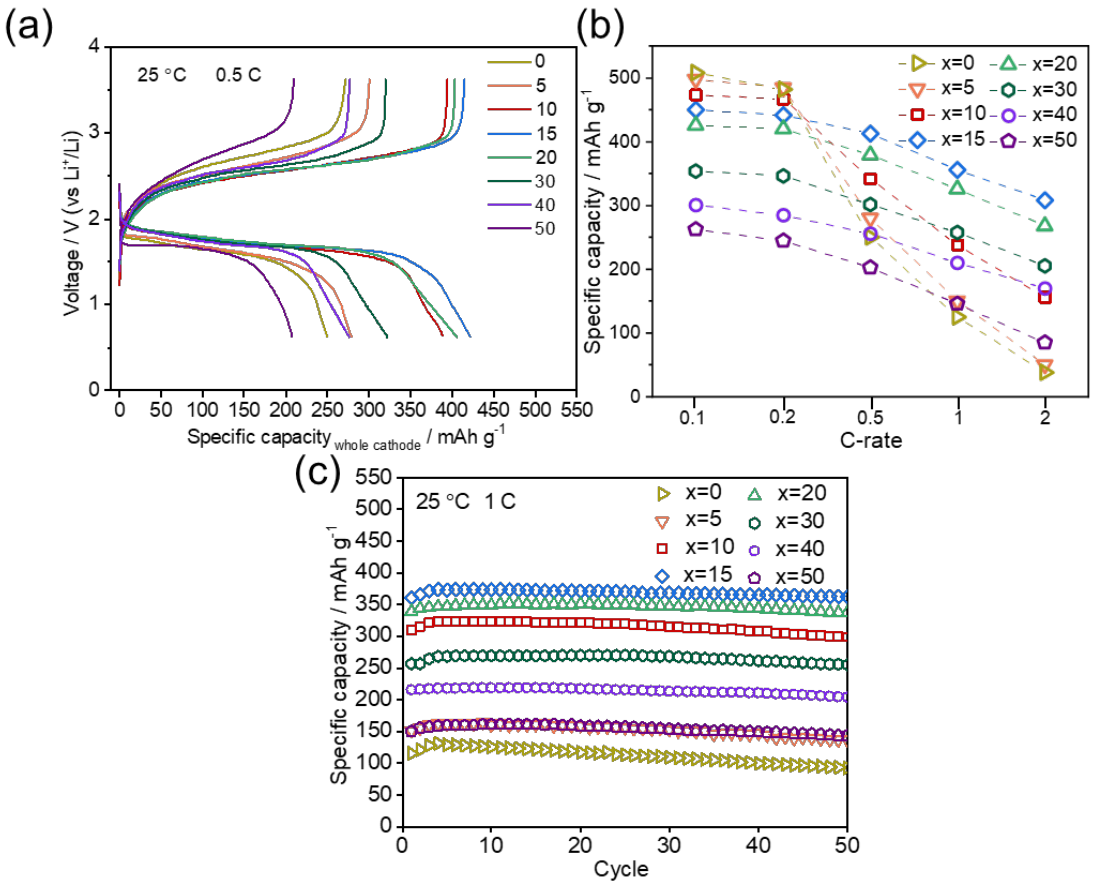

Figure 4.6 The electrochemical performance of (100-x)Li_2S-LiI-MoS_2-xLi_6PS_5Cl (x=0, 5, 10, 15, 20, 30, 40, 50, 100 (wt%)). (a) Charge-discharge curves at 0.5 C at 25 °C. (b) The rate capability. (c) The cycling stability at 1 C at 25 °C.

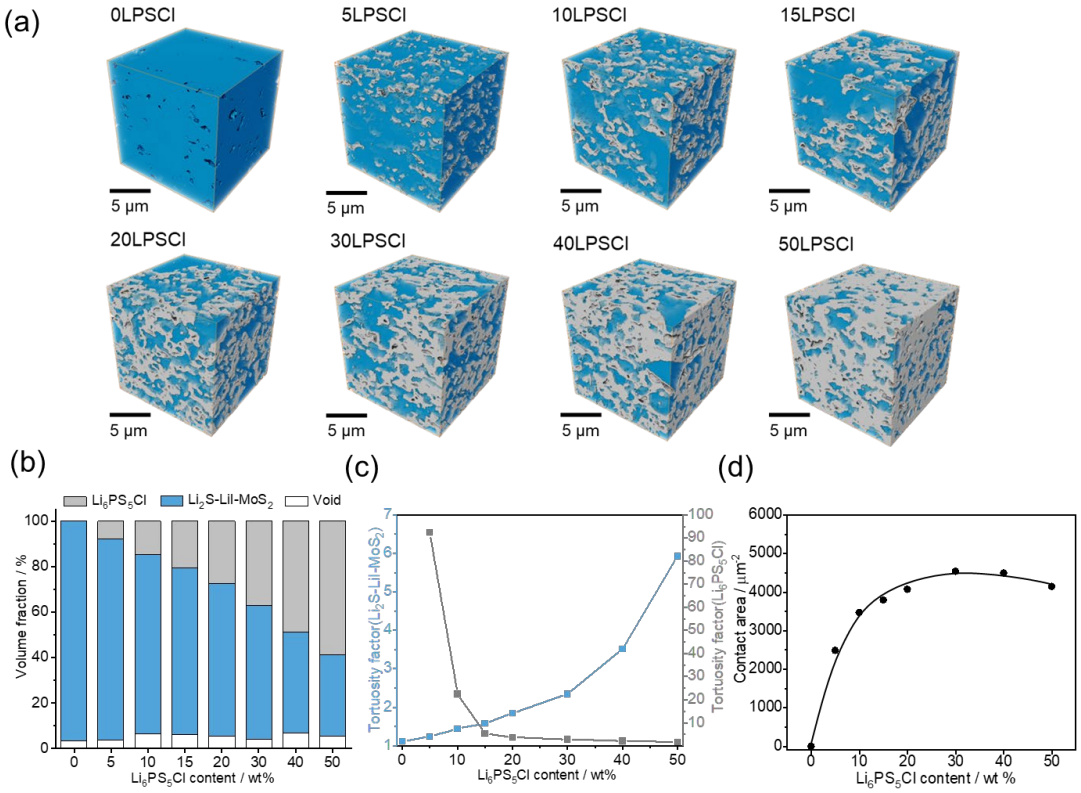

Figure 4.7 The morphology of the pellets of (100-*x*)Li_2S-LiI-MoS_2-*x*Li_6PS_5Cl (*x*=0, 5, 10, 15, 20, 30, 40, 50 (wt%)) composite cathodes. (a) Computed Tomography (CT) of (100-*x*)Li_2S-LiI-MoS_2-*x*Li_6PS_5Cl (*x*=0, 5, 10, 15, 20, 30, 40, 50 (wt%)) composite cathodes. The blue region corresponds to Li_2S-LiI-MoS_2 and grey region corresponds to Li_6PS_5Cl solid state electrolyte. (b) The volume fraction of Li_2S-LiI-MoS_2, Li_6PS_5Cl and void in composite cathodes. (c) Corresponding tortuosity factors of Li_2S-LiI-MoS_2 and Li_6PS_5Cl. (d) Corresponding contact area between Li_2S-LiI-MoS_2 and Li_6PS_5Cl.

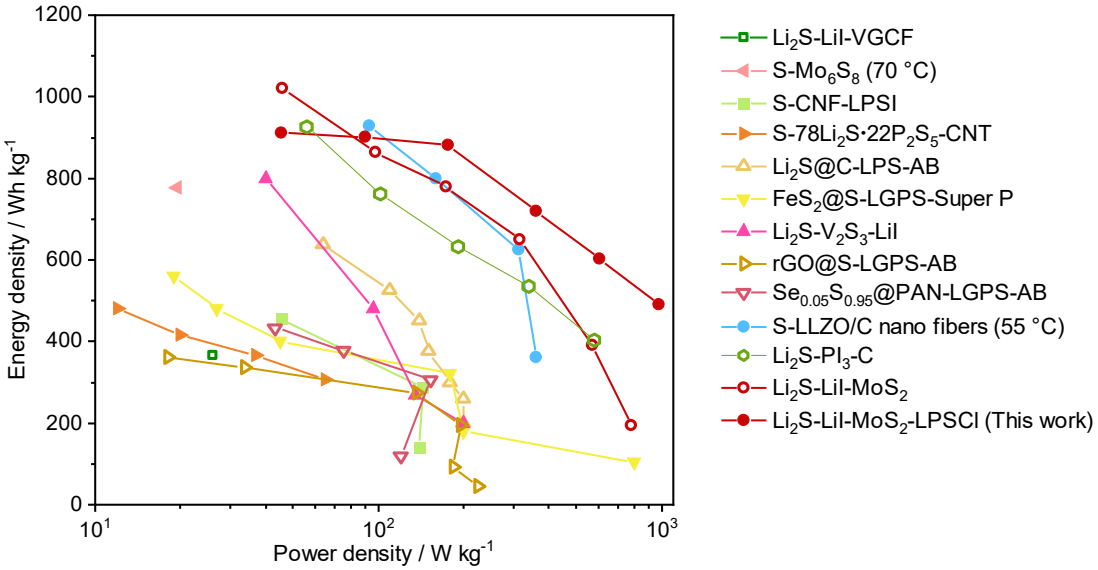

Figure 4.8 The comparison of energy density and power density among different cathode composites for all-solid-state lithium-sulfur batteries and lithium metal as anode. The composite cathodes reported previously include Li_2S-LiI-vapor grown carbon fiber[38], S-Mo_6S_8[46], S-0.67Li_3PS_4•0.33LiI-carbon nano fiber[16], S-78Li_2S·22P_2S_5-carbon nanotubes[47], Li_2S@C-$Li_7P_3S_{11}$-acetylene black[48], FeS_2@S-$Li_{10}GeP_2S_{12}$-Super P[49], Li_2S-V_2S_3-LiI[50], reduced graphene oxide@S-$Li_{10}GeP_2S_{12}$-acetylene black[13], $Se_{0.05}S_{0.95}$-$Li_{10}GeP_2S_{12}$-carbon nanotubes[51], S-lithium lanthanum oxide/caron nanofibers[52], Li_2S-PI_3-CNovel[39], Li_2S-LiI-MoS_2[40], and 85(Li_2S-LiI-MoS_2)-15Li_6PS_5Cl (wt%) in this work.

Table 4.1 The volume ratio of Li_2S-LiI-MoS_2 to Li_6PS_5Cl in composite cathode (100-*x*)Li_2S-LiI-MoS_2-*x*Li_6PS_5Cl (*x*=0, 5, 10, 15, 20, 30, 40, 50 (wt%)) calculated based on their mass ratio and densities.

Sample name	Active material (Li_2S-LiI-MoS_2)	Solid-state electrolyte (Li_6PS_5Cl)
0LPSCl	100	0
5LPSCl	92.05	7.95
10LPSCl	84.58	15.42
15LPSCl	77.31	22.69
20LPSCl	70.92	29.08
30LPSCl	58.72	41.28
40LPSCl	47.76	52.24
50LPSCl	37.87	62.13

Table 4.2 The volume proportion of Li_2S-LiI-MoS_2, Li_6PS_5Cl and void in composite cathode (100-*x*)Li_2S-LiI-MoS_2-*x*Li_6PS_5Cl (*x*=0, 5, 10, 15, 20, 30, 40, 50 (wt%)) calculated based on X-ray CT images.

Sample name	Active material (Li_2S-LiI-MoS_2)	Solid-state electrolyte (Li_6PS_5Cl)	Void
0LPSCl	96.60	0	3.40
5LPSCl	88.86	7.58	3.56
10LPSCl	78.98	14.56	6.46
15LPSCl	73.39	20.64	5.97
20LPSCl	66.95	27.46	5.59
30LPSCl	58.62	37.08	4.30
40LPSCl	44.48	48.82	6.70
50LPSCl	35.74	58.64	5.62

Table 4.3 The tortuosity factor of Li_2S-LiI-MoS_2 and Li_6PS_5Cl in composite cathode (100-*x*)Li_2S-LiI-MoS_2-*x*Li_6PS_5Cl (*x*=0, 5, 10, 15, 20, 30, 40, 50 (wt%)) calculated based on X-ray CT images.

Sample name	Tortuosity factor of Li_2S-LiI-MoS_2	Tortuosity factor of Li_6PS_5Cl
0LPSCl	1.11	-
5LPSCl	1.23	92.39
10LPSCl	1.44	22.44
15LPSCl	1.58	5.40
20LPSCl	1.84	3.65
30LPSCl	2.34	2.83
40LPSCl	3.51	2.15
50LPSCl	5.92	1.63

Table 4.4 The contact area between Li_2S-LiI-MoS_2 and Li_6PS_5Cl of composite cathode (100-*x*)Li_2S-LiI-MoS_2-*x*Li_6PS_5Cl (*x*=0, 5, 10, 15, 20, 30, 40, 50 (wt%)) calculated based on X-ray CT images.

Sample name	Contact area (μm^{-2})
0LPSCl	0
5LPSCl	2477.58
10LPSCl	3467.63
15LPSCl	3786.00
20LPSCl	4064.91
30LPSCl	4539.64
40LPSCl	4485.26
50LPSCl	4140.45

References

(1) Zhou, H. New energy storage devices for post lithium-ion batteries. *Energy Environ. Sci.* **2013**, *6* (8), 2256-2256.

(2) Harper, G.; Sommerville, R.; Kendrick, E.; Driscoll, L.; Slater, P.; Stolkin, R.; Walton, A.; Christensen, P.; Heidrich, O.; Lambert, S. Recycling lithium-ion batteries from electric vehicles. *Nature* **2019**, *575* (7781), 75-86.

(3) Manthiram, A.; Chung, S. H.; Zu, C. Lithium–sulfur batteries: progress and prospects. *Adv. Mater.* **2015**, *27* (12), 1980-2006.

(4) Seh, Z. W.; Sun, Y.; Zhang, Q.; Cui, Y. Designing high-energy lithium–sulfur batteries. *Chem. Soc. Rev.* **2016**, *45* (20), 5605-5634.

(5) Sadd, M.; De Angelis, S.; Colding-Jørgensen, S.; Blanchard, D.; Johnsen, R. E.; Sanna, S.; Borisova, E.; Matic, A.; Bowen, J. R. Visualization of Dissolution-Precipitation Processes in Lithium–Sulfur Batteries. *Adv. Energy Mater.* **2022**, *12* (10), 2103126.

(6) Ding, B.; Wang, J.; Fan, Z.; Chen, S.; Lin, Q.; Lu, X.; Dou, H.; Nanjundan, A. K.; Yushin, G.; Zhang, X. Solid-state lithium–sulfur batteries: Advances, challenges and perspectives. *Mater. Today* **2020**, *40*, 114-131.

(7) Lei, D.; Shi, K.; Ye, H.; Wan, Z.; Wang, Y.; Shen, L.; Li, B.; Yang, Q. H.; Kang, F.; He, Y. B. Progress and perspective of solid-state lithium–sulfur batteries. *Adv. Funct. Mater.* **2018**, *28* (38), 1707570.

(8) Bandyopadhyay, S.; Nandan, B. A review on design of cathode, anode and solid electrolyte for true all-solid-state lithium sulfur batteries. *Mater. Today Energy* **2022**, 101201.

(9) Shin, M.; Gewirth, A. A. Incorporating solvate and solid electrolytes for all-solid-state Li_2S batteries with high capacity and long cycle life. *Adv. Energy Mater.* **2019**, *9* (26), 1900938.

(10) Yue, J.; Yan, M.; Yin, Y. X.; Guo, Y. G. Progress of the interface design in all-solid-state Li–S batteries. *Adv. Funct. Mater.* **2018**, *28* (38), 1707533.

(11) Umeshbabu, E.; Zheng, B.; Yang, Y. Recent progress in all-solid-state Lithium− Sulfur batteries using high Li-ion conductive solid electrolytes. *Electrochem. Energy Rev.* **2019**, *2*, 199-230.

(12) Lee, S.-K.; Lee, Y. J.; Sun, Y.-K. Nanostructured lithium sulfide materials for lithium-sulfur batteries. *J. Power Sources* **2016**, *323*, 174-188.

(13) Yao, X.; Huang, N.; Han, F.; Zhang, Q.; Wan, H.; Mwizerwa, J. P.; Wang, C.; Xu, X. High-performance all-solid-state lithium–sulfur batteries enabled by amorphous sulfur-coated reduced graphene oxide cathodes. *Adv. Energy Mater.* **2017**, *7* (17), 1602923.

(14) Jiang, M.; Liu, G.; Zhang, Q.; Zhou, D.; Yao, X. Ultrasmall Li_2S-carbon nanotube nanocomposites for high-rate all-solid-state lithium–sulfur batteries. *ACS Appl. Mater. Interfaces* **2021**, *13* (16), 18666-18672.

(15) Zhang, Q.; Huang, N.; Huang, Z.; Cai, L.; Wu, J.; Yao, X. CNTs@ S composite as cathode for all-solid-state lithium-sulfur batteries with ultralong cycle life. *J. Energy Chem.* **2020**, *40*, 151-155.

(16) Phuc, N. H. H.; Takaki, M.; Muto, H.; Reiko, M.; Kazuhiro, H.; Matsuda, A. Sulfur–carbon nano fiber composite solid electrolyte for all-solid-state Li–S batteries. *ACS Appl. Energy Mater.* **2020**, *3* (2), 1569-1573.

(17) Eom, M.; Son, S.; Park, C.; Noh, S.; Nichols, W. T.; Shin, D. High performance all-solid-state lithium-sulfur battery using a Li_2S-VGCF nanocomposite. *Electrochim. Acta* **2017**, *230*, 279-284.

(18) Zhu, J.; Cheng, H.; Zhu, P.; Li, Y.; Gao, Q.; Zhang, X. Electrospun nanofibers enabled advanced lithium–sulfur batteries. *Acc. Mater. Res.* **2022**, *3* (2), 149-160.

(19) Yang, H.; Wu, N. Ionic conductivity and ion transport mechanisms of solid-state lithium-ion battery electrolytes: A review. *Energy Sci. Eng.* **2022**, *10* (5), 1643-1671.

(20) Wang, Y.; Wu, Y.; Wang, Z.; Chen, L.; Li, H.; Wu, F. Doping strategy and mechanism for oxide and sulfide solid electrolytes with high ionic conductivity. *J. Mater. Chem. A* **2022**, *10* (9), 4517-4532.

(21) Ye, H.; Li, M.; Liu, T.; Li, Y.; Lu, J. Activating Li_2S as the lithium-containing cathode in lithium–sulfur batteries. *ACS Energy Lett.* **2020**, *5* (7), 2234-2245.

(22) Su, D.; Zhou, D.; Wang, C.; Wang, G. Toward high performance lithium–sulfur batteries based on Li_2S cathodes and beyond: status, challenges, and perspectives. *Adv. Funct. Mater.* **2018**, *28* (38), 1800154.

(23) Hänsel, C.; Kundu, D. The stack pressure dilemma in sulfide electrolyte based Li metal solid-state batteries: a case study with Li_6PS_5Cl solid electrolyte. *Adv. Mater. Interfaces* **2021**, *8* (10), 2100206.

(24) Chang, D.; Oh, K.; Kim, S. J.; Kang, K. Super-ionic conduction in solid-state $Li_7P_3S_{11}$-type sulfide electrolytes. *Chem. Mater.* **2018**, *30* (24), 8764-8770.

(25) Kamaya, N.; Homma, K.; Yamakawa, Y.; Hirayama, M.; Kanno, R.; Yonemura, M.; Kamiyama, T.; Kato, Y.; Hama, S.; Kawamoto, K. A lithium superionic conductor. *Nat. Mater.* **2011**, *10* (9), 682-686.

(26) Kato, Y.; Hori, S.; Saito, T.; Suzuki, K.; Hirayama, M.; Mitsui, A.; Yonemura, M.; Iba, H.; Kanno, R. High-power all-solid-state batteries using sulfide superionic conductors. *Nat. Energy* **2016**, *1* (4), 1-7.

(27) Li, Y.; Song, S.; Kim, H.; Nomoto, K.; Kim, H.; Sun, X.; Hori, S.; Suzuki, K.; Matsui, N.; Hirayama, M. A lithium superionic conductor for millimeter-thick battery electrode. *Science* **2023**, *381* (6653), 50-53.

(28) Choi, S.; Yoon, I.; Nichols, W. T.; Shin, D. Carbon-coated Li_2S cathode for improving the electrochemical properties of an all-solid-state lithium-sulfur battery using Li2S-P2S5 solid electrolyte. *Ceram. Int.* **2018**, *44* (7), 7450-7453.

(29) Chen, Y.-X.; Kaghazchi, P. Metalization of Li_2S particle surfaces in Li–S batteries. *Nanoscale* **2014**, *6* (22), 13391-13395.

(30) Cai, K.; Song, M.-K.; Cairns, E. J.; Zhang, Y. Nanostructured Li_2S–C composites as cathode material for high-energy lithium/sulfur batteries. *Nano Lett.* **2012**, *12* (12), 6474-6479.

(31) Wu, F.; Kim, H.; Magasinski, A.; Lee, J. T.; Lin, H. T.; Yushin, G. Harnessing steric separation of freshly nucleated Li_2S nanoparticles for bottom-up assembly of high-performance cathodes for lithium-sulfur and lithium-ion batteries. *Adv. Energy Mater.* **2014**, *4* (11), 1400196.

(32) Han, F.; Yue, J.; Fan, X.; Gao, T.; Luo, C.; Ma, Z.; Suo, L.; Wang, C. High-Performance All-Solid-State Lithium-Sulfur Battery Enabled by a Mixed-Conductive Li_2S Nanocomposite. *Nano Lett.* **2016**, *16* (7), 4521-4527.

(33) Lorger, S.; Usiskin, R. E.; Maier, J. Transport and charge carrier chemistry in lithium sulfide. *Adv. Funct. Mater.* **2019**, *29* (6), 1807688.

(34) Norris, D. J.; Efros, A. L.; Erwin, S. C. Doped nanocrystals. *Science* **2008**, *319* (5871), 1776-1779.

(35) Luo, G.; Zhao, J.; Wang, B. First-principles study of transition metal doped Li2S as cathode materials in lithium batteries. *J. Renew. Sustain. Energy* **2012**, *4* (6).

(36) Takeuchi, T.; Kageyama, H.; Taguchi, N.; Nakanishi, K.; Kawaguchi, T.; Ohara, K.; Fukuda, K.; Sakuda, A.; Ohta, T.; Fukunaga, T. Structure analyses of Fe-substituted Li_2S-based positive electrode materials for Li-S batteries. *Solid State Ionics* **2018**, *320*, 387-391.

(37) Fujita, Y.; Hakari, T.; Sakuda, A.; Deguchi, M.; Kawasaki, Y.; Tsukasaki, H.; Mori, S.; Tatsumisago, M.; Hayashi, A. Li_2S–LiI Solid Solutions with Ionic Conductive Domains for Enhanced All-Solid-State Li/S Batteries. *ACS Appl. Energy Mater.* **2022**, *5* (8), 9429-9436.

(38) Hakari, T.; Hayashi, A.; Tatsumisago, M. Li_2S-Based Solid Solutions as Positive Electrodes with Full Utilization and Superlong Cycle Life in All-Solid-State Li/S Batteries. *Adv. Sustain. Syst.* **2017**, *1* (6), 1700017.

(39) Wenli, P.; Yamamoto, K.; Machida, N.; Matsunaga, T.; Kumar, M.; Thakur, N.; Watanabe, T.; Sakuda, A.; Hayashi, A.; Tatsumisago, M. Improving electrochemical performance of Li_2S cathode based on point defect control with cation/anion dual doping. *J. Mater. Chem. A* **2023**, *11*, 24637-24643.

(40) Wenli, P.; Yamamoto, K.; Matsunaga, T.; Watanabe, T.; Kumar, M.; Thakur, N.; Uchiyama, T.; Uesugi, M.; Takeuchi, A.; Sakuda, A. An Electron/Ion Dual Conductive Integrated Cathode Using Cationic/Anionic Redox for High-Energy-Density All-Solid-State Lithium-Sulfur Batteries. *Batteries & Supercaps*, e202300427.

(41) Takeuchi, A.; Uesugi, K.; Uesugi, M.; Toda, H.; Hirayama, K.; Shimizu, K.; Matsuo, K.; Nakamura, T. High-energy x-ray nanotomography introducing an apodization Fresnel zone plate objective lens. *Rev. Sci. Instrum.* **2021**, *92* (2), 023701.

(42) Asano, T.; Yubuchi, S.; Sakuda, A.; Hayashi, A.; Tatsumisago, M. Electronic and ionic conductivities of $LiNi_{1/3}Mn_{1/3}Co_{1/3}O_2$-$Li_3PS_4$ positive composite electrodes for all-solid-state lithium batteries. *J. Electrochem. Soc.* **2017**, *164* (14), A3960.

(43) Santhosha, A.; Medenbach, L.; Buchheim, J. R.; Adelhelm, P. The indium–lithium electrode in solid-state lithium-ion batteries: phase formation, redox potentials, and interface stability. *Batter. Supercaps* **2019**, *2* (6), 524-529.

(44) Cooper, S. J.; Bertei, A.; Shearing, P. R.; Kilner, J. A.; Brandon, N. P. TauFactor: An open-source application for calculating tortuosity factors from tomographic data. *SoftwareX* **2016**, *5*, 203-210.

(45) Ohno, S.; Zeier, W. G. Toward practical solid-state lithium–sulfur batteries: challenges and perspectives. *Acc. Mater. Res.* **2021**, *2* (10), 869-880.

(46) Li, M.; Liu, T.; Shi, Z.; Xue, W.; Hu, Y. s.; Li, H.; Huang, X.; Li, J.; Suo, L.; Chen, L. Dense All-Electrochem-Active Electrodes for All-Solid-State Lithium Batteries. *Adv. Mater.* **2021**, *33* (26), 2008723.

(47) Zhang, Y.; Liu, T.; Zhang, Q.; Zhang, X.; Wang, S.; Wang, X.; Li, L.; Fan, L.-Z.; Nan, C.-W.; Shen, Y. High-performance all-solid-state lithium–sulfur batteries with sulfur/carbon nano-hybrids in a composite cathode. *J. Mater. Chem. A* **2018**, *6* (46), 23345-23356.

(48) Yan, H.; Wang, H.; Wang, D.; Li, X.; Gong, Z.; Yang, Y. In situ generated Li_2S–C nanocomposite for high-capacity and long-life all-solid-state lithium sulfur batteries with ultrahigh areal mass loading. *Nano Lett.* **2019**, *19* (5), 3280-3287.

(49) Mwizerwa, J. P.; Zhang, Q.; Han, F.; Wan, H.; Cai, L.; Wang, C.; Yao, X. Sulfur-embedded FeS_2 as a high-performance cathode for room temperature all-solid-state lithium–sulfur batteries. *ACS Appl. Mater. Interfaces* **2020**, *12* (16), 18519-18525.

(50) Shigedomi, T.; Fujita, Y.; Kishi, T.; Motohashi, K.; Tsukasaki, H.; Nakajima, H.; Mori, S.; Tatsumisago, M.; Sakuda, A.; Hayashi, A. Li_2S–V_2S_3–LiI Bifunctional Material as the Positive Electrode in the All-Solid-State Li/S Battery. *Chem. Mater.* **2022**, *34* (21), 9745-9752.

(51) Zhang, Y.; Sun, Y.; Peng, L.; Yang, J.; Jia, H.; Zhang, Z.; Shan, B.; Xie, J. Se as eutectic accelerator in sulfurized polyacrylonitrile for high performance all-solid-state lithium-sulfur battery. *Energy Storage Mater.* **2019**, *21*, 287-296.

(52) Wang, L.; Yin, X.; Li, B.; Zheng, G. W. Mixed Ionically/Electronically Conductive Double-Phase Interface Enhanced Solid-State Charge Transfer for a High-Performance All-Solid-State Li–S Battery. *Nano Lett.* **2021**, *22* (1), 433-440.

Chapter 5 Clarifying the Degradation Mechanism of Sulfide Solid Electrolyte under Traces of Moisture by Using In-situ X-ray Absorption Spectroscopy

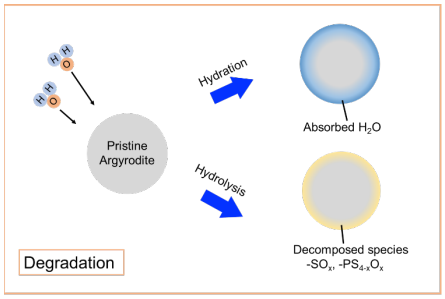

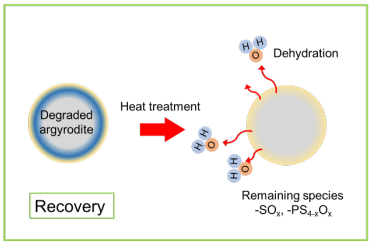

Sulfide-based solid electrolytes (SEs) have gained much attention for application in all-solid-state batteries (ASSBs), due to their remarkable ionic conductivities and suitable mechanical properties. However, these sulfide SEs usually suffer from poor air stability and react with a trace of water, thus generating toxic H_2S gas and reducing the lithium-ion conductivity. Besides, it has also been found that the ionic conductivity of the sulfide SE exposed to moisture can be partially recovered by a suitable heat-treated in vacuum. In this study, multiple analyses using X-ray diffraction, high-frequency electrochemical impedance spectroscopy and in-situ X-ray absorption spectroscopy were performed on argyrodite-type sulfide solid electrolyte to clarify the degradation mechanism during exposure to a trace of moisture, comparable to a dry room, as well as the recovery mechanism of a deteriorated SE by vacuum heat treatment. And the real-time degradation mechanism of sulfides and the hydration/dehydration on the grain surface of the electrolyte were correlated with the lithium-ion conductivity.

5.1 Introduction

The rapid developments of electric vehicles and large-scale stationary energy storages require high energy density and good safety for advanced secondary batteries[1, 2]. All-solid-state batteries (ASSBs) have drawn enormous attention because solid-state electrolytes (SEs) enable lithium metal as anode and have non-flammable nature compared to organic liquid electrolytes[3]. Functioning as both the ionic conductor and the separator in ASSBs, SEs are required to possess high ionic conductivity and good mechanical properties[4]. Among them, sulfide-based SEs are attractive due to their high ionic conductivities of 10^{-3} to 10^{-2} S cm^{-1} that are comparable to liquid organic electrolytes, enhanced safety and facile pelletization by cold press at room temperature[5, 6]. Those merits make sulfide SEs one of the most promising SEs for ASSBs.

However, the practical application of sulfide SEs is hindered by their poor air stability[7, 8]. When sulfide SEs are exposed to ambient air, highly toxic H_2S gas is generated, with the decrease in ionic conductivity. Such the instability in ambient air limits the material preparation and battery fabrication using sulfide-based SEs in the globe box with inert gas atmosphere, which consequently increases the production cost and hampers large-scale fabrication. Therefore, it is important to understand the degradation mechanism of sulfide SEs in air for development of air-stable sulfide SEs. Much effort has been put into characterizing the degradation of SE through H_2S generation[9], morphology[10], microscopic structure and components[9, 11], electrochemical performance in humid ambient air[12]. Tatsumisago's group[13, 14] have investigated the degradation process of sulfide SEs in ambient air with a relative humidity of 40–80% at room temperature which corresponds to water concentration of tens of thousands of ppm in air. It is found that the moisture durability of sulfide SEs varies depending on their composition and chemical bonding state[7]. Tufail et al.[12] correlated the amount of H_2S gas formation under the humid air with relative humidity of 41–43% with the local structure of glass-ceramic $Li_7P_3S_{11}$ and Zr- and O-doped $Li_{6.95}Zr_{0.05}P_{2.9}S_{10.8}O_{0.1}I_{0.4}$ electrolytes. These characterizations reveal that the air-instable sulfide SEs, such as Li_3PS_4, Li_6PS_5Cl and $Li_{10}GeP_2S_{12}$ have dramatic and irreversible decrease in ionic conductivities after exposure to humid ambient air, since they undergo violent hydrolysis reaction and generate undesired products[15]. As for air-stable

sulfide SEs, such as oxygen or softer-cation substitutional SEs, their ionic conductivities show reversible decrease due to hydration and could recover after heat treatment[16].

Though the degradation mechanisms have been clearly studied for sulfide-based SEs exposure to ambient air, however, it should be noted that the large-scale fabrication of LIBs usually occurs in a low-humidity environment called "dry room" [17], with a dew point between −20 °C and −50 °C [18], corresponding to the water concentration of tens to hundreds of ppm. Therefore, it is more important to investigate the degradation of electrolytes in a dry room environment, which is more in line with the actual production condition. Chen et al.[11] evaluated the dry room compatibility with dew point of -45 °C for Li_6PS_5Cl. Even exposure for 24 hours, no obvious structural change was observed by XRD, Raman, ^{31}P NMR and ^{7}Li NMR. Despite a slight drop of ionic conductivity from 2.92×10^{-3} S cm^{-1} to 2.33×10^{-3} S cm^{-1} after 24-hour exposure, the ionic conductivity could recover to 2.77×10^{-3} S cm^{-1} after heat treatment at 550 °C for 8h. Later, Sano et. al[19] and Morino et. al[20] found that the grain surface of argyrodite-type sulfide-based SE is probably degenerated by moisture with the dew point of -20 °C and its ionic conductivity can partially recover by heat treatment at 170 °C under vacuum. Recently, Morino et. al[21] conducted the exposure experiments with the air of -20 °C dew point for 1 hour and for 24 hours, and reported the argyrodite sulfide-based SE has two deterioration mechanism: irreversible chemical decomposition with phosphate, disulfide, and carbonate as products, and reversible absorption of water at surface. These results magnify the interests in the fundamental investigation for sulfide SEs under low dew point. However, unlike the exhaustive investigations with exposure to the ambient air [12, 22, 23], it is unclear that how the hydration and hydrolysis deteriorate the air-instable sulfide SEs during consecutive exposure time with a trace of water. And there is a lack of characterization that can investigate the real-time degradation mechanism under the exposure condition.

In this study, the degradation behavior and mechanism of the common sulfide SE, argyrodite $Li_{7-x}PS_{6-x}Cl_x$ ($x \approx 1$) after exposure to dew point of -20 °C were investigated and understood by XRD, high-frequency impedance and in-situ X-ray absorption spectroscopy (XAS). The degradation mechanism during moisture exposure and the recovery mechanism under different heat treatment conditions were understood by in-situ XAS. The

change in ionic conductivities was correlated with the real-time electronic structure during exposure to traces of moisture and being heat-treated in vacuum.

5.2 Experimental Section

5.2.1 The Exposure to the Air of -20 °C Dew Point (d.p.)

The argyrodite-type sulfide SE $Li_{7-x}PS_{6-x}Cl_x$ ($x \approx 1$) provided by the Lithium Ion Battery Technology and Evaluation Center (LIBTEC) was used and investigated in this study. The preparation and moisture exposure conditions are as follows:

In a glove box (MIWA MFG Co., Ltd., DB0-1KP-U type) with Ar atmosphere, about 125 mg of sulfide solid electrolyte was weighed, placed in a sample bottle with 9 ml, and sealed in a sample holder. The sample holder was connected to a water vapor exposure set, which was connected to a compressed air cylinder (Diving System Service Co., Ltd.). The argyrodite powder was exposed to air with the dew point of -20 ± 1 °C, which monitored by a dew point meter (VAISALA, Model DMT143L). The flow rate was 0.1 L min^{-1}, with a mixture of dry air with flow rate of 0.088 L min^{-1} and the humidified air of 0.012 L min^{-1}, which were controlled by the mass flow controllers (KOFLOC, type 8500MC-0-1-1). After the moisture exposure test, high-purity Ar gas (Kyoto Teic acid Co., Ltd.) was flow into the sample holder at 0.100 mL min^{-1} for 30 min, then the samples were collected in the glove box.

5.2.2 The Heat Treatment after Exposure to the Air of -20 °C Dew Point (d.p.)

Samples after the water vapor exposure test were laid on an alumina boat in a glove box in an Ar atmosphere, and then were processed using a glass tube oven (BÜCHI, Model B-585TO) connected to a mechanical vacuum pump (ULVAC Corporation, GLD-137CC). The heat treatment was carried out at low pressure about 0.67 Pa. The temperature increased at 5 °C min^{-1}, kept at the target temperature for 2 h and then allowed to cool naturally. After heat treatment, the powder was collected in the glove box with an Ar atmosphere.

5.2.3 Phase and Conductivity Measurement

The samples at pristine state, after exposure to moisture and with different heat treatment conditions were measured by using powder X-ray diffractometer RINT-2000 (Rigaku) with

a Cu Kα ray source (= 1.54056 × 10^{-10} m), tube voltage of 40 kV, tube current of 40 mA, diffraction angle 2θ = 10~60 °, scan speed as 2 ° min^{-1}, and the scan interval of 0.01 °.

As for ionic conductivity measurement, about 120 mg of sulfide solid electrolyte was pelletized under 360 MPa for 2 min using PEEK (polyether ether ketone) cylinder with a inner diameter of 10 mm. High-frequency impedance measurements were performed at 25 °C with frequency range from 100 MHz to 20 Hz with the amplitude of 10 mV. Resistance values were calculated from the obtained Nyquist plots by fitting using ZView. The ionic conductivity was calculated based on $\sigma = \rho^{-1} = \frac{L}{RA}$. L is the thickness of the SE pellet, which is usually about 1.06 ± 0.02 mm. R is the total resistance of the pellet, obtained by the sum of R_{bulk} and $R_{interficial}$. A is the cross-section area of the pellet.

5.2.4 In-situ XAS Measurement

The in-situ soft X-ray XAS of S *K*-edge and P *K*-edge were measured at the BL27SU beamline at SPring-8, Japan, and performed by developing the in-situ cell. The moisture exposure measurement was performed with the dew point value to -20 ± 1 °C. About 120 mg of sulfide solid electrolyte was pressed under 360 MPa using a 10 mm diameter die for 2 min. All pellets were sealed in Al laminate pack in the glove box in order to keep the sample from air. The polyimide with thickness of 12 μm was used for X-ray transmission and the in-situ cell was sealed by O-ring to maintain the pressure conditions inside and outside the in-situ cell.

5.3 Results and Discussion

5.3.1 Degradation behavior and mechanism

To investigate the degradation behavior of argyrodite-type $Li_{7-x}PS_{6-x}Cl_x$ with a trace of water, the pristine $Li_{7-x}PS_{6-x}Cl_x$ powder was exposure to the moisture with the dew point of -20 °C for different time from 20 min to 12 h. The morphology and element distribution of pristine $Li_{7-x}PS_{6-x}Cl_x$ was measured by SEM-EDS mapping. As Figure 5.1 shows, the primary particle size varies under 5 μm and the elements distribute uniformly. The structural evolution of $Li_{7-x}PS_{6-x}Cl_x$ SE with moisture exposure was understood by XRD and Rietveld refinement (Figure 5.2, Figure 5.3 and Table 5.1). The pristine SE is argyrodite structured (space group: $F\bar{4}3m$, lattice parameter: 9.8313 Å)[24] with a trace of LiCl (space group: $Fm\bar{3}m$)[25] as observed from XRD pattern. S is at 4*a*, 4*d* and 16*e*

Wyckoff sites [24]. The S at 16e site forms PS_4 tetrahedra with P at 4b site, while the S/Cl anion disorder exists at 4*a* and 4*d* sites, which is in agreement with other papers [26, 27]. As for the exposed samples, no additional peak besides argyrodite-type can be clearly observed within 4 h exposure, indicating negligible structure evolution occurs in bulk SE[19]. However, from the results of Rietveld refinement, S occupancy at 4*a*, 4*d* and 16*e* sites decrease with 1h-exposure time. Compared with S at 16e site with slight decrease in occupancy, the occupancy of the S atom at other two sites, especially at 4*a* site, exhibits a notable decrease with exposure time, indicating the S at 4a site that without bonding with P is more reactive with moisture and PS_4^{3-} has higher air stability[9]. With longer exposure time from 4 to 12 h, the peaks of degraded phase were detected by XRD, with LiCl and $P_4O_6S_3$ matched by Le Bail fitting method, suggesting LiCl and P-S-O species as hydrolysis products[28-30]. However, since their weak and few diffraction peaks, it is difficult to confirm quantitative fraction by Rietveld refinement. The structural information of argyrodite obtained from Rietveld refinement shows the consecutive decrease in the S occupancy at 4*a* and 16*e* sites with the increasing exposure time. While the S at 16*e* site shows a moderate decrease in occupancy, the occupancy of S at 4*a* site decrease significantly, indicating the consecutive reaction of S at 4a site with moisture.

To examine the impact of moisture on Li-conduction, high-frequency impedance (100 MHz to 20 Hz) was conducted on the $Li_{7-x}PS_{6-x}Cl_x$ pellets with different exposure time and fitted by Z-view. The Nyquist plots and the fitting parameters are shown in Figure 5.4 and Table 5.2, respectively. The corresponding ionic conductivities were shown in Figure 5.2 (b). Within the first 4 h exposure, the ionic conductivities decline significantly from 1.50×10^{-3} S cm^{-1} to 3.85×10^{-5} S cm^{-1}, and show a modest decrease to 5.23×10^{-6} S cm^{-1}. To understand the origin of decreased ionic conductivities, the Nyquist plots were well fitted with the equivalent circuit shown in Figure 5.5. As Figure 5.1 and Table 5.2 show, R_{bulk} keeps small and relatively stable value, while $R_{interficial}$ increases with exposure time. These results indicate the surface of SE instead of inner bulk suffers from moisture attack, which is consistent with other papers [8, 19, 20]. In addition, the values of capacitances C are of the order of 10^{-10} F, corresponding to a grain boundary response[31-33], suggesting the increased half-arc is due to the surface degradation and the degraded surface inhibit the lithium-ion conduction. However, since lack of indexed degraded phase by XRD, a

technique which is sensitive to local structure and electronic structure is needed for understanding the degradation mechanism.

In-situ XAS S *K*-edge and P *K*-edge were conducted for $Li_{7-x}PS_{6-x}Cl_x$ with the air of -20 °C after different exposed time. As Figure 5.6 shows, the pristine $Li_{7-x}PS_{6-x}Cl_x$ shows similar S *K*-edge and P *K*-edge spectra to those of Li_3PS_4, which is probably because their similar local structural of S and P as PS_4 tetrahedra. As for pristine $Li_{7-x}PS_{6-x}Cl_x$, its S K-edge XANES spectrum exhibits three characteristic peaks at 2470.4, 2472.2 and 2475.4 eV, which are similar to the spectrum of Li_3PS_4. Within exposure time of 60 min, while the peak at 2470.4 eV keeps stable, the other two peaks, especially the peak at 2475.6 eV, shift to higher value, which is accordance with the peak at 2476.4 eV of a series Li_3PS4-Li_3PO_4 mixtures with different ratio, indicating the fraction of S in PS_4 tetrahedra is decreased with the increased fraction of O from H_2O. Meanwhile, a peak at 2481.2 eV appears, which can match the peak from $Na_2S_2SO_4$ and K_2SO_4, suggesting the formation of species[34]. With extended exposure to 480 min, the peak at 2476.4 eV slightly shift to higher value and the intensity of peak at 2481.2 eV also increase slightly, which indicates the consecutive but slowing down formation of SO_x species. As for P *K*-edge XANES, a peak at 2151.7 eV appears and can match the peak of Li_3PO_4. The intensity of the peak at 2151.7 eV increases gradually with exposure to moisture, which is consistent with the tendency of stronger peak at 2151.7 from Li_3PS_4-Li_3PO_4 mixture with higher Li_3PO_4 ratio. The results from S *K*-edge and P *K*-edge XANES are accordance with the decreasing S occupancy obtained from XRD refinement, showing O from moisture gradually replaces S in PS_4 tetrahedra and forms $PS_{4-x}O_4$ and SO_x species[35].

5.3.3 The Recovery Mechanism of Sulfide Solid Electrolytes After Heat Treatment under Vacuum

To test if the degradation of SE with a trace of water is reversible or not, $Li_{7-x}PS_{6-x}Cl_x$ was heated at different temperatures from 50 to 170 °C under vacuum for 2h after 1h-exposure to the moisture with -20 °C dew point. High-frequency impedance was measured for $Li_{7-x}PS_{6-x}Cl_x$ pellets after heat treated under vacuum. Nyquist plots are shown in Figure 5.7 and ionic conductivities were calculated. As shown in Figure 5.8, with the increasing temperature, the ionic conductivities are improved gradually. With heat treatment temperature of 170 °C, the ionic conductivity recovers to 1.23×10^{-3} S cm^{-1}, corresponding

to 82.5% of pristine $Li_{7-x}PS_{6-x}Cl_x$, demonstrating the degradation of partially reversible. The fitting parameters in Table 5.3 demonstrates the impedances of inner bulk are stable while $R_{interficial}$ with grain boundary response decreases with the enhanced temperature for heat treatment, indicating a partial recovery of degraded surface by heat treatment[11, 21]. To understand the origin of the partial reversibility, XRD was conducted accordingly to investigate the structure evolution. As Figure 5.8 (b) shows, no obvious change can be observed in diffraction peaks because of little degraded phase in the bulk of $Li_{7-x}PS_{6-x}Cl_x$ with short exposure to a trace of water. However, the structure information from Rietveld refinement in Figure 5.9 and Table S4 shows the increased occupancy of S at 16*e* site, and the increase tendency is consistent with the enhanced temperatures and recovered ionic conductivities. Since XRD is not sensitive to surface, the change in the local structure of S atoms with enhanced heat treatment need to be further investigated.

In-situ XAS S *K*-edge and P *K*-edge were conducted for the exposed $Li_{7-x}PS_{6-x}Cl_x$ sample with heat treatment at different temperature. As shown in Figure 5.10, the peak at 2475.4 eV shifts to 2476.4 eV after 1 h-exposure to moisture, indicating the S partially replaced by O from H_2O. With heat treatment, the peak at 2476.4 eV gradually shifts to lower value, indicating the decoupling O from $PS_{4-x}O_4$ tetrahedra after heat treatment. After heat treatment at 170 °C, the peak shift to 2475.8 eV, showing a partial recovery compared with the pristine peak at 2475.6 eV. This result suggests the absorbed H_2O during exposure to moisture can be removed by heat treatment. In addition, a peak at 2481.2 eV can be observed after heat treatment, suggesting the residue of SO_x species and the incomplete recovery. As for P *K*-edge XANES, the broadening peak at 2147.8 eV might due to the enhanced temperature. The peak at 2151.7 eV of P *K*-edge XAS ascribed to $PS_{4-x}O_4$ shows slightly decrease in intensity with the enhanced temperature of heat treatment, suggesting the reduced fraction of O in $PS_{4-x}O_4$ tetrahedra. The incomplete reversibility of local structure results in the partial recovery of Li-conduction. The in-situ XAS spectra provide a lucid explanation for the changes in the local structure of PS_4, which is accordance with the results from XRD refinement.

5.3.4 The Model of Degradation and Recovery

Combined the results from XRD patterns, Rietveld refinement, high-frequency impedance and in-situ XAS for moisture exposure and heat treatment under vacuum, the

model of argyrodite $Li_{7-x}PS_{6-x}Cl_x$ of degradation and recovery mechanism are shown in Figure 5.10. With exposure to a trace of water, the surface of the $Li_{7-x}PS_{6-x}Cl_x$ particles suffer from H_2O attack, while the inner bulk keep stable. For the degraded surface, there are two degradation routes: one is hydration process, which is due to the absorbed moisture on the surface of $Li_{7-x}PS_{6-x}Cl_x$. It is reversible because the absorbed moisture can be removed with heat treatment. However, the other degradation is hydrolysis. The degraded surface gets irreversible structural evolution due to the formation of $PS_{4-x}O_4$ and SO_x species. Even after heat treatment, these degraded phases still remain at interface and inhibit the Li-conduction.

Conclusion

With exposure to the moisture of -20 °C, the degradation of an argyrodite-type $Li_{7-x}PS_{6-x}Cl_x$ was studied to simulate the sulfide SE under dry room environment during practical large-scale battery fabrication. Revealed by the combination of XRD, high-frequency impedance and in-situ XAS, the degradation behavior and mechanism were investigated. The degradation occurs on the surface of SE, while the inner bulk can keep stable. With the local structure of PS_4^{3-} polyanion revealed by in-situ S *K*-edge and P *K*-edge XAS, we found that the surface undergoes two degradation routes: the reversible hydration and irreversible hydrolysis. The PS_4^{3-} unit could absorb H_2O as well as react with H_2O, causing the elimination of S and oxidation products of phosphate and sulphate. The correlation between lithium-ion conduction and structural evolution with a trace of water could pave the way for practical large-scale production of sulfide-based solid-state batteries.

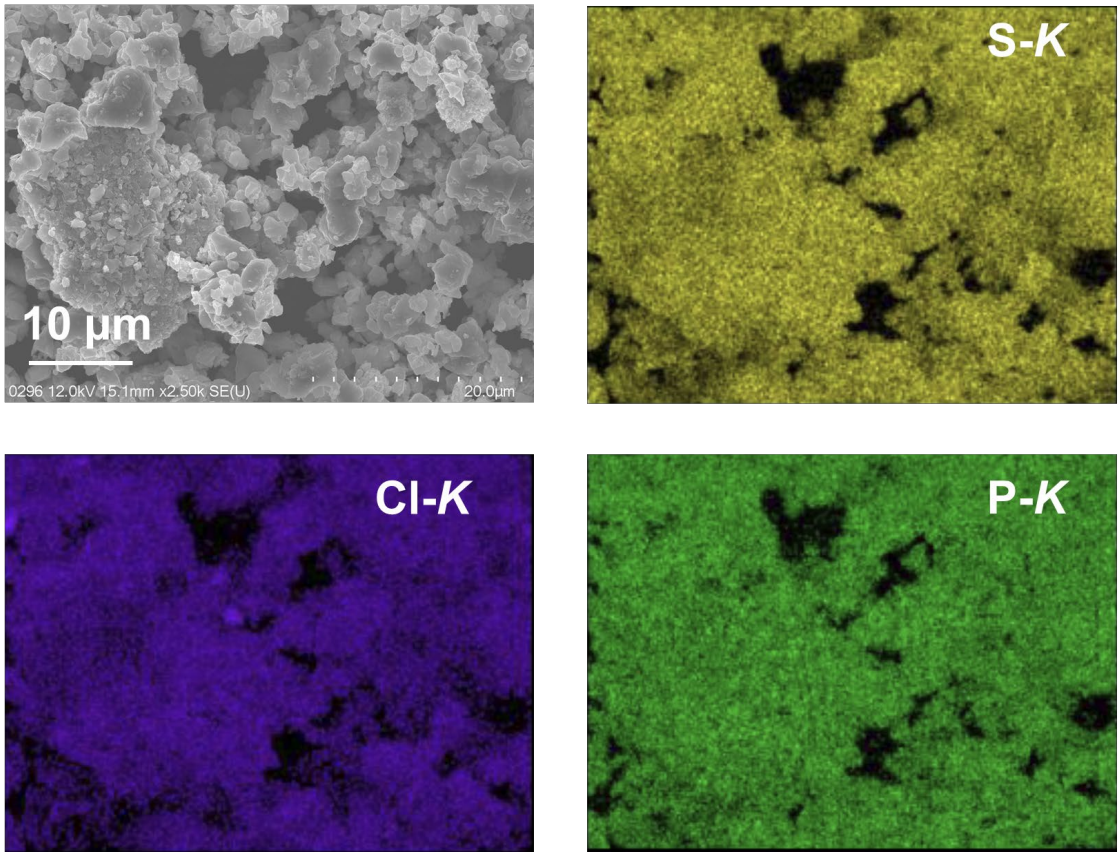

Figure 5.1 SEM-EDS mapping of pristine $Li_{7-x}PS_{6-x}Cl_x$.

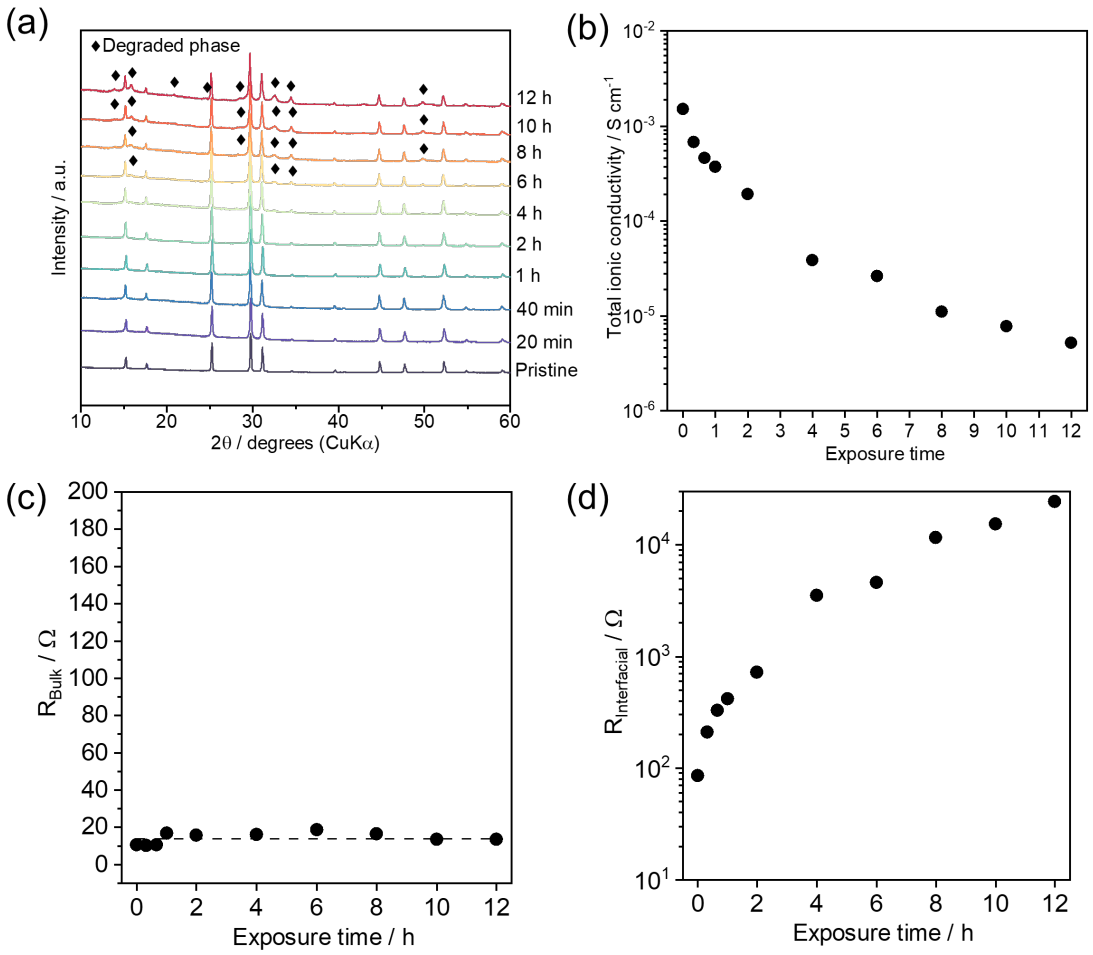

Figure 5.2 (a) The structure evolution and change of ionic conductivity of $Li_{7-x}PS_{6-x}Cl_x$ solid electrolyte after moisture exposure. The XRD patterns of $Li_{7-x}PS_{6-x}Cl_x$ at pristine, and after exposure to the air of - 20°C dew point for different time from 20 min to 12 h (b) The relationship between the exposure time and ionic conductivity for $Li_{7-x}PS_{6-x}Cl_x$. (c) The plot of bulk resistance with different exposure time. (d) The plot of interfacial resistance with different exposure time.

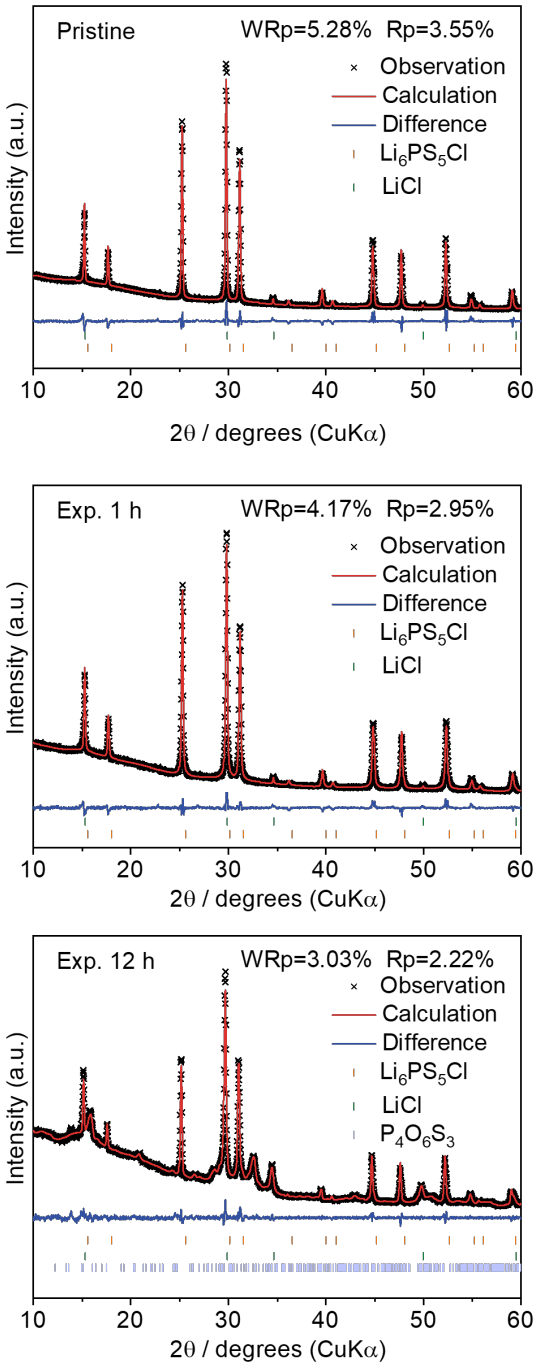

Figure 5.3 XRD refinement of $Li_{7-x}PS_{6-x}Cl_x$ for pristine, exposed to -20°C moisture for 1 h and exposed to -20 ° C moisture for 12 h. The main phase ($Li_{7-x}PS_{6-x}Cl_x$) is refined with Rietveld refinement, and LiCl and $P_4O_6S_3$ are refinement with Le Bail method.

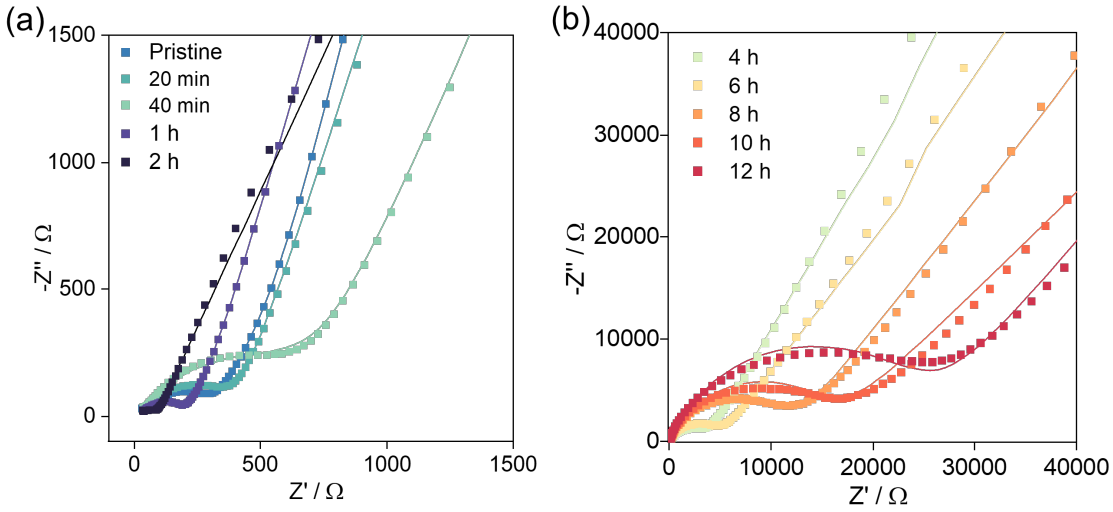

Figure 5.4 The Nyquist plots of $Li_{7-x}PS_{6-x}Cl_x$ samples after exposure to moisture with dew point of -20 °C for 0, 20 min, 40 min, and 1 h, 2 h, 4 h, 6 h, 8 h, 10 h and 12 h. The points are experimental data and the curves correspond to fitting result.

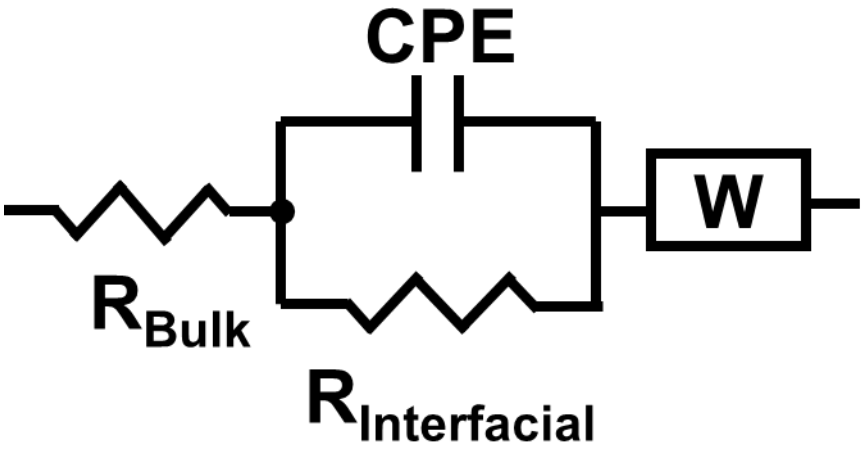

Figure 5.5 The equivalent circuit for fitting the Nyquist plots.

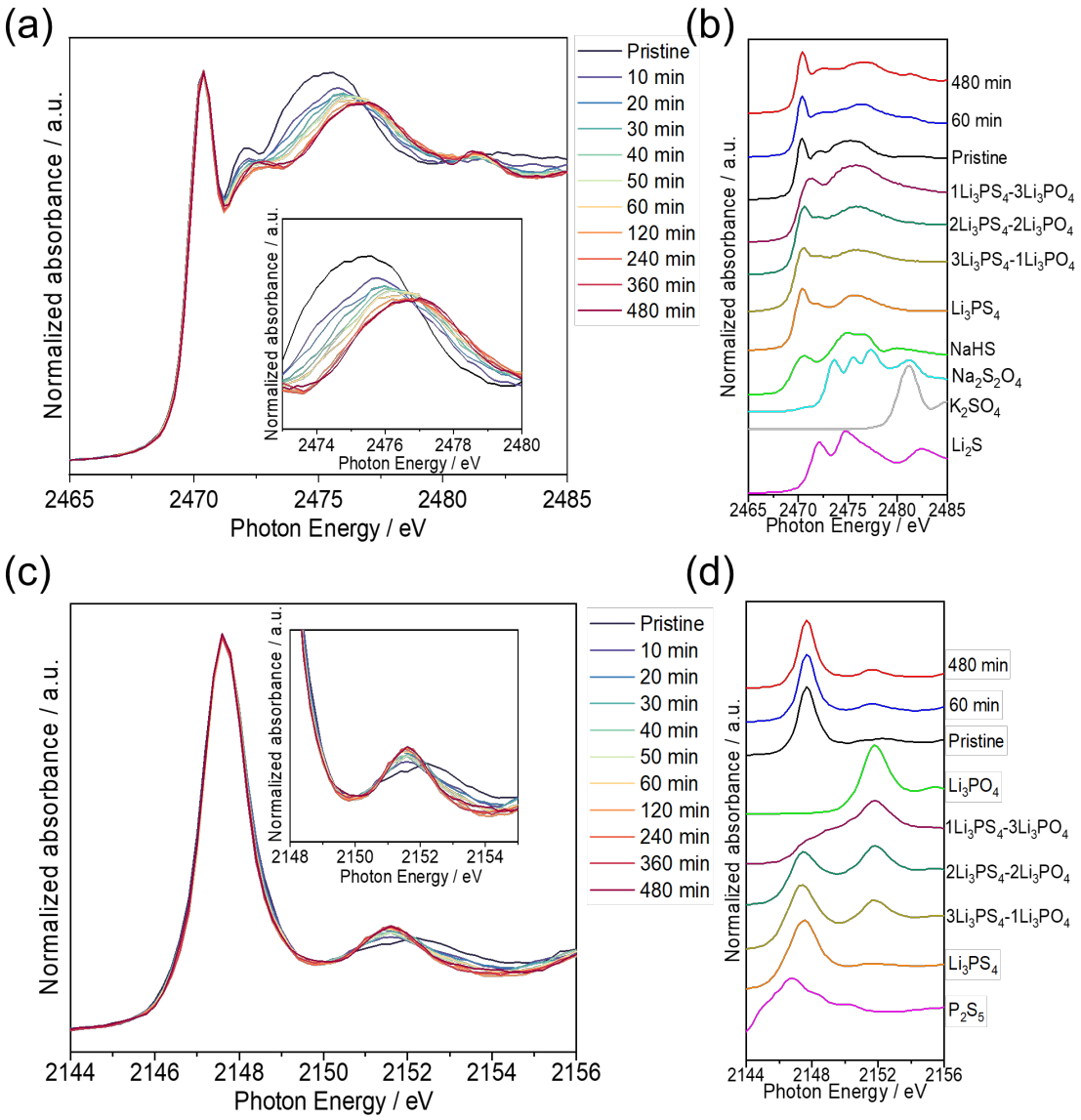

Figure 5.6 In-situ XAS spectra of S *K*-edge at -20°C dew point with different exposure time (a) for $Li_{7-x}PS_{6-x}Cl_x$ and (b) compared with standard materials. In-situ XAS spectra of P *K*-edge at -20°C dew point with different exposure time (c) for $Li_{7-x}PS_{6-x}Cl_x$ and (d) compared with standard materials.

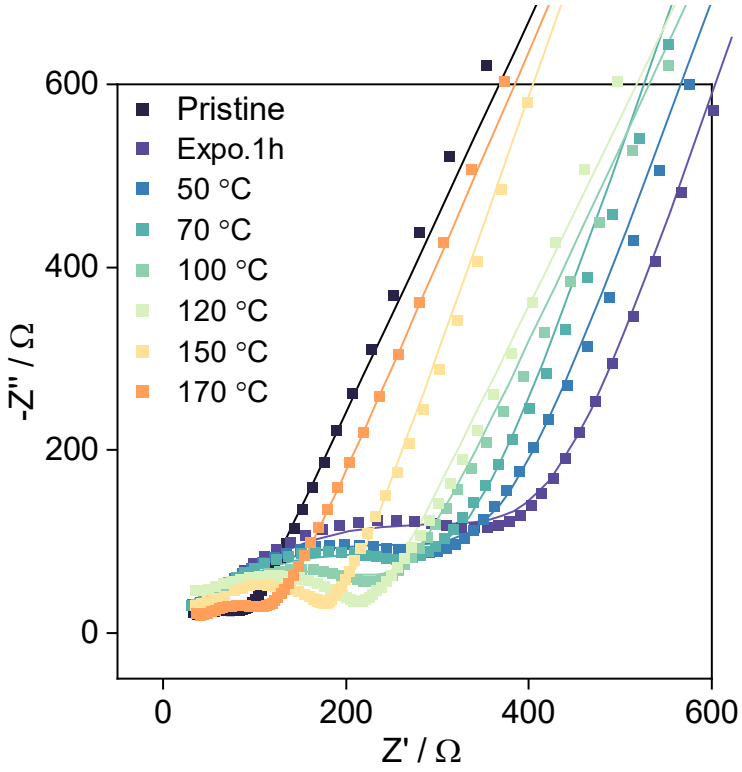

Figure 5.7 The Nyquist plots of $Li_{7-x}PS_{6-x}Cl_x$ samples after exposure to moisture with dew point of -20 °C for 1 h and then heat treatment at 100, 150, 170 and 250 °C for 2 h. The points are experimental data and the curves correspond to fitting result.

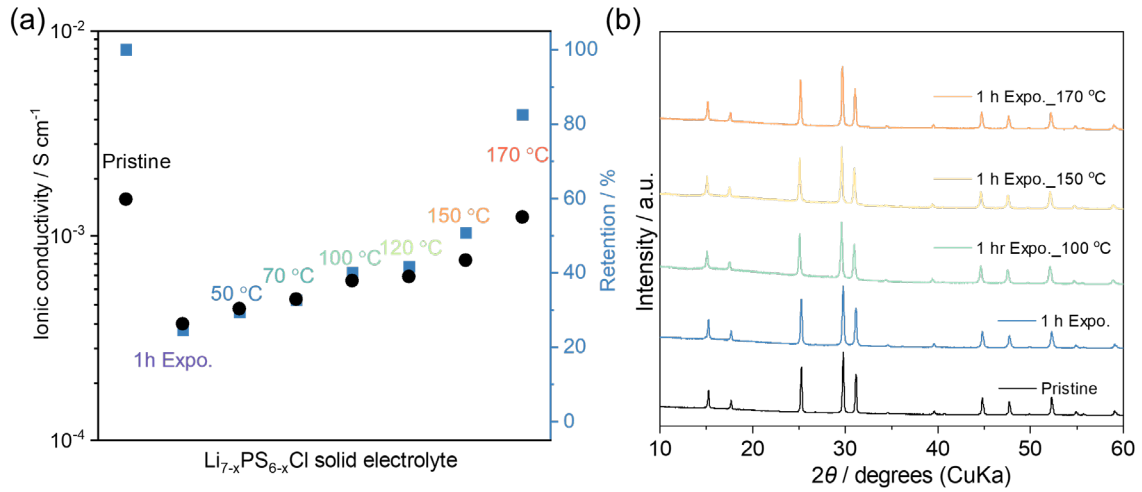

Figure 5.8 (a) The ionic conductivities and corresponding ionic conductivity retention of $Li_{7-x}PS_{6-x}Cl_x$ at pristine state, after 1 h-exposure to the moisture of -20°C dew point, and with heat treatment for 2h at different temperatures under vacuum after 1 h-exposure to the moisture of -20°C dew point. (b) The XRD patterns of $Li_{7-x}PS_{6-x}Cl_x$ samples after exposure to moisture with dew point of -20 °C for 1 h and heat treatment at 100, 150 and 170 °C for 2 h under vacuum.

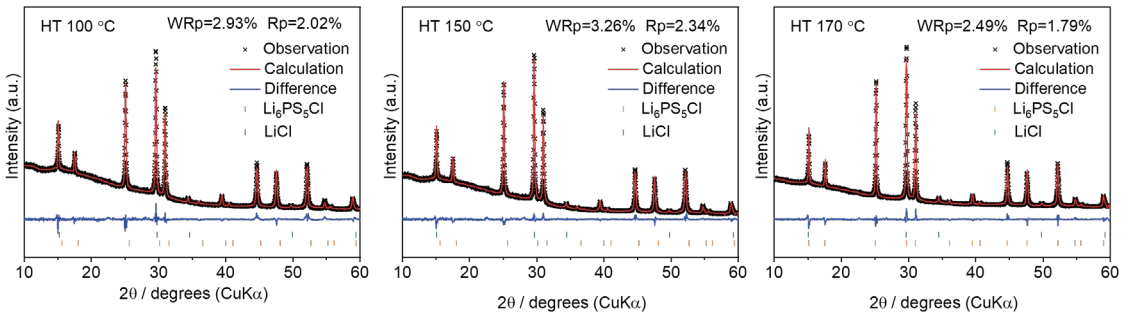

Figure 5.9 XRD refinement of $Li_{7-x}PS_{6-x}Cl_x$ with heat treatment at 100, 150 and 170 °C for 2 h after exposed to -20°C moisture for 1 h. The main phase ($Li_{7-x}PS_{6-x}Cl_x$) is refined with Rietveld refinement, and LiCl is refined with Le Bail method.

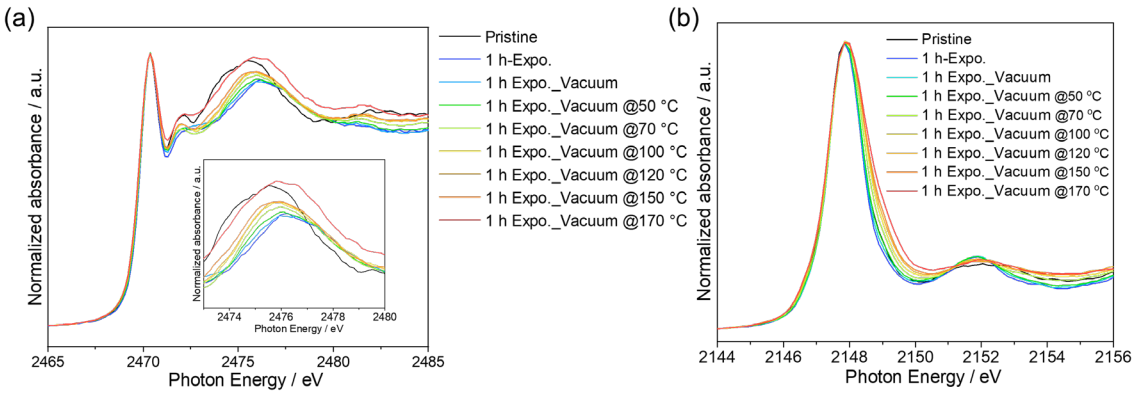

Figure 5.10 (a) In-situ XAS spectra of S *K*-edge for $Li_{7-x}PS_{6-x}Cl_x$ exposed to the moisture of -20°C dew point for 1 h, then with heat treatment for 2h at different temperatures under vacuum. (b) In-situ XAS spectra of P *K*-edge for $Li_{7-x}PS_{6-x}Cl_x$ exposed to the moisture of -20°C dew point for 1 h, then with heat treatment for 2h at different temperatures under vacuum.

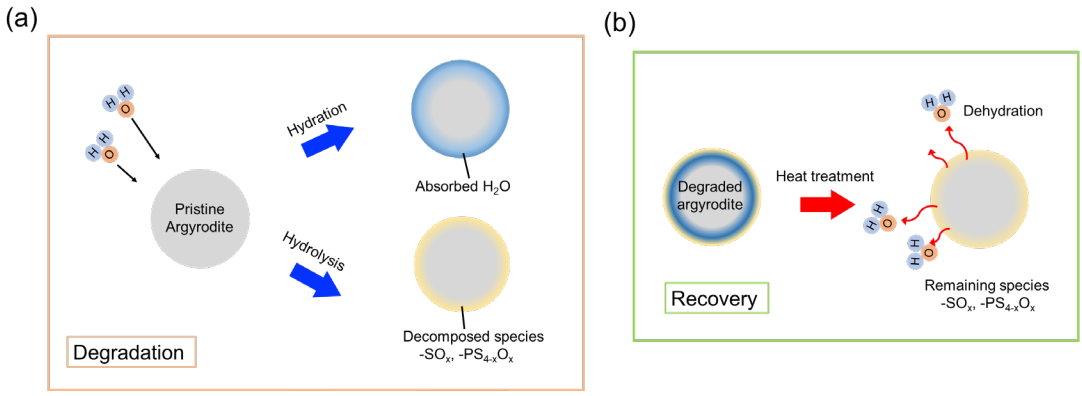

Figure 5.11 The model of $Li_{7-x}PS_{6-x}Cl_x$ (a) degradation due to moisture exposure with a trace of water and (b) recovery via heating treatment under vacuum.

Table 5.1 Structure information of $Li_{7-x}PS_{6-x}Cl_x$ for pristine, exposed to moisture of -20 °C dew point for 1 h and exposed to -20 ° C moisture for 12 h, obtained from Rietveld refinement.

(a) Pristine $Li_{7-x}PS_{6-x}Cl_x$. The space group is $F\bar{4}3m$, a=b=c=9.8310(2) Å. The final R factors are R_p=3.55% $_wR_p$=5.28%.

Atom site	Wyckoff	x/a	y/b	z/c	Occ.	U
Li1	48h	0.35567	0.35567	-0.00702	0.5	0.16
P	4b	0.5	0.5	0.5	1	0.013
S1/Cl1	4a	0	0	0	0.596/0.404	0.012
S2/Cl2	4d	0.75	0.75	0.75	0.404/0.596	0.013
S3	16e	0.12625	-0.12625	0.62625	1	0.02

(b) $Li_{7-x}PS_{6-x}Cl_x$ after 1 h exposure to the moisture of -20 °C dew point. The space group is $F\bar{4}3m$, a=b=c=9.8190(8) Å. The final R factors are R_p=2.95% $_wR_p$=4.17%.

Atom site	Wyckoff	x/a	y/b	z/c	Occ.	U
Li1	48h	0.35354	0.35354	-0.00777	0.447	0.125
P	4b	0.5	0.5	0.5	1	0.02
S1/Cl1	4a	0	0	0	0.536/0.449	0.021
S2/Cl2	4d	0.75	0.75	0.75	0.382/0.618	0.015
S3	16e	0.12625	-0.12625	0.62625	0.936	0.025

(c) $Li_{7-x}PS_{6-x}Cl_x$ after 12 h exposure to the moisture of -20 °C dew point. The space group is $F\bar{4}3m$, a=b=c=9.8306(2) Å. The final R factors are R_p=2.22% $_wR_p$=3.03%.

Atom site	Wyckoff	x/a	y/b	z/c	Occ.	U
Li1	48h	0.35155	0.35155	-0.04091	0.405	0.219
P	4b	0.5	0.5	0.5	1	0.021
S1/Cl1	4a	0	0	0	0.272/0.728	0.022
S2/Cl2	4d	0.75	0.75	0.75	0.370/0.630	0.014
S3	16e	0.12625	-0.12625	0.62625	0.873	0.033

Table 5.2 Fitting parameters of high-frequence impedance for $Li_{7-x}PS_{6-x}Cl_x$ samples after exposure to moisture with dew point of -20 °C for 0, 20 min, 40 min, 1 h, 2 h, 4 h, 6 h, 8 h, 10 h and 12 h.

	$R_{Bulk}(\Omega)$	CPE-T	CPE-P	$R_{Interfacial}(\Omega)$	W-R	W-T	W-P	C(F)
Pristine	10.68	3.10×10^{-7}	0.538	78.29	266710	0.0583	0.7234	4.98×10^{-10}
20 min	10.38	3.10×10^{-7}	0.558	210.5	290370	0.0618	0.8008	2.18×10^{-10}
40 min	10.62	2.64×10^{-7}	0.567	326.1	420550	0.0608	0.805	1.67×10^{-10}
1 h	16.71	1.99×10^{-7}	0.586	415.2	499490	0.0607	0.8026	2.16×10^{-10}
2 h	15.74	1.01×10^{-7}	0.616	720.3	407390	0.0371	0.7487	1.52×10^{-10}
4 h	16.25	8.78×10^{-9}	0.731	3520	203500	0.027	0.6593	1.86×10^{-10}
6 h	18.65	3.28×10^{-9}	0.775	4597	155540	0.0359	0.5771	1.30×10^{-10}
8 h	16.59	2.24×10^{-9}	0.777	11581	234260	0.0388	0.5764	3.50×10^{-10}
10 h	13.59	2.94×10^{-9}	0.752	15212	208150	0.0808	0.4938	2.75×10^{-10}
12 h	13.59	2.44×10^{-9}	0.762	24167	286590	0.0454	0.5581	1.89×10^{-10}

Table 5.3 Fitting parameters of high-frequence impedance for $Li_{7-x}PS_{6-x}Cl_x$ samples at pristine state, after exposure to moisture with dew point of -20 °C for 1 h and with heat treatment at 50, 70, 100, 120, 150 and 170 °C for 2 h after exposed to -20°C moisture for 1 h.

	$R_{Bulk}(\Omega)$	CPE-T	CPE-P	$R_{Interfacial}(\Omega)$	W-R	W-T	W-P	C(F)
Pristine	10.68	3.10×10^{-7}	0.538	85.29	266710	0.0583	0.7234	4.98×10^{-10}
1 h	16.71	1.99×10^{-7}	0.586	415.2	499490	0.0607	0.8026	2.16×10^{-10}
50 °C	10.59	2.91×10^{-7}	0.556	363.4	424220	0.061	0.7865	2.21×10^{-10}
70 °C	10.59	3.50×10^{-7}	0.555	328.1	356940	0.0606	0.7944	2.54×10^{-10}
100 °C	13.53	1.54×10^{-7}	0.583	250.2	247460	0.0664	0.7282	2.52×10^{-10}
120 °C	10.53	1.63×10^{-7}	0.777	220.2	234260	0.0668	0.7143	2.90×10^{-10}
150 °C	14.74	1.23×10^{-7}	0.654	180.2	371820	0.0621	0.7847	3.00×10^{-10}
170 °C	18.74	2.48×10^{-7}	0.571	110.6	302510	0.0392	0.7421	5.13×10^{-10}

Table 5.4 Structure information of $Li_{7-x}PS_{6-x}Cl_x$ with heat treatment at 100, 150 and 170 °C for 2 h under vacuum after exposed to -20 °C moisture for 1 h.

(a) $Li_{7-x}PS_{6-x}Cl_x$ with heat treatment at 100 °C. The space group is $F\bar{4}3m$, a=b=c=9.8235(6) Å. The final R factors are R_p=2.02% $_WR_p$=2.93%.

Atom site	Wyckoff	x/a	y/b	z/c	Occ.	U
Li1	48h	0.33143	0.33143	-0.00669	0.499	0.066
P	4b	0.5	0.5	0.5	1	0.014
S1/Cl1	4a	0	0	0	0.481/0.519	0.027
S2/Cl2	4d	0.75	0.75	0.75	0.380/0.620	0.019
S3	16e	0.12518	-0.12518	0.62518	0.943	0.005

(b) $Li_{7-x}PS_{6-x}Cl_x$ with heat treatment at 150 °C. The space group is $F\bar{4}3m$, a=b=c=9.8190(8) Å. The final R factors are R_p=2.34% $_WR_p$=3.26%.

Atom site	Wyckoff	x/a	y/b	z/c	Occ.	U
Li1	48h	0.34699	0.34699	0.00489	0.513	0.068
P	4b	0.5	0.5	0.5	1	0.005
S1/Cl1	4a	0	0	0	0.486/0.513	0.02
S2/Cl2	4d	0.75	0.75	0.75	0.342/0.658	0.009
S3	16e	0.12507	-0.12507	0.62507	0.993	0.025

(c) $Li_{7-x}PS_{6-x}Cl_x$ with heat treatment at 170 °C. The space group is $F\bar{4}3m$, a=b=c=9.8306(2) Å. The final R factors are R_p=1.79% $_WR_p$=2.49%.

Atom site	Wyckoff	x/a	y/b	z/c	Occ.	U
Li1	48h	0.35665	0.35665	0.01072	0.479	0.172
P	4b	0.5	0.5	0.5	1	0.012
S1/Cl1	4a	0	0	0	0.493/0.507	0.022
S2/Cl2	4d	0.75	0.75	0.75	0.349/0.651	0.014
S3	16e	0.12571	-0.12571	0.62571	0.993	0.024

References

(1) Armaroli, N.; Balzani, V. Towards an electricity-powered world. *Energy Environ. Sci.* **2011**, *4* (9), 3193-3222.

(2) Dunn, B.; Kamath, H.; Tarascon, J.-M. Electrical energy storage for the grid: a battery of choices. *Science* **2011**, *334* (6058), 928-935.

(3) Famprikis, T.; Canepa, P.; Dawson, J. A.; Islam, M. S.; Masquelier, C. Fundamentals of inorganic solid-state electrolytes for batteries. *Nat. Mater.* **2019**, *18* (12), 1278-1291.

(4) Gao, Z.; Sun, H.; Fu, L.; Ye, F.; Zhang, Y.; Luo, W.; Huang, Y. Promises, challenges, and recent progress of inorganic solid-state electrolytes for all-solid-state lithium batteries. *Adv. Mater.* **2018**, *30* (17), 1705702.

(5) Wang, C.; Liang, J.; Zhao, Y.; Zheng, M.; Li, X.; Sun, X. All-solid-state lithium batteries enabled by sulfide electrolytes: from fundamental research to practical engineering design. *Energy Environ. Sci.* **2021**, *14* (5), 2577-2619.

(6) Wu, J.; Liu, S.; Han, F.; Yao, X.; Wang, C. Lithium/sulfide all-solid-state batteries using sulfide electrolytes. *Adv. Mater.* **2021**, *33* (6), 2000751.

(7) Nikodimos, Y.; Huang, C.-J.; Taklu, B. W.; Su, W.-N.; Hwang, B. J. Chemical stability of sulfide solid-state electrolytes: stability toward humid air and compatibility with solvents and binders. *Energy Environ. Sci.* **2022**, *15* (3), 991-1033.

(8) Lu, P.; Wu, D.; Chen, L.; Li, H.; Wu, F. Air stability of solid-state sulfide batteries and electrolytes. *Electrochem. Energy Rev.* **2022**, *5* (3), 3.

(9) Muramatsu, H.; Hayashi, A.; Ohtomo, T.; Hama, S.; Tatsumisago, M. Structural change of Li_2S–P_2S_5 sulfide solid electrolytes in the atmosphere. *Solid State Ion.* **2011**, *182* (1), 116-119.

(10) Tan, D. H. S.; Banerjee, A.; Deng, Z.; Wu, E. A.; Nguyen, H.; Doux, J.-M.; Wang, X.; Cheng, J.-h.; Ong, S. P.; Meng, Y. S.; et al. Enabling Thin and Flexible Solid-State Composite Electrolytes by the Scalable Solution Process. *ACS Appl. Energy Mater.* **2019**, *2* (9), 6542-6550.

(11) Chen, Y.-T.; Marple, M. A. T.; Tan, D. H. S.; Ham, S.-Y.; Sayahpour, B.; Li, W.-K.; Yang, H.; Lee, J. B.; Hah, H. J.; Wu, E. A.; et al. Investigating dry room compatibility of sulfide solid-state electrolytes for scalable manufacturing. *J. Mater. Chem. A* **2022**, *10* (13), 7155-7164.

(12) Khurram Tufail, M.; Ahmad, N.; Zhou, L.; Faheem, M.; Yang, L.; Chen, R.; Yang, W. Insight on air-induced degradation mechanism of $Li_7P_3S_{11}$ to design a chemical-stable solid electrolyte with high Li_2S utilization in all-solid-state Li/S batteries. *Chem. Eng. J.* **2021**, *425*.

(13) Muramatsu, H.; Hayashi, A.; Ohtomo, T.; Hama, S.; Tatsumisago, M. Structural change of Li_2S–P_2S_5 sulfide solid electrolytes in the atmosphere. *Solid State Ionics* **2011**, *182* (1), 116-119.

(14) Ohtomo, T.; Hayashi, A.; Tatsumisago, M.; Kawamoto, K. Glass Electrolytes with High Ion Conductivity and High Chemical Stability in the System LiI-Li_2O-Li_2S-P_2S_5. *Electrochemistry* **2013**, *81* (6), 428-431.

(15) Li, Y.; Li, J.; Cheng, J.; Xu, X.; Chen, L.; Ci, L. Enhanced Air and Electrochemical Stability of $Li_7P_3S_{11}$–Based Solid Electrolytes Enabled by Aliovalent Substitution of SnO_2. *Adv. Mater. Interfaces* **2021**, *8* (14).

(16) Banerjee, A.; Park, K. H.; Heo, J. W.; Nam, Y. J.; Moon, C. K.; Oh, S. M.; Hong, S. T.; Jung, Y. S. Na_3SbS_4 : A Solution Processable Sodium Superionic Conductor for All-Solid-State Sodium-Ion Batteries. *Angew. Chem. Int. Ed.* **2016**, *55* (33), 9634-9638.

(17) Liu, Y.; Zhang, R.; Wang, J.; Wang, Y. Current and future lithium-ion battery manufacturing. *iScience* **2021**, *24* (4), 102332.

(18) Zhang, Y. S.; Courtier, N. E.; Zhang, Z.; Liu, K.; Bailey, J. J.; Boyce, A. M.; Richardson, G.; Shearing, P. R.; Kendrick, E.; Brett, D. J. L. A Review of Lithium-Ion Battery Electrode Drying: Mechanisms and Metrology. *Adv. Energy Mater.* **2021**, *12* (2).

(19) Sano, H.; Morino, Y.; Yabuki, A.; Sato, S.; Itayama, N.; Matsumura, Y.; Iwasaki, M.; Takehara, M.; Abe, T.; Ishiguro, Y.; et al. AC Impedance Analysis of the Degeneration and Recovery of Argyrodite Sulfide-Based Solid Electrolytes under Dry-Room-Simulated Condition. *Electrochemistry* **2022**, *90* (3), 037012-037012.

(20) Morino, Y.; Sano, H.; Kawaguchi, S.; Hori, S.; Sakuda, A.; Takahashi, T.; Miyashita, N.; Hayashi, A.; Kanno, R. High-Frequency Impedance Spectroscopic Analysis of Argyrodite-Type Sulfide-Based Solid Electrolyte upon Air Exposure. *J. Phys. Chem. C* **2023**, *127* (37), 18678-18683.

(21) Morino, Y.; Sano, H.; Kawamoto, K.; Fukui, K.-i.; Takeuchi, M.; Sakuda, A.; Hayashi, A. Degradation of an argyrodite-type sulfide solid electrolyte by a trace of water: A spectroscopic analysis. *Solid State Ion.* **2023**, *392*.

(22) Hayashi, A.; Muramatsu, H.; Ohtomo, T.; Hama, S.; Tatsumisago, M. Improvement of chemical stability of Li_3PS_4 glass electrolytes by adding M_xO_y (M = Fe, Zn, and Bi) nanoparticles. *J. Mater. Chem. A* **2013**, *1* (21).

(23) Kimura, T.; Kato, A.; Hotehama, C.; Sakuda, A.; Hayashi, A.; Tatsumisago, M. Preparation and characterization of lithium ion conductive Li_3SbS_4 glass and glass-ceramic electrolytes. *Solid State Ion.* **2019**, *333*, 45-49.

(24) Morgan, B. J. Mechanistic Origin of Superionic Lithium Diffusion in Anion-Disordered Li_6PS_5X Argyrodites. *Chem. Mater.* **2021**, *33* (6), 2004-2018.

(25) Cortona, P. Direct determination of self-consistent total energies and charge densities of solids: A study of the cohesive properties of the alkali halides. *Phys. Rev. B* **1992**, *46* (4), 2008.

(26) Schlenker, R.; Hansen, A.-L.; Senyshyn, A.; Zinkevich, T.; Knapp, M.; Hupfer, T.; Ehrenberg, H.; Indris, S. Structure and Diffusion Pathways in Li_6PS_5Cl Argyrodite from Neutron Diffraction, Pair-Distribution Function Analysis, and NMR. *Chem. Mater.* **2020**, *32* (19), 8420-8430.

(27) Zhou, L.; Park, K.-H.; Sun, X.; Lalère, F.; Adermann, T.; Hartmann, P.; Nazar, L. F. Solvent-Engineered Design of Argyrodite Li_6PS_5X (X = Cl, Br, I) Solid Electrolytes with High Ionic Conductivity. *ACS Energy Lett.* **2018**, *4* (1), 265-270.

(28) Zhang, J.; Gu, X. Hydrolysis mechanism of Li-argyrodite Li_6PS_5Cl in air. *Rare Metals* **2022**, *42* (1), 47-55.

(29) Seol, K.; Kaliyaperumal, C.; Uthayakumar, A.; Yoon, I.; Lee, G.; Shin, D. Enhancing the Moisture Stability and Electrochemical Performances of Li_6PS_5Cl Solid Electrolytes through Ga Substitution. *Electrochim. Acta* **2023**, *441*.

(30) Indrawan, R. F.; Gamo, H.; Nagai, A.; Matsuda, A. Chemically Understanding the Liquid-Phase Synthesis of Argyrodite Solid Electrolyte Li6PS5Cl with the Highest Ionic Conductivity for All-Solid-State Batteries. *Chem. Mater.* **2023**, *35* (6), 2549-2558.

(31) Zhang, W.; Richter, F. H.; Culver, S. P.; Leichtweiss, T.; Lozano, J. G.; Dietrich, C.; Bruce, P. G.; Zeier, W. G.; Janek, J. Degradation Mechanisms at the $Li_{10}GeP_2S_{12}/LiCoO_2$

Cathode Interface in an All-Solid-State Lithium-Ion Battery. *ACS Appl. Mater. Interfaces* **2018**, *10* (26), 22226-22236.

(32) Zhang, W.; Weber, D. A.; Weigand, H.; Arlt, T.; Manke, I.; Schroder, D.; Koerver, R.; Leichtweiss, T.; Hartmann, P.; Zeier, W. G.; et al. Interfacial Processes and Influence of Composite Cathode Microstructure Controlling the Performance of All-Solid-State Lithium Batteries. *ACS Appl. Mater. Interfaces* **2017**, *9* (21), 17835-17845.

(33) Irvine, J. T.; Sinclair, D. C.; West, A. R. Electroceramics: characterization by impedance spectroscopy. *Adv. Mater.* **1990**, *2* (3), 132-138.

(34) Kim, K. J.; Balaish, M.; Wadaguchi, M.; Kong, L.; Rupp, J. L. Solid-state Li–metal batteries: challenges and horizons of oxide and sulfide solid electrolytes and their interfaces. *Adv. Energy Mater.* **2021**, *11* (1), 2002689.

(35) Nikodimos, Y.; Jiang, S.-K.; Huang, S.-J.; Taklu, B. W.; Huang, W.-H.; Desta, G. B.; Tekaligne, T. M.; Muche, Z. B.; Lakshmanan, K.; Chang, C.-Y.; et al. Moisture Robustness of Li_6PS_5Cl Argyrodite Sulfide Solid Electrolyte Improved by Nano-Level Treatment with Lewis Acid Additives. *ACS Energy Lett.* **2024**, *9* (4), 1844-1852.

Chapter 6 General Conclusion

ASSLSBs are one of the most promising candidates for next generation large-scale energy storage devices due to the potential high energy density, good safety and long-term cyclability. However, the insulating nature of sulfur and lithium sulfide as cathode impedes the development of ASSLSBs towards practical application. To solve this issue, high conductive cathodes were developed in this work.

In chapter 1, the working principles of lithium-ion batteries and lithium-sulfur batteries have been briefly introduced. ASSLSBs are promising yet facing many challenges, which are divided into cathodes, solid-state electrolytes and anodes. And fundamental problems in cathodes and related improvement research were introduced.

In chapter 2, a high-performance Li_2S-PI_3-C composite cathode has been developed and investigated. By cation-anion dual doping, point defect was introduced into Li_2S structure, leading to dramatically increased ionic conductivity, which enables elimination of SSE in composite cathode.

In chapter 3, Li_2S-LiI-MoS_2 integrated cathode with high electronic and ionic conductivities over 10^{-4} S cm^{-1} by one-step ball-milling method. Without any carbon and solid electrolytes additives in cathode composite, the optimized Li_2S-LiI-MoS_2 integrated cathode delivers the highest energy density of 1020 Wh kg^{-1} at the cathode level and superior power density to other cathodes for ASSLSB. The utilization of the reversible cationic redox of Mo and anionic redox of S in the Li_2S-LiI-MoS_2 cathode leads to the high energy density. The high electronic and ionic conductivities at pristine state and the formed LiI domain during charging lead to the high power density.

In chapter 4, the electron and ion paths were modified by tuning Li_2S-LiI-MoS_2 active material and Li_6PS_5Cl SSE. By optimizing their ratio, Li_2S-LiI-MoS_2-Li_6PS_5Cl composite cathode realized high overall cathode capacity and good rate capability. X-ray CT image reveals the three-dimensional conductive pathway through the composite cathode.

In chapter 5, the degradation behavior and mechanism of the typical argyrodite sulfide solid electrolyte, $Li_{7-x}PS_{6-x}Cl_x$ ($x\approx1$), exposed to a trace of water, was investigated degradation behavior and mechanism by Rietveld refinement of XRD, high-frequency impedance and in-situ X-ray absorption spectroscopy (XAS). The decreased ionic

conductivities, change in electronic structure and degradation mechanism with different exposure time were carefully analyzed. The partial recovery of ionic conductivities and electronic structure could be achieved by vacuum heat treatment after moisture exposure. And the recovery mechanism under different heat treatment conditions, and corresponding structural evolution were also understood by in-situ XAS.

List of Publications

Chapter 2

Improving electrochemical performance of Li_2S cathode based on point defect control with cation/anion dual doping

Wenli Pan, Kentaro Yamamoto*, Nobuya Machida, Toshiyuki Matsunaga, Mukesh Kumar, Neha Thakur, Toshiki Watanabe, Atsushi Sakuda, Akitoshi Hayashi, Masahiro Tatsumisago and Yoshiharu Uchimoto

Journal of Materials Chemistry A, **2023**, 11, 24637-24643

Chapter 3

An electron/ion dual conductive integrated cathode using cationic/anionic redox for high-energy-density all-solid-state lithium-sulfur batteries

Wenli Pan, Kentaro Yamamoto*, Toshiki Watanabe, Mukesh Kumar, Neha Thakur, Tomoki Uchiyama, Kentaro Uesugi, Akihisa Takeuchi, Atsushi Sakuda, Akitoshi Hayashi, Masahiro Tatsumisago, Toshiyuki Matsunaga and Yoshiharu Uchimoto

Batteries & Supercaps, **2024**, 7, e202300427

Chapter 4

Tuning the ionic and electronic paths in Li_2S-based cathode for high-rate performance all-solid-state lithium-sulfur batteries

Wenli Pan, Toshiki Watanabe*, Toshiyuki Matsunaga, Mukesh Kumar, Neha Thakur, Kentaro Yamamoto, Masayuki Uesugi, Akihisa Takeuchi, Atsushi Sakuda, Akitoshi Hayashi, Masahiro Tatsumisago and Yoshiharu Uchimoto

Solid State Ionics, **2024**, 406, 116479

Acknowledgement

I would like to express my gratitude to all those who helped me during the writing of this thesis.

Firstly, I would like to express my sincere gratitude to my supervisor Prof. Uchimoto for his continuous support and help during my whole doctoral research. Without his general help, it could never be accomplished like present form.

Special thanks are expressed to Prof. Yamamoto, who has given me much advice in detail and patiently for these years. I am also grateful to Prof. Matsunaga, who taught me how to do refinement with XRD, PDF and neutron diffraction and always encouraged me with smile, to Prof. Watanabe, who is a real expert at CT analysis, and to Prof. Uchiyama, who helped me measure XAFS carefully. I also would like to thank Dr. Kumar and Dr. Thakur, who helped me to revise my manuscripts a lot.

Many thanks for Ms. Yu-han Tang's countless help, support and company for over two years. I feel so lucky and grateful to meet you in Mizuki-dorm.

I would like to thank all members of Uchimoto lab for their helps, discussions and encouragement throughout this study.

Finally, I appreciate my parents support all the time. Your love inspires me no matter where I go. And I would like to thank my boyfriend, Dr. Wen-hao Guan. You are the star in my life and shine me during my doctoral course.

Wenli Pan

Kyoto, Japan

April, 2024

※　著作権等

Improving electrochemical performance of Li_2S cathode based on point defect control with cation/anion dual doping

Wenli Pan, Kentaro Yamamoto, Nobuya Machida, Toshiyuki Matsunaga, Mukesh Kumar, Neha Thakur, Toshiki Watanabe, Atsushi Sakuda, Akitoshi Hayashi, Masahiro Tatsumisago and Yoshiharu Uchimoto

(“Journal of Materials Chemistry A”, October 2023, Volume 11, pp 24637-24643). DOI: 10.1039/D3TA05426H

The final publication is available at RSC Publishing via https://doi.org/10.1039/D3TA05426H

An electron/ion dual conductive integrated cathode using cationic/anionic redox for high-energy-density all-solid-state lithium-sulfur batteries

Wenli Pan, Kentaro Yamamoto, Toshiki Watanabe, Mukesh Kumar, Neha Thakur, Tomoki Uchiyama, Kentaro Uesugi, Akihisa Takeuchi, Atsushi Sakuda, Akitoshi Hayashi, Masahiro Tatsumisago, Toshiyuki Matsunaga and Yoshiharu Uchimoto

(“Batteries & Supercaps”, January 2024, Volume 7). DOI: 10.1002/batt.202300427

The final publication is available at Wiley Publishing via https://doi.org/10.1002/batt.202300427

Tuning the ionic and electronic paths in Li_2S-based cathode for high-rate performance all-solid-state lithium-sulfur batteries

Wenli Pan, Toshiki Watanabe, Toshiyuki Matsunaga, Mukesh Kumar, Neha Thakur, Kentaro Yamamoto, Masayuki Uesugi, Akihisa Takeuchi, Atsushi Sakuda, Akitoshi Hayashi, Masahiro Tatsumisago and Yoshiharu Uchimoto

(“Solid State Ionics”, March 2024, Volume 406, p 116479). DOI: 10.1016/j.ssi.2024.116479

The final publication is available at Elsevier Publishing via https://doi.org/10.1016/j.ssi.2024.116479